



NIST Special Publication 792

NIST
PUBLICATIONS

Technical Digest Symposium on Optical Fiber Measurements, 1990

Sponsored by the National Institute of Standards and Technology
in cooperation with the IEEE Optical Communications Committee
and the Optical Society of America

QC
100
U57
#792
1990
C.2



NATIONAL INSTITUTE OF STANDARDS &
TECHNOLOGY

Research Information Center
Gaithersburg, MD 20899

Technical Digest—Symposium on Optical Fiber Measurements, 1990

Digest of a Symposium sponsored by the
National Institute of Standards and Technology
in cooperation with the
IEEE Optical Communications Committee
and the Optical Society of America

September 11–12, 1990
National Institute of Standards and Technology
Boulder, Colorado 80303-3328

Edited by
G. W. Day
D. L. Franzen

Electromagnetic Technology Division
Center for Electronics and Electrical Engineering
National Engineering Laboratory
National Institute of Standards and Technology
Boulder, Colorado 80303-3328



U.S. DEPARTMENT OF COMMERCE, Robert A. Mosbacher, Secretary
NATIONAL INSTITUTE OF STANDARDS AND TECHNOLOGY, John W. Lyons, Director
Issued September 1990

National Institute of Standards and Technology Special Publication 792
Natl. Inst. Stand. Technol. Spec. Publ. 792, 210 pages (Sept. 1990)
CODEN: NSPUE2

U.S. GOVERNMENT PRINTING OFFICE
Washington: 1990

For sale by the Superintendent of Documents, U.S. Government Printing Office, Washington, DC 20402

PREFACE

This volume contains summaries of the papers presented at the sixth biennial Symposium on Optical Fiber Measurements, held at the Department of Commerce Laboratories in Boulder, Colorado, September 11-12, 1990.

There are 45 papers included — 9 invited and 36 contributed. Invited speakers were nominated and reviewed by the committee and selected by the chairmen. Contributed papers were solicited, ranked by the committee, and then selected by those rankings.

We have found that both the quality and quantity of contributed papers has increased over the years. To accommodate that, we have found ways to increase the number of papers accepted; this year, for the first time, the program included a poster session. Also this year, for the first time, the number of papers accepted from outside the U.S. exceeded those from within.

Optical time domain reflectometry (OTDR) has been an important topic at many of the Symposia, and this year advanced variants of the technique are featured prominently. Fiber geometry is another major topic. And, this year we have a full session of contributed papers on measurements in integrated optics.

G. W. Day
D. L. Franzen
Boulder, Colorado
September 1990

Except where attributed to NIST authors, the content of individual sections of this volume has not been reviewed or edited by the National Institute of Standards and Technology. NIST therefore accepts no responsibility for comments or recommendations therein. The mention of trade names in this volume is in no sense an endorsement or recommendation of the National Institute of Standards and Technology.

SYMPOSIUM COMMITTEE

D. L. Franzen, NIST, General Chair
G. W. Day, NIST, Program Chair
W. T. Anderson, Bellcore
A. H. Cherin, AT&T Bell Labs
P. L. François, CNET
R. L. Gallawa, NIST
A. H. Hartog, York
W. T. Kane, Corning
P. S. Lovely, Photon Kinetics
Y. Nagaki, Anritsu
S. A. Newton, Hewlett Packard
W. A. Reed, AT&T Bell Labs
P. R. Reitz, AMP
C. Saravanos, Northern Telecom

CONTENTS

PREFACE	iii
SYMPOSIUM COMMITTEE	iv
Industry standard measurements: A user's perspective Felix P. Kapron, William T. Anderson, Bellcore	1
COST 217 interlaboratory comparison of optical measurements on single-mode fibre couplers J. W. Burgmeijer, W. J. deVries, Netherlands PTT Research; M. Artiglia, P. DiVita, CSELT; R. P. Novák, Swiss PTT; E. Sundberg, Swedish Telecom; L. Nykjoor Kragh, Telecom Denmark; J. Allen, GEC Research; J. Pelayo, Univ. de Zaragoza; N. Gisin, Université de Genève	7
COST 217 mode field diameter measurements intercomparison B. Walker, COST 217 Group	11
Post-mortem analysis of optical fibers H. H. Yuce, J. P. Varachi, P. L. Key, Bellcore	15
Optical frequency domain reflectometry using network analysis techniques David W. Dolfi, Roger L. Jungerman, Hewlett-Packard	21
Long and short range measurements using coherent FMCW reflectometry W. V. Sorin, D. K. Donald, Hewlett-Packard	27
Very low optical return loss measurement using OTDR technique P. Blanchard, P-H. Zongo, P. Facq, J. Rochereau, IRCOM-EOGI and CEDEPE	31
Comparison between OTDR and OLCR with micrometer spatial resolution. New improved OLCR detection scheme and latest measurement results on IOC. R. P. Novák, H. H. Gilgen, P. Beaud, W. Hodel, Swiss PTT and Univ. Berne ...	35
Multiphoton pulse approach in photon-timing OTDR yields enhanced dynamic range and shorter measurement time M. Ghioni, G. Ripamonti, S. Vanoli, S. Pitassi, Politecnico di Milano	39
Characterization of hydrogen diffusion in hermetically coated optical fibers P. J. Lemaire, K. L. Walker, K. S. Kranz, R. G. Huff, F. V. DiMarcello, AT&T Bell Labs	43
The anomalous structure observed in single-mode fiber cutoff wavelength measurements: Theory and solutions Steven A. Jacobs, David W. Peckham, AT&T Bell Labs	49

A recent advance in the measurement of the refractive index profile of optical fibre preforms D. A. Svendsen, I. D. Cook, York Technology	55
Refractive index measurements on single-mode fiber as functions of product parameters, tensile stress and temperature J. J. Carr, S. L. Saikkonen, D. H. Williams, Corning	59
Spatially resolved measurement of high attenuation in integrated optical polarizers Robert K. Hickernell, David L. Veasey, J. Andrew Aust, NIST	63
Waveguide loss and effective indices determination by optical frequency scan of integrated resonant cavities C. DeBernardi, S. Morasca, CSELT	67
Measurement of mode indices of channel waveguides by interferometry Christopher P. Hussell, Ramakant Srivastava, Ramu V. Ramaswamy, Univ. Florida	71
Comparison of time and frequency domain measurement methods for high speed optical modulators W. Charczenko, D. R. Hjelm, A. R. Mickelson, Univ. Colorado	75
Characterization of the dynamic response of a waveguide phase modulator by means of an optical frequency discriminator N. Caponio, P. Gambini, M. Puleo, CSELT	79
Fiber discriminator measurements of phase modulation in an integrated Mach-Zehnder intensity modulator Kok Wai Chang, Geraldine Conrad, Wayne V. Sorin, Hewlett-Packard	83
Characterisation of erbium-doped fibre amplifiers R. I. Laming, Univ. Southampton	87
Measurement of the spectral dependence of absorption cross section for erbium-doped single-mode optical fiber M. P. Singh, D. W. Oblas, J. O. Reese, W. J. Miniscalco, T. Wei, GTE Labs	93
Wavelength characterisation of components for optical networking applications in the 1.5 μm transmission window P. J. Chidgey, B. P. Cavanagh, P. D. D. Kilkelly, H. J. Westlake, BTRL; J. Lyle, Univ. Nottingham	97
Measurement of laser diode intensity noise below the shot noise limit C. M. Miller, L. F. Stokes, Hewlett-Packard	101

An optical synthesizer with sinusoidal-modulated Michelson interferometer for generation of an absolutely stabilized carrier frequency comb A. Mattheus, L. Giehmann, M. Rocks, Deutsche Bundespost TELEKOM	105
Characterization of high birefringence fiber for sensor applications John Feth, James Blake, Honeywell	109
Interpretation of polarization dispersion in a single-mode fiber Makoto Tsubokawa, Masaharu Ohashi, NTT	115
Polarization mode dispersion of short and long single-mode fibers Nicolas Gisin, J. P. Pellaux, Univ. Geneva; Jean-Pierre Von der Weid, Pontificia Universidade Catholica, Brazil	119
Distributed strain measurements in optical fibers using Brillouin optical-fiber time domain analysis Tsuneo Horiguchi, Mitsuhiro Tateda, Toshio Kurashima, NTT	123
Standards for optical fiber geometry measurements Matt Young, NIST	129
A comparison of interferometric techniques for fiber cladding diameter measurements K. A. Emig, Corning	135
Accurate determination of cladding diameter and noncircularity of optical fibers Bennett Wong, Costas Saravanos, Northern Telecom	139
Calibration of fiber diameter measurements K. W. Raine, J. G. N. Baines, A. G. Hallam, N. P. Turner, NPL and York Technology	143
Fibre geometry measurement and quality of parameter estimation D. A. Svendsen, N. MacFarlane, York Technology	147
Pulse-delay measurement for long zero-dispersion fibers Yoshiaki Yamabayashi, Hidehiko Takara, NTT	151
Measurement of reduced germania (GeO) defect levels in optical fibers by fluorescence and absorption spectroscopy R. M. Atkins, AT&T Bell Labs	155
Standardized measurements for determining the radiation-induced attenuation in optical fibers E. W. Taylor, AFSC Weapons Lab; E. J. Friebele, NRL, P. B. Lyons, LANL . . .	159
Test method for fiber optic connector parameters directly affecting return loss Z. Pasturczyk, T. Chepyha, C. Saravanos, H. Wood, Northern Telecom and Univ. Saskatchewan	163

Differentiating core and cladding loss contributions in single mode fiber attenuation measurements	
W. Liese, R. Kerslake, K. Kowaliuk, P. Pilon, Northern Telecom	167
A single launch technique to determine loss and dispersion in multimode fiber systems	
Michael Yadlowsky, Alan Mickelson, Univ. Colorado	171
Measurement of fiber coating geometry using a transversely scanning laser beam	
Gregory E. Smith, Corning	175
Reliability testing of a fiber optic system for subscriber loop applications	
T. S. Frank Lee, Bellcore	179
Accurate modal characterization of passive components based on selective excitation of optical fibers	
D. Pagnoux, P. Facq, J-F. Seignole, J-M. Blondy, Institut de Recherches en Commun. Optique et Microondes	183
The MTF for coupling components	
Shao Yang, Alan R. Mickelson, Univ. Colorado	187
Low reflectance, in-line, continuously variable attenuator for lightwave systems characterization	
V. Shah, L. Curtis, D. D. Mahoney, W. C. Young, Bellcore	191
Photorefractive intermodal exchangers (PRIME) in optical fiber: Theory and applications	
François Ouellette, Université Laval	195
AUTHOR INDEX	199

Industry Standard Measurements: A User's Perspective

Felix P. Kapron & William T. Anderson
Bellcore
445 South St.
Morristown, NJ 07869-1910

1. Introduction

Industry standard measurements provide benefits to both users and suppliers. Users benefit by being able to compare the performance of different suppliers' products, while suppliers benefit by having common testing requirements across diverse groups of users. However, users and suppliers have different motivations. In the supplier's high-volume production environment standard measurements must be repeatable, easily automated, and uniform in application across a range of products. These attributes are important to users also, but more importantly standard measurements must be relevant to their applications. Specified parameters are commonly used in system design, so the correct parameters must be measured in ways directly applicable to the end use of the fiber.

This need to design systems around specified parameters often places users at odds with suppliers. As users better understand their applications or as they develop new applications for existing products, they see the need for additional standard measurements. However, suppliers may see additional standard measurements for existing products as a needless proliferation of costly tests.

Several national and international standards bodies are active in setting fiber optic standards. Prominent are the Telecommunication Industries Association within the Electronics Industry Association (EIA/TIA), the T1 Committee, IEEE 802, CCITT (Consultative Committee for International Telephony & Telegraphy), IEC (International Electrotechnical Commission), the military, and FDDI (Fiber Distributed Data Interface). They cover a range from software aspects of systems down through the physical layer into subsystems and components. Specifications for the physical layer are often given in generic, sectional, and detail form, supported by test procedures for the numerous specifiable parameters found therein. The measurements are sometimes divided into reference test methods (carried out in strict accordance with the parameter definition) and alternate test methods (relatable to the first but easier to implement).

2. Cutoff Wavelength

The cutoff wavelength, as determined by measurements of transmitted power referenced either to a multimode fiber or to a fiber with a bend inserted, has been widely accepted since about 1984. The measurement length and bend condition were standardized, initially in the CCITT and quickly followed in the EIA/TIA and other organizations, as a 2 m fiber length and a 280 mm diameter loop [1]. While adoption of this arbitrary deployment condition led to much improved agreement among suppliers and users, this fiber cutoff wavelength is an overly conservative estimate of the maximum system operating wavelength to maintain single-mode operation. Since the measured cutoff wavelength depends on both the length and the bend condition of the fiber, and may change when a fiber is cabled, a less conservative measurement method for cabled fiber was adopted [2].

The deployment condition for the measurement of cable cutoff wavelength is application-dependent. A default deployment condition, 20 meters of cable with two 75 mm loops at each end, is suggested in the test procedure. This deployment is appropriate for long-haul telecommunications applications, where the minimum length of cable between splices, required for example when

repairing a damaged section of cable, is 20 meters. The loops are intended to simulate the effect of splice case organizers at each end of the repair section. Other applications, such as intrabuilding, data communications, or short-haul telecommunications (as fiber in the subscriber loop) require somewhat different deployment conditions.

This cable cutoff wavelength measurement has both advantages and disadvantages. While such a measurement is most directly applicable to the users' needs for maintaining single-mode operation, requirements based on a multiplicity of different applications will produce a proliferation of different fiber cutoff wavelength requirements that will be difficult for suppliers to implement. This difficulty can be mitigated by developing mapping functions between the easily measured fiber cutoff wavelength, which is readily performed on a routine, high-volume basis, and the several cable cutoff wavelengths, which are application-dependent. Such mapping functions are widely used to assure conformance to user-specified cable cutoff wavelength measurements through routine measurement of fiber cutoff wavelength [3].

Recently, anomalous peaks or humps in the transition region have been reported [4]. These peaks lead to poor measurement repeatability, and their causes are not well understood. The measurement repeatability could be improved if steps were taken to eliminate the peaks, for example by introducing controlled microbending, but until it can be shown that the peaks are a measurement anomaly and have no effect on system operation, no agreement to eliminate them will be reached.

3. Dispersion

Originally, dispersion was specified as a worst-case value over a particular wavelength window. There were difficulties with this. First, the specified value was worst-case and ignored the lower values attainable nearer the center of the window. Second, the specification was inflexible in that various system applications defined different wavelength regions and/or dispersion values. Third, the specification gives pessimistic results when applied to fiber concatenation behavior; furthermore, it did not allow for any statistical averaging of dispersion data for those users willing to accept some small probability of link dispersion failure in return for lower end-to-end dispersion values most of the time. Finally, the specification ignores second-order dispersion that can become important for transmitters with central wavelengths sufficiently close to the fiber zero-dispersion wavelength. This occurs with LEDs and some multilongitudinal-mode laser diodes.

The dispersion coefficient is now given as a function of wavelength in terms of the specified maximum and minimum values of the zero-dispersion wavelength and the maximum zero-dispersion slope [5]. The mathematical expressions differ for dispersion-unshifted and dispersion-shifted fiber; the former is shown in Figure 1. These 3 parameters have been used to define a multimode fiber FDDI "template." Another example is SONET and the SDH (Synchronous Digital Hierarchy) [6]. From various models and field experiences, it can be shown [7] that with a power penalty due to intersymbol interference and mode-partition noise, the maximum allowable dispersion coefficient equals a ratio. The numerator depends on the allowed level of power penalty (typically 1 dB) and on the source spectrum k -value and system bit-error-ratio. The denominator is the product of bitrate, cable length, and source spectral width. From the maximum dispersion coefficient and Figure 1, the dispersion-limited wavelength window is thereby determined. The calculation is readily repeated for other applications (a benefit to the user) without need of changing the specification (a benefit to the supplier).

4. Attenuation

Attenuation is the most mature of the many optical fiber measurements. However, the utility of attenuation specifications for system design has recently been called into question. In the most simplistic terms, the attenuation at the center of the various regions (e.g., 1310 nm, 1550 nm, and perhaps 850 nm) is universally accepted. However, some range of wavelengths about the nominal must be accepted to permit the economical manufacture of sources. In addition, source wavelengths may change with temperature and age.

The single trade-off between allowable source spectral variations and source cost cannot be made across all applications. For long-haul applications, where each source may activate 30 to 50 km of fiber, a tighter tolerance and higher source cost may be acceptable if these tighter tolerances permit longer transmission distances without amplification. For a shorter range application such as the subscriber loop, where only 2 to 4 km range is needed, a broader range of source wavelengths may be required to permit the use of inexpensive, uncooled lasers and to ease the future use of wavelength division multiplexing. For data communications applications, an even broader range of source wavelengths may achieve the optimum trade-off between source cost, fiber cost, and performance.

At present, no wavelength "windows" are universally accepted. In recent debate in CCITT, two windows in each of the single-mode regions, one wide for short distance applications and one narrow for longer distances, were suggested. These windows were intended to optimize the performance for the SDH. Somewhat different windows may be needed for optimum use under Broadband ISDN, for subscriber loop applications, or for data communications applications such as FDDI.

The proliferation of specified attenuation windows, each of which is optimum for one application, benefits neither users nor suppliers. A more desirable approach would be to develop a flexible attenuation specification, similar to the parametric representation of dispersion discussed above. One approach to parametric representation is well-known, using the scattering coefficients, the water peak, and other physical phenomena. However, this representation may be difficult to implement. A more promising approach would be to specify attenuation at several discrete wavelengths (in the 1310 nm region, three possible choices would be 1260 nm, 1310 nm, and 1385 nm) and to develop robust design rules for interpolation between these specified wavelengths to estimate the attenuation over any wavelength window selected by the user. Similar design rules could be constructed for each of the wavelength regions of interest.

5. Mode Field Diameter and Fiber Geometry

Mode field diameter and fiber geometry are grouped together here because together they determine the attenuation that can be achieved in splices and connectors. For mode field diameter, the measurement methods are numerous and mature. Recently in the CCITT, the definition of mode field diameter was changed to improve the consistency from method to method, especially for non-step-index (e.g., dispersion-shifted) fibers. The new definition uses the second moment in the far field rather than the gaussian fit previously accepted. Revised EIA/TIA test procedures incorporating this second moment definition are still awaiting approval. Also, the CCITT has accepted the far-field scan as the Reference Test Method.

The measurement of fiber geometry is not as well advanced. A recently conducted international round-robin revealed considerable variability between laboratories [8]. Much of this appears to be related to the calibration of the geometry measurement systems, and the lack of primary standards for such systems may limit possible improvements in interlaboratory agreement. One promising measurement method, video grey scale analysis, is not yet incorporated in an approved procedure

because of uncertainties over calibration; moreover, the widely-used image shearing method is also undocumented.

Recent studies [9] of the effects of fiber geometry on splice and connector loss have shown that present levels of control of fiber geometry may not be sufficient for all applications. For long-haul applications, where several kilometers separate splices and where the cost of the splice is significantly less than the cost of the fiber between the splices, reduced splice cost at the expense of tighter fiber geometry control, and higher fiber cost, is not warranted. However, for subscriber loop applications, where there will typically be only several hundred meters between splices, such a trade-off may be attractive.

6. Fiber Reliability

Standardized test procedures for characterizing the in-service reliability of optical fibers have two general purposes. One allows different fibers to be directly compared with each other in ways agreed to by the industry. This should eliminate the "specsmanship" among vendors which sometimes occurs. Another purpose is to estimate the lifetime of various fibers in different service conditions.

Some measurements performed on uncabled fiber are environmental, simulating extremes of temperature, humidity, hydrogen, and nuclear radiation. Others relate to deployment conditions, as under tension or macrobending and microbending. Common fiber deployment conditions are under low tension as in a cable, undersea cable, uniform bending as for wound bobbins or with some optical taps, and 2-point bending (between parallel surfaces) as in splice cases. The optical and mechanical properties of the fiber may be monitored.

There has been recent activity in strength testing. The EIA/TIA proof test procedure has been revised, and procedures on static and dynamic fatigue testing (to failure) are in preparation. One problem is how to apply data taken in a convenient experimental configuration (such as high-stress 2-point bending for which numerous samples can be tested simultaneously) to a more common field conditions such as low tension or uniform bending. Another is to account for stress-free aging due to environmental effects. Finally, a document is being prepared concerning the use of test data in making predictions of lifetime in the field.

7. Active & Passive Components

A considerable body of standards work has been developed in the EIA/TIA, IEC, and Bellcore on splices and connectors, and to a lesser degree on sources and detectors. As interest has grown in utilizing fiber optics in data communications, the subscriber loop, and CATV, for example, passive components such as couplers of various types and wavelength-division multiplexers/demultiplexers (WDMs) are attaining increasing importance.

These components may not experience the benign environment as does fiber within a cable structure. They are being deployed increasingly outside of environmentally controlled buildings so that specifications and testing must now reference a wider latitude of temperature, humidity, vibration, chemicals, etc. This is particularly stressful for the optoelectronic components with which one wants to avoid the expense of device heating and cooling. The variations in transmitter power outputs and receiver sensitivities are forcing standards targeting wider wavelength windows. Moreover, new efforts on optical component and system reliability standards have begun.

For passive components, a measurement trend in the laboratory has been to utilize optical switches in order that statistically meaningful data can be taken on a large number of samples. Another is to use optical time-domain reflectometers (OTDRs) to replace several direct power

measurements, not only in the field but also in the laboratory. The OTDR method has obvious advantages in measuring concatenated components. Some problems do remain unsolved, however. Although OTDR anomalies such as "gainers" observed at joints are by now generally understood and sometimes corrected for, multiport couplers have more parameters to determine and these have not yet been satisfactorily probed with OTDRs. Then WDMs add another layer of complexity that would make desirable a new generation of wavelength-tunable OTDRs.

The technology of these components and the system design employing them is still rapidly developing. Even some standard definitions are evolving. For example, port-to-port directivity gives the ratio of power reflected back at a port due to excitation at another port. Although this is a convenient specification and necessary measurement for the vendor, the user may be more interested in a total directivity resulting from the worst-case excitation of all other ports. Mapping between the two must be established.

8. Reflections

Transmission problems due to component reflections can occur at high bitrates, especially with coherent lasers and with fiber having high dispersion at the wavelength of operation. Three parameters have been identified for specification and measurement.

The optical return loss (ORL, in positive dBs) gives the maximum fraction of launched power that can feed back from the cable plant into the transmitter. Measurement is taken in the downstream direction (towards the receiver) using an optical continuous-wave reflectometer (OCWR) or an OTDR (with computation). The maximum discrete reflectance (MDR, in negative dBs or %) causes multiple-reflection effects leading to intersymbol interference at the receiver or interferometric noise back at the transmitter. An OTDR in the upstream or downstream direction can be used. Finally, in a multivendor environment in which the receiver is specified separately, its maximum reflectance (including connector) is measured with an OCWR or OTDR.

Measurements of reflections occur on a component and system level. The latter can be related to a system power penalty for single or multiple reflections, and such test procedures are being prepared in the EIA/TIA. Specifications must relate to the application (e.g., digital or analog), and as such may need to distinguish between new plant installations (for which provision of low-reflectance components is simple) and existing plant (for which replacement of higher reflectance yet adequate components would be prohibitively expensive).

9. Standard System Measurements

This is the least mature area of the standards process. The goals here are to develop standard interfaces for system applications such that a user may design a link using components from a variety of unrelated suppliers. This has been done largely for data networks (e.g., IEEE 802 and FDDI), and to a lesser extent for digital networks (e.g., SONET), but analog and distribution network standardization is still far behind. Generic Specifications and standard test procedures for all three types are being developed in the IEC.

10. Conclusions

In this paper we have summarized standards activities from a user perspective. Users need and supplier needs for standard measurements are often in conflict, and successful resolution of this conflict is essential to cost-effective mass deployment of optical fiber. The various standards bodies have been necessary forums for resolving these conflicting needs for the mature long-haul telecommunications applications. Future activities in these standards bodies should now be focused on newer applications, which may require somewhat different standard measurements.

11. References

- [1] CCITT Recommendation G.650 and EIA/TIA FOTP-80 (Oct. 1988)
- [2] EIA/TIA FOTP-170 (Nov. 1989)
- [3] Bellcore TR-TSY-000020, Issue 4 (March 1989)
- [4] K. Emig, OFC (Feb. 1989); V. Shah & L. Curtis, JLT, p.1181 (Aug. 1989); D. Peckham & S. Jacobs, OFC (Jan. 1990)
- [5] CCITT Recommendation G.652; F. Kapron, OFC/IOOC (Jan. 1987)
- [6] CCITT Recommendation G.957
- [7] F. Kapron, NFOEC (April 1990)
- [8] D. Franzen et al., JLT (to be published)
- [9] A. Johnson & W. Anderson, SPIE (Sept. 1989) and NFOEC (April 1990)

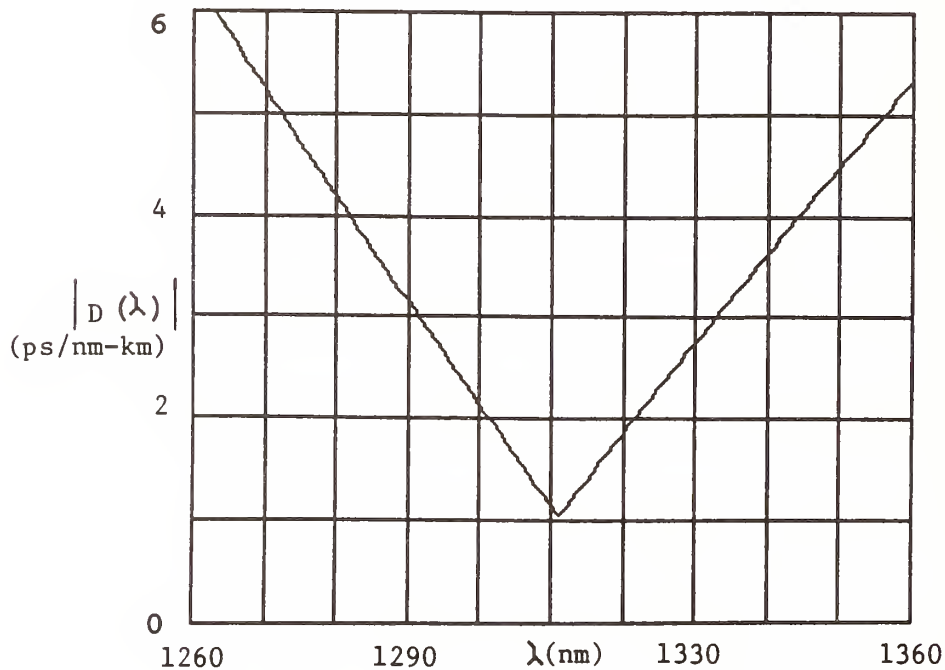


Figure 1 - Wavelength Dependence of the Worst-Case Absolute Value of the Dispersion Coefficient for Dispersion-Unshifted Fibers

COST 217 interlaboratory comparison of optical measurements on single-mode fibre couplers

J.W. Burgmeijer, W.J. de Vries, PTT Research, the Netherlands
M. Artiglia, P. Di Vita, CSELT, Italy; R.P. Novák, Swiss PTT
E. Sundberg, Swedish Telecom; L. Nykjoor Kragh, Telecom Denmark
J.Allen, GEC Research, United Kingdom; J. Pelayo, Un. de Zaragoza, Spain
N. Gisin, Université de Genève, Switzerland

1 Introduction

Single-mode 2×2 optical fibre couplers have important applications in optical fibre networks, instrumentation and sensor systems. Bidirectional couplers made using the fused biconical taper technique are now provided by a large number of manufacturers. The transmission characteristics are inherently wavelength and polarization dependent, which may be of use for wavelength multiplexers and polarization splitters respectively, but is unwanted for optical power splitters [1].

The COST 217 project group decided in October 1988 to start a new Working Group (WG5) in order to develop measurement procedures for optical characterization of these and other branching devices. Up to now final agreement on such procedures is still lacking [2]. Like it was done in the other working groups [3], the 8 participants decided to start an interlaboratory comparison of measurements using different techniques.

For this round robin 7 fibre couplers (named A to G) were circulated among the participants. The couplers, constructed with two identical 1300 nm single-mode fibres, were either 1300/1550 nm wavelength multiplexers or power splitters. After discussion of the first measurement results, the definitive experimental procedures were agreed on. These procedures as well as some experimental results are summarized in this paper.



- | | | | |
|----|----------------|---|--|
| A. | Coupling Ratio | $\frac{I_2}{I_2 + I_3} \times 100\%$ | $\text{and } \frac{I_3}{I_2 + I_3} \times 100\%$ |
| B. | Excess Loss | $-10 \cdot \log \left(\frac{I_2 + I_3}{I_1} \right)$ | |
| C. | Directivity | $10 \cdot \log \left(\frac{I_4}{I_1} \right)$ | |

Figure 1: Definitions of optical properties of fibre couplers

The definitions of the optical parameters of fibre couplers used in this paper are given in Figure 1. These properties can be measured as a function of wavelength and as a function of linear polarization angle with the degree of polarization of the light beam launched into the coupler to be 0 and 1 respectively. By rotating an analyzer in the beam, the maximum (I_1) and minimum (I_2) transmitted intensity can be determined. The degree of polarization P is then defined to be:

$$P = (I_1 - I_2)/(I_1 + I_2) \quad (1)$$

2 Polarization sensitivity of coupling ratio

The measurement set-up of a polarization scan is given in Figure 2. The light source used may be a broadband lamp with a monochromator or a laser source. In this round robin a wavelength of 1300 nm

was chosen. To perform a polarization scan a polarizer and a device to rotate the polarization angle are needed. Participants 1 to 3 used a Glan Thompson polarizer and participant 4 a polymer film polarizer for this purpose. Participant 5 used a polarized light source combined with an all-fibre polarization rotator based on Berry's topological phase [4]. The polarization sensitivity is defined as the maximum change in the coupling ratio, while the polarization angle of the incident light is rotated through 360° .

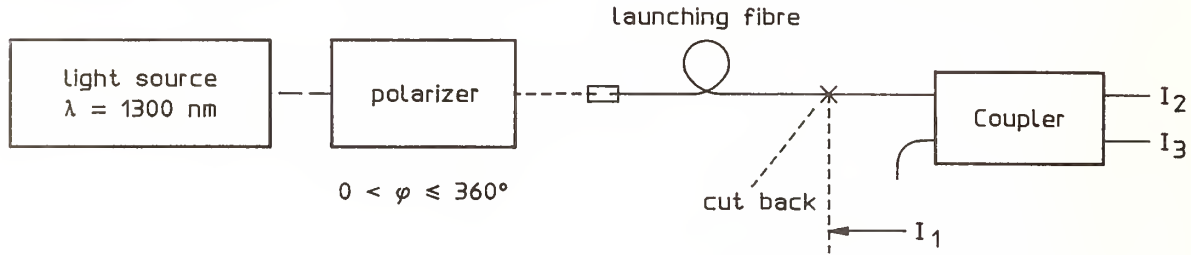


Figure 2: Measurement set-up of polarization scan

The degree of polarization P of the light launched into the coupler under test includes the (de-)polarization effects of monochromator, polarizer, coupling optics, splices, fibre clamps and launching fibre. If P is lower than 1, the measured polarization sensitivity of the coupler is lower with the same relative amount. The measurement results of couplers A, B and C are summarized in the table below.

Coupler	Part.1	Part.2	Part.3	Part.4	Part.5	Mean Value	Standard Deviation
A	2.0%	1.4%	1.3%	-	4.1%	2.2%	1.3%
B	11.6%	14.8%	10.0%	12.4%	-	12.2%	1.8%
C	4.0%	4.2%	-	4.4%	4.2%	4.2%	0.2%

The variation of measured values for the five participants may be due to an insufficient degree of polarization of the launched light beam. Some of the participants did not verify this at the time of each measurement.

The couplers D, E, F and G have polarization sensitivities which are measured by the participants to be lower than 1%.

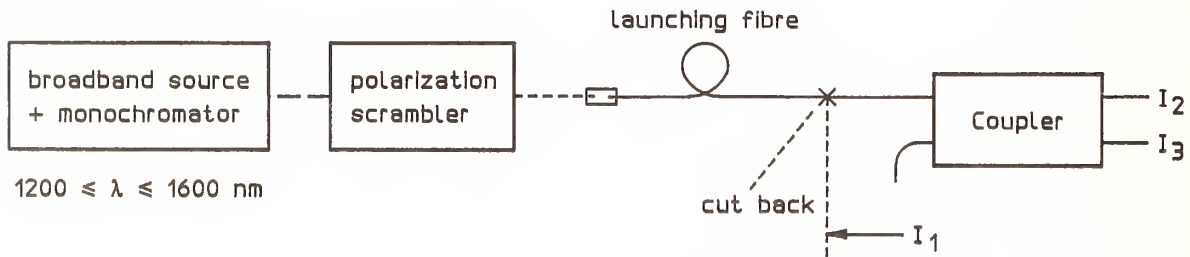


Figure 3: Measurement set-up of wavelength scan

3 Wavelength dependence of coupling ratio

The measurement set-up of a wavelength scan is given in Figure 3. The light source used may be a LED or a tungsten lamp. A monochromator is used to scan the wavelength between 1200 and 1600 nm with a spectral width (FWHM) smaller than 10 nm. A step size of 50 nm has been chosen.

A polarization scrambler should be used to get unpolarized light ($P = 0$) at the cut-back point. This is important when measuring polarization sensitive couplers. If the light is partially polarized ($P > 0$) variations in the measured coupling ratio appear.

The participants used different types of depolarizers; a multimode scrambler, a Lyot depolarizer [5] or

just a piece of multimode fibre. Three participants did not use a depolarizer at all. One participant measured P at 2 stages of the set-up with 3 different depolarizers:

P measured directly after the tungsten lamp and monochromator: $P = 0.6$

P including 2 meter of multi-mode fibre: $P = 0.07$ (1300 nm) and $P = 0.2$ (1550 nm)

P including a Lyot depolarizer: $P < 0.05$

P including a multi-mode scrambler: $P < 0.05$

The degree of polarization using the last two depolarizers is sufficiently small to achieve insignificant variations in measuring fibre couplers with moderate (below 20%) polarization sensitivity.

Coupler B with a measured polarization sensitivity of 12% was measured in the first phase of the round robin when most of the participants did not use a depolarizer. Assuming P to be 0.6 the variations in coupling ratio are estimated to be $\pm 4\%$, which agrees well with the measured values (Fig. 4a).

Couplers D to G, having a low polarization sensitivity, showed a better interlaboratory reproducibility with a standard deviation between 0.2% and 1.5%. This is illustrated by the measurements of coupler G (Fig. 4b).

4 Excess loss

The excess loss of the coupler under test as well as any additional loss in the splice between launching fibre and coupler pig-tail has no influence on the measured coupling ratio. However, if the excess loss of the coupler under test is measured, this additional loss should be avoided. The cut-back method, with the cut-back made in the pig-tail of the coupler under test, is preferred. This was only possible with the coupler B, because the pig-tails of the other couplers were too short. With these couplers the cut-back point has been made at the splice point between launch fibre and coupler pig-tail.

Figures 5a and 5b shows the measured results of the excess loss of coupler B and F respectively. For coupler F the measurements include the loss of the splice which is of course quite different for the different participants.

5 Directivity

In order to measure the directivity it is necessary that the two output ports (2 and 3) should be terminated in such a way that their reflectivities are lower than the directivity of the coupler itself.

Methods to overcome reflections, which have been used by the participants, are:

1. An obliquely polished end-face for both fibre pig-tails [6].
2. The termination of both output ports with index matching liquid.
3. The use of small loops (typical diameter of 4 mm) in the fibre tails of both output ports for a strong light attenuation combined with low reflectivity.

The directivity of all the couplers in this round robin is below -70 dB. Thus the measurement results reveal something about the quality of the termination of the output ports.

With methods 1 and 3 directivities up to -75 dB could be measured.

Method 2 is insufficient as it results in measured directivities of about -55 dB. Method 3 is normally used in combination with 1 or 2. A useful technique is to decrease the loop diameter while monitoring the output power at port 4. If this power does not decrease further the minimum level, determined by the directivity of the coupler or the sensitivity of the detector, is reached.

6 Conclusions

Measurement procedures for the optical characterization of fibre couplers are proposed which are suitable for couplers which are both wavelength and polarization dependent. The necessity of using unpolarized light ($P < 0.05$) when measuring the wavelength dependence of coupling ratio has been demonstrated. For the measurement of the polarization sensitivity of the coupling ratio one should verify the degree of polarization ($P = 1$) of the launched light beam. On measuring the excess loss the cut-back must be made in the pig-tail of the coupler under test, in order to get measurement errors < 0.1 dB. The termination

of the output ports with index matching liquid is not sufficient if the directivity to be measured is lower than -55 dB.

References

1. M. Eisenmann and E. Wiesel, IEEE J. Lightwave Technol., Vol.LT6, 113-119 (1988)
2. IEC publication 875-1 (1986)
3. COST 217 Group, ECOC '89, paper TuB12-4 and IEE proc., Vol.136, 307-314 (1989)
4. A. Tomita and R.Y. Chiao, Phys.Rev.Lett., Vol.57, 937-940 (1986)
5. K. Bohm et al., IEEE J.Lightwave Technol., Vol.LT1, 71-74 (1983)
6. R.P. Novák, et al., IOOC'89, paper 19B2-4, Kobe, Japan (1989).

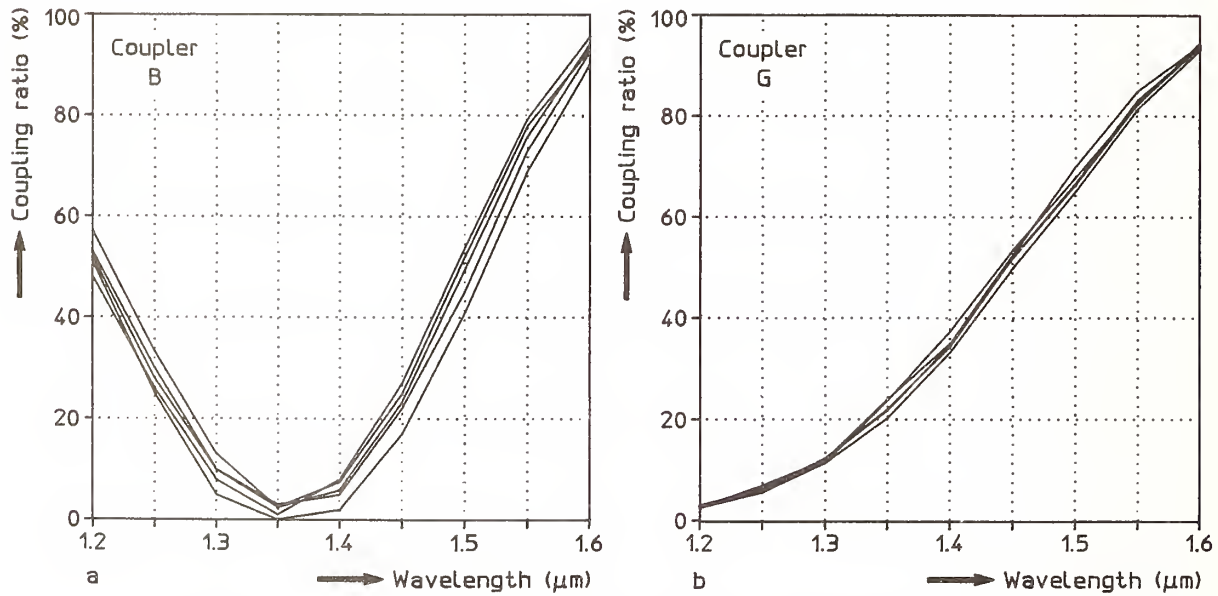


Figure 4: Wavelength dependence of coupling ratio of 2 fibre couplers with high (B) and low (G) polarization sensitivity

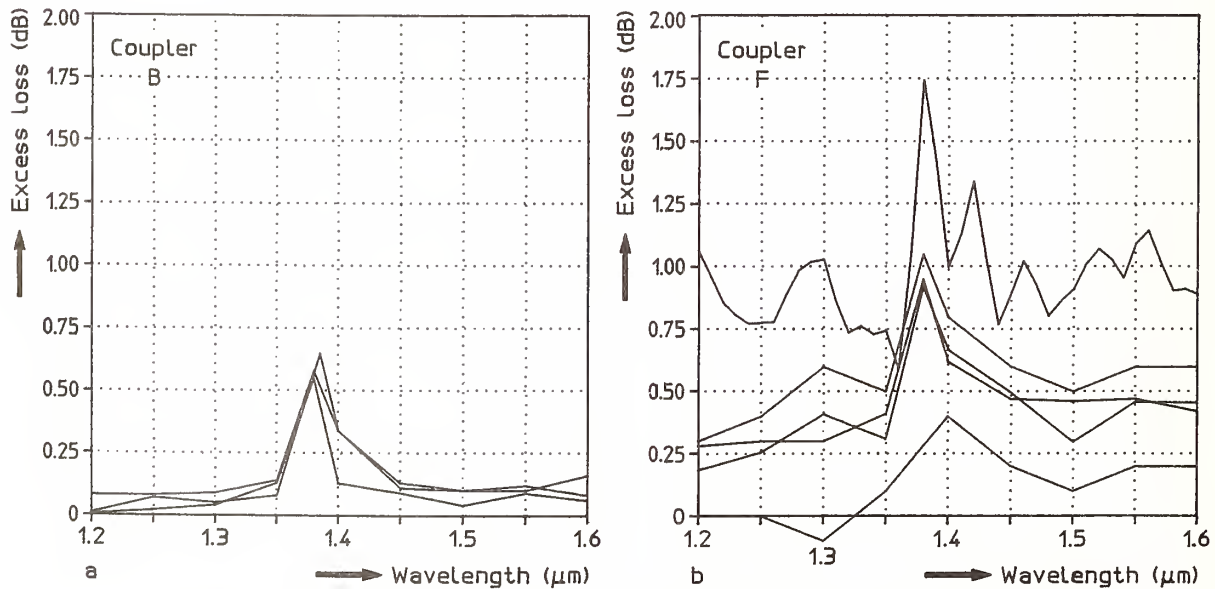


Figure 5: Measured excess loss of 2 fibre couplers using the cut-back method (B) and the insertion-loss method (F) respectively

COST 217 MODE FIELD DIAMETER MEASUREMENTS INTERCOMPARISON

by

B. WALKER, COST 217 Group*

Introduction

Within the CEC COST 217 programme (Optical Measurement Techniques for Advanced Fibre Systems and Devices) 15 laboratories from 9 European countries previously measured a range of parameters, including mode field diameter (MFD), of six types of nominally circular single-mode fibre⁽¹⁾. The results showed large variations ($> 1 \mu\text{m}$) in measured MFD's even for conventional matched clad fibres. As a result of this initial intercomparison, a second round of measurements has been carried out on the same six fibres under more well defined measurement conditions. Fourteen laboratories took part in this second intercomparison. The fibre types were matched clad (MC), depressed clad (DC), two dispersion shifted fibres (SC, DS), a pure silica core fibre (PS) and a dispersion flattened fibre (DF). All the MFD's were measured according to CCITT Recommendation G652 using the Petermann II definition of MFD.

Results and Discussion

The MFD results for the six fibres from participating laboratories are shown graphically in Figs. 1(a)-(f) along with their standard deviation. The interlaboratory reproducibility (defined as the standard deviation between measurements performed in the different laboratories, see Ref. (1), and shown as dotted lines) is approximately half that of the first intercomparison. Tables 1 (a) and (b) show the difference in MFD between the value obtained by a particular laboratory and the mean of all the laboratories' results for each fibre at 1300 and 1550 nm respectively. The shaded boxes in the table indicate that the value is greater than the mean for a particular fibre and unshaded that it is lower. The average value of the difference for a particular laboratory is also given.

It is clear from Fig. 1(a)-(f) and Table 1 that the results of a given laboratory tend to be either higher than the mean MFD, e.g. 8, or lower than the mean, e.g. 9. This suggests that the major sources of error in the measurements are systematic rather than random. Further examination of the data indicates that it is the method used that is the predominant factor. The results for each method are discussed briefly below.

*This paper is the result of joint collaboration by the following members of the COST 217 Group: B Walker, J M Benson (NPL, UK); N Haigh (BICC Cables, UK); M Artiglia, P Di Vita, M Potenza (CSELT, Italy); E Sundberg (Swedish Telecom); L Nykjoer Kragh (Telecom Denmark); F Villuendas (Cables de Comunicaciones SA, Spain); L Oksanen (Nokia Cable, Finland); G Kuyt (Philips Optical Fibre, The Netherlands); J Vobian (Research Institute of the DBP at the FTZ, Darmstadt, FRG); A Witschi (Swiss PTT); K Sjölin (Ericsson, Sweden); N Gisin (Univ. de Geneve, Switzerland); J W Burgmeijer (PTT Research, The Netherlands).

Far Field Scan (FFS):- The MFD's obtained using this method were consistently below the mean. However the standard deviation of the measurements between the five laboratories using this method were approximately half those of the group as a whole. All the participants in the study employed measurement systems with dynamic ranges ≥ 50 dB, scan angles $\geq \pm 25^\circ$, step size $< 0.5^\circ$ and angular resolutions of $< 0.4^\circ$. From the results of a previous study⁽²⁾ (and confirmed by studies carried out in this work), under the conditions outlined above, errors from any of the above factors should be $\leq 0.5\%$. Thus, whilst the results using this method were lower than average there is no obvious reason for this. It would seem to be a suitable technique to use as a reference test method for MFD measurements.

Variable Aperture Far Field (VAFF):- The MFD's obtained using this method by participants 8 and 10 had higher than average values, especially for dispersion modified fibres whilst those of participant 9 were lower than average. The latter were however in good agreement with the FFS results. MFD's obtained using this method depend on the NA of the collection optics⁽³⁾, too low an NA leading to a high value for the MFD. This result is confirmed by the present work since participants 8 and 10 both used apparatus with a claimed NA of 0.24 whilst that used by 9 had an NA of 0.45. It would thus appear that an NA of 0.45 (with 22 apertures) gives MFD's in good agreement with FFS results. Parton who used reflective high NA collection optics in a VAFF system also obtained MFD's close to those obtained by FFS⁽⁴⁾.

Far Field Knife Edge/Slit (KE):- Two participants used this method. One, 6, used the conventional method of measuring the power passed by on knife-edged placed in the far field. The other, 7, a variant of this which measured the power transmitted through a slit of variable width placed on the axis of the far field radiation pattern. Both participants produced results close to or slightly above the mean, more so in the case of participant 7. The numerical aperture requirements of this method are similar to those of the VAFF method⁽²⁾. However, the results obtained by laboratory 7 which used a 0.4 NA system tend to be larger than those of 6 which used a 0.3 NA system. The reason for this is unknown at present.

Near Field Scan (NFS):- Both laboratories using this method produced results below the mean, particularly laboratory 11. Those of laboratory 12, whilst lower than average were quite close to those obtained by the FFS method. The difference between the two laboratories results is attributed to the different NA used in the measurement, these being 0.4 and 0.65 for participants 11 and 12 respectively. Participant 11 repeated the measurements using an NA of 0.65 and then obtained results in good agreement with those of participant 12. An NA of at least 0.65 would thus appear to be required for this method.

Transverse Offset (TO):- For this method no clear result emerged, laboratory 12 producing lower and 14 higher than average MFD's. Further work is required to fully evaluate this method.

Conclusions

The following conclusions are drawn from the results of this work:-

- Far Field Scan - Preferred Test Method
- VAFF/Knife Edge - Requires NA of ≥ 0.4
- Near Field Scan - Requires NA of ≥ 0.65
- Transverse Offset - More Work Needed.

References

1. Interlaboratory Measurement Campaign on Single-mode Fibres. COST 217 Group, IEE Proceedings, Vol 136, Pt J, No. 6, December 1989.
2. Mode Field Diameter Measurements on Fibres With Non-Gaussian Field Profiles. W.T. Anderson et al, JLT, LT5, 211, (1987).
3. Interlaboratory Comparisons of Far-field Methods For Determining Mode Field Diameter using both Gaussian and Petermann Definitions. T.J. Drapela. Symposium on Optical Fiber Measurements 1988, NBS Special Publication 748.
4. Improvements to the VAMFF System for Accurately Measuring the Mode Field Diameter of Dispersion Shifted Fibres. J.R. Parton, Symposium on Optical Fibre Measurements 1988, NBS Special Publication 748.

1300 NM

METHOD	FFS					KE		VAFF			NFS		TO	
LAB FIBRE	1	2	3	4	5	6	7	8	9	10	11	12	13	14
DC	-0.13	-0.19	+0.15	-0.06	-0.04	-0.04	+0.06	+0.09	-0.18	+0.08	-0.13	+0.07	-0.16	+0.55
PS		-0.06	+0.01		+0.02	-0.21	+0.16	+0.09	-0.10		-0.18	-0.03		+0.25
MC	+0.01	-0.09	-0.20	-0.11	-0.10	+0.07	+0.02	+0.13	-0.14	+0.10	+0.03	-0.06	-0.09	+0.44
SC	-0.19	-0.35	-0.09	-0.19	-0.23	+0.13	+0.26	+0.50	-0.24	+0.46	-0.37	-0.37	+0.09	+0.53
DS	-0.06	-0.16	+0.08	-0.05	-0.11	+0.10	+0.08	+0.43	-0.15	+0.41	-0.37	-0.24	-0.10	+0.13
DF		-0.08	-0.14	+0.00	-0.05	-0.08	+0.00	+0.30	-0.15	+0.26	-0.41	-0.04	+0.32	+0.02
$\langle \text{MFD} - \overline{\text{MFD}} \rangle$	-0.09	-0.15	-0.03	-0.08	-0.08	-0.01	+0.10	+0.26	-0.16	+0.26	-0.24	-0.11	+0.01	+0.32

(a)

1550 NM

METHOD	FFS					KE		VAFF			NFS		TO	
LAB FIBRE	1	2	3	4	5	6	7	8	9	10	11	12	13	14
DC	-0.01	-0.16	-0.09	-0.04	+0.03	-0.04	-0.01	+0.14	-0.11	+0.07	-0.00	+0.11	-0.05	+0.10
PS		-0.14	+0.02		+0.02	-0.18	+0.42	+0.07	-0.11		-0.44	+0.01		+0.33
MC	+0.03	-0.07	-0.24	+0.05	-0.00	-0.00	+0.24	+0.22	-0.09	+0.08	-0.37	-0.07	-0.16	+0.41
SC	-0.26	-0.32	-0.13	-0.28	-0.29	+0.27	+0.38	+0.74	-0.31	+0.71	-0.48	-0.17	-0.36	+0.47
DS	-0.11	-0.24	-0.12	-0.25	-0.15	+0.16	+0.07	+0.69	-0.18	+0.65	-0.37	-0.11	-0.17	+0.11
DF		-0.23	-0.05	-0.21	-0.16	+0.02	+0.10	+0.75	-0.24	+0.71	-0.47	-0.12	-0.05	-0.03
$\langle \text{MFD} - \overline{\text{MFD}} \rangle$	-0.09	-0.19	-0.10	-0.15	-0.09	+0.04	+0.20	+0.43	-0.17	+0.44	-0.36	-0.06	-0.16	+0.24

(b)

Table 1: Differences in MFD for a particular fibre between a given laboratory and the average MFD for all the participants, (a) at 1300 NM (b) at 1550 NM

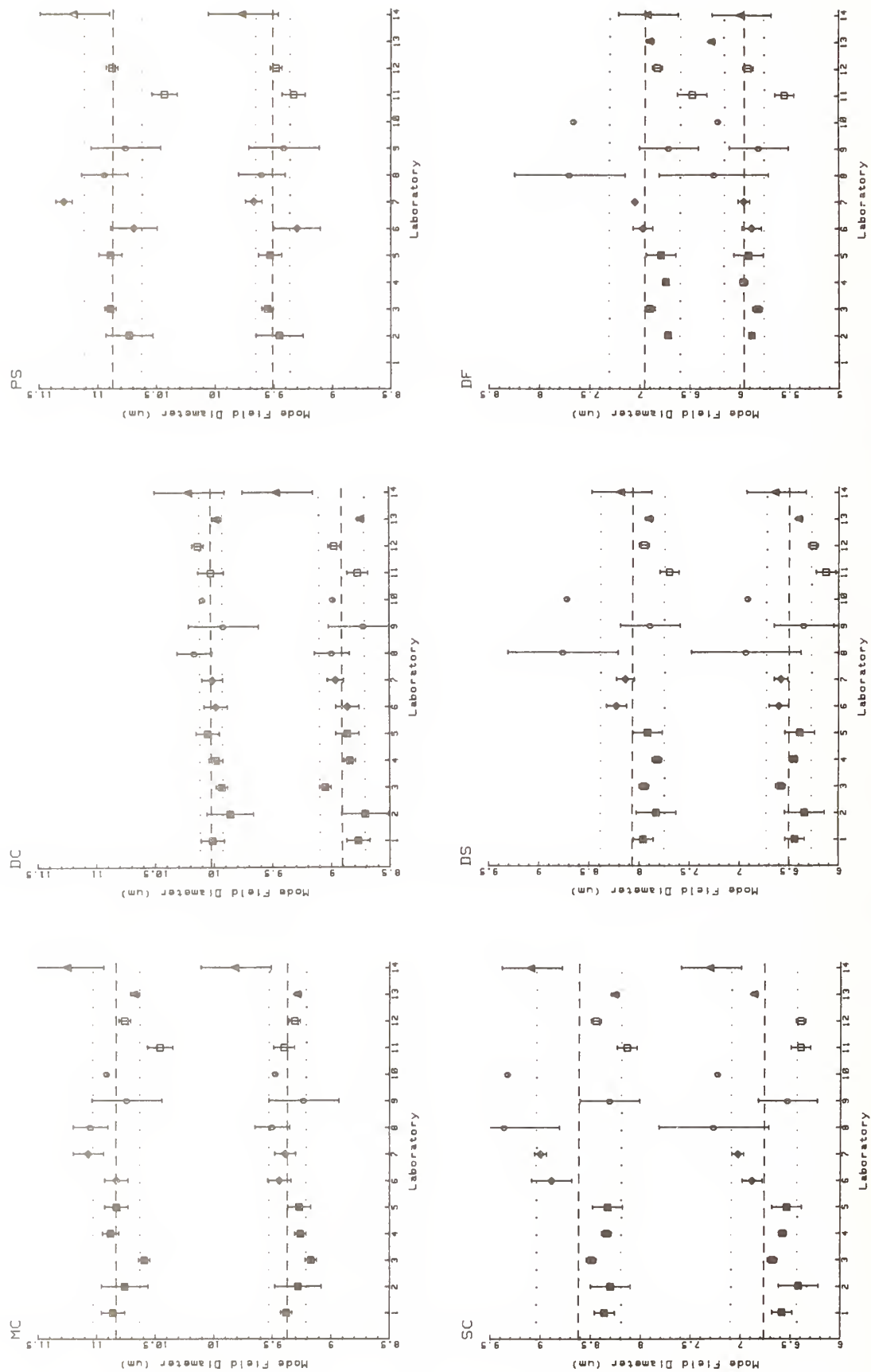


FIG.1-1. MFD vs PARTICIPANT FOR THE SIX FIBRES AT 1300 NM (LOWER DATA) AND 1550 NM (UPPER DATA). MEANS AND STANDARD DEVIATIONS ARE ALSO SHOWN. (KEY ■ - FFS, ◆ - KE, ○ - VAFF, □ - NFS, ▲ - TO).

POST-MORTEM ANALYSIS OF OPTICAL FIBERS

H.H. Yuce, J.P. Varachi
Bellcore, 445 South Street, Morristown, NJ 07960

P.L. Key
Bellcore, 331 Newman Springs Road, Red Bank, NJ 07701

[Invited]

1. ABSTRACT

Although optical fibers have moved rapidly from the laboratory to widespread deployment, there have been relatively few field failures reported, and most of these have been due to external causes such as dig-ups. Initial concerns about fiber breakage due to the brittle nature of glass have fortunately not been realized. In this paper, we examine one of the few, actual field failures involving fiber breaks resulting from overstressing or from fiber damage. Although there have not been many such failures reported, mechanical failures are still considered a possible cause of reliability problems and continue to receive considerable attention. We show how fracture mechanics and fractography can frequently be used to analyze the cause of fiber failures. Such information can be very useful in determining liability for repair or replacement.

2. INTRODUCTION

Optical fibers are being deployed rapidly into the telephone plant; by the end of 1989, there were almost 7 million fiber-km installed. The average age of installed fiber optic cables is about 7 years for multimode fibers (11 years maximum) and 3 years for single mode fibers (7 years maximum). Considering the rapidity with which this technology moved from the laboratory to the field and the large amount of installed cable with significant exposure, there have been relatively few failures of fiber optic cables. This trend, if continued, bodes well for the long term reliability of this technology. To develop reliability data on fiber cables, Bellcore has been collecting data from its clients on field failures. To date, approximately 2000 fiber outages have been reported to Bellcore¹. Connolly has summarized 145 of these failures indicating that most were due to causes unrelated to the cable itself, such as dig-ups or craft error². In several cases where the cause of failure was not obvious, sections of the failed cables have been sent to Bellcore for analysis. In this paper, we will focus on a cable containing fibers broken due to surface damage.

3. FAILURE ANALYSIS PROCEDURES

In general, a successful failure analysis requires an understanding of possible failure mechanisms. In the case of optical fibers, this requires an understanding of the mechanical behavior of glass. At normal exposure temperatures for telecommunications cables, glass is inherently brittle due to a lack of inelastic flow mechanisms, but it is not inherently weak. The theoretical strength and ductility are in excess of 2 million pounds per square inch (Mpsi) and a strain at fracture of about 15%³. Such strengths have been achieved in the laboratory and commercial fibers have strengths approaching 1 Mpsi today.

If fibers could be produced routinely having strengths of 2 Mpsi and 15% elongation, there would be less concern over mechanical reliability. However, two effects prevent the achievement of such properties. It has long been recognized that real glass objects contain flaws which range in size from the atomic level to the macroscopic, such as inclusions and scratches. These latter flaws generally arise during production of the glass and act as stress concentrators which, due to the lack of inelastic flow in glass, produce very high local stresses. As shown by Griffith⁴, these high local stresses and the low energy absorption due to the lack of inelastic flow lead to fracture at a low stress level with the size of the crack as the principal parameter:

$$\sigma = [2 E \gamma / \pi a]^{1/2}$$

where σ is the fracture strength, E is the tensile modulus, γ is the fracture energy per unit of fracture surface area, and a

is the crack radius.

The second factor affecting the strength of glass fibers is that flaws in glass can increase in size under the action of stress in the presence of certain chemical species. This slow crack growth can result in fracture at stresses below that which would occur in an inert environment for a given stress level and flaw size. A recent model of this process has led to criteria to recognize chemicals likely to cause slow flaw growth⁵; such common chemicals as water and ammonia are among those identified by the model. The fracture behavior of glass in the presence of such chemicals is called dynamic fatigue if the stress is varying and static fatigue for constant stress conditions. Note that the use of the term fatigue when applied to glass describes an entirely different process from that occurring in fatigue of metals under cyclic or fluctuating stresses where inelastic deformation leads to failure. In glass, cyclic stresses produce slow crack growth due to the dynamic fatigue process.

The last part of a description of fiber strength is recognition that the flaws occurring in fibers vary in size and in location along the fiber length. The strength of an individual section of a fiber is thus only a sample of the population of strengths along the fiber length. Similarly, the time to failure in a static or dynamic fatigue test is a sample from the population of failure times. The breadth of the statistical distributions of strength and failure times can be very large. Strength variations in a kilometer length can range from less than 100 thousand pounds per square inch (ksi) to over 700 ksi. Failure times in static fatigue can range over several orders of magnitude. It has been found empirically that the strength of a group of fibers can be fit by a Weibull distribution⁶:

$$F(\sigma, L) = 1 - \exp[-(L/L_0)(\sigma/\sigma_0)^m]$$

where $F(\sigma, L)$ is the cumulative probability that a fiber of length L will fracture at a stress less than or equal to σ and m , L_0 , and σ_0 are parameters determined by fitting the data to the assumed distribution.

The principal tools required for failure analysis of a broken fiber are a scanning electron microscope (SEM) and fracture mechanics. The SEM is necessary for examining the fracture surfaces of a fiber since the depth of field of an optical microscope is usually insufficient. Fracture mechanics can be used to quantitatively estimate the stress that caused a fracture from measurements of features on the fracture surface. In addition to SEM and fracture mechanics, tests to determine the mechanical properties of fibers are useful.

The most important and widely observed features on a glass fracture surface are the sequentially formed mirror, mist, hackle, and crack-branching patterns (Figure 1). Failure originates from a flaw, which may or may not be sharp crack, but from which, in any case, a sharp crack develops and propagates. The velocity increases rapidly as the crack propagates, approaching terminal velocities of $\approx 10^3$ m/s within 3 to 6 times the length of the original crack⁷. Over, and generally substantially beyond, the region of acceleration, the crack generates a rather smooth fracture surface, which, because of its mirrorlike reflectivity, is called the fracture mirror. This flat, smooth mirror region is bounded by small, radially shaped ridges, or flakes, called mist; shortly beyond this region, larger, radially shaped ridges, called hackle, generally begin. The onset of hackle is, in turn, frequently followed by macroscopic crack branching (Figure 1).

These patterns are important for identifying the location, if not the specific source, from which fracture initiates, because they are usually symmetric about the fracture origin and the mist and hackle are generally radially oriented. In addition, the radii (R_i) from the center of the origin to each subsequent feature tend to be inversely related to the fracture stress (σ_f)⁷, i.e.,

$$\sigma_f = YK_{IC} / (c)^{1/2} = A_i / (R_i)^{1/2}$$

where K_{IC} is the critical stress intensity, Y and A_i are constants (each A_i value corresponding to the type of R_i as shown in Figure 1, i.e., R_m , R_h), and c is the crack depth.

The test procedures used in our analyses are summarized below.

Defect Analysis - In order to identify defects on the coating, the fibers were examined under a stereo microscope.

Fractographic Analysis - The fracture surfaces of broken fibers were examined with a scanning electron microscope. The protective polymer coatings on the fibers were removed in the vicinity of the break using a chemical stripper. The fiber ends were carefully cleaned by soaking the fibers in acetone for a short period of time to remove dirt and cable filling compound. The fracture surfaces were coated with a gold deposit 10-12 nm thick. Any particles or inclusions present on the fracture surface were identified with the help of energy dispersive x-ray analysis.

Tensile Strength - The tensile strengths of the fibers were measured with a screw-driven universal tensile testing machine in a laboratory environment of 22° C and relative humidity of 45%. Samples were gripped on 5 cm (2 inches) diameter capstans covered with a soft elastomeric sleeve. Masking tape was used to secure the ends of the fiber securely to the capstans. Tensile strength was determined at a strain rate of 5%/min with a gage length of 50 cm (19.6 inches).

Two-point Bending Strength - Fiber strength was also measured using a dynamic two-point bending method⁸. This technique is especially useful if there is a problem in handling the fiber; for example, when the coating is defective or damaged. The test consists of bending a fiber sample in a 180° loop between two parallel plates which are driven together. The fiber is bent to a continuously smaller radius until it eventually fractures, and by measuring jaw separation at the instant of fracture, the fiber strength can be determined.

Stripping Test - The force required to strip the coating was measured using a commercial stripping tool mounted on a screw-driven universal tensile testing machine. The gage length of the stripped section was 3 cm (1.2 inches) and the test was conducted at the rate of 50.8 cm/min (20 inches/min).

4. FIBER FAILURES

We shall now present a summary of one of our analyses of fiber failures to illustrate the procedures used.

A fiber optical cable was installed in a 1-1/4 inch inner duct in an underground conduit system. The cable was an all-dielectric, slotted core design; strength was provided by a layer of aramid yarn stranded around the slotted core. The fibers were a depressed clad design with a single layer, acrylate coating. The cable contained 16 fibers placed in the six slots. The cable, which connected two central offices, was about 15,000 feet in length and had been placed in one continuous piece in eight separate pulling operations utilizing seven "figure eights."

The cable was shipped from the factory with one broken fiber. After installation, splicing, and testing, four additional broken fibers were detected. Four transposition splices were made to recover service on four of the fibers. Two years after installation, an increase in attenuation in one fiber (fiber number 15) in this cable caused a system failure. When the system failure occurred, transmission was switched to a protection fiber, which was the last available good fiber in the cable. As a result, two replacement cable sections were installed to replace the portion of the cable containing the transposition splices. The defective cable sections containing the broken fibers were shipped to Bellcore for a post-mortem examination.

A high resolution OTDR was used to observe the condition of each fiber and to verify that no additional damage had occurred during the removal process. Our initial findings matched the information received from the field about the location of the fiber breaks. The cable was cut approximately 7 meters beyond the fiber break that caused the field failure (fiber 15). A helium neon laser was connected to end of the broken fiber to assist in locating the break. All sheath and core wrap over the fibers were removed in short pieces until the fiber break was clearly observed by the presence of the laser light. The end faces of the fibers were approximately 1/8 inch apart. The fibers were removed from the cable and it was noted that the coating on the broken fiber had disintegrated. An examination of the sheath and core materials in the area of the break did not indicate any defects which may have caused the fiber break or the coating disintegration.

The process described above was used to locate two other fiber breaks (in fibers 10 and 12) in the cable. The break in fiber 10 was located and it was observed that the end faces were separated by approximately 1/8 inch. An examination of the cable showed no imperfections which may have contributed to this fiber failure. It was observed that fiber 12 was also broken with the end faces separated by approximately 1/8 inch. The sheath and core components were intact and did not contribute to this fiber break. Fibers 10 and 12 were removed from the cable and initial examination revealed no unusual bubbles or other coating defects as had been noted on fiber 15.

From the size of the features on the fracture surface (Figure 2), we estimate that fiber 10 failed at 27 ksi. Based on the fractographic analysis of fiber 12 shown in (Figure 3), we estimate that it failed at 32 ksi. The boundaries of the mirror or mist region are shaped in the form of a circular arc. The flaw where the fracture originated is located at the center of this imaginary arc. Based on the scanning electron microscope analysis, these low strength failures were probably caused by surface scratches. The surface of the preform or the fiber may have been scratched by contact with other surfaces such as the coating applicator.

Fiber 15 was examined around the broken area with a stereo microscope. Numerous coating defects were observed for seven feet either side of the break (Figures 4 and 5). Within this 14 foot distance, difficulties apparently developed in the coating application procedure. Figure 4 shows the physical evidence of irregularities in the thickness of the coating. In some areas of fiber 15 the coating thickness is so thin that the glass fiber is directly exposed to the environment (Figure 5). Eccentricity of the coating can also be observed in Figure 10. At many locations bubbles were observed in the coating and in some cases these bubbles caused local holes in the coating.

Because fiber 15 exhibited coating problems and there was a defect in the cable jacket 28 feet away from the failure point, further investigations were conducted on fibers in the same core slot. The fibers in this slot are designated as fibers 13, 14, 15, and 16. Figure 6 shows the coating stripping test results for these four fibers in the vicinity the break point of fiber 15. At a location 4 feet from the point of failure, fiber 15 had a 33% lower stripping force than fiber 13 and a 42% reduction compared to fiber 14. Figure 12 summarizes the stripping test results for fiber 15 at 7 different locations surrounding the area of defective coating.

Dynamic tensile test results for all fibers are summarized in Figure 8. As shown in Figure 5, coating irregularities made it impossible to grip the samples around the capstans. Therefore, tensile strength tests could not be conducted near the defective coating. However, at other similar locations, fiber 15 showed the lowest mean strength.

The two-point bending test was done near the defective coating and from a non-defective zone. The results are summarized in Figure 9. Since the effective gage length is only 0.5 mm (0.02 inches) for the bending test, the probability of a flaw being located in the gage length is very small, and consequently the results tend to be uniform and unimodal as was the case in the non-defective coating area (see Figure 5). However, in the defective coating region, the strength distribution was very broad.

Both ends of the fractured fiber 15 were examined in a scanning electron microscope (Figure 10). The fracture surfaces did not show any "mist" and "hackle" regions. The mirror area covered the entire cross section which is indicative of a very low strength failure. The surface of a fracture occurring at less than 24.5 ksi (for 125 μ m glass diameter) will consist mostly of a mirror area and will not display other features. Since this failure happened 47 months after the fiber was put into service, it appears that a low stress, static fatigue mechanism was the main reason for this failure. Figure 10 also shows the damaged fiber surface which was probably caused during manufacturing as explained for fibers 10 and 12, or by handling of the fiber in preparation for cabling because of defective coating.

In summary, the fracture characteristics of all three broken fibers were typical of low strength, tensile failures. The estimated breaking strengths of these fibers are less than the proof test level of 50 ksi. This suggests that the flaws that caused the failures were (a) introduced during fiber fabrication and the fibers were not proof tested, (b) introduced after proof testing, or (c) existing but grew in size during service (by static fatigue). The breaking stress levels are sufficiently low that failure could have been caused by installation and/or cabling stresses. The coating on fiber 15 was defective, which was probably caused during coating of the fiber and which allowed subsequent damage to the fiber surface. Although the coatings on the other two fibers (fiber 10 and fiber 12) were undamaged, there was some evidence of surface damage on both fibers. In this case, the surface of the preform or the fiber may have been scratched by contact with a surface during manufacturing.

CONCLUSIONS

We have shown how an understanding of glass behavior coupled with fracture mechanics and modern instrumentation can be used to analyze failures of optical fibers. The examples shown here illustrate that most fiber failures are caused by defects in the glass produced during fabrication or installation. Undamaged fibers appear to have very good mechanical reliability.

ACKNOWLEDGMENTS

We would like to thank our colleagues at Bellcore for their assistance including A. DeVito and C. J. Wieczorek for cable dissection and analysis. We also wish to thank our clients for supplying the fiber cables for our analysis.

REFERENCES

1. W.T. Anderson; Bellcore; Morristown, NJ; private communication.
2. R. A. Connolly; Bellcore, unpublished work.
3. R. Lawn and T. R. Wilshaw; *Fracture of Brittle Solids*; Cambridge University Press; 1975.
4. A. A. Griffith; *Phil Trans Royal Soc London, Ser A*; **192**; 162 (1920).
5. T. A. Michalske and S. W. Freiman; *J Am Cer Soc*; **66**; 284; (1983).
6. W. Weibull; *Proc Royal Swedish Inst Eng Res*; no 151 (1939).
7. J.J. Mecholsky et al; *Fiber Optics: Advances in Research and Development*; Ed. B. Bendow and S. S. Mitra, Plenum, New York; 84(1979).
8. H. Yuce et al; *Proceedings of IOOC'89*; ; 44 (1989)

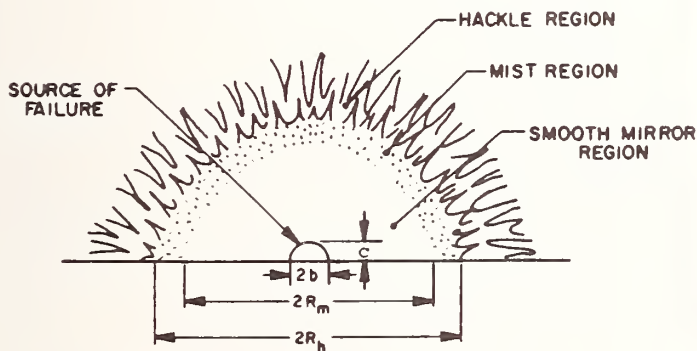


Figure 1 : Shape and General Appearance of Fracture Surface

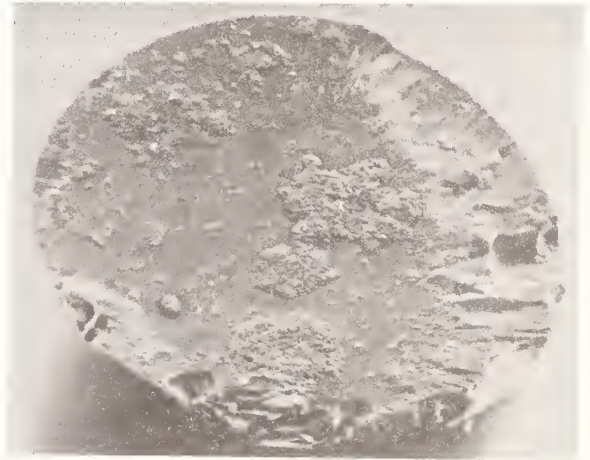


Figure 2: Fracture Surface of Fiber 10

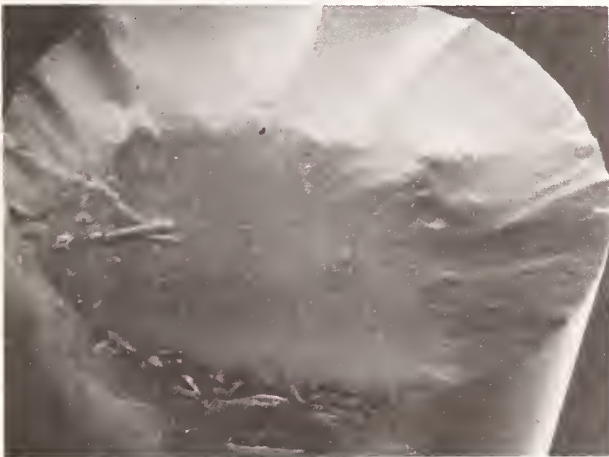


Figure 3: Fracture Surface of Fiber 12

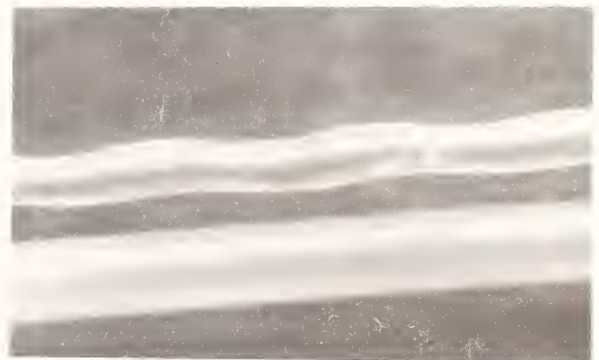


Figure 4: Defective Coating on Fiber 15
Fiber 14 (Top) Shown for Comparison

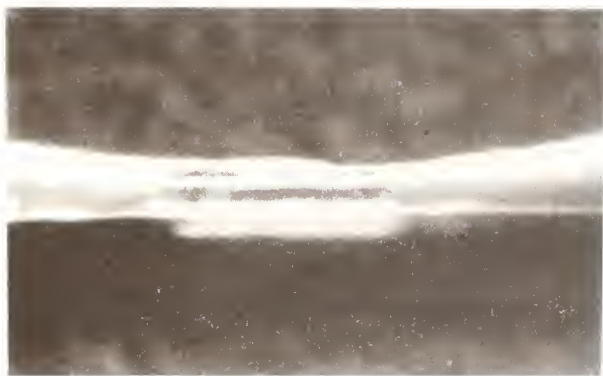


Figure 5: Defective Coating on Fiber 15

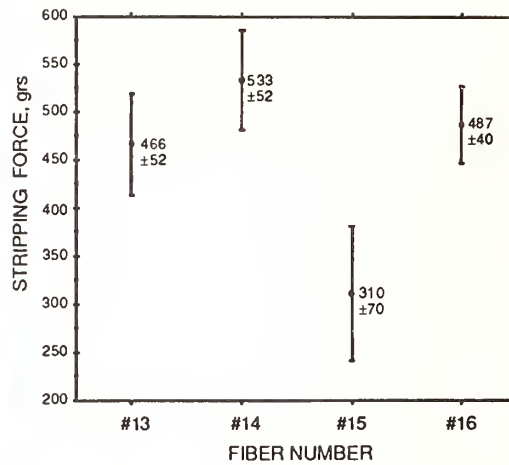


Figure 6: Coating Stripping Force

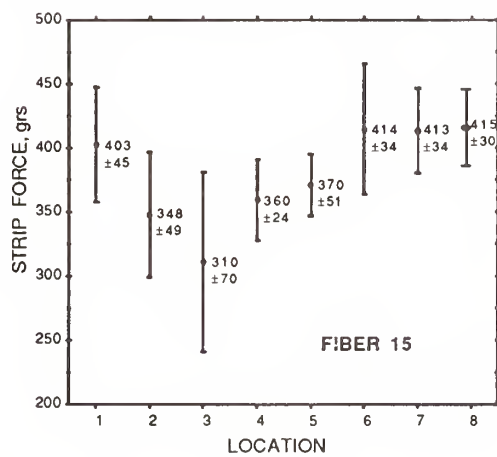


Figure 7: Coating Stripping Force for Fiber 15 at Different Locations Along Fiber Length. (Defective Coating Occurred at Location 3)

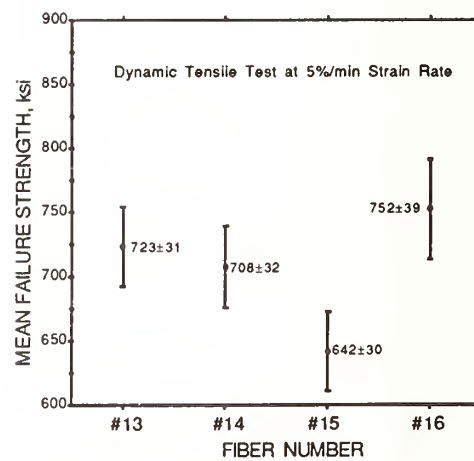


Figure 8: Dynamic Tensile Strength of Fibers

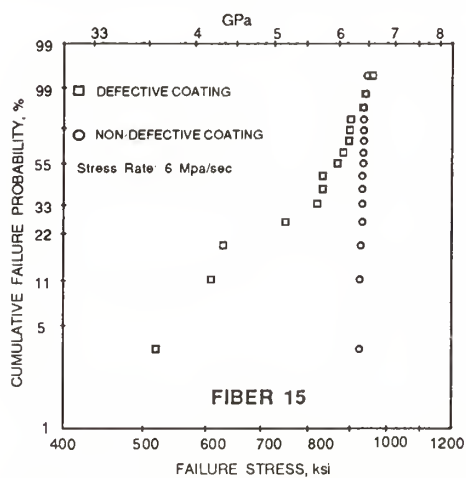


Figure 9: Two-Point Dynamic Bending Strength Test Results

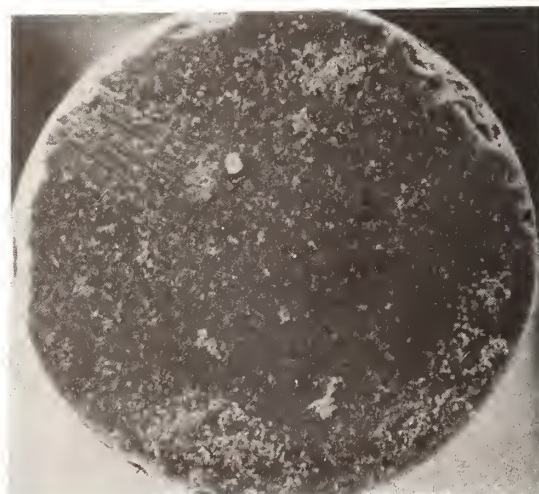


Figure 10: Fracture Surface of Fiber 15

Optical frequency domain reflectometry using network analysis techniques

David W. Dolfi

Hewlett-Packard Laboratories

Palo Alto, CA 94304

Roger L. Jungerman

Microwave Technology Division, Hewlett-Packard

Santa Rosa, CA 95403

Abstract

Optical Frequency Domain Reflectometry (OFDR) has achieved millimeter resolution through the use of wide bandwidth integrated optic modulators. A modulator based OFDR system which uses methods analogous to microwave network analysis is described, and compared to both time domain and other frequency domain methods. Several figures of merit for reflectometry systems are identified and discussed.

Summary

Optical Time Domain Reflectometry (OTDR) is a widespread and commercially successful technique for performing several types of measurements on fiber optic networks and components. This method consists of probing with repetitive optical pulses and detecting the resulting reflections and/or backscattered light from the system under test. An alternative method, also in widespread use, is Optical Frequency Domain Reflectometry (OFDR). This technique uses continuous wave (cw) light which is either stepped or swept continuously in frequency. The reflected or backscattered light, as a function of the frequency, can yield equivalent information about the

system under test. Under these conditions, detection of the signal can take place in a restricted bandwidth much smaller than in the time domain case. Thus, frequency domain techniques hold out the possibility of reduced noise and superior dynamic range.

There are several figures of merit which can be used to evaluate a given reflectometry method or system. One is the system resolution, which determines how closely spaced two optical reflections can be — in time or distance — and still be resolved. A second figure of merit is the range, or how far apart these same two reflections can be and still be measured accurately. In frequency domain based systems these two figures of merit are often complimentary, in the sense that one can be improved at the expense of the other. A third figure of merit is the system dynamic range. This is usually defined as the ratio (in decibels) between the maximum and minimum reflection the system can accurately measure. The former limit is normally determined by the available optical power or the onset of system nonlinearities. The latter limit is determined by the level of the noise floor. A fourth figure of merit is the time required for a measurement to be made, or more precisely, the measurement time required to achieve a given signal-to-noise ratio (SNR). While not always considered in discussion of reflectometry, measurement time is an important factor since SNR (and hence dynamic range) can always be improved at its expense. This can be accomplished in the frequency domain by narrowing the resolution bandwidth of the measurement, and in the time domain by averaging. For a commercial instrument application, there are two other figures of merit which are significant. The first is the accuracy and ease with which the system can be calibrated. The second is the versatility of the system or technique; that is, the variety of measurements which it can perform.

In the first part of this talk, various reflectometry methods will be reviewed in the context of the figures of merit given above. One such method is Frequency Modulated Continuous Wave (FMCW) OFDR, adapted from radar. Both coherent [1,2] and incoherent [3,4] versions of this technique have been implemented. Another is the Optical Coherence Domain Reflectometry

(OCDR) technique [5-7], which is capable of sub-millimeter resolution. In addition, there is the Network Analysis (NA-OFDR) technique [8-11], which is closely analogous to conventional microwave network analysis. It will be shown that this latter technique offers an excellent compromise with respect to the various figures of merit discussed above.

The second part of the talk will focus on the details of the NA-OFDR method, a generic representation of which is shown in Fig. 1a. In this method, the optical source which probes the system under test is amplitude modulated at a given frequency. The return signal, containing the system response, is measured directly. Stepping the modulation frequency over the range of interest and measuring at each frequency point results in the total frequency domain characterization of the system under test. If both amplitude and phase response have been measured, Fourier transformation can be employed to yield the time domain response. Referring to Fig. 1a, the measurement system contains a conventional microwave network analyzer which drives an independent optical test set. The latter consists of a modulated optical source and a receiver. With this modular approach, a variety of measurements can be made. The network analyzer alone provides purely electrical measurement capability, while the optical test set allows optical transmission and reflection measurements to be made. Finally, by using different combinations of the optical and electrical ports for stimulus and response, various electrical-to-optical and optical-to-electrical converters can be characterized, including sources and detectors. An example of a reflection measurement made with such a system [10] is shown in Fig. 1b. The signal represents two optical reflections separated in time by ≈ 100 psec, corresponding to a distance separation in optical fiber of 1 cm.

Several possible options for the source and receiver will be discussed. Of particular interest is the use of wide bandwidth integrated optic modulators. These can serve both as the source of modulation in such systems [10,11] and as optical/electrical mixers at the receiver end to downconvert the return signal, directly in the optical domain, to a low intermediate frequency [4,11].

Finally, a commercially available system [12] based on the NA-OFDR technique, which contains integrated optic components to achieve high resolution, will be described,

References

- [1] W. Eickhoff and R. Ulrich, "Optical frequency domain reflectometry in single-mode fiber," *Appl. Phys. Lett.*, **39**, pp. 693-695 (1981).
- [2] A.J. Hyman and B. Culshaw, "Precision time domain reflectometry in optical fiber systems using a frequency modulated continuous wave ranging technique," *J. Lightwave Tech.*, **LT-3**, pp. 917-977 (1985).
- [3] R. I. MacDonald, "Frequency domain optical reflectometer," *Appl. Opt.*, **20**, pp. 1840-1844 (1981).
- [4] Shalini Venkatesh and David W. Dolfi, "Incoherent frequency modulated cw optical reflectometry with centimeter resolution," *Appl. Opt.*, **29**, pp. 1323-1326 (1990).
- [5] R. C. Youngquist, S. Carr, and D.E.N. Davies, "Optical coherence domain reflectometry: A new optical evaluation technique," *Opt. Lett.*, **12**, pp. 158-160 (1987).
- [6] K. Takada, I. Yokohama, K. Chida, and J. Noda, "New measurement system for fault location in optical waveguide devices based on an interferometric technique," *Appl. Opt.*, **26**, pp. 1603-1606 (1987).
- [7] B. L. Danielson and C. D. Whittenberg, "Guided-wave reflectometry with micrometer resolution," *Appl. Opt.*, **26**, pp. 2836-2842 (1987).
- [8] F. P. Kapron, D. G. Kneller, and P.M. Garel-Jones, "Aspects of optical frequency domain reflectometry," in *Technical Digest, IOOC '81* (Optical Society of America, Washington, D.C., 1981), paper WF-2.

- [9] J. Nakayama, K. Iizuka, and J. Neilsen, "Optical fiber fault locator by the step frequency method," *Appl. Opt.*, **26**, pp. 440-443 (1987).
- [10] David W. Dolfi, Moshe Nazarathy, and Steven A. Newton, "5 mm resolution optical-frequency-domain reflectometry using a coded phase-reversal modulator," *Opt. Lett.*, **13**, pp. 678-680 (1988).
- [11] D. W. Dolfi and Moshe Nazarathy, "Optical frequency domain reflectometry with high sensitivity and resolution using optical synchronous detection with coded modulators," *Electron Lett.*, **25**, pp. 160-161 (1989).
- [12] P. Hernday, R. Wong, and R. L. Jungerman, "20-GHz lightwave component analysis instrumentation using an integrated optical modulator," in *Technical Digest, OFC '90* (Optical Society of America, Washington, D.C., 1990), paper WM-26.

Figure Captions

Fig. 1. (a) Schematic representation of a reflectometry system based on the Network Analysis method. (b) Measurement made with system depicted in (a). The peaks represent reflections from two fiber ends whose length difference is ≈ 1 cm. The resolution of the system is 5 mm.

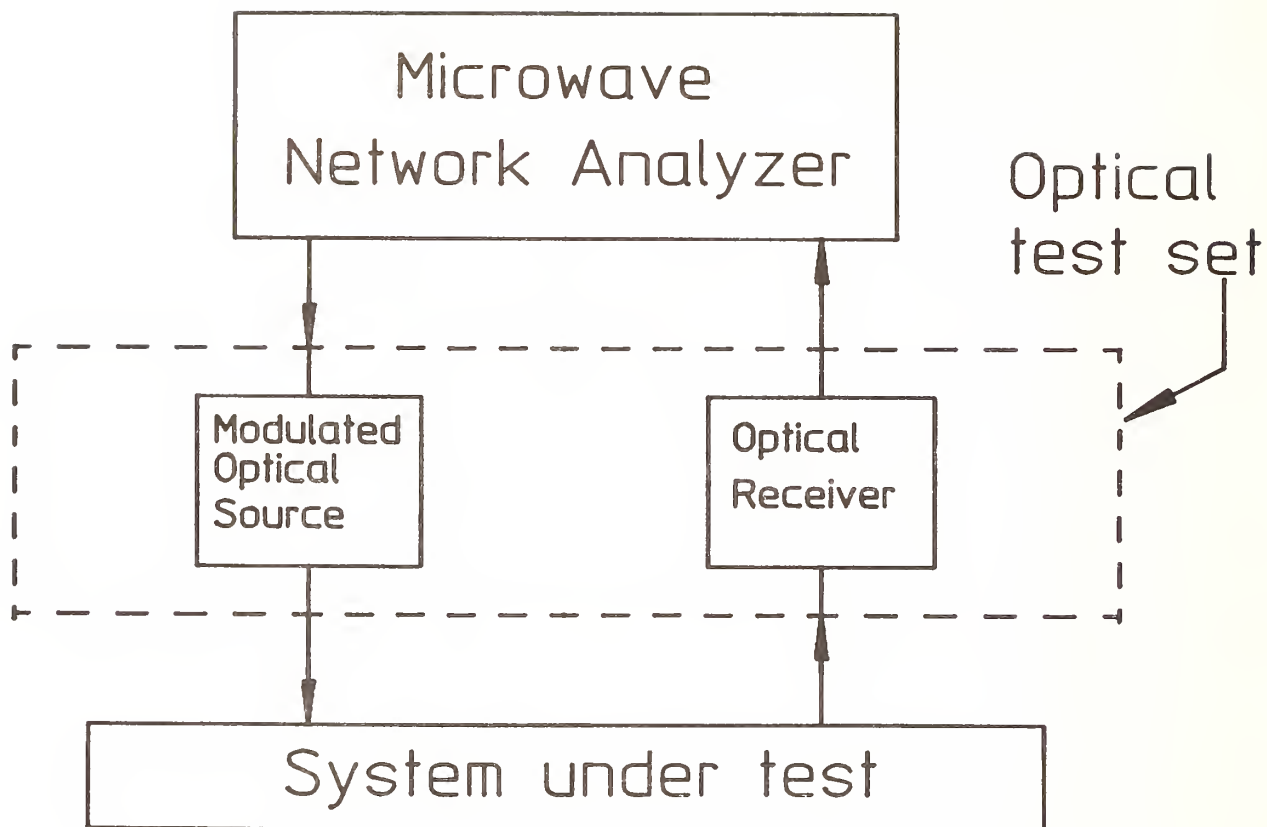


Fig. 1a

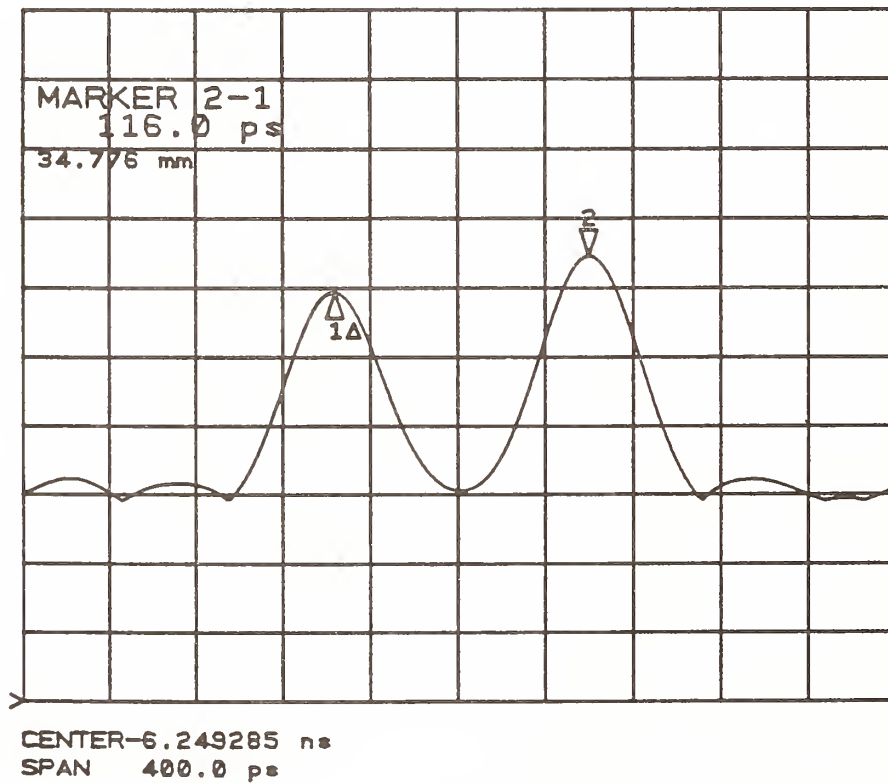


Fig. 1b

Long and Short Range Measurements Using Coherent FMCW Reflectometry

W. V. Sorin and D. K. Donald

Hewlett-Packard Laboratories
3500 Deer Creek Road, Palo Alto, California 94303

ABSTRACT

A long coherence length monolithic Nd:YAG laser operating at 1.32 microns is used to perform coherent FMCW reflectometry measurements. The optical frequency chirp is generated by temperature ramping the laser crystal. Experimental results demonstrate two-point resolution of less than 10 cm, and two way optical dynamic range in excess of 60 dB.

SUMMARY

Optical reflectometry using a coherent FMCW technique¹⁻³ offers the possibility of high resolution combined with a large dynamic range. In this paper, coherent FMCW reflectometry refers to time delay (i.e. length) measurements made by interferometric mixing of a laser signal whose optical frequency has been linearly chirped in a phase continuous manner. Optical reflectivity as a function of fiber length is obtained by displaying the frequency spectrum of the photocurrent power on an electrical spectrum analyser.

Previous FMCW measurements using frequency chirped semiconductor lasers reported measurement ranges limited to only a few meters due to the relatively short coherence length of these sources.^{2,3} Short coherence length also contributes to large amounts of phase noise which limits the dynamic range of these measurements. This paper will discuss experimental results obtained using a long coherence length, Nd:YAG ring laser⁴ operating at a wavelength of 1.32 microns. Measurement of both distance and dynamic range are greatly improved by the long coherence length of this source.

The experimental set-up is shown in figure 1. The laser source is a single-frequency monolithic Nd:YAG nonplanar ring laser which oscillates in only one direction due to the presence of an external magnetic field.⁴ The monolithic nature of the laser provides a stable cavity which is relatively immune to environmental perturbations. The optical frequency is chirped by ramping the temperature of the Nd:YAG crystal. Phase continuous chirps were obtained over a 13 GHz range, which corresponded to the longitudinal mode spacing of the laser. Five to six mode hops were experienced during the ramp period, this allowed for relatively linear frequency chirps near the end of the ramp after initial temperature transients had died away.

The chirped laser signal passes through an optical isolator and then into a single-mode

fiber 3 dB directional coupler. A mirror is used in the upper arm to provide a single reflection which acts as the undelayed local oscillator (LO) signal. The signal coupled into the lower arm is sent into the fiber under test. Backscattered power from the fiber under test mixes with the LO signal and produces a beat frequency which is proportional to the differential time delay (or fiber length) that it experienced. The output of the photodetector is sent to an electrical spectrum analyser which displays electrical power as a function of the beat frequency. The output from the spectrum analyser is proportional to the desired result, which is backscattered optical power versus fiber length. Since coherent detection is used with constant LO power, the electrical power on the spectrum analyser is proportional to the backscattered optical power. The proportionality factor between beat frequency and fiber length is determined by the slope of the optical chirp (i.e. rate of change of optical frequency with time).

Figure 2 shows the Rayleigh backscatter at 1.32 microns from 50 Km of single-mode optical fiber. This figure experimentally demonstrates the extremely long coherence length of the Nd:YAG source. After traveling 100 Km (distance to end of fiber and back) the reflected signal can still coherently interfere with the LO. This corresponds to a coherence time in excess of 500 microseconds or a laser linewidth much less than 2 KHz. Ignoring environmental perturbations, theoretical calculation of the laser linewidth based on the Schawlow-Townes limit is on the order of a few hertz.⁵

The absence of Rayleigh backscatter can easily identify the end of the 50 Km length of fiber. The 1 KHz resolution bandwidth of the spectrum analyser corresponds to a 380 meter resolution cell for the capture of Rayleigh backscattered power. The measured two-way dynamic range in excess of 60 dB compares favorably with the best commercial OTDRs available (note: commercial OTDRs typically display one-way dynamic range). The limiting noise floor is believed to be due to intensity noise from the optical source. The estimated chirp rate for this measurement is 260 MHz/sec, this corresponds to beat frequencies of 130 kHz for scattered signals from the end of the 50 Km fiber length.

Besides exhibiting potential for long range applications, this source also has the ability to perform short range measurements. Figure 3 shows the Rayleigh backscatter from a 20 meter length of fiber. This measurement was taken using a HP3582A fourier transform spectrum analyser. The displayed frequency range is from 0 to 100 Hz with the end of the 20 meter fiber length corresponding to beat frequencies at about 75 Hz. From the measurement bandwidth of 1.45 Hz a length resolution of 38 cm is calculated. This length of 38 cm determines the level of Rayleigh backscattered power, which is about 30 dB above the noise floor. The noise floor was dominated by laser intensity noise which becomes large at frequencies close to DC. No attempt was made to remove polarization or coherence speckle noise which may have caused the large amplitude uncertainty in the Rayleigh backscattered signal in figure 3.

Figure 4 demonstrates the high two-point resolution possible with the Nd:YAG source. In this measurement, a 10 cm section of fiber was connected to the end of a 5 meter length. The Fresnel reflections from each joint can easily be seen. On the spectrum analyser display the 5 meter length and the 5 cm resolution corresponds to a beat frequency of 37 Hz and a resolution bandwidth of 0.363 Hz. The maximum resolution from this source is about

8 mm which is related to the 13 GHz sweep range (without a mode hop). The above resolutions are degraded from this value since the measurement times (i.e. reciprocal of resolution bandwidths) correspond to sweep ranges less than the maximum value of 13 GHz.

The above measurements demonstrate the potential of using narrow linewidth Nd:YAG lasers for coherent FMCW measurements. Although these results look very encouraging, there are still many problems that need to be solved. The strengths and weaknesses of this approach to reflectometry measurements will be discussed.

References

- (1) W. Eickhoff and R. Ulrich, "Optical frequency domain reflectometry in single-mode fibers," *Appl. Phys. Lett.*, **39**, 693 (1981).
- (2) D. Uttam and B. Culshaw, "Precision time domain reflectometry in optical fiber systems using a frequency modulated continuous wave ranging technique," *IEEE J. Light-wave Technol.*, **LT-3**, 971 (1985).
- (3) S. A. Kingsley and D. E. N. Davies, "OFDR diagnostics for fibre and integrated-optic systems," *Electron. Lett.*, **21**, 434 (1985).
- (4) W. R. Trutna, Jr., D. K. Donald and M. Nazarathy, "Unidirectional diode-laser-pumped Nd:YAG ring laser with a small magnetic field," *Opt. Lett.*, **12**, 248 (1987).
- (5) P. Fritschel, A. Jeffries and T. J. Kane, "Frequency fluctuations of a diode-pumped Nd:YAG ring laser," *Opt. Lett.*, **14**, 993 (1989).

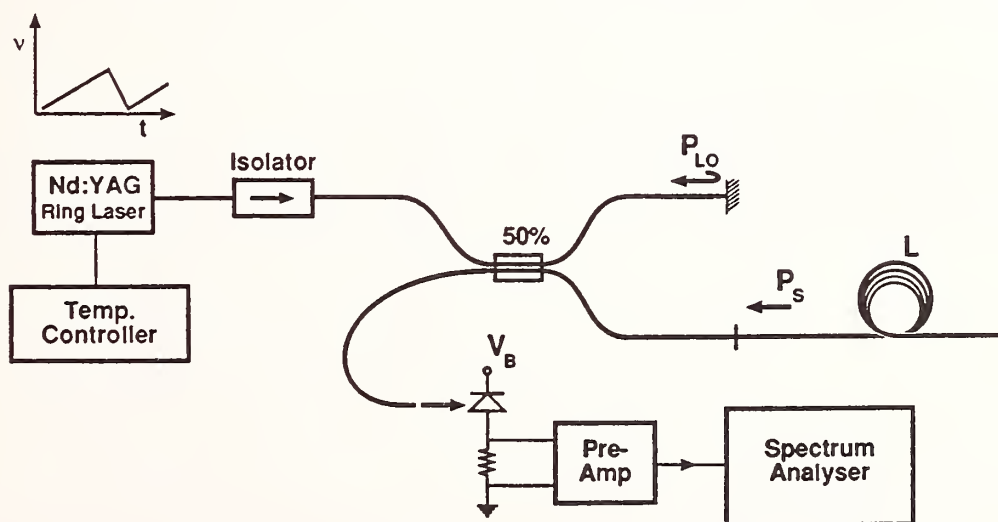


Figure 1. Experimental arrangement used for coherent FMCW measurements. The frequency chirp is generated by temperature ramping the laser crystal.

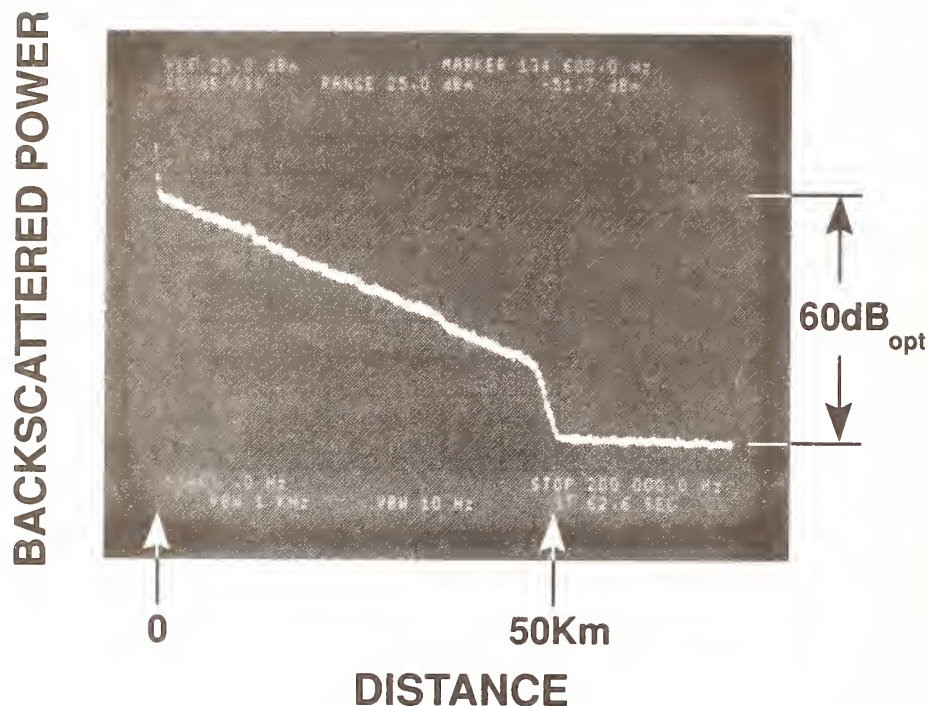


Figure 2. Rayleigh backscattered power from a 50 Km fiber length. Frequency range on spectrum analyser is 0 to 200 KHz.

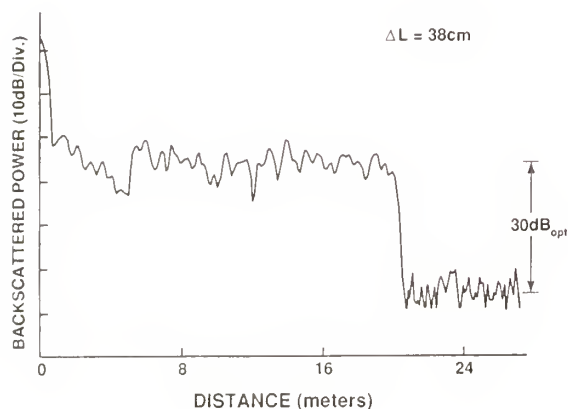


Figure 3. Rayleigh backscattered power from a 20 m fiber length. Frequency range on spectrum analyser is 0 to 100 KHz.

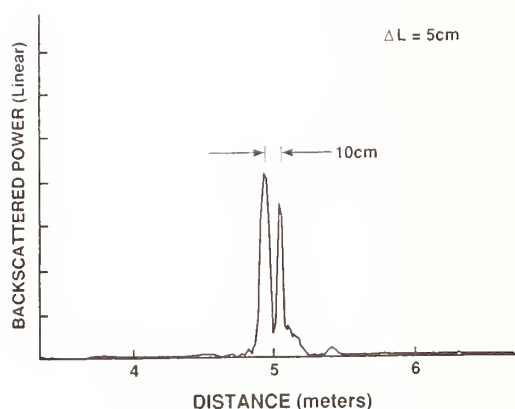


Figure 4. Fresnel reflections from a 10 cm section of fiber spliced onto the end of a 5 m length.

VERY LOW OPTICAL RETURN LOSS MEASUREMENT USING OTDR TECHNIQUE

P. BLANCHARD*, P-H. ZONGO*, P. FACQ*, J. ROCHEREAU°

* IRCOM-EOGI - 123, avenue Albert Thomas - 87060 LIMOGES Cédex, FRANCE

° CEDEPE - 49, avenue de la Libération - 87570 RILHAC RANCON, FRANCE

ABSTRACT

A new reflection modelling which gives great accuracy for reflectance measurements in fiber optic communications has been evolved. This modelling uses OTDR technique and is particularly suitable for very low reflectance evaluation where large discrepancy is observed in the results. The new model can introduce substantial improvements to the OTDR technique use. It takes into consideration the pulse waveform, the fiber optic and the receiver impulse responses. A specific reflectometer has been constructed allowing the use of that model. An optical return loss of -75 dB can be measured with a multimode optical time domain reflectometer.

INTRODUCTION

In fiber optic communications, reflections occur unavoidably. They are induced by refractive index discontinuities and provided from fiber ends, splices and optical devices such as connectors and couplers. These reflections along the fiber optic link can bring penalties to high-bit rate systems performances or damage the laser diodes in coherent transmissions [1]. Many solutions have been developed to minimize reflection phenomena such as anti-reflection coatings, refractive index matching, fiber ends bevelling. Even if significant results can be obtained using these methods, residual reflections remain.

Two main methods can be used for optical return loss (ORL) measurements : OCWR and OTDR techniques. The first one entails a significant inconvenience since it gives a global effect of all the link reflections, making difficult the separation of each contribution, and is somewhat cumbersome and lengthy to employ [2]. The second one is more attractive since it allows both magnitude and location efficient measurements of a sequence of reflections, but current reflectometers are not optimized for ORL evaluation [3], [4].

Measuring very low level reflections, visible or not, on an optical reflectometer display is a difficult task and cannot be achieved with traditional instruments or techniques at present levels. This paper introduces a new concept to reflection modelling and its uses. It also shows how substantial accuracy is brought to reflectance measurement, and how this modelling allows successful very low level ORL evaluation.

OTDR REFLECTANCE EVALUATION

The reflectance R in decibels is usually defined by :

$$R(\text{dB}) = 10 \log_{10} \{ P_R / P_I \}$$

where P_R is the reflected power and P_I the incident one. The accuracy of the reflectance measurement depends on the way the power P_R is evaluated in relation to P_I and the characteristics of the optical reflectometer.

When OTDR technique is used to establish a diagnostic of a fiber optic link which includes any kind of reflective element, a signal like that which is shown in figure 1-a is observed at the reflectometer display.

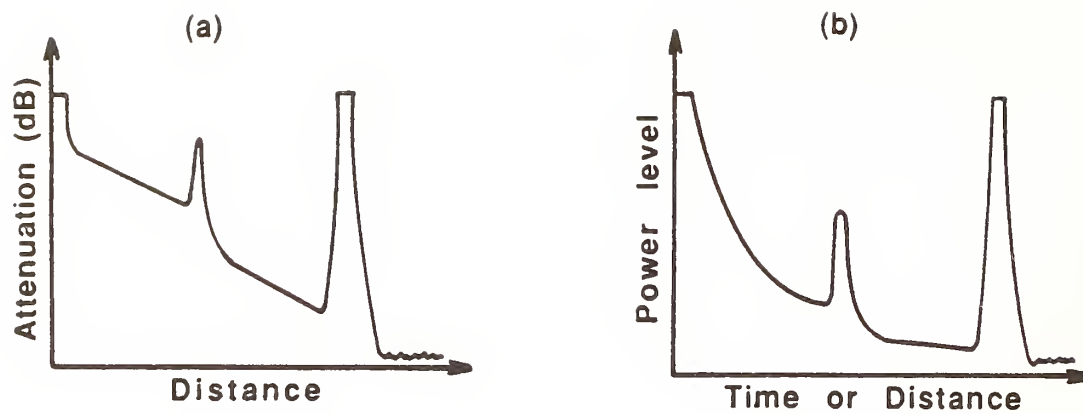


Figure 1 : OTDR traces : (a) logarithmic display (b) linear display

In a theoretical approach, three main time dependant signals denoted $P_I(t)$, $P_R(t)$ and $P_S(t)$ can be distinguished. $P_I(t)$ is the input power while $P_R(t)$ and $P_S(t)$ are respectively the backreflection and the backscattering powers. They can be expressed by :

$$P_I(t) = P_0 e^{-\alpha v_g t} ; P_R(t) = R P_0 e^{-\alpha v_g t} ; P_S(t) = 0.5 P_0 W \alpha_S v_g e^{-\alpha v_g t}$$

where :

P_0 : peak power	α_S : scattering attenuation coefficient
W : optical pulse width	α : average of forward and backward attenuation
S : Backscattering factor	R : reflection coefficient
v_g : average group velocity	t : time

The reflection coefficient R at the index discontinuity is commonly derived from measuring the backscattered power level P_S immediately in front of the discontinuity abscissa, and the reflected pulse characteristics : width, height, with rectangular pulse assumption [fig 2].

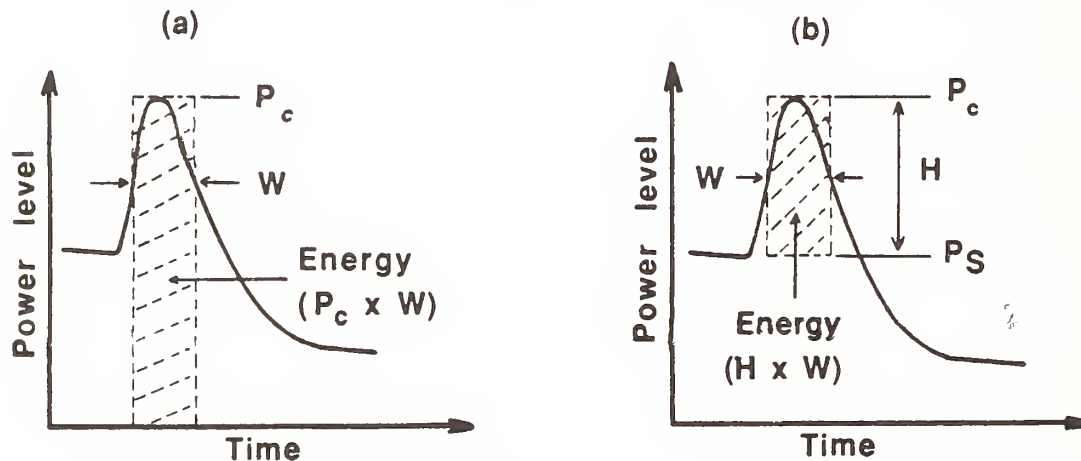


Figure 2 : Reflected energy evaluation : (a) [5], [6] (b) [4].

The reflection coefficient R can be written as :

$$R = K \frac{W.H}{P_S} \rightarrow R(\text{dB}) = 10 \log_{10} \left\{ K \cdot \frac{W.H}{P_S} \right\}$$

where K is defined by the fiber parameters ($K=0.5 \alpha_S v_g S$). Calibration method has been developed. A precise determination, based on a calibrated reflection can be made. Details will be given at the conference.

However, ambiguity exists in pulse width W and pulse height H determination. Moreover, it is difficult to determine pulse duration or width with accuracy with current optical time reflectometers. This is why we have evolved a new concept of reflection modelling that works with the backward pulse real wave form, and which defines better the reflected signal contribution.

NEW REFLECTION MODELLING

We assume that all the systems which are involved in the reflectance measurement process are linear and time invariant, so convolution can be applied. The backward OTDR signal $B(t)$ is taken from the linear amplifier before logarithm processing. The signal $B(t)$ can be considered as the sum of two signals [fig 3].

$$B(t) = R(t) + S(t)$$

where $R(t)$ and $S(t)$ represent respectively the reflected power and the backscattered power at time t . These two signals correspond to two independent phenomena. The reflected signal $R(t)$ is given by :

$$R(t) = B(t) - S(t)$$

Therefore the reflection coefficient R is proportional to the reflected pulse energy obtained by integration.

$$R = C \int_{t_0}^{t_1} [B(t) - S(t)] dt$$

The time t_0 ($t_0 = 2z_0/v_g$) corresponds to the reflective element abscissa z_0 and the time t_1 depends on the receiver recovery and the required accuracy. The constant C contains the fiber parameters and is equal to $K/S(t_0)$. The value $S(t_0)$ is known while the signal $S(t)$ is unknown between t_0 and t_1 . The numerical values of R can be calculated if the signal $S(t)$ can be determined.

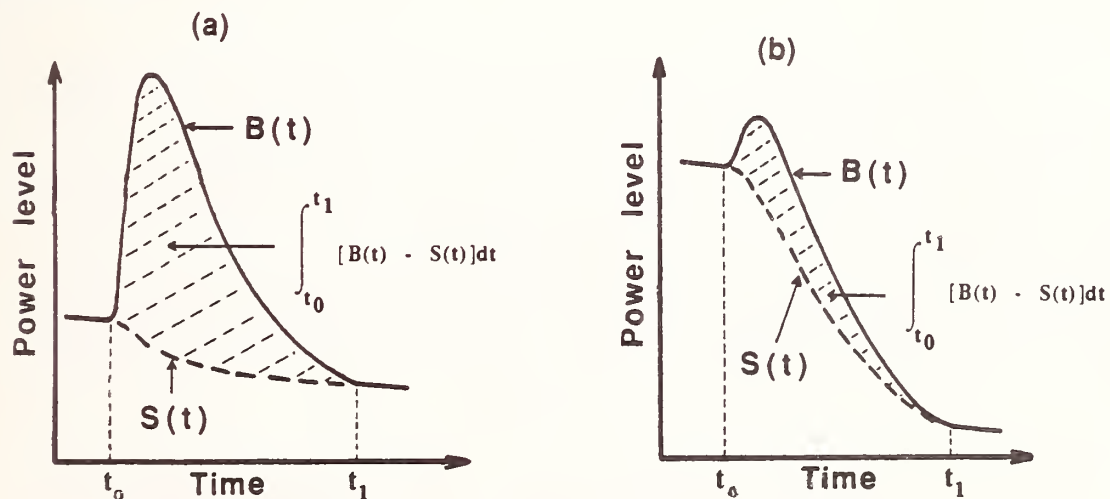


Figure 3 : The new reflected energy evaluation :

--- backscattered signal $S(t)$ — total backward signal $B(t)$ /// reflected energy

THE SIGNAL $S(t)$ DETERMINATION

Using time dependant analytic expressions of launched pulse, fiber optic, and receiver impulse responses, an analytic formula of the signal $S(t)$ has been deduced [7]. It can be written as :

$$S(t) = B(t_0) e^{-\alpha v_g(t-t_0)} \left\{ 1 - \left[1 - \frac{B(t_1) e^{\alpha v_g(t_1-t_0)}}{B(t_0)} \right] I(t) \right\}$$

where :

$$I(t) = \int_0^{t-t_0} e^{\alpha v_g u} R(t_0+u) du / \int_0^{t_1-t_0} e^{\alpha v_g u} R(t_0+u) du$$

The experimental results of the signal $S(t)$ taken from the linear output of the optical time reflectometer after the reflection has been eliminated, have been compared to those obtained from the $S(t)$ formula. A good agreement has been observed. The difference between the reflected energy calculations from $S(t)$ experimental and theoretical values is less than 2% [fig 4].

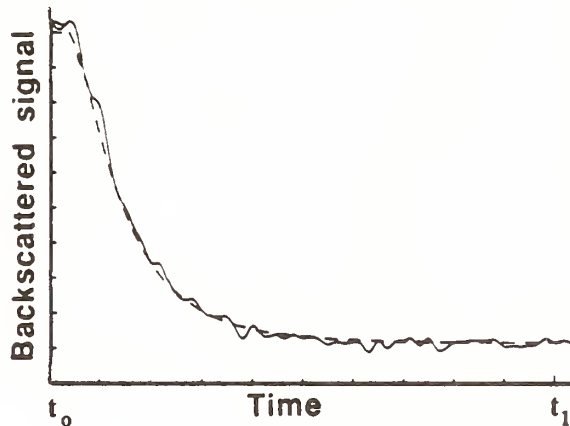


Figure 4 : Backscattered signal between t_0 and t_1
— measured (after the reflection was cancelled)
---calculated from the formula

CONCLUSION

A new reflection modelling is proposed. It takes into account the actual pulse wave form and the optical time reflectometer receiver recovery tail. No simplifying assumption is made about either the shape, width or height, of the launched pulse or the reflected pulse.

Taking into account not only the backscatter signal level immediately ahead of the reflected spike, but also its trace over the duration of two or three pulses, when the reflexion is completely suppressed, leads to a better reflectance measurement.

The constructed reflectometer offers the possibility of simultaneously analysing five reflected spikes. A computer is connected to the measurement system for improved signal processing. The new technique has been applied successfully to interrogate five networked reflective analogical fiber optic sensors. Low reflection measurement can be achieved with this model, thereby increasing the dynamic range measurement.

REFERENCES

- [1] J.L. GIMLETT, N.K. CHEUNG, J. Lightwave Tech., Vol.7, N°6, p.888, june 1989.
- [2] S.K. DAS, A.F. JUDY, G.M. ALAMEEL, R.M. JOPSON, T.F. ADDA, Tech. Dig. Symp. Opt. Fiber Meas., NBS Special Pub. 748 (Boulder, Co), pp.25-30, sept. 1988.
- [3] P.R. REITZ, Tech. Dig. Symp. Opt. Fiber Meas. NBS Special Pub. 748 (Boulder, Co), pp.31-34, sept. 1988.
- [4] F.P. KAPRON, B.P. ADAMS, E.A. THOMAS, J.W. PETERS, J. Lightwave Tech., Vol.7, N°8, p.1234, august 1989.
- [5] E.G. NEUMANN, AEÜ, Band 34 [1980], Heft 4.
- [6] P. HEALEY, Opt. and Quantum Elect., 16, p.267, 1984.
- [7] P. BLANCHARD, P.H. ZONGO, P. FACQ, J. ROCHEREAU, (To be published).

R.P. Novák, H.H. Gilgen
Swiss PTT, Technical Centre, 3000 - Berne
P. Beaud, W. Hodel,
University of Berne, 3000 - Berne
Switzerland

1. Introduction

Optical reflectometry in the micrometer range has become a very important nondestructive diagnostic tool for investigating small structures like integrated optical circuits (IOC), optical connectors, splices, couplers etc.

In our previous work [1,3] we already have reported on the development of an infrared (1300nm) Optical Time Domain Reflectometer (OTDR) using pulses of 300fs duration and balanced heterodyne detection. Another very promising tool with approximately the same features - Optical Low Coherence Reflectometer (OLCR) - is based on homodyne coherent correlation of a backscattered and a phase or frequency modulated signal [2,3].

In this paper we report on a significant improvement on the OLCR system and compare the features and the measurement results achieved with results of the OTDR system.

2. Experimental arrangements and results.

The basic arrangement of a high resolution reflectometer consists of a Michelson interferometer. The light of a source is split into a reference and a probe beam. The probe beam is launched into the sample under investigation. The backscattered light from the sample is recombined with the modulated reference light (local oscillator) at the detector. The detector consists of suitable optics and photodiodes in order to investigate the coherent overlapping of the two beams. The degree of overlapping is varied by changing the length of the delay line of the reference beam. This allows a spatially resolved investigation of the sample.

The experimental OTDR set-up used for these experiments is shown in Fig.1. This system consists of a synchronously pumped mode locked dye laser as light source. Balanced heterodyne detection is used in order to achieve sensitivities higher than -100dB. For a more detailed description of this system see reference [4]. Fig.2 shows a comparison between the measured and calculated signal trace in a logarithmic scale for the OTDR system. The standard resolution of the system at FWHM is given for this experiment as 60 μm in air. The calculated curve represents the heterodyne signal amplitude assuming Gaussian bandwidth limited pulses with a spectral width of 2.15THz. The agreement with the experimental data is good alt-

though the dye laser pulses are in reality not bandwidth limited under the selected experimental conditions. A pedestal at an intensity level of -50dB is observed which decreases only slowly towards the final noise level of -80dB. This pedestal can probably be attributed to fluctuations of the pulse duration resulting from inhomogeneities in the dye jet. The calculated curve predicts a correlation width of 270 μ m at the -100dB level. In reality, using the balanced heterodyne detection the corresponding width at -100dB was measured as 1.5 mm.

The schematic arrangement of the OLCR technique is shown in Fig.3. An edge emitting LED ($\lambda=1300$ nm, $\Delta\lambda=60$ nm, $P=3\mu$ W in SMF) is used as a light source. An all fiber polarizer and a polarizer controller assures that only one desired mode is propagating through the whole set-up. The polarization maintaining fiber coupler is used for coupling light into the test sample and for superimposing the backscattered light with the modulated "local oscillator" signal. The output of the interferometer (path PMF4) is detected by an InGaAs photodiode and measured by a lock-in amplifier. Special attention has been paid to the modulation conditions in the local oscillator part (path PMF3). About 3cm of the fiber has been fixed to the flat piezo crystal driven by a saw-tooth voltage. As a result, the stress applied to this fiber has changed its index of refraction and therefore the delay (phase) between the reference and probe beams. The modulation voltage has been chosen to guarantee the phase shift corresponding to the 1/2 wavelength of the optical carrier. The modulation frequency was around 117Hz. It can be shown that under these conditions the photodiode current which corresponds to the superposition of the phase modulated reference beam and non-modulated measuring beam has a stable AC component of the same modulation frequency as the piezo crystal and can therefore be measured by the very sensitive lock-in amplifier technique. The output of the lock-in amplifier corresponds to the envelope of two interfering beams. Moreover, assuming a constant power of the local oscillator, the output amplitude is proportional to the square root of the backscattered intensity.

As a result, the considerable dynamic range of -120dB has been achieved with the given LED. The "electrical" floor noise level lay even below -130dB.

Fig.4 shows the dynamic range and the linearity of the OLCR system. Zero dB corresponds to the power at the output of the measuring path (PMF2). This measurement has been made on a piece of fiber (the length A-B was about 2mm) attached as a modified "FC-PC connector" to this path. Peak "1" is the "return loss" of this "physical contact" at the transition point "A" (-31.8dB). Peak "2" corresponds to the Fresnel reflection of the free fiber end "B" (about -14.4dB). The echoes "3" (\sim -61dB) and "4" (\sim -107dB) are results of the multireflections between points "A" and "B". The signal form around each strong reflection peak represents a Lorentzian shape and is determined by the Fourier transformed spectral density of the LED source. This signal trace is probably influenced by Rayleigh scattering as well.

Fig.5 shows the signal reflected from a glass-air interface measured with the OLCR system. The envelope of the observed signal trace resembles a Lorentzian shape. The different satellite peaks are most probably due to small ripples or peaks in the central region of the emission spectrum. The achieved spatial resolution for this specific LED is 15 μm at FWHM level. The resolution measured at -100dB below the maximum peak level i.e. the system blindness is 2 mm. Despite the higher resolution related to the FWHM of the OLCR, compared with the OTDR, the two resolutions at the -100dB level are comparable. The relatively increased blindness of the OLCR system is due to the mentioned Lorentzian shaped wings of the source.

3. Conclusions.

Optical reflectometry in the micrometer range is based on correlation detection. Both OLCR and OTDR allow high resolution measurements and a high dynamic range. The last parameter has been increased to -120dB with the OLCR technique by applying new modulation and signal treatment schemes. Owing to very high power with the OTDR, the study of nonlinear propagation mechanisms in waveguides is feasible. The FWHM spatial resolution was 15 μm (OLCR) and 60 μm (OTDR) in air, respectively. Nevertheless, it must be added that the OTDR equipment is a typical rather expensive laboratory set-up. The OLCR is on the contrary a small, practical, and less expensive operating system. The work is still in progress and more examples will be presented at the symposium.

4. References.

1. R.P.Novák, H.H.Gilgen, R.P.Salathé, W.Hodel, P.Beaud, J.Schütz and H.P.Weber. "Investigation of optical components in micrometer range using an OTDR system with balanced heterodyne detection". Techn. Dig. NBS Special Publ. 748, 1988. pp. 7 - 10.
2. K.Takada, H.Nagai, N.Takato and J.Noda. "OTDR experiment for glass optical waveguides by usig interferometric technique with 1.3 μm SLD. Techn. Dig. NBS Special Publ. 748, 1988. p. 19.
3. H.H.Gilgen, R.P.Novák, R.P.Salathé, W.Hodel, and P.Beaud. "Submillimeter optical reflectometry". Journal of Lightwave Technology. Vol.7.No.8. August 1988. pp 1225 - 1233.
4. P.Beaud, J.Schütz, W.Hodel, H.P.Weber, H.H.Gilgen and R.P.Salathé. "Optical reflectometry with micrometer resolution for the investigation of integrated optical devices". IEEE J.of Quant.El. Vol 25.No4.April 89.

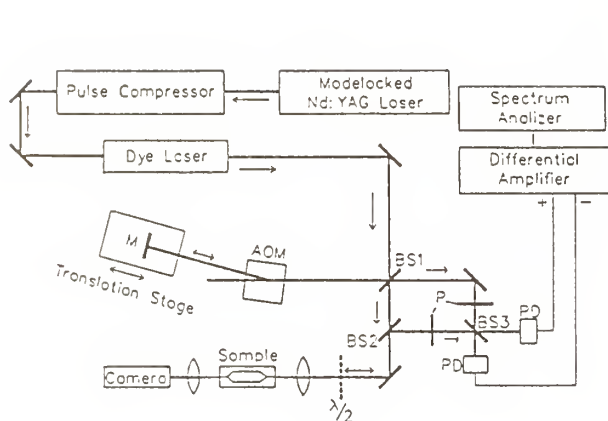


Fig. 1. OTDR set-up.

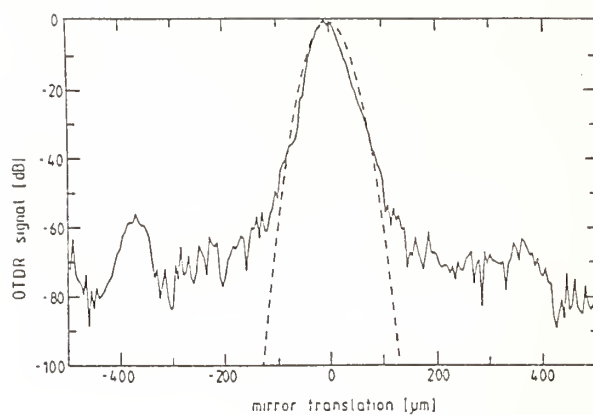


Fig. 2. Signal trace of a single reflection.

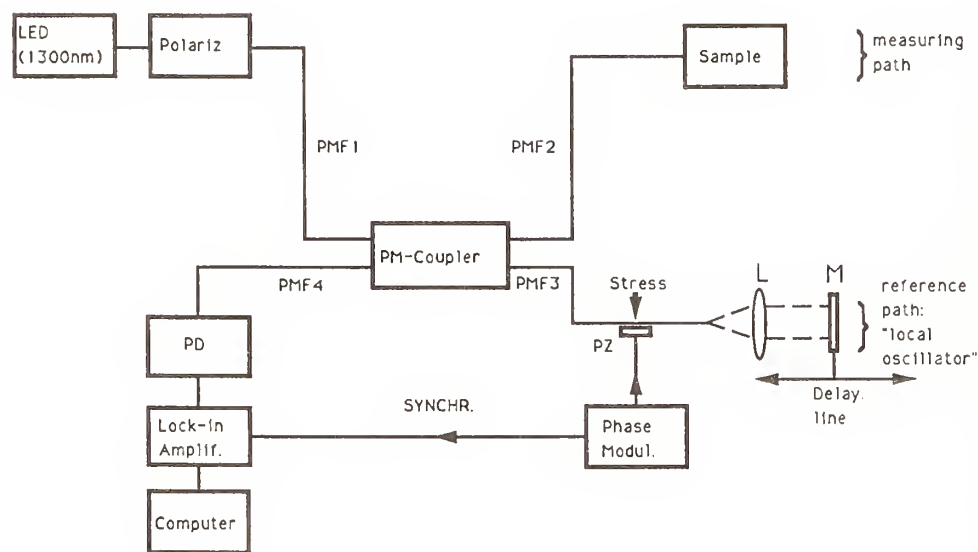


Fig.3. Schematic arrangement for OLCR-measurements.

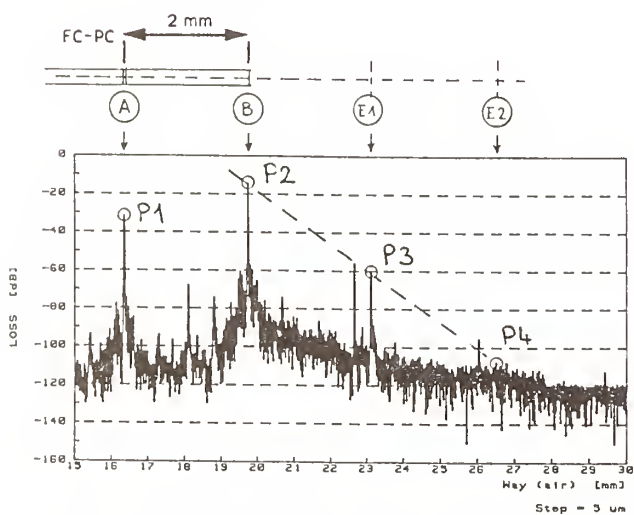


Fig. 4. OLCR scan: "FC-PC connector".

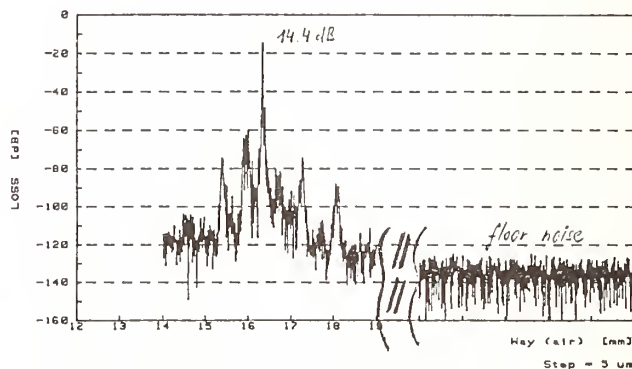


Fig. 5. OLCR: Fibre end reflection.

Multiphoton pulse approach in photon-timing OTDR yields enhanced dynamic range and shorter measurement time

M. Ghioni, G. Ripamonti, S. Vanoli and S. Pitassi

*Politecnico di Milano, Dipartimento Di Elettronica and CEQSE-CNR,
piazza Leonardo da Vinci, 32, Milano, 20133 Italy*

ABSTRACT

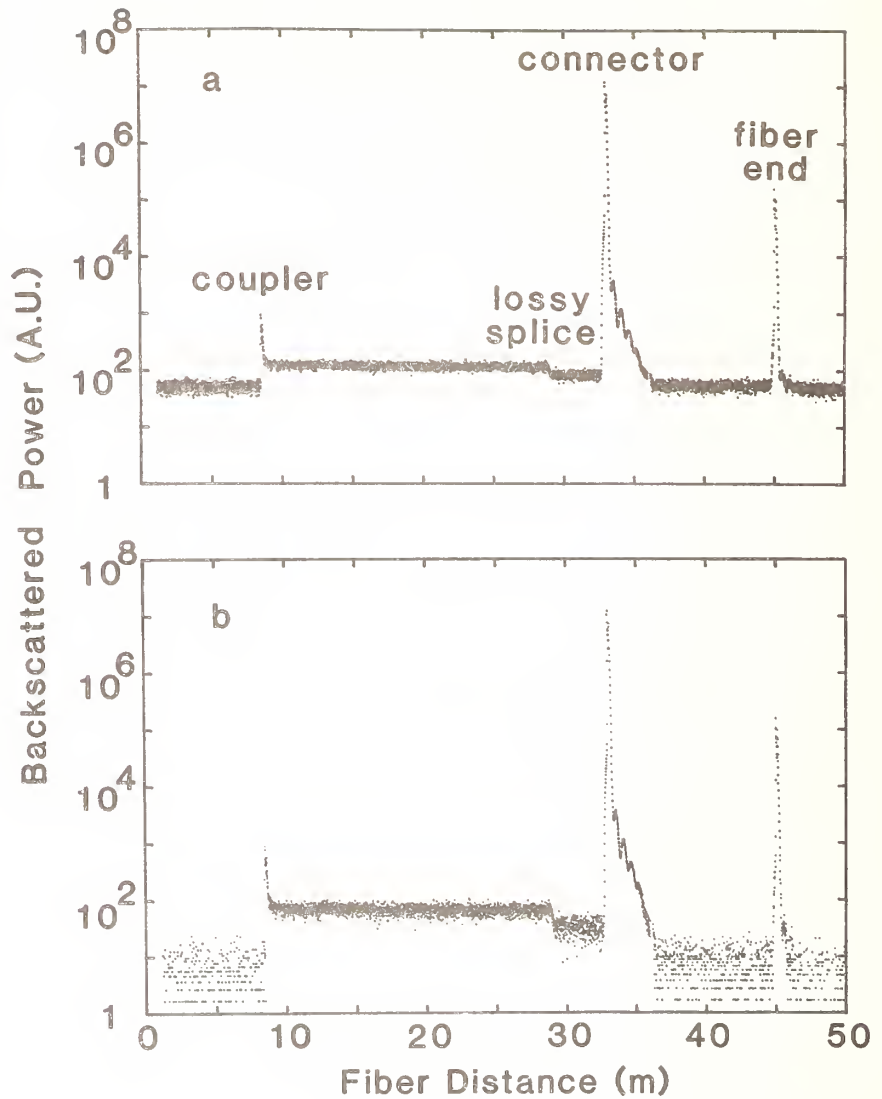
High performance levels are attained by optical time domain reflectometers (OTDR) based on single-photon techniques. Commercial apparatus with about 300 ps resolution (full-width-at-half-maximum FWHM), i.e., 3 cm, are available. We reported 50 ps FWHM resolution (i.e., 0.5 cm), with capability of measuring Rayleigh scattering, by employing special detectors (SPADs) and time-correlated photon-counting (TCPC). Straightforward application of TCPC, However, implies a drawback: long measurement times. A new approach, based on an accurate analysis of TCPC, is here presented. TCPC with multiphoton backscattered pulses and an appropriate data analysis are employed. Dramatically reduced measurement times (by a factor ≈ 50 , i.e., down to a few minutes) and remarkably improved dynamic range (better than 100 dB) at subcentimeter resolution are experimentally demonstrated.

1. OTDR WITH SINGLE-PHOTON BACKSCATTERED PULSES

A photon-counting commercial OTDR apparatus¹ employs a gated avalanche photodiode detector. The diode bias voltage is pulsed above the breakdown for a short time. A gate window is thus defined, delayed by a controlled amount with respect to the picosecond laser pulse. A photon arriving within this time slot can trigger an avalanche current pulse. The backscatter probability in the window is measured by counting the number of triggered avalanches for a given number of laser pulses. The OTDR trace is obtained by scanning the delay. The available resolution of the detector is not fully exploited, since the overall resolution in the OTDR measurement depends on the gate pulse duration also. Furthermore, the measurement time may be long, since the gating and scanning procedure is not efficient in the collection of the available information.

In our previous OTDR², the avalanche photodiode is not gated and TCPC is employed. In essence: a) the arrival time of a backscattered photon, marked by the current pulse from the single photon detector, is measured and, b) a statistical histogram of many such measurements is collected. The time resolution of the detector (that can attain³ ≈ 20 ps) is fully exploited. In a straightforward TCPC scheme as above outlined, however, the collection time is quite long, due to a peculiarity of the available high-resolution time-sorters. In fact, they can process only the first stop pulse (photon pulse) following the start pulse (laser pulse). If a backscattered pulse contains more than one photon within the measurement time range, only the first is measured. The collected histogram represents the probability distribution of *the first* photon, while the correct OTDR trace would be the probability distribution of *a* photon. The difference between the two is practically negligible only if the probability of multiple (two or more) photons P_M is negligible with respect to that of just one photon P_1 . This is simply obtained by attenuating the light, so that the total event probability P_T (probability of one or more photons) be of the order of 10^{-2} . In this case, it is easily shown (Poisson statistics of the backscattered photons) that $P_1 = P_T$ and $P_M = (P_T)^2$. For instance, with $P_T = 0.05$ and a laser repetition rate of 10 kHz, only 500 measurements per second are collected. For measuring the Rayleigh scattering over moderate fiber lengths with high time resolution, measurement times of hours are necessary, as illustrated by the example in fig.1.

Fig.1: a) OTDR trace of a 37 m 50/125 μm graded-index optical fiber. The diode laser outputs 80 ps FWHM pulses at 904 nm with a repetition rate of 30 kHz. The backscattering probability P_T is ≈ 0.05 photons per pulse. Measurement time is 14 hours. b): same as a) after background subtraction.



2. PHOTON-TIMING OTDR WITH MULTIPHOTON BACKSCATTERED PULSES

By reducing the attenuation of the detected light, the data collection rate is strongly increased and the signal-to-background ratio is enhanced, but multi-photon backscattered pulses are detected and the collected data are distorted. However, a correction equation⁴ makes it possible to derive the true distribution from TCPC data, recorded with not-negligible P_M (the number of laser pulses employed is the only additional information required). The computation routine is very simple. The correct probability for backscatter to arrive at a given time (i.e., from a given location in the fiber) is computed from the ratio: (photon pulses recorded at that time) / (employed laser pulses - photon pulses recorded at preceding times). Fig.2, trace a, reports the corrected result of a measurement on the same fiber of Fig.1, but with higher detected intensity, corresponding to almost unity P_T . The comparison with Fig.1 is striking: the measurement time is reduced from 14 hours to 2 minutes, and the signal-to-noise ratio is remarkably improved. However, the backscatter from the fiber portion after the connector cannot be measured. In fact, the backscatter probability from the preceding part is unity. A separate measurement was therefore performed, by inhibiting the detector operation for all the time interval corresponding to

Fig.2: Measurement of the same fiber of Fig.1, but with higher P_T and data correction (see text). Trace a) was taken in 2 minutes with $P_T = 1$. Trace b) was taken in 6 minutes, $P_T = 0.8$ and gated detector operation (see text).

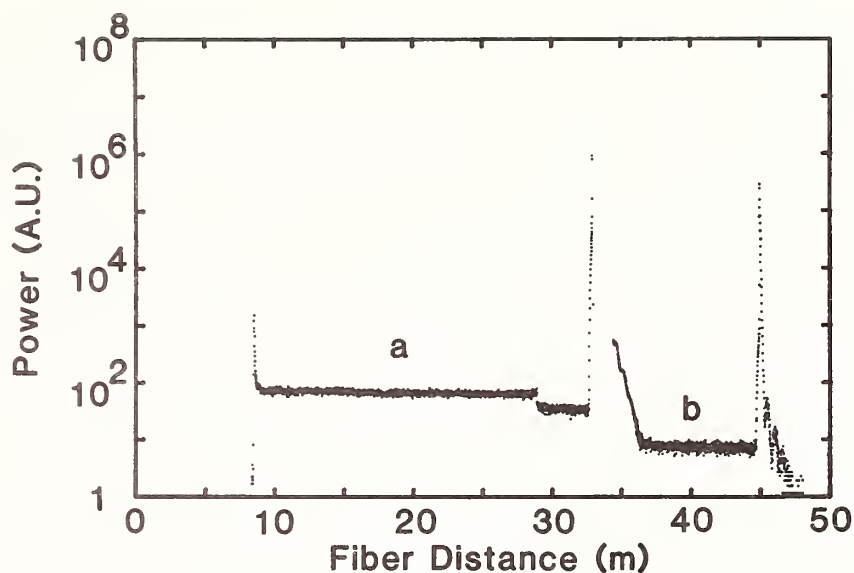


Fig.3: Same as Fig.2 trace b) but with $P_T = 0.5$ and modified gate to show the connector reflection (see text). Measurement time is 9 minutes.

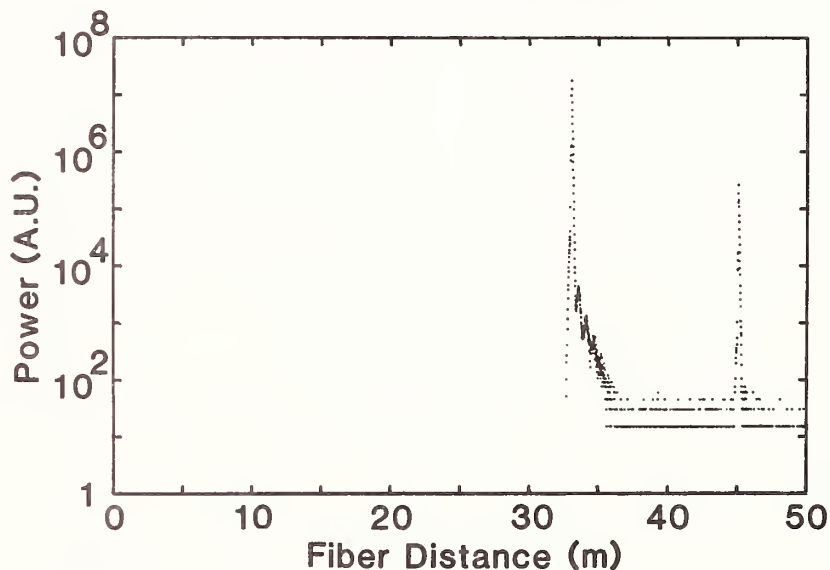
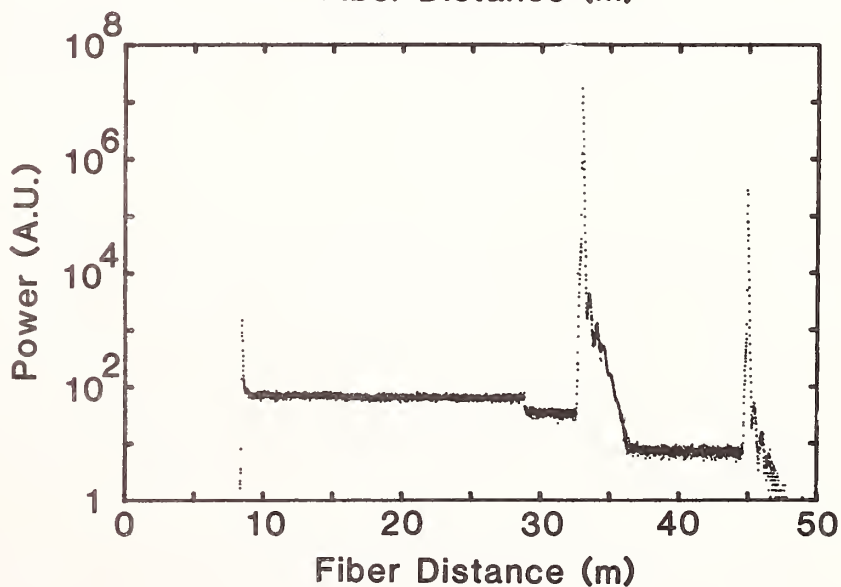


Fig.4: Complete OTDR trace obtained with composition of the measurements of Figs. 2 and 3. Total measurement time is 17 minutes. Compare with Fig.1b.



the first fiber portion and the connector. This was obtained by switching the bias voltage below the breakdown voltage. The corrected result is shown in Fig.2, trace b: the signal-to-noise ratio is much better than in Fig.1, and the background level after the fiber end (dark count rate) is at least 20 dB below the Rayleigh scattering level. A section of 1.2 m just after the connector is excluded from this measurement. This results from the fact that, at this level of detected intensity, the inhibited interval must include the connector reflection, and that the voltage transition from off-state (below the breakdown voltage) to on-state (10 V above breakdown) takes 10 ns. In order to complete the OTDR trace, another measurement was performed with reduced intensity, enabling the detector just before the connector reflection ($P_T \approx 0.5$). The corrected result is shown in Fig.3.

3. RESULTS AND DISCUSSION

By merging the three measurements of Figs.2 and 3, the final OTDR trace of Fig.4 is obtained. The total measurement time is 17 minutes, to be compared with the 14 hours required by the straight TCPC measurement in Fig.1. The trace of Fig.4 shows much lower statistical dispersion of the data points, in particular for the second fiber section. Furthermore, the dynamic range is enhanced by at least 20 dB, as illustrated by the ratio of the Rayleigh scattering level to the dark level after the fiber end. An accurate comparison of the OTDR traces in the measurements in Fig.1 and Fig.4 does not reveal any detectable difference in the scattering levels. It is therefore verified that the correction procedure does not introduce systematic errors and, in particular, that the simple correction routine yields reliable results.

In summary, the multiphoton backscattered pulse approach to photon counting OTDR offers remarkable advantages. Accurate measurements with subcentimeter resolution and dynamic range exceeding 100 dB are obtained in fairly short times, suitable for practical applications.

ACKNOWLEDGEMENT

Work supported in part by CNR through "P.F. Telecomunicazioni" and by MURST. The authors thank S.Cova for the helpful discussions.

REFERENCES

1. B.K.Garside, *Photonics Spectra*, 22 no.9, pp. 79-86 (1988).
2. G.Ripamonti and S.Cova, *Electron.Lett.* 22, pp. 818-819 (1986)
3. S.Cova, A.Lacaita, M.Ghioni, G.Ripamonti and T.A.Louis, *Rev.Sci.Instrum.* 60, pp. 1104-1110 (1989).
4. D.V.O'Connor and D.Phillips: "Time-correlated single photon counting", Academic Press, London, 1984; pag. 164.

CHARACTERIZATION OF HYDROGEN DIFFUSION IN HERMETICALLY COATED OPTICAL FIBERS

P.J. Lemaire, K.L. Walker, K.S. Kranz, R.G. Huff, and F.V. DiMarcello
AT&T Bell Laboratories, 600 Mountain Avenue, Murray Hill, NJ 07974

INTRODUCTION

Hermetic coatings on optical fibers are generally intended to protect the fibers from attack by water or hydrogen. The presence of water can lead to corrosion of the silica surface of a nonhermetic fiber, potentially resulting in a long term degradation in the fiber strength. Hydrogen, on the other hand, can readily diffuse into the core of a nonhermetic fiber, where it can cause undesired loss increases. The ideal hermetic coating would prevent any "significant" amounts of hydrogen, water, or other undesired chemical species from ever reaching the underlying silica portion of an optical fiber. As hermetic fibers find more widespread use, it is becoming necessary to establish meaningful tests that will allow prediction of their long term performance. This paper focuses on the use of hydrogen testing as a means of characterizing the quality of amorphous carbon coatings that are currently being used as hermetic barriers.^{[1] [2]} The methods described, however, are equally pertinent to the study of any other type of hermetic coating for use on an optical fiber. A particular aim of our work has been to obtain data that will allow prediction of the long term performance of hermetic coatings.

During a hydrogen test a hermetically coated fiber is intentionally exposed to a constant high concentration of H_2 , and hydrogen related loss increases (if any) are measured as a function of exposure time, preferably using an *in-situ* spectral measurement technique.^[3] In general, elevated temperatures must be used if loss changes are to be observed in reasonable time periods. After measuring the hydrogen induced loss increases at several high temperatures, one then attempts to extrapolate to the lower temperatures that the fiber will see during actual use. If a fiber can be shown to be hermetic with respect to hydrogen, it will be safe to assume that it will be even more impervious to the diffusion of larger molecules, such as H_2O . Thus, hydrogen testing can be viewed as an extreme test of the quality of a hermetic coating.

Other methods that are used to assess the quality of hermetic coatings include static and dynamic fatigue experiments,^{[4] [5]} measurement of the electrical resistance in the coating,^[6] electron microscopy,^[7] and scanning tunneling microscopy (STM)^[8]. These methods are not discussed in detail in this paper. Fatigue experiments characterize how well the coatings are able to limit the diffusion of water, and thus how efficiently the coatings prevent fiber weakening. While such tests can reasonably assure that the fiber strength will not degrade over time, they can not guarantee that a coating will also be hermetic with respect to hydrogen. Electron microscopy, STM, and measurement of electrical resistance are direct and indirect ways of measuring the coating thickness and, in the case of STM, its "roughness". These techniques are useful in optimizing and controlling the application of hermetic coatings, but by themselves do not give any information regarding the hermetic properties of the coating.

BASIC CONSIDERATIONS

In an accelerated test, some H_2 molecules will eventually penetrate the hermetic coating. Once in the silica portion of the fiber, the hydrogen can either remain as H_2 molecules, or it can react at defect sites in the glass. Hydrogen that is present as H_2 will quickly distribute itself across the silica cross-section, and can be detected by observing changes in spectral features associated with H_2 in silica.^{[9] [10]} Defect sites where hydrogen may react can be in the lightguiding core region, or they can be in optically inactive parts of the fiber. If the reactions are in the core region there will often be associated loss changes (such as increases in OH absorption) that can be directly observed. However, reactions that occur outside of the lightguiding region can only be detected by indirect methods, if they can be detected at all. If the concentration of these reactive sites is high enough, this can greatly complicate the data analysis, especially when it becomes necessary to extrapolate the results to lower temperatures.

There are several species associated with hydrogen induced losses. Among these the primary types are: (1) molecular H_2 ^[9], (2) OH, and (3) a germanium related defect which, when reacted with hydrogen, causes a short wavelength absorption edge that extends out to 1.31 and 1.55 μm .^[11] In performing accelerated hydrogen tests it

is necessary to decide which type of hydrogen induced loss will be monitored. Molecular H_2 has associated with it loss peaks from 1.08 to 1.24 μm , as well as a rising loss edge and other peaks beyond about 1.5 μm .^{[9] [10]} The 1.24 μm first overtone is usually the most easily measured of the H_2 features. Losses due to molecular H_2 are unique in that they do not rely on having the hydrogen react at defect site in the glass. The strengths of the various H_2 absorptions are well known and do not vary significantly from one type of fiber to another. For these reasons it is quite easy to determine the concentration of H_2 from a measured loss spectrum.

On the other hand, the growth of OH peaks or of the Ge related short wavelength edge, are due to the chemical reaction of hydrogen at defect sites in the glass.^[11] Fiber reactivities will depend on the defect concentrations present in a fiber, as well as on the temperature and the internal hydrogen pressure which exists in a hermetically coated fiber. The defect concentrations are not always well characterized and may vary depending on the glass composition and on the processing used in making the fiber.^[12] Therefore, any change in the strength of the OH overtone, for instance, is an indirect measure of the H_2 concentration in a fiber, and depends on the integrated H_2 level over the course of the experiment, as well as on the test temperature and the defect concentration in the fiber.

During an accelerated hydrogen test the fiber core is being used as a hydrogen detector. Monitoring the growth of H_2 amounts to using a well calibrated detector, while monitoring OH growth or the short wavelength loss edge is equivalent to using a detector with a sometimes uncertain response. On the other hand, by monitoring the OH wavelength (1.39 μm) lower concentrations of hydrogen can be detected than by monitoring the molecular H_2 wavelength (1.24 μm). For instance, at 150°C the lowest level of H_2 that can be detected using standard optical loss measurements is about 0.4 ppm. This corresponds to about 0.01 atm of H_2 . (1 ppm is defined as 10^{-6} moles of H_2 per mole of SiO_2 .) When hydrogen is present as OH it is detectable at levels of as low as 3 ppb. This gives an improvement of more than a factor of 100 in sensitivity (assuming that reactions to form OH are fast). Thus, one can choose to use a well calibrated but less sensitive "detector", (molecular H_2), or alternatively can decide to use a more sensitive "detector" (e.g. OH) whose response is not so easily characterized.

In general, it is preferable to structure an experiment so as to have as little depletion as possible of the diffusing molecular H_2 . This allows one to use simple diffusion equations^[13] to model the hermetic fiber behavior, and permits one to monitor well understood molecular H_2 features. Experiments can be accelerated using high temperatures and/or high P_{H_2} 's. Using high P_{H_2} 's (e.g. 2000 psi) and moderate temperatures (e.g. $T < 150^\circ C$) tends to minimize the depletion of H_2 by reaction.^[14] Conversely, the use of higher temperatures and lower P_{H_2} 's (e.g. 1 atm) accentuates the reactions and often results in the lack of any observable molecular H_2 spectrum. The main advantage of the high temperature/low P_{H_2} experiments is that they do not require high pressure equipment, and therefore are more easily set up in the laboratory. Theory and results for each regime will be discussed in the remainder of this paper.

DIFFUSION OF HYDROGEN WITHOUT REACTION

The diffusion of hydrogen into a hermetic fiber has two main stages. At short times, characterized by a time constant τ_i , the hydrogen has diffused a short distance and is present solely in the hermetic coating. In the second stage, characterized by another time constant τ_f , the hydrogen has penetrated to the underlying silica and a linear concentration gradient exists across the coating. The concentration of H_2 in the silica plotted versus time shows an initial "lag time" where the concentration is zero, followed by a period where the rate of increase is constant, and finally an approach to the equilibrium value. If $t \ll \tau_f$, and the diffusion of H_2 in silica is assumed to be fast, the loss change due to H_2 is given by:^[14]

$$\Delta\alpha_{H_2}(t) = A_H P_{H_2} K_s \left[\frac{t}{\tau_f} - \frac{\tau_i}{6\tau_f} - \frac{2\tau_i}{\pi^2\tau_f} \sum_{n=1}^{\infty} \frac{(-1)^n}{n^2} \exp \frac{-n^2\pi^2 t}{\tau_i} \right] \quad (1)$$

where A_H is the optical absorptivity due to a given concentration of H_2 in SiO_2 , P_{H_2} is the external hydrogen pressure, K_s is the solubility of H_2 in SiO_2 per unit hydrogen pressure, and K_c is the comparable solubility term for the coating material. The elapsed time is given by t , and the two characteristic time constants, τ_i and τ_f are defined as follows:

$$\tau_i = \frac{\delta^2}{6D_c} \quad \tau_f = \frac{r\delta K_s}{2D_c K_c} \quad (2,3)$$

where δ is the coating thickness, D_c is the diffusivity of H_2 in the coating, r is the fiber radius, and K_c is the solubility of H_2 in the coating per unit hydrogen pressure.

Eq. 1 describes a curve that is zero for a time of the order of $\tau_i/2$, and then approaches a straight line of slope of $\Delta\alpha_{H_2}(\infty)/\tau_f$, where $\Delta\alpha_{H_2}(\infty) = A_H P_{H_2} K_s$. Values for τ_i and for τ_f can be obtained graphically by plotting experimental values for molecular hydrogen loss versus time.^{[13] [14]} The value for τ_i is obtained by extrapolating the constant slope part of the line back to zero loss, and noting the time axis intercept. The region of constant slope is inversely related to τ_f as just noted. The only additional information required is $\Delta\alpha_{H_2}(\infty)$ which can be calculated from molecular H_2 absorption data obtained at 1 atm, and from P_{H_2} . (That is, assume that the hydrogen absorptivity scales linearly with pressure, a justified assumption.) Alternatively, $\Delta\alpha_{H_2}(\infty)$ can be obtained experimentally by testing a short length of non-hermetic fiber at the same high pressure and temperature used for testing the hermetic fiber.

Experimental results for a single mode fiber with a hermetic carbon coating are shown in Figs. 1 and 2. Features associated with molecular H_2 are clearly seen in Fig. 1, most notably the 1.24 μ m first overtone. Small increases in loss due to OH growth and due to the growth of the Ge related short wavelength loss edge are also noted, but indicate only a small depletion of the available H_2 . In Fig. 2 loss increases due to the growth of the 1.24 μ m H_2 peak are plotted versus time, for three different temperatures. (A correction is included that accounts for a small component of the 1.24 μ m peak that is due to the OH combination band. This correction is based on an empirically observed ratio of 15:1 between the OH overtone at 1.39 μ m and the OH combination band at 1.24 μ m.)

The form of the experimental loss versus time curves are in excellent agreement with the theoretical predictions, indicating that any depletion of H_2 by reaction with defects is negligible. Values for τ_f and τ_i were calculated from the constant slope regions and from the zero loss intercept, as previously described. These values are shown as functions of inverse temperature in Fig. 3, for a fiber with a hermetic carbon coating. Using the experimental values for τ_i and τ_f and Eq. 1 it is possible to predict the internal hydrogen concentrations at different temperatures, as shown in Fig. 4. The behavior of a nonhermetic fiber is shown for comparison. For instance, at 21°C after 25 years the internal hydrogen level will be 7.74×10^{-5} times that of the applied pressure. Alternatively, a rough estimate for the internal hydrogen pressure at time t can be made by ignoring the initial lag period: $P_{H_2}(\text{int})/P_{H_2}(\text{ext}) = t/\tau_f$, where $P_{H_2}(\text{ext})$ is the external applied hydrogen pressure seen by a hermetic fiber. The data in Fig. 3 was extrapolated to 21°C resulting in $\tau_f = 2.24 \times 10^5$ yrs. In this way, a value for $P_{H_2}(\text{int})/P_{H_2}(\text{ext})$ can be estimated to be about 1.1×10^{-4} , a result reasonably close to the more exact calculation.

It is important to note that these predictions rely on fully characterizing the diffusion process in the coating, especially the temperature dependence. In most cases, the temperature dependence for hydrogen diffusion in new types of coatings will not be known *a priori*, and thus it is important to perform experiments that can yield such information. It is quite possible for one coating to appear to be "better" than another at high temperatures, but to be worse at lower temperatures, due to differing temperature dependences for hydrogen diffusion in the two coatings.

DIFFUSION OF HYDROGEN WITH SIMULTANEOUS REACTION

Frequently it is desired to test a hermetic fiber without using high pressure hydrogen. Fig. 5 shows results for a carbon coated fiber exposed to 1 atm of hydrogen at 200°C. The small loss increase at the 1.24 μ m peak is only partially due to molecular H_2 . About half of the peak can be attributed to the OH combination band. Obviously, it would be difficult to characterize the concentration of molecular H_2 in an experiment such as this. On the other hand, loss increases due to OH growth and due to the Ge short wavelength edge are prominent in Fig. 5. The magnitudes of the loss increases depend both on the reactivity of the fiber and on the internal level of hydrogen, both of which can be changing with time. In the simplest case, the fiber reactivity is relatively constant and the hydrogen concentration grows linearly with time. (This assumes that the initial time lag, τ_i , is negligible.) The net loss change, $\Delta\alpha$, is obtained by integrating the *rate* of loss change, which in this case is assumed to be proportional to P_{H_2} .

$$\Delta\alpha = \int_0^t A P_{H_2}(\text{int}) R \, dt = \frac{A P_{H_2}(\text{ext}) R}{2 \tau_f} t^2 \quad (4)$$

In Eq. (4) A is the absorptivity of a hydrogen defect (e.g. the Ge defect responsible for the short wavelength edge), and R is the fiber reactivity, which is a function of temperature and defect concentration. The important point is that the loss change is normally expected to be proportional to t^2 . That is, the rate of loss increase is expected to accelerate with time, since the hydrogen concentration is steadily increasing.

Fig. 6 shows results obtained using an OTDR to monitor 1.31 μm losses in a hermetic fiber that was at 150°C with $P_{H_2} = 1$ atm. The data at early times does show a trend that is possibly consistent with a t^2 dependence - that is, the curve is concave upwards. More interesting, however, is that the loss increases linearly with time after about 200 hours. In fact, at first glance the overall behavior looks quite similar to that seen in the high pressure tests: an initial lag time followed a region where the slope is constant. However, the loss increases in this case are *not* due to molecular H_2 , but rather are due to the growth of the Ge related short wavelength loss edge. The region of constant slope suggests that the molecular hydrogen concentration is at a constant level. The simplest explanation would be that the fiber had equilibrated and that the fiber was seeing an effective pressure of 1 atm of H_2 . However, spectral loss results showed no evidence of any molecular H_2 features. Using the observed rate of growth of the short wavelength loss edge, and previous results for nonhermetic fibers tested in low levels of H_2 , it was estimated that the internal hydrogen level was only about 9.8×10^{-3} atm. Simple diffusion without reaction would not account for this constant but low level of hydrogen. We have shown that a constant low concentration of H_2 can occur in a hermetic fiber if there are reactive defects which partially deplete the hydrogen which is diffusing through the hermetic coating.^[14] That is, the increasing flux of hydrogen through the coating is exactly offset by a reaction rate that increases linearly with the concentration of hydrogen. As long as the reactive sites are not significantly depleted they will act to maintain a hydrogen level that is considerably lower than that which would occur if the sites were not present. It is worth noting that the defects could, in principle, be either in the lightguiding regions of the fiber, or in the outerlying optically inactive part of the fiber. In order to predict the internal hydrogen level in such a fiber at lower temperatures, it would be necessary to know how the hydrogen reaction rate at these sites varies with P_{H_2} and temperature. For instance, sites that are reactive at high temperatures may cease to be reactive at lower temperatures, thus eliminating any potential "gettering" behavior.

Despite complications such as these, low pressure tests are attractive, primarily because of the relative ease of performing the experiments. In addition, experiments like the one above, although they are somewhat difficult to interpret, do give important information about the behavior of the hermetic fiber as a whole. This is in contrast to the high pressure experiments, which although easy to interpret, characterize only the coating, ignoring some potentially important properties of the glass portion of the fiber.

CONCLUSIONS

The use of high P_{H_2} 's and moderate temperatures can be a valuable experimental technique for testing hermetically coated optical fibers. Because these high pressure experiments are structured to characterize only the coating itself, the data analysis is relatively simple and prediction of long term coating behavior is straightforward. Tests performed at lower hydrogen pressures and higher temperatures also give useful information regarding the quality of hermetic coatings, but the results will depend not only on the coating but also on the type and concentration of reactive defects in the silica portion of the fiber. Analysis of such data requires a detailed understanding of hydrogen reactions as a function of temperature, both in the optically active and inactive portions of the silica fiber.

REFERENCES

1. R.G. Huff, F.V. DiMarcello, and A.C. Hart Jr., Optical Fiber Communications Conference: Technical Digest, (OFC 88 Conf. Proc., New Orleans, LA 1988) Paper TUG2.
2. K.E. Lu, M.T. Lee, D.R. Powers, and G.S. Glaesemann, Optical Fiber Communications Conference: Postdeadline Papers, (OFC 88 Conf. Proc., New Orleans, LA 1988) Paper PD1-1.

3. P.J. Lemaire, K.S. Kranz, K.L. Walker, R.G. Huff, and F.V. DiMarcello, *Electr. Lett.* **24**, 1323 (1988).
4. J.T. Krause, C.R. Kurkjian, F.V. DiMarcello, and R.G. Huff, *European Fiber Optic Conference / Local Area Networks*, (EFOC/LAN, Amsterdam, 1988)
5. K.E. Lu, G.S. Glaesemann, R.V. Vandewoestine, and G. Kar, *J. Lightwave Tech.*, **6**, 240 (1988).
6. M. Ooe et al, *International Conference on Integrated Optics and Optical Fiber Communication*, (IOOC 89, Kobe, 1989).
7. C.M.G. Jochem, H. Schaper, M.J.M.J. Swarts, and J.W.M. Smits, *Conference of Optical Fiber Communication: Postdeadline Papers*, (OFC 89 Conf. Proc., Houston, TX 1989). Paper PD8-1.
8. N. Yoshizawa and Y. Katsuyama, *Electr. Lett.*, **25**, 1429 (1989).
9. J. Stone, A.R. Chraplyvy, and C.A. Burrus, *Opt. Lett.*, **7**, 297 (1982).
10. K.J. Beales, D.M. Cooper, and J.D. Rush, *Electr. Lett.*, **19**, 917 (1983).
11. A. Tomita and P.J. Lemaire, *Electr. Lett.*, **21**, 71 (1985).
12. K.T. Nelson et al, *Conference on Optical Fiber Communication: Technical Digest*, (OFC 90 Conf. Proc., San Francisco, CA 1990) Paper TuB2.
13. J. Crank, *The Mathematics of Diffusion*, (Oxford University Press, London, 1975) pp. 47-53.
14. P.J. Lemaire, K.S. Kranz, K.L. Walker, R.G. Huff, and F.V. DiMarcello *Mat. Res. Soc. Symp. Proc.*, **172**, 85, 1990. (Proceedings of Materials Research Society Fall Meeting, Boston, Nov. 1989)

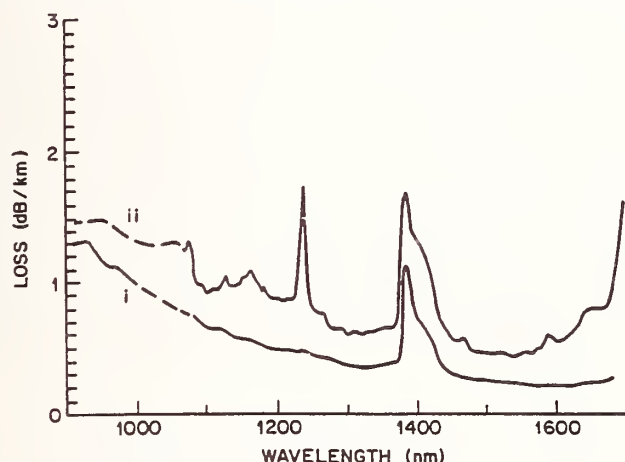


Fig. 1. Spectral loss results for a fiber with a hermetic carbon coating, before (i) and after (ii) exposure to high pressure hydrogen.

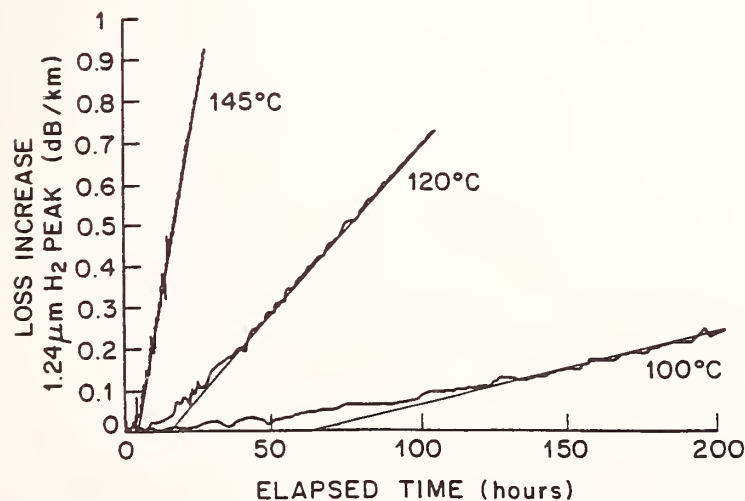


Fig. 2. Loss increases due to the growth of the 1.24 μ m hydrogen peak.

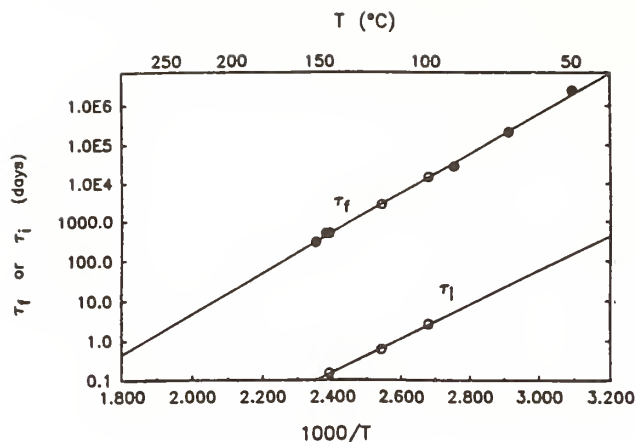


Fig. 3. Calculated values for the the characteristic time constants, τ_f and τ_i . Open circle data were obtained from *in-situ* experiments. Closed circle data were obtained by measuring the fiber loss before and after exposure to high pressure hydrogen.

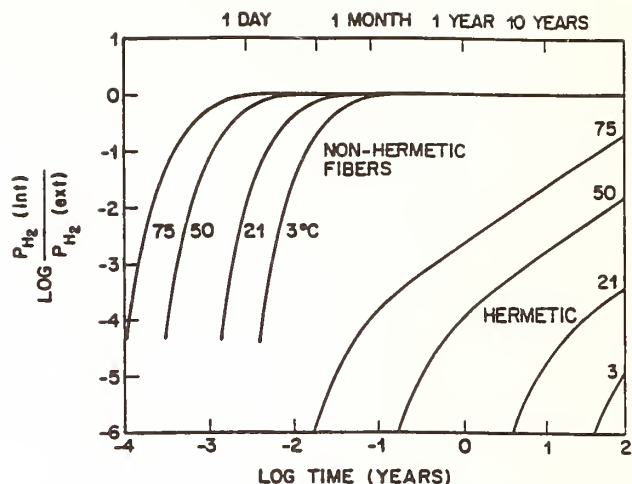


Fig. 4. Predictions for a carbon coated fiber, and for a non-hermetic fiber. Vertical axis shows the ratio of the internal hydrogen pressure to that outside of the hermetic coating.

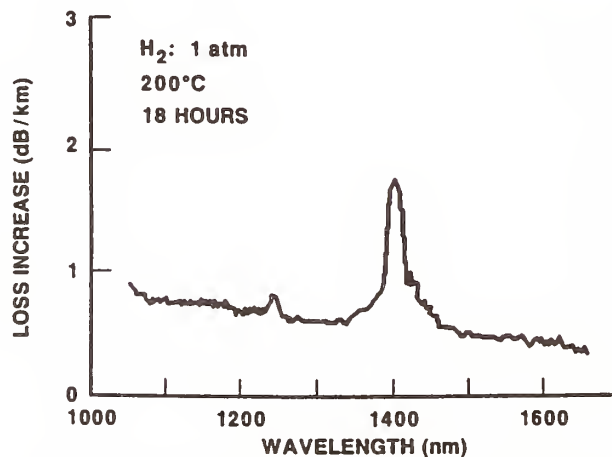


Fig. 5. Spectral loss increase for a carbon hermetic fiber treated in hydrogen.

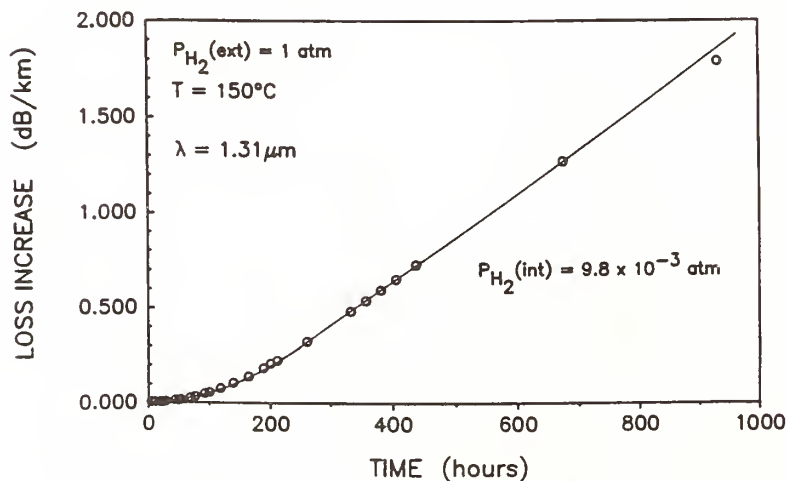


Fig. 6. Loss increase at $1.31\mu\text{m}$ for a fiber with a hermetic carbon coating, in 1 atm of H_2 at 150°C .

The Anomalous Structure Observed in Single-Mode Fiber Cutoff Wavelength Measurements: Theory and Solutions

Steven A. Jacobs
David W. Peckham

AT&T Bell Laboratories
2000 N.E. Expressway, Norcross, Georgia, 30071

ABSTRACT

The characteristics of the anomalous structures in single-mode fiber cutoff wavelength measurements are discussed. The transmitted power through a waveguide with a finite cladding and lossy coating is calculated using the scalar wave approximation. The transmitted power obtained with this model exhibits oscillations in qualitative agreement with empirical observations. The system aspects of the anomalous cutoff behavior and possible solutions are discussed.

1. INTRODUCTION

Many transmission properties of optical fibers can be explained by modeling the fiber with a cladding of infinite extent. However, as the cutoff wavelength of a bound mode is approached, the mode spreads out further and further into the cladding and eventually "discovers" that the cladding is in fact finite and bounded by layers of coating and air with different optical properties. Therefore, we expect that the infinite cladding model would fail to provide accurate predictions of cutoff related phenomena. Indeed, with a fiber designed to have a fundamental mode cutoff, observed fundamental mode spectral loss and spot size variations could not be explained using the infinite cladding model.^[1] However, by modeling the fiber with a finite cladding and a lossy plastic coating, satisfactory agreement with experiment was obtained.^[1]

Recently, anomalous oscillations or "bumps" have been observed in single-mode fiber cutoff wavelength measurements.^{[2] [3] [4] [5]} The cause of this phenomenon was originally hypothesized^{[3][4][5]} to be wavelength dependent coupling between the LP_{11} mode and whispering gallery modes in the curved fiber. Subsequent observations of the characteristics of the "bumps"^[2] conflicted with this hypothesis. The finite cladding/coating model is employed to explain this phenomenon, and qualitative agreement with experiment is obtained.

2. MODEL

A typical depressed clad fiber geometry is shown in Figure 1. The cladding layer extends to a radius of 62.5 microns and is surrounded by a coating layer with a thickness of 60 microns. The coating is surrounded by air. The index in the core region is also composed of several layers of constant index. We refer to an index with this form as a multilayer index. The structure shown in Figure 1 supports an enormous number of bound modes whose properties can be obtained by solving Maxwell's Equations with the appropriate multilayer index. In the following, we employ the scalar wave approximation.

Within each layer, for a given propagation constant, the mode field is a linear combination of Bessel type functions. At the layer boundaries, we require continuity of the field and its radial derivative. For an index consisting of N layers, these conditions lead to a homogeneous system of $2(N-1)$ equations in $2(N-1)$ unknowns. Such a system will have a non-trivial solution if and only if the associated determinant vanishes. The allowed values of the propagation constant are roots of this determinant. The system of homogeneous equations is "almost block diagonal" in structure and this structure can be exploited to find the roots of the determinant in an efficient manner.^[6] Once the allowed propagation constants are found, the associated mode fields can be readily obtained. The imaginary part of the index of refraction, which causes absorptive loss, is treated as a small perturbation on the real part of the index and axial decay with distance for a given mode is obtained using first-order perturbation theory.

The finite cladding/coating/air structure supports three types of modes, characterized by their radial power distribution. These are core modes, cladding modes, and coating modes; examples of core and coating mode types are displayed in Figures 2(a) and 2(b). We use the LP_{mn} mode designations, where m defines the angular variation of the mode and n is the number of its radial roots. The modes have an interesting dependence on wavelength. For example, as the wavelength increases a core mode will spread into the cladding and undergo a rapid transition to a coating mode and experience a dramatic increase in attenuation. Similarly, a lossy coating mode will undergo a rapid transition to a low loss core mode. These transitions are illustrated in Figure 3 where we show the fraction of power within the core as a function of wavelength for the $LP_{1,26}$ and $LP_{1,25}$ modes. For the "single mode" core structures and wavelength ranges we consider, only LP_{0n} and LP_{1n} modes become core modes.

3. TRANSMITTED POWER

The time averaged power flow through an infinite plane transverse to the fiber axis is given by

$$\bar{P}(z) = \sum_{m=0}^{m=\infty} \sum_{n=1}^{n=\infty} A_{mn} e^{-\alpha_{mn}z}$$

where the A_{mn} include normalization and excitation factors and we have assumed excitation by an incoherent source.^[7] We define the normalized power flow by

$$\frac{\bar{P}(z)}{P_{mm}}$$

where P_{mm} is a linear fit to the calculated power flow through a multimode fiber with a length of 1 meter under the same incoherent excitation condition.

In Figure 4(a), we show the normalized power flow as a function of wavelength for a matched clad profile. The base power flow arises from an LP_{0n} core mode. Only one LP_{0n} mode of this form is present at any given wavelength. At lower wavelengths, additional power is carried by an LP_{1n} core mode, for example the $LP_{1,26}$ mode displayed in Figure 2(a). As the wavelength increases, this mode undergoes a transition to a coating mode with an associated increase in attenuation and the transmitted power returns to its base level. With further wavelength increases, another coating mode will change to a core mode and the transmitted power rises. This pattern of transitions repeats, giving rise to a series of oscillations. However, for higher wavelengths the new LP_{1n} core mode is not as tightly confined as its predecessor and has a higher attenuation. Therefore, the height of the subsequent oscillations decrease. In addition, the size of the any particular oscillation decays with increasing fiber length. For comparison, the experimental results are shown in Figure 4(b). In Figures 5(a) and (b), we show the analogous results for a depressed clad profile.

Though the agreement with experiment is impressive, there are some deficiencies in the model. First, the shape of the transmitted power curves are very sensitive to the indices of the core and coating. For example, in Figure 6, we show the result of changing the coating index from 1.1 to 1.12 percent. Also, to obtain oscillations of the same magnitude as experiment, we used a coating loss of 5 dB/mm. Although accurate losses for the coating material are not known, we expect that this value is too high. Currently, we are addressing these deficiencies by including mode interference in the calculation of the power flow. Extensions to the model to account for curvature (macro-bending and micro-bending) and an axial dependence of the core and coating indices are also contemplated.

4. SYSTEM CONSIDERATIONS

The dominant system concern when setting telecommunication fiber cutoff specifications is ensuring single-mode operation in the 1300 nm window so that the possibility of modal noise related transmission degradation is eliminated. The presence of the oscillations in the cutoff wavelength measurements has raised the concern that if the oscillations are also present when

the fiber is deployed in a system, i. e., that they are not a measurement artifact, then the energy carried by them could interfere with the fundamental mode and generate modal noise. In this section we present experimental results showing interference between the fundamental mode and the LP_{1n} mode that cause the oscillations.

The situation where modal noise generation is possible in a typical system is when two high loss splices are separated by a short high cutoff wavelength fiber, as illustrated in Figure 7. The power transmitted through the fiber/splice system when both the fundamental and first higher order modes are present has been modeled as^[8]

$$P = A(\eta_1, \eta_2) + B(\eta_1, \eta_2, \alpha_1, L) + 2B^{1/2}(\eta_1, \eta_2, \alpha_1, L) \cos(\Delta\beta L)$$

where η_1 and η_2 are the splice transmission efficiencies, α_1 is the attenuation of the higher order mode, $\Delta\beta$ is the difference in the longitudinal propagation constants of the fundamental and first higher order modes, L is the fiber length between the splices, A is the fraction of power that travels through the system solely as the fundamental mode and B is the fraction of the fundamental mode power that gets coupled into the higher order mode of the second fiber by the first splice and subsequently gets coupled back into the fundamental mode of the last fiber by the second splice. The third term, the interference term, is what gives rise to modal noise generation.

When the splice loss and fiber attenuation are fixed, the transmission through the system will vary sinusoidally with changes in $\Delta\beta$ and changes in L . Therefore, the modal interference can be observed with transmitted power measurements by 1) varying the propagation constants (by changing the excitation wavelength for example) or 2) by changing the fiber length. The change in length required for a 2π phase change is 0.4 mm, since $\Delta\beta$ is approximately $0.016 \text{ micron}^{-1}$, for typical telecommunication fibers.

A fiber/splice system as discussed above was assembled using a straight 1 meter length of fiber, with a large oscillation above the normal cutoff wavelength, in the fiber section between the splices. Transverse offset was used to generate 3 dB splice losses. We observed interference between the fundamental mode and the oscillation by fixing the excitation wavelength at the oscillation peak wavelength (using a single line DFB laser diode) and varying the fiber length. The fiber length was varied by applying an axial load to a 0.4 meter section of the 1 meter long fiber between the splices. The load was applied with a piezoelectric transducer driven at 0.5 Hertz with triangle waveform while the transmitted power was monitored on an oscilloscope. At the low levels of load applied (inducing strains of less than 0.5 percent) the stress induced changes in $\Delta\beta$ can be ignored. As shown in Figure 8 (a), the transmitted power went through one complete sinusoidal oscillation as the strain was increased from 0 to 0.25 percent. Figure 8 (b) shows the effective cutoff wavelength of the fiber in the test configuration and the excitation wavelength at the oscillation peak. Although the conditions of the experiment were severe compared to normal system conditions, i. e., 3 dB splice loss, a 1 meter long straight fiber between the splices, the results confirm that interference can occur between the fundamental mode and the LP_{1n} mode that causes the oscillation.

5. SOLUTIONS

Since the energy carried in the cutoff wavelength oscillations can interfere with the fundamental mode and generate modal noise, the oscillations should be considered in a cutoff wavelength specification strategy. The difficulty in dealing with the oscillations at a practical level is that since the LP_{1n} modes that are causing their presence are loosely bound and lossy, they are very sensitive to fiber configuration, e.g., length, macro- and micro- bending, both when measuring cutoff wavelength and when deploying the fiber in a system. We see three ways of developing a strategy of dealing with the oscillations:

1. Eliminate the oscillations in the measurement by altering the measurement configuration to selectively attenuate the less tightly bound LP_{1n} modes causing the oscillations and then accounting for the behavior of the oscillations in the system design. A few

possible approaches are increasing fiber length,^[9] introducing microbending^[4] or macrobending into the measurement configuration. In addition to the potential measurement repeatability problems that could arise when these approaches are implemented in a factory environment, the issue of how to account for the oscillations in system design has yet to be addressed.

2. Ensure that the oscillations are always included in the measurement by very rigidly controlling the measurement configuration. This could be implemented with the existing standard fiber configuration or using a worst case measurement configuration where the oscillations are exaggerated, e.g., a short straight length of fiber. A drawback to this approach is that ostensibly insignificant differences in the fiber layout can dramatically effect oscillation behavior resulting in measurement repeatability problems. Exaggerating the oscillations by altering the configuration might help measurement repeatability but could result in a potentially severe fiber production penalty that is probably unbalanced with the system performance risks.
3. Eliminate the oscillations all together by changing the fiber cutoff behavior by altering the coating attenuation and/or index properties. This option has not been explored but is possibly the the most appealing in the long run.

6. CONCLUSIONS

We have presented a theory for the presence of the oscillations in the cutoff wavelength measurements that can account for all aspects of observed oscillation behavior. The observation of modal interference between the fundamental mode and the LP_{1n} modes that cause the oscillations confirms the potential for modal noise generation in a system. Possible strategies for handling the cutoff wavelength measurement in the presence of oscillations have been discussed.

REFERENCES

1. P. L. Francois and C. Vassallo, "Finite Cladding Effects in W Fibers: A New Interpretation of Leaky Modes," *Appl. Optics*, Vol. 22, No. 19, Oct. 1983, p. 3109.
2. D. W. Peckham and S. A. Jacobs, "Characteristics of the Anomalous Structure Observed in Single-Mode Fiber Cutoff Wavelength Measurements", in *Tech. Dig. 13TH OSA Conf. Opt. Fiber Comm.*, (San Francisco, CA), Jan. 22-26, 1990, p. 86.
3. V. Shah, L. Curtis, and W. C. Young, "Cutoff Characteristics of Dispersion- Shifted and Dispersion-Unshifted Fibers," in *Tech. Dig., Symp. on Opt. Fiber Meas.*, (Boulder, CO), Sept. 20-21, 1988, p. 135.
4. K. A. Emig, "Transmitted Cutoff Wavelength Measurement Imprecision : Cause and Effect," in *Tech. Dig., 12TH OSA Conf. Opt. Fiber Comm.*, (Houston, TX), Feb 6-9, 1989, p. 133.
5. A. S. Sudbo and E. Nasset, "Attenuation Coefficient and Effective Cutoff Wavelength of LP_{11} Modes in Curved Optical Fibers," *J. of Lightwave Tech.*, Vol. 7, No 5, May 1989, p. 785-790.
6. C. DeBoor and R. Weiss, "Solveblok: A Package for Solving Almost Block Diagonal Linear Systems," *ACM Trans. on Mathematical Software*, Vol 6., No. 1, March 1980, p. 80.
7. A. W. Snyder and C. Park, "Incoherent Illumination of an Optical Fiber," *J. Opt. Soc. Am.*, Vol. 63, No. 7, July 1973, p.806.
8. D. G. Duff, F. T. Stone, "Measurements of Modal Noise in Single-Mode Lightwave Systems," in *Tech. Dig. Conf. on Opt. Fiber Comm.*, Feb. 11-13, 1985, p. 52.
9. E. L. Buckland, Discussions at EIA F.O-6.6.5 Working Group Meeting, June 29, 1989.

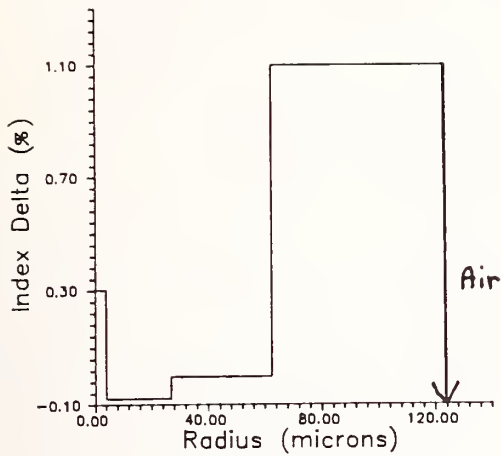


Figure 1

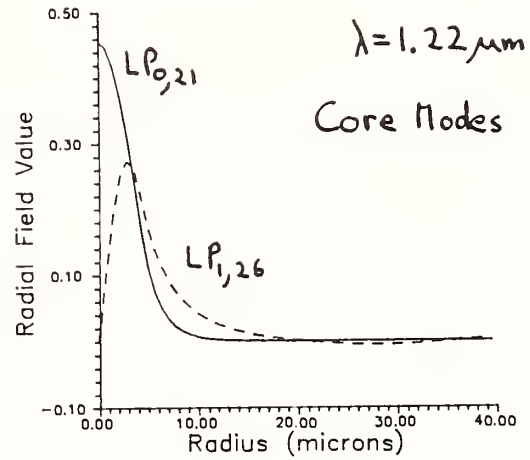


Figure 2a

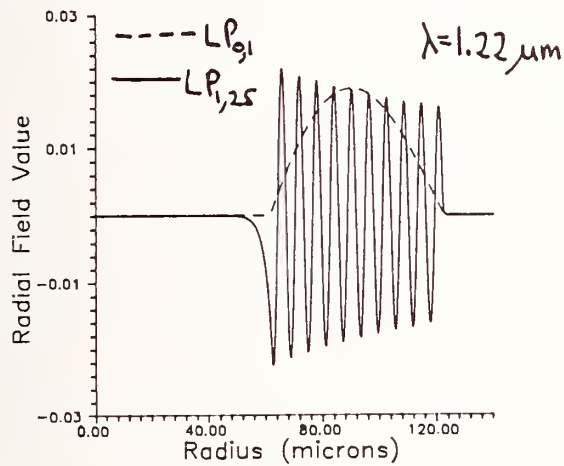


Figure 2b

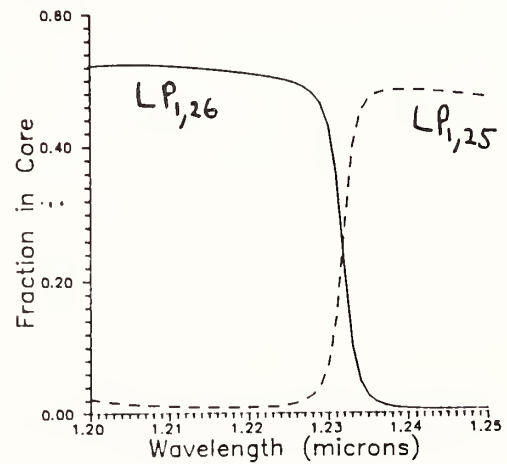
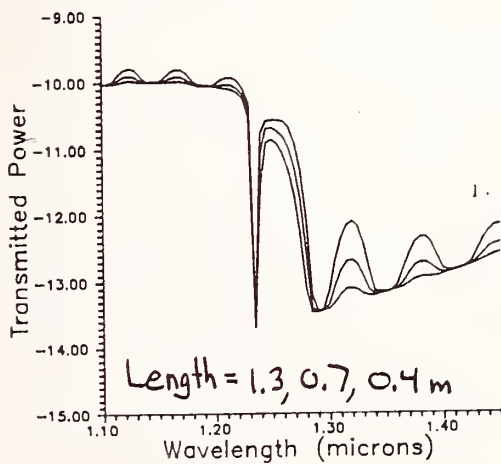
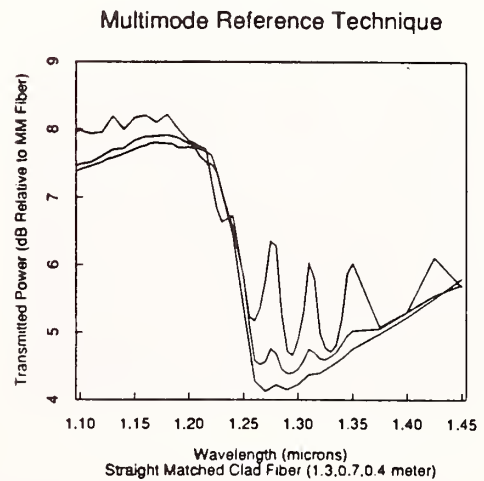


Figure 3

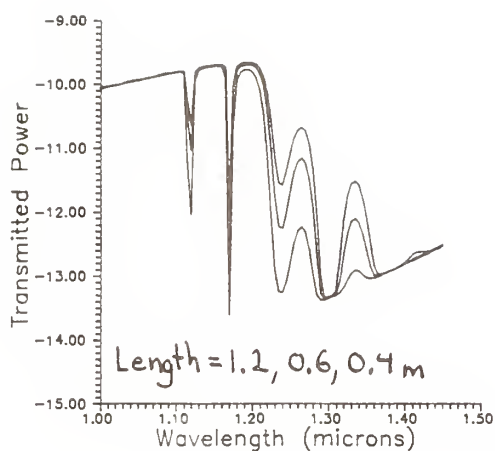


(a)

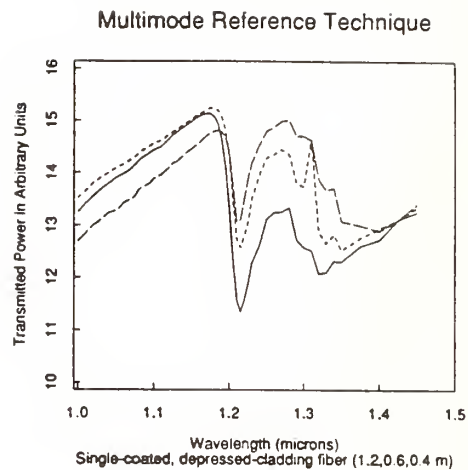


(b)

Figure 4: Matched cladding fiber transmitted power; (a) Theory, (b) Experiment.



(a)



(b)

Figure 5: Depressed cladding fiber transmitted power; (a) Theory, (b) experiment.

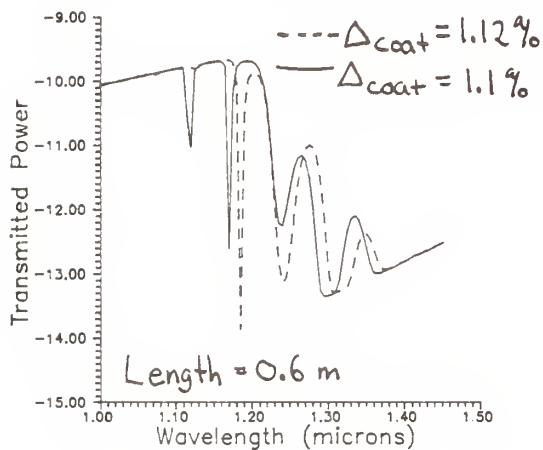


Figure 6

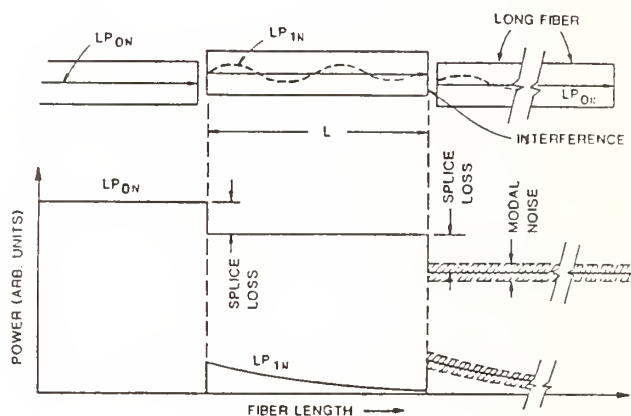
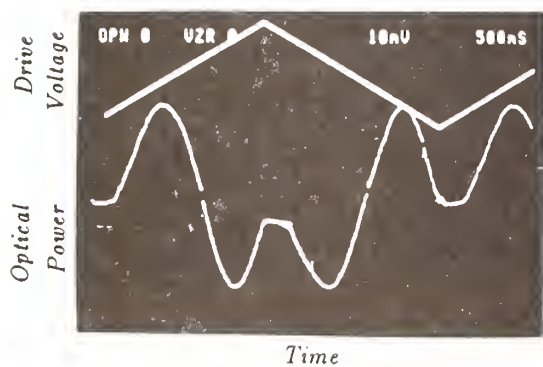
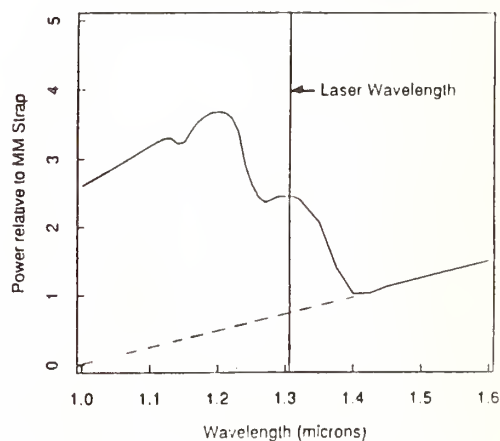


Figure 7: Schematic diagram of modal noise generation.



(a)



(b)

Figure 8: (a) Transmitted power and piezo drive voltage versus time. (b) Transmitted power through 1 meter, straight sample of test fiber.

A recent advance in the measurement of the refractive index profile of optical fibre preforms

D A Svendsen, I D Cook

York Technology Limited, York House, School Lane
Chandlers Ford, Hampshire S05 3DG United Kingdom

Introduction

The measurement of the refractive index profile of optical fibre preforms is important for quality control and research in the optical fibre industry. The supremacy of non-destructive transverse illumination methods has been established since the early developments in the techniques ten years ago (1,2,3). However, there is a major aspect of the transverse illumination measurement technique which has a significant bearing on the quality of measurement but which has not received apparent attention, and that is the effect of the index matching liquid. This paper reports on a recent advance in this area (4) which promises to improve measurement quality significantly and hence keep the measurement technique abreast of the requirements of an increasingly demanding industry.

The Problem

Although a transverse illumination technique not using index matching liquid was proposed first (1), it rapidly became evident that the large refractive index difference between air and the outer boundary of the preform placed too many restrictions and demands upon the nature of the preform and its surface. The natural solution is to surround the preform with a liquid whose refractive index minimises the mismatch at the preform boundary, and this is the approach that has been universally adopted in the industry, despite the potential problems of cost, convenience, and, in some cases, toxicity. Although successful in eliminating the mismatch problem, it is unfortunate that other characteristics of the liquid have a deleterious effect on measurement quality. These problems fall into two classes, namely, contamination and bulk refractive index changes, the most important of which arises from temperature. The liquid and preform are enclosed within a chamber, or analyser cell, and the measurement illumination enters and leaves the cell via plane glass windows. Figure 1 shows the schematic cross-section of such a cell. It is usual for the liquid to be pumped automatically into and out of the cell and the liquid inevitably collects small particulate matter and air, both in and out of solution. These act as scatter centres within the measurement optical path and thus degrade signal to noise ratios. However, the greatest problems arise from the fact that the liquid has a significant temperature coefficient of refractive index, with a magnitude of about $-0.0004/\text{deg C}$. Since the measurement technique can easily resolve refractive index differences of 0.00001 , the temperature coefficient places requirements on temperature stabilities of the order of few hundredths of a degree Celsius. The reason for this is that the technique relies on the volume of liquid being at constant refractive index so that it acts as the reference against which refractive index changes are measured. With reference to the cross-section of a typical cell as shown in Figure 1, the measurement is made by scanning the beam transversely across the preform and sequentially measuring the deflection of the beam as a function of radial position. This deflection function, $D(y)$, is converted into

the refractive index difference profile for axisymmetric preforms by means of an Abel transform:

$$n(r) - n(a) = \frac{n(a)}{\pi} \int_r^a \frac{D(y) dy}{\sqrt{(y^2 - r^2)}} \quad (i)$$

where: $D(y)$ is the angle of refraction at entry radius y , $n(r)$ is the absolute refractive index at radius r , and a is the maximum radius above which the refractive index for all radii is a constant and equal to $n(a)$. Thus $n(a)$ is the refractive index of the medium surrounding the preform, that is, the index matching fluid. When the whole volume changes uniformly with temperature then $n(a)$ in expression (i) changes, and so the index profile changes by a constant offset and scale but retains its relative shape. However, a much more serious problem occurs when the liquid is not isothermal and therefore not homogeneous in refractive index. The measured refractive index becomes distorted by this non-homogeneity and the problem is compounded when the temperature changes during the measurement period, which it almost always does in practical situations, where heat flows between the environment and the preform through the analyser cell. These distortions degrade both accuracy and repeatability of measurement and are most noticeable in regions of known constant refractive index within the preform.

A Solution

Both the problems of contamination and unwanted refractive index changes may be tackled simultaneously by confining the liquid layer to be a thin cylindrical annulus which interfaces between a solid transparent material and the preform itself. Essentially, this is equivalent to the region marked A in Figure 1 between the outer windows and the inner dashed boundary becoming a solid with the liquid restricted to the region marked B. The solid is typically a

rectilinear silica glass plate with a cylindrical hole within it but the crucial feature is that the temperature coefficient of refractive index of the plate, $n(a)$, is negligible with respect to that of the liquid. The thinness of the liquid layer reduces the contaminant problem because it means that very small volumes of fresh liquid may be used for each measurement.

However, the major advantage of the liquid being restricted to a thin annular layer is that it then has a greatly reduced effect on the measured results.

Firstly, the measurement becomes referred to the solid of constant refractive index and so the problem of varying $n(a)$ disappears from expression (i).

It then becomes useful to assign absolute refractive indices to the measurement as it is sufficient to measure the refractive index of the solid, $n(a)$, once and for all. Secondly, any axisymmetric refractive index profile of the layer of liquid, arising from uniform radial temperature gradients, has no effect on the measurement since it is precisely what the system is designed to measure and is thus indistinguishable from any such layer within the preform itself.

Finally, any change in refractive index of this layer during the course of the measurement is confined to the annular region and not spread throughout the optical path within the cell. As may be seen from expression (i), the deflection angle of any layer contributes to the estimation of refractive index of a layer at a smaller radius with a weighting which reduces with increasing distance between the layers. In contrast, changes in the refractive index of a

layer during the course of a measurement have an increased effect with increasing distance between the layers as a consequence of the sequential measurement time of the layers. This latter effect tends to compensate for the former which leads to high quality results. Expression (i) contains the implicit assumption of cylindrical symmetry and so it is also important to achieve thermal as well as physical cylindrical symmetry within the liquid layer. The natural tendency for heat to flow radially to and from the preform may be enhanced by use of good thermal conductors and insulators to impose cylindrical symmetry upon the total thermal environment of the measurement region and the liquid within the optical path. Figure 2 shows the cross-section of a practical analyser cell which embodies the features described here.

Performance

Figures 3 and 4 show the results of measurements made upon a silica rod shortly after it had been cooled to about 5 degrees Celsius, that is, 15 degrees below ambient (solid), and again after it had been left to temperature stabilise (dotted). Figure 3 is the result obtained using the standard liquid filled cell. The index profile is obviously so distorted by the thermal behaviour of the liquid that it is impossible to identify with any certainty the nature of the sample. Figure 4 shows the result obtained using the new cell with the cylindrical layer of liquid and thermal cylindrical symmetry. Even under this extreme test the measurement shows a clearly recognisable silica rod. The high quality of the silica plate can be seen by its very smooth refractive index profile in contrast to the poorer quality of the rod itself. The liquid regions shows both the temperature gradients and their change in time. Under normal conditions the temperature differences are much smaller than have been shown here, and so the new analyser cell can be expected to give results essentially undistorted by temperature changes in the liquid. However, the good thermal cylindrical symmetry of the liquid region may also be advantageous within a production facility where preforms need to be measured before they have fully cooled to ambient temperature.

Summary

A new analyser cell has been described which practically eliminates the effects of temperature on measurement and reduces the likelihood of liquid contamination. Accuracy and repeatability are increased and an absolute refractive index reference is an inherent feature. This advance in preform measurement offers a new level of capability for the routine measurement of optical fibre preforms.

Acknowledgements

The authors are grateful to the Directors of York Technology for permission to publish this paper.

References

- (1) P.L.Chu, Electronic Letters, Vol. 13, No. 24, pp 736-738, 1977.
- (2) L.S.Watkins, Applied Optics, Vol. 18, No. 13, pp 2214-2222, 1979.
- (3) I.Sasaki, D.N.Payne, M.J.Adams, Electronic Letters, Vol. 16, No. 6, pp219-221, 1980.
- (4) D.A.Svendsen, UK patent application, 1990.

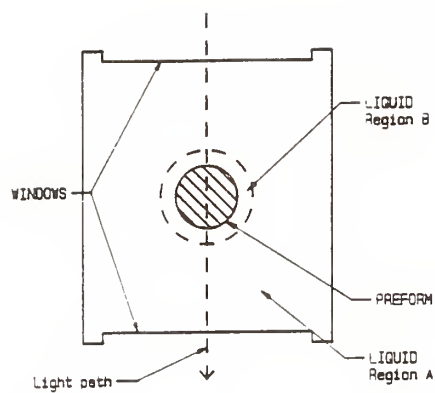


Figure 1. Standard analyser cell

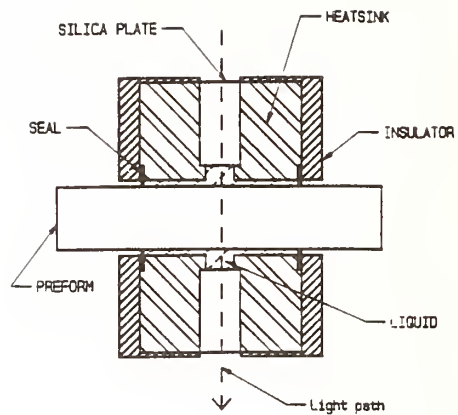


Figure 2. New cell schematic

Figure 3. Silica Rod: Standard cell

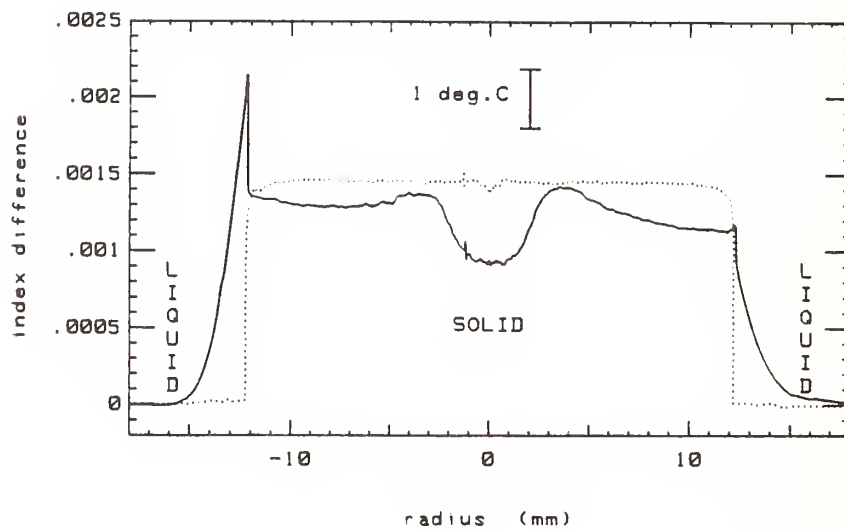
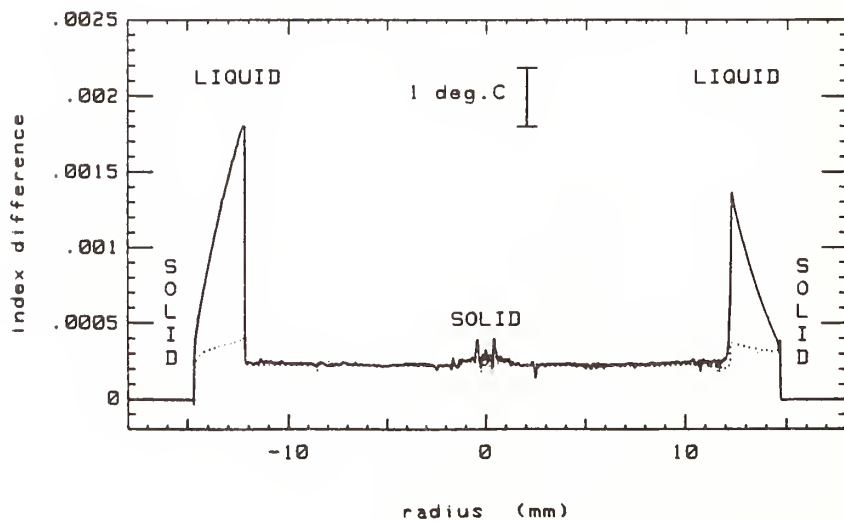


Figure 4. Silica Rod: New cell



Refractive Index Measurements on Single-Mode Fiber as Functions of Product Parameters, Tensile Stress and Temperature

J. J. Carr, S. L. Saikkonen, and D. H. Williams

Corning Incorporated
Product Engineering Laboratory
Corning, New York 14831

Introduction

Understanding effective index of refraction (EIOR) dependence on product parameter variations, tensile stress and temperature has numerous applications in the fiber and fiber-related industries. For a variety of reasons, such measurements require sample fiber lengths tens of meters or more. In order to measure the subtle influence of product variations on index, at least four decimal place accuracy is necessary.

Fiber Types Measured

Standard unshifted and dispersion-shifted, matched-clad single-mode optical fibers were measured at the nominal operating wavelengths of 1300 and 1550 nanometers. Samples were selected that represented a typical manufactured product range for delta (Δ) and mode-field diameter (MFD) parameters.

Measurement Methods

Sample lengths, L_o , were deployed in a straight line and measured between fifty-meter benchmarks surveyed to within an accuracy of two millimeters. One end of the fiber was coupled to a Fresnel reflection optical time domain reflectometer (OTDR) capable of 10-picosecond time of flight resolution, $\Delta\tau$. The associated index measurement resolution, ΔN , follows using equation (1), where c is the speed of light (3×10^8 m/s).

$$\Delta N = (c/2L_o) \Delta\tau \quad . \quad (1)$$

Evaluating (1) yields a resolution of 0.00003, which assures confidence in reporting measured index to the fourth decimal place. The initial stage of the work involved an index of refraction characterization measurement on each sample fiber in a relaxed (unstressed) condition at room temperature (22°C).

Once characterized, each sample was prepared in the same deployment setting for index versus stress measurements. Both fiber ends were epoxied to grooved aluminium blocks. The OTDR end was fixed, while tensile loads were applied in approximately 0.2-pound (20 kpsi) increments to the free end. Fiber elongations under load were measured to determine strain and correct for associated length changes in the index computations.

Refractive index as a function of temperature comprised the third stage of measurements. Characterized fiber samples were wound in loose coils and placed in a temperature chamber. Initially, index measurements were performed at room temperature to serve as controls and confirm any effect due to the coiled configuration. Measurements were taken over a temperature range of -60 to +85 degrees Celcius in 10-degree steps. Length changes, ΔL , due to thermal expansion and contraction were accounted for in the index calculations applying equation (2). The coefficient of linear expansion, α , for fused silica is $8 \times 10^{-7}/^{\circ}\text{C}$ and the temperature change, ΔT , is measurement temperature minus room temperature.

$$\Delta L = L_0 \alpha \Delta T \quad . \quad (2)$$

Results

Characterization measurements over the entire sample range for delta and mode-field diameter revealed index of refraction variations in the fourth decimal place for unshifted fibers and in the third decimal place for dispersion-shifted fibers. Unshifted samples exhibited an EIOR range of 0.0006 at both 1300 and 1550 nanometer wavelengths of operation, with average values of 1.4675 and 1.4681 respectively. The dispersion-shifted EIOR

sample range was 0.0017 for both 1300 and 1550 nanometer wavelengths; corresponding average refractive indices were 1.4718 and 1.4711.

Example graphs, figures 1 and 2, of EIOR versus tensile stress for an unshifted and dispersion-shifted fiber sample show nearly linear relationships. Slopes for both fiber types were quite consistent at $-0.000024/\text{kpsi}$ ($-0.0027/\%$ strain) across all samples measured at either wavelength. Negative slope means flight time, and therefore index, decreases with increasing tensile stress as photo-elastic theory predicts¹. The magnitude of the slope also is close to the $-0.000035/\text{kpsi}$ value one would obtain from a previous study on multimode fiber ($\text{P}_2\text{O}_5/\text{GeO}_2$ doped silica core), by Hartog, Conduit and Payne².

Plots shown in figures 3 and 4 are representative of EIOR versus temperature results for unshifted and dispersion-shifted fiber types. Again, all samples measured at either wavelength displayed strong consistency in the rate of change of index with temperature, $0.000012/^\circ\text{C}$. Hartog, et al also measured temperature effects on fiber index² obtaining data which translates to a slope of $0.000010/^\circ\text{C}$. Cohen and Fleming³ reported $0.000010/^\circ\text{C}$ as well, measuring a depressed clad single-mode fiber (with a B_2O_3 doped silica core).

References

1. Mueller, Hans. 1938. The Theory of Photoelasticity. Journal of the American Ceramic Society 21: 27-33.
2. Hartog, A.H., A.J. Conduit and D.N. Payne. 1979. Variation of Pulse Delay with Stress and Temperature in Jacketed and Unjacketed Optical Fibres. Optical and Quantum Electronics 11: 265-273.
3. Cohen, L.G. and J.W. Fleming. 1979. Effect of Temperature on Transmission in Lightguides. The Bell System Technical Journal 58: 945-951.

Effective Index vs Stress
(dispersion shifted single-mode - 1532nm)

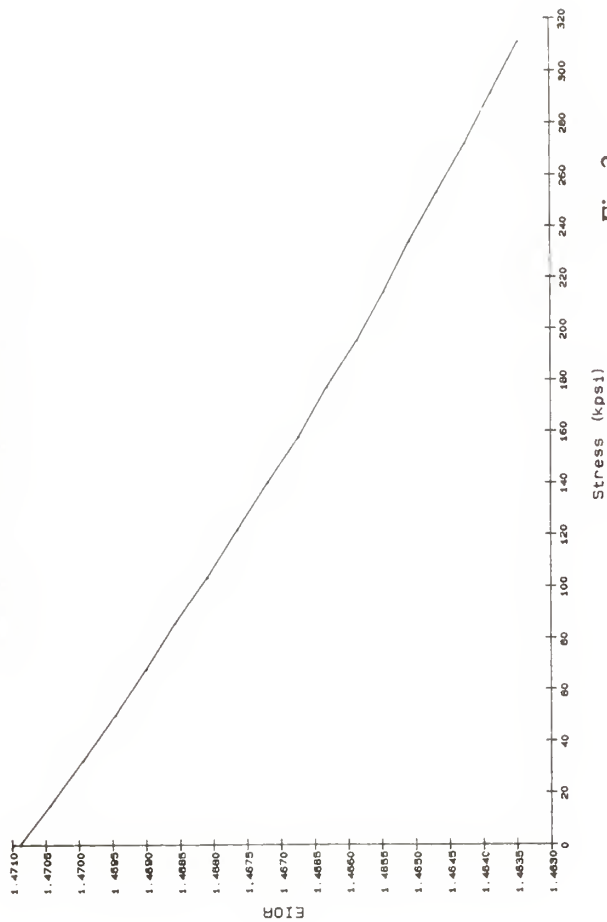


Fig. 2

Effective Index vs Temperature
(dispersion shifted single-mode - 1532nm)

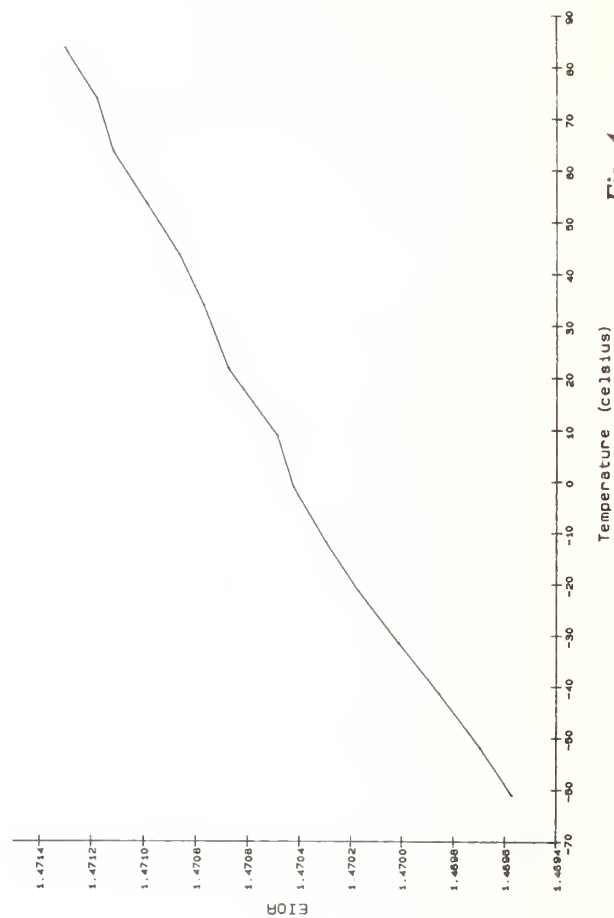


Fig. 4

Effective Index vs Stress
(unshifted single-mode - 1295nm)

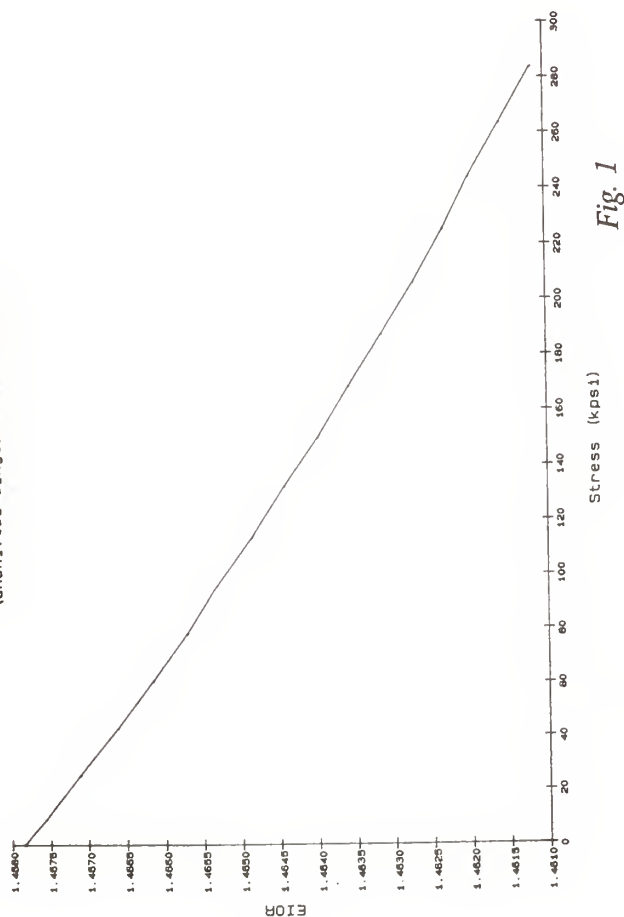


Fig. 1

Effective Index vs Temperature
(unshifted single-mode - 1295nm)

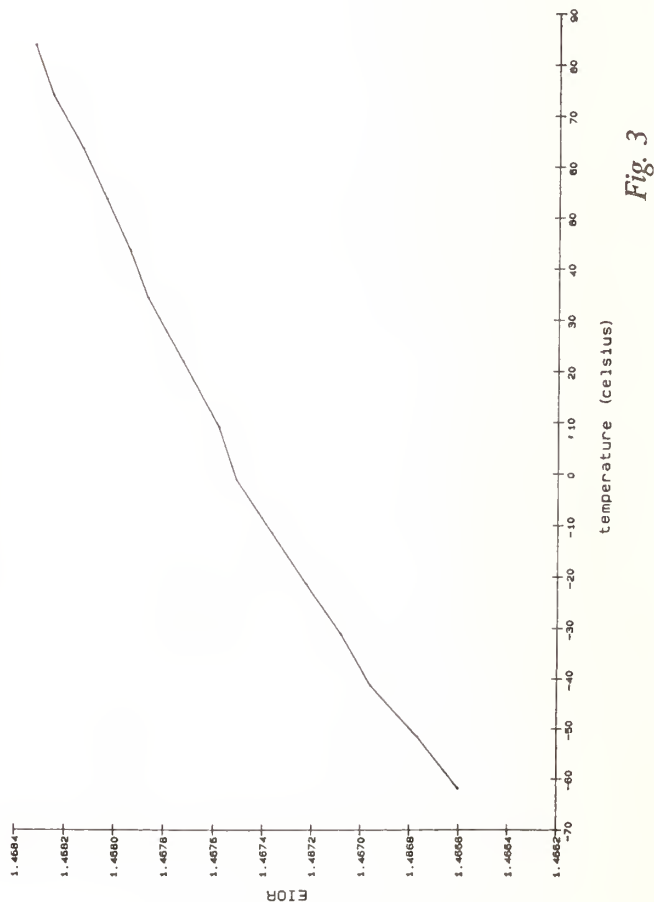


Fig. 3

Spatially Resolved Measurement of High Attenuation in Integrated Optical Polarizers*

Robert K. Hickernell, David L. Veasey and J. Andrew Aust
National Institute of Standards and Technology
325 Broadway
Boulder, CO 80303

Abstract

Photothermal deflection is used to spatially resolve attenuation in waveguide polarizers made with metal or semiconductor overlayers. 760 dB/cm loss was measured for TM polarization in ion-exchanged, silicon-clad glass guides.

Introduction

Integrated optical polarizers with high polarization extinction and low insertion loss are critical components in fiber sensor systems. Polarizers in Ti:LiNbO_3 waveguides typically consist of a proton-exchanged waveguide section which supports only the extraordinary mode¹ or a metal cladding with dielectric buffer to preferentially attenuate the TM mode.² The metal cladding technique is also applicable to glass and semiconductor guides. TM- or TE-pass polarizers can be made with a semiconductor cladding.³

The most common method for measuring polarizer extinction ratio and loss is a comparison of the guided throughput power for TE and TM input polarization. Extinction ratios greater than 50 dB have been reported, but are limited by depolarization in the measurement optics.⁴ Attenuation per unit length has been measured by fabricating polarizers of different lengths on the same substrate. An attenuation of 280 dB/cm was reported for a LiNbO_3 waveguide with an aluminum overlayer,⁵ and 500 dB/cm was reported for an InGaAsP guide loaded with an InGaAs absorbing layer.⁶ The precision of the measurement depends on the care taken to achieve equal coupling in each guide and in each polarization state.

We present a method for measuring attenuation in channel waveguides with absorbing overlayers. Based on the photothermally induced deflection of a probe laser beam, the technique permits *in situ* probing along a single guide to measure attenuation as high as 10^3 dB/cm. High spatial resolution of loss variation is achieved. The measurement is not limited by the irreproducibility of coupling and is minimally affected by depolarization in the input optics.

Experimental Technique

When guided light is absorbed nonradiatively, it produces a small temperature gradient in the guide and surrounding region. The photothermally induced index gradient refracts a probe laser beam which passes through the substrate; alternatively, thermal expansion deflects a probe beam which reflects from the substrate surface. For channel guides of uniform width and absorption, the photothermal deflection (PTD) as a function of distance along the guide gives a measure of attenuation.⁷ We have employed PTD with a transmitted⁷ or a reflected⁸ probe beam to measure loss less than 1 dB/cm in glass channel waveguides with an uncertainty as small as 0.03 dB/cm.

*Contribution of the U.S. Government, not subject to copyright.

Figures 1 and 2 depict the experimental apparatus used to measure PTD in waveguides with a transmitted and with a reflected probe beam, respectively. We have employed a variety of lasers as the pump source. The pump light path consists of a mechanical chopper, a Glan-Thompson polarizer with 50 dB extinction ratio, a half-wave plate, and a stress-free objective to couple light into the waveguide. 1-5 mW of coupled power is sufficient to obtain a good SNR over the extent of the measurement. Throughput power is monitored with a Si or Ge detector.

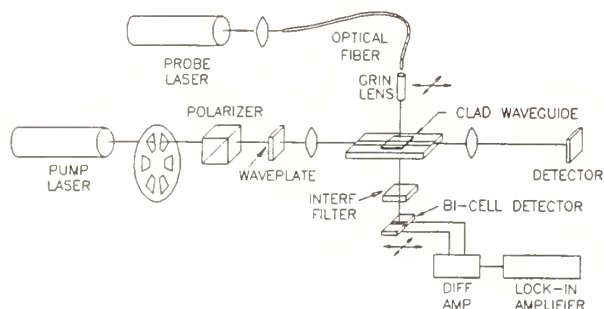


Fig. 1. Photothermal deflection measurement apparatus using refracted probe beam.

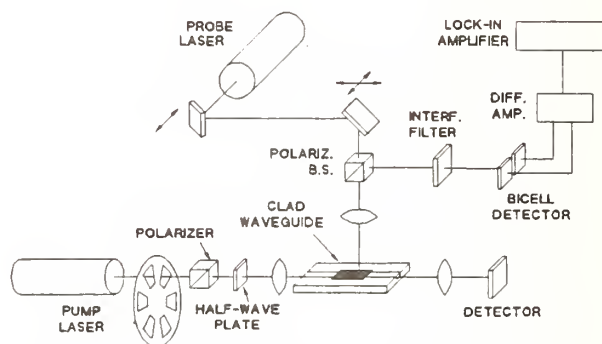


Fig. 2. Photothermal deflection measurement apparatus using thermoelastically displaced probe beam.

In Fig. 1 the probe beam is from a 750 nm laser diode coupled to a single-mode fiber; approximately 1 mW of power is focussed to an $18\text{ }\mu\text{m}$ diameter spot on the substrate with a 0.29-pitch GRIN lens. A silicon bi-cell detects the deflection of the expanding beam; the beam is centered in the bi-cell to reject common mode intensity fluctuations. In Fig. 2 the free-space beam from a 5 mW HeNe laser operating at 632.8 nm is focussed with a 5x microscope objective, and the beam reflected from the polarizer surface is recollimated and directed to the bi-cell through a polarization beamsplitter. The reflected probe geometry is particularly useful for characterizing guides on substrates which are opaque to the probe beam or which have rough or inaccessible bottom surfaces. Computer-controlled translation stages position the probe beam spot and the bi-cell. The difference between the bi-cell voltages is monitored by a lock-in amplifier using a 3 s time constant. The PTD signal is normalized to the dc sum of the bi-cell voltages and to the relative throughput of the guided beam to account for any fluctuations in laser power. Factors that limit the loss measurement precision are material inhomogeneities, fabrication tolerances, mechanical vibration, and pointing fluctuations of the probe beam.

Experimental Results

We fabricated polarizers by depositing hydrogenated amorphous silicon (a-Si:H) on glass waveguides. Since the ratio of guided intensity in the low-loss dielectric guide to that in the high-loss semiconductor layer varies periodically as a function of cladding thickness,³ polarizers which attenuate either TE or TM polarization can be fabricated. Channel waveguides were formed in glass microscope slides by potassium-sodium ion exchange through $3\text{ }\mu\text{m}$ windows in an aluminum mask. Exchange in a melt of potassium nitrate at a temperature of 400°C for 35 min produced single-mode waveguides at the wavelength of operation, 632.8 nm. A-Si:H was deposited over the guides to a thickness of

approximately $0.45\ \mu\text{m}$ by rf plasma-enhanced chemical vapor deposition and was photolithographically patterned to form 1.2 mm long pads. Each cladding pad was rf plasma-etched in an atmosphere of CF_4 and O_2 to a different thickness.

The transmitted probe beam apparatus depicted in Fig. 1 was used to measure the loss of the glass waveguide polarizers. Figures 3 and 4 illustrate their performance; the magnitude of the PTD signal at the position of peak photothermally induced index gradient is plotted as a function of position along the length of the guide. The slope of the least-squares fit line through the semi-logarithmic plot yields the loss coefficient. Data in Fig. 3 for a TM-pass polarizer with a cladding thickness of 407 nm indicate a loss of $369 \pm 6\ \text{dB/cm}$ for TE input polarization and $85 \pm 3\ \text{dB/cm}$ for TM polarization. The measurement uncertainty is due to local waveguide inhomogeneities and not the SNR of the measurement system.

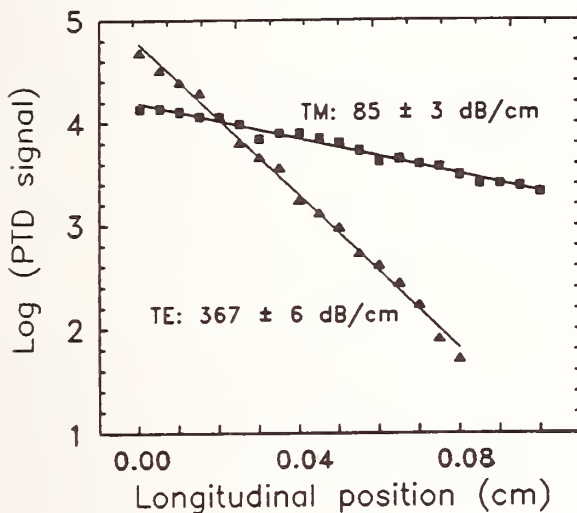


Fig. 3. Measurement of loss in a silicon-clad, TM-pass, glass waveguide polarizer.

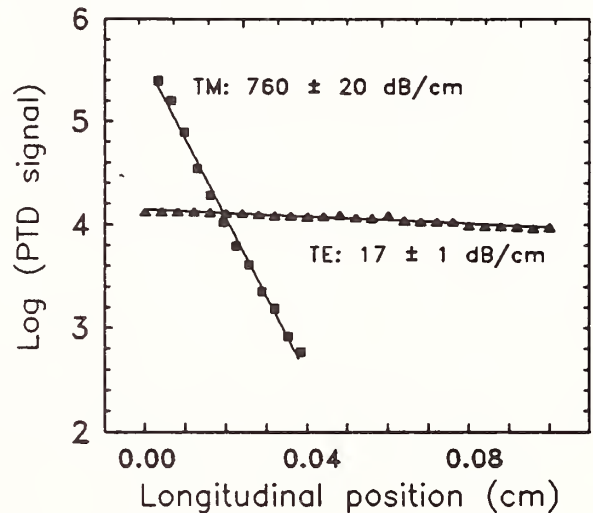


Fig. 4. Measurement of loss in a silicon-clad, TE-pass, glass waveguide polarizer.

An efficient TE-pass polarizer resulted from a cladding thickness of 428 nm. Figure 4 shows the measurement of $760 \pm 20\ \text{dB/cm}$ loss for TM input polarization. At longitudinal positions beyond the first 0.4 mm of polarizer, the signal was masked by random noise due to mechanical vibration. We reversed the direction of the polarizer, made the measurement again, and verified that the loss was uniform across the sample. The first point in the scan was taken about $50\ \mu\text{m}$ from the front of the polarizer pad to avoid skewing of the data due to thermal end effects and optical coupling transients.

The TE loss of the polarizer was $17 \pm 1\ \text{dB/cm}$; therefore, the extrapolated polarization extinction ratio for the 1.2 mm long device was 89 dB, and the excess insertion loss was 2 dB. We directly measured an extinction ratio of 42 dB by comparing total device throughput for the two orthogonal input polarizations. In contrast to common practice, this measurement was made without a bulk polarizer on the output side of the guide, in order to include the effect of depolarization in the guide. The extinction ratio measured with an output polarizer was 48 dB, which was at the measurement limit. The discrepancy between extrapolated and directly measured extinction appears to be due to stray unguided light and depolarization.

Using the apparatus of Fig. 2, we measured the attenuation of polarizers made by overcoating Ti-indiffused LiNbO_3 channel waveguides with a 2 mm long SiO_2 buffer layer and an aluminum absorbing layer. Typical data shown in Fig. 5 indicate an average loss of 92 ± 2 dB/cm for TM polarization at a pump wavelength of 840 nm. Since the repeatability of each data point was $\pm 2\%$, the dip in the data near 0.045 cm is due not to noise but to a local variation in absorption coefficient. A simple model of the spatial variation in PTD signal suggests that the loss decreases to 79 dB/cm near that point. Spatial resolution of defects was limited in this measurement to roughly $70 \mu\text{m}$, twice the thermal diffusion length of LiNbO_3 at the 500 Hz chopping frequency. For TE input polarization this waveguide was double-moded, with a loss of roughly 12 dB/cm.

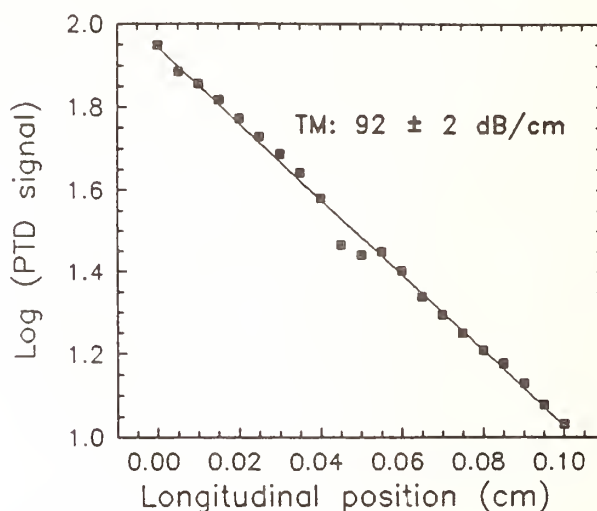


Fig. 5. Measurement of loss for metal-clad Ti:LiNbO_3 waveguide polarizer.

Conclusion

Photothermal deflection has proven useful for nondestructively studying large attenuation in waveguide polarizers *in situ*. Absorptive inhomogeneities can be probed with spatial resolution depending on the thermal properties of the substrate and inversely on the square root of the pump modulation frequency; $20 \mu\text{m}$ resolution is feasible. This technique may allow the distinguishing of longitudinal spatial transients in the optical intensity distribution in waveguide polarizers or detectors.⁶ Based on the data of Fig. 4, the present apparatus allows measurement of absorption-induced attenuation in glass waveguides as high as 3000 dB/cm over a distance of $120 \mu\text{m}$ for 1 mW coupled power. Dynamic range can be increased by increasing the coupled power and reducing mechanical noise. The reflected probe beam is more sensitive to the cleanliness and vibration of the substrate than the transmitted probe beam.

References

1. T. Findakly and C. L. Chen, *Appl. Opt.* 17, 464 (1978).
2. J. N. Polky and G. L. Mitchell, *J. Opt. Soc. Am.* 64, 274 (1974).
3. R. F. Carson and T.E. Batchman, accepted for publication, *Appl. Opt.* (1990).
4. P. G. Suchoski, T. K. Findakly and F. J. Leonberger, *Proc. SPIE*, Vol. 835, Integrated Optical Circuit Engineering V, p. 40 (1987).
5. D. E. Leslie, J. L. Nightingale and M. M. Fejer, *Integrated and Guided Wave Optics*, 1989 Technical Digest Series, Vol. 4, p. 266 (1989).
6. R. J. Deri, N. Yasuoka, M. Makiuchi, O. Wada, A. Kuramata, H. Hamaguchi and R. J. Hawkins, *Appl. Phys. Lett.* 56, 1737 (1990).
7. R. K. Hickernell, D. R. Larson, R. J. Phelan, Jr. and L. E. Larson, *Appl. Opt.* 27, 2636 (1988).
8. R. K. Hickernell, J. A. Aust and D. R. Larson, *Sixth Int'l Top. Mtg. on Photoacoustic and Photothermal Phenomena*, Conf. Digest, p. 310 (1989).

WAVEGUIDE LOSS AND EFFECTIVE INDICES DETERMINATION BY OPTICAL FREQUENCY SCAN OF INTEGRATED RESONANT CAVITIES

C. De Bernardi and S. Morasca

CSELT S.p.A. - Via G. Reiss Romoli 274, 10148 Torino, ITALY

Abstract

A technique is presented to accurately determine optical loss, effective indices of propagating modes and modal dispersion in optical waveguides. The present method is based on frequency scanning an optical Fabry-Perot resonator, formed by the waveguide itself, and represents a significant improvement on a similar technique based on thermal scans of a cavity. Experimental data and further developments are presented for semiconductor waveguides.

1 Introduction

The current trend in reduction of attenuation in integrated optical waveguides, particularly on semiconductors, calls for accurate and reproducible techniques for the determination of guide loss: at the 0.1 dB/cm level, the ordinary methods (e.g. cut-back, total insertion loss etc.) are no longer sensitive enough to provide correct indications, needed for optimization of the overall guide performance. Another very important problem is the determination of the effective indices of the guided modes: precise values of these parameters are needed for the design of optical guided-wave devices, but also, from a more fundamental point of view, to test the validity of the theoretical methods used to calculate the waveguide propagation constants.

A technique providing reliable attenuation values of low-loss stripe waveguides is based on the fringe contrast of a Fabry-Perot cavity, formed by the waveguide itself; its known implementation is based on a temperature scan of the cavity itself [1, 2].

For the measurement of effective indices, the only accurate method available, to our knowledge, is based on the well-known prism coupler; although applied in some cases to stripe waveguides, it is practically useful only for planar waveguides.

We describe here a technique, which provides directly at the same time losses and effective indices of guided modes of stripe waveguides, without restrictive conditions or assumptions on the guide structure itself, even in the case of non strictly singlemode guides. The method is based on a wavelength scan of a resonant cavity formed by the guide under measurement; it is particularly suitable for semiconductor waveguides, whose cleaved facets provide sufficient reflectivity, but can be extended to any type of waveguide with little or no extra preparation.

2 Principle of the method

The transmission T of a Fabry-Perot cavity as function of the incident wavelength λ is given by:

$$T = C \frac{e^{-\alpha L}}{1 + R^2 e^{-2\alpha L} - 2 R e^{-\alpha L} \cos \frac{4\pi L n_{\text{eff}}}{\lambda}} \quad (1)$$

where α is the cavity internal loss, L its length, n_{eff} the effective index of the propagated mode, R the cavity facet reflectivity for the mode itself and C a constant; the cavity loss is obtained from R , L and the measured fringe contrast $u = T_{\text{min}}/T_{\text{max}}$, as shown by the following relationship:

$$L\alpha = \ln R + \ln \frac{1 + \sqrt{u}}{1 - \sqrt{u}} \quad (2)$$

If R is not known, eq (2) allows also its determination from the measurement of the contrast u for two different lengths of the same waveguide. The function (1) has a period which depends only on λ , L and n_{eff} ; using a tunable, narrow linewidth laser source it is easy to cover several periods of the cavity characteristics, hence to determine the period itself; L can be accurately measured under a microscope, the wavelength even more precisely by a monochromator or wavemeter, and therefore n_{eff} comes in a very straightforward way. In this case the only assumption is that n_{eff} is constant over the scanned wavelength range: this is certainly reasonable, since the range in practical cases covers only few hundred picometers, or about 10^{-4} of the central wavelength.

While for loss determination this technique provides the same capability as the mentioned temperature scan, its value is obvious for the index measurement: thermal scans produce a periodic pattern in the transmission function, but this period is not linked in a well-defined way to easily and accurately measurable quantities. In fact, the period depends on the temperature coefficients of the materials forming the guiding structure and on the temperature distribution in the structure itself; these quantities usually are either entirely unknown or very difficult to measure with the accuracy required to provide useful results, and the only directly usable quantity is the fringe contrast.

Since a high value of the cavity contrast is required only for accurate loss measurements, no special coating of the guide facets is necessary to enhance R if only the effective index is required; therefore, effective indices can be measured also for waveguides in low-index materials.

The present technique is not limited to strictly singlemode excitation of waveguides: in fact, a theoretical analysis of the propagation of multiple modes in the cavity leads to a complex characteristic, composed of multiple patterns, corresponding to each of the different wavelength periods and their beats. A Fourier analysis is therefore able to provide the spectrum of the effective indices of all the modes present in the cavity with a sufficient level.

3 Experiment

The technique described above has been tested with the experimental set-up sketched in Fig. 1. A DFB laser (Fujitsu 2XFLD150F1ASJ-A) is used, and tuning is achieved by changing the injection current; the source linewidth is less than 25 MHz in the 45-75 mA current range, used in the measurements; the output power is coupled to an optical fibre, which in turn is coupled to the guide under measurement. The optical power transmitted by the guide is collected and collimated by a

microscope objective, filtered by a calcite polarizer and detected by a germanium photodiode. The sample is mounted on a heat sink to stabilise its temperature during the measurement; however, a fast current scan can be easily performed (up to several hundred Hz in our present case), the signal being displayed on an oscilloscope; this further guarantees negligible temperature effects on the results.

An example of the detected signal (normalized to the laser output level) for a ridge InGaAsP/InP waveguide, grown by MOCVD, is shown in Fig. 2: the measured loss and reflectivity are 0.43 dB/cm and 0.382 for the TE mode, as obtained by two sections of the same guide; the reflectivity is in very good agreement with the predicted value for the adopted guide structure.

Experimental results relative to a multimode excitation are shown in Figure 3: in Fig. 3a a high-order mode is excited, with some power coupled to other modes, as indicated by the secondary peaks, while in Fig. 3b (same waveguide) the fundamental mode is excited predominantly, with very small secondary peaks.

A discrete Fourier transform algorithm [3] is being implemented to analyse the transmitted power: in fact the conditions imposed by the use of the common FFT algorithm are too tight for an easy application to real measurements of this type. The relationship between wavelength and current for the laser source is also being calibrated; from this and from the drive current period provided by the Fourier analysis the effective index values and the modal dispersion will be determined. The results will be presented at the Conference.

4 Conclusions

A new technique has been developed and tested, which provides directly at the same time loss and effective indices of guided modes of single- or multi-mode stripe waveguides, without restrictive conditions or assumptions on the guide structure itself. The method is based on the optical frequency scan of a resonant cavity formed by the guide under measurement; it is particularly suitable for semiconductor waveguides, whose natural cleaved facets provide sufficient reflectivity; experimental results are presented for this case, but if effective indices only are required, it can be extended to any type of waveguide with little or no extra preparation.

Acknowledgements

The authors thank G. Schiavini, D. Bertone and A. Stano for providing the semiconductor samples. This work has been partially supported by EEC as part of RACE Project 1027

References

- [1] R.G. Walker "Simple and accurate loss measurement technique for semiconductor optical waveguides", *Electron. Lett.*, Vol. 21, pp. 581-583, 1985.
- [2] M.W. Austin and P.C. Kemeny "Measurement of semiconductor optical waveguide loss using a Fabry-Perot interference technique", *Proc. ECIO '85* pp.140-143.
- [3] E.P. Belserene, "Rhythms of a variable star", *Sky & Telescope*, pp. 288-290, Sept. 1988.

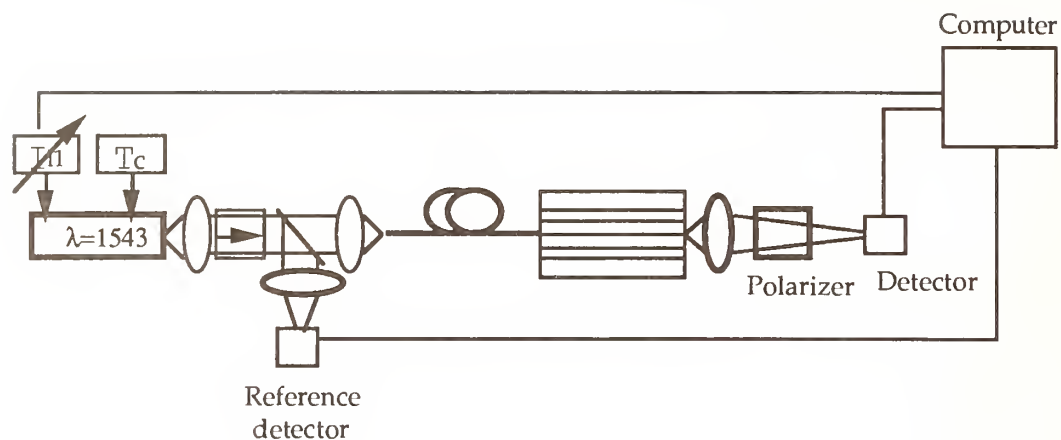


Fig. 1. Schematic of the set-up for Fabry-Perot cavity characterization.

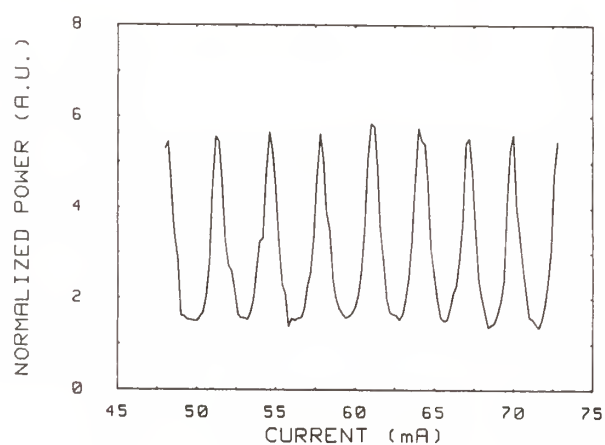


Fig. 2. Cavity transmission characteristic of a $4\mu\text{m}$ wide, 14.842 mm long InGaAsP/InP ridge waveguide; loss value 0.43 dB/cm .

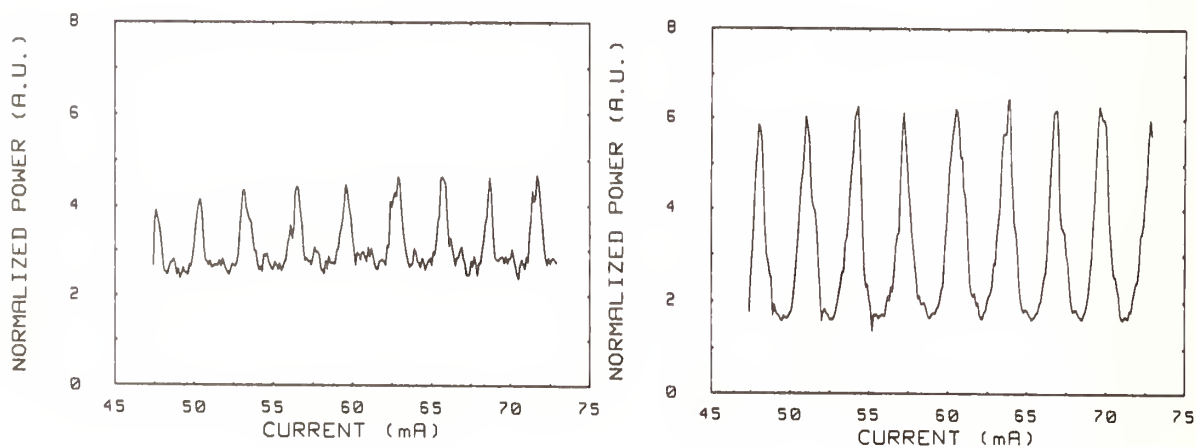


Fig. 3. Cavity transmission characteristics of a $9\mu\text{m}$ wide multimode waveguide: a) different high-order modes excited (secondary peaks); b) fundamental mode predominantly excited (very small secondary peaks).

Measurement of Mode Indices of Channel Waveguides by Interferometry

CHRISTOPHER P. HUSSELL, RAMAKANT SRIVASTAVA, AND RAMU V. RAMASWAMY

Department of Electrical Engineering
University of Florida
Gainesville, FL 32611

An accurate measurement of the difference in the propagation constants of adjacent waveguides is essential in designing several integrated optical devices. For example, tapered velocity couplers [1] or cross couplers [2,3,4] require adiabatic transitions which can be designed only if an accurate knowledge of the mode index of each of the two individual guides is available. Customarily, prism couplers are used for such measurements with accuracies approaching 1×10^{-4} . However, buried waveguides, waveguides of high index materials, and optical fibers are not always amenable to characterization using prism coupler.

In this paper, we demonstrate the use of a Mach-Zehnder interferometer to measure differences in mode indices between adjacent waveguides on a substrate, reproducible to an accuracy of 1×10^{-4} . The technique can also be used to determine the absolute value of the mode index in cases where waveguides near cutoff are available on the same substrate. Other applications include determination of fiber uniformity, waveguide reproducibility, and birefringence.

Fig. 1 is a diagram of the experimental setup used. The samples are planar glass substrates with several identical bands of straight channel waveguides. In each band, the channel width increases monotonically from one side to the other such that those with the smallest width are near cutoff and the ones with the largest width support the fundamental as well as the next higher-order mode. There are always several single mode waveguides in each band. The samples to be measured were cut to a length of

$$L < \frac{\pi}{\Delta\beta} \quad (1)$$

where $\Delta\beta$ is the difference in the propagation constants of two successive waveguides in the band. Usually $\Delta\beta$ can be estimated a priori allowing a reasonable guess for L . The system is aligned such that the desired guided mode of a single channel is dominantly excited and a vertical fringe pattern appears on the video camera. This requires interfering the defocused near field image of the waveguide with the reference beam on the video tube until the two wavefronts have the same curvature. Moreover, since the mode size depends weakly on the channel widths and the modal field is slightly defocused, the fringe spacing does not vary from channel to channel. A sampling oscilloscope is used to scan one

horizontal line of the video signal and the data is transferred to a personal computer. The light is then coupled to the next channel by translating the substrate and the new fringe pattern corresponding to the same mode is recorded in the same manner. Measurements are repeated for the entire band of waveguides. If L is chosen to satisfy Eq. 1, the phase of the fringes will shift in one direction by less than π as the successive guides are excited.

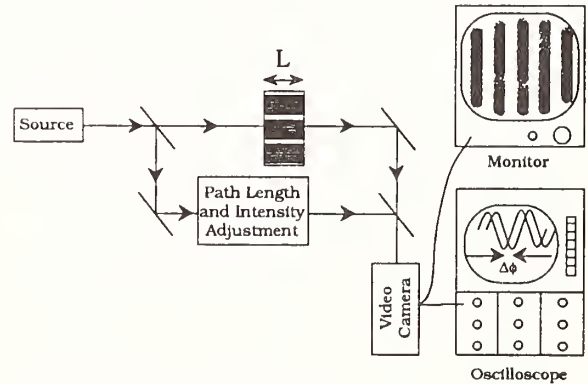


Fig. 1 Experimental arrangement used for interferometric measurements.

Next, the Discrete Fourier Transform (DFT) is used to find the relative values of the phase of each set of fringes. The DFT is defined by

$$X(k) = \frac{1}{M} \sum_{n=0}^{M-1} x(n) e^{-j2\pi kn/M} \quad (2)$$

where $X(k)$ is the discrete frequency domain representation of $x(n)$, $x(n)$ is the sampled waveform, and M is the number of data points. k is an integer which is related to the frequency, f , by $f = k/W$ where W is the window width in time, space, or any other domain over which the sampled segment of data is taken. In our case, $x(n)$ lies in space domain and f has the dimensions of m^{-1} . To simplify the calculation for determining the discrete Fourier component at the fundamental frequency, $X(f_{\text{fund}})$, $f_{\text{fund}} \times W$ must be an integer. This simply means that an integral number of fringes must be taken in the data segment. For our measurements, we chose $k=4$ and $M=256$. Use of such

a large number of data points over several fringes greatly decreases the effect of noise inherent in the video tube.

The relative phase value for the fringe pattern of each waveguide is given by

$$\phi_i = \text{sign}(\text{Im } X(k)) \cos^{-1} \frac{\text{Re } X(k)}{\sqrt{\text{Re } X(k)^2 + \text{Im } X(k)^2}} \Big|_{k=f_{\text{fund}} \times W} \quad (3)$$

where the subscript i identifies the waveguide. These phase values are relative to the initial conditions of the system (ie. path length difference, focus, region of field which is sampled, etc.) and have no meaning by themselves. As long as the initial system conditions are kept constant, the phase shift in the fringe pattern caused by switching from waveguide $i-1$ to i , $\Delta\phi_i$, may be found. Thus, $\Delta\phi_i = \phi_i - \phi_{i-1}$ where ϕ_i and ϕ_{i-1} are the phase values found from the DFT for the two consecutive waveguides which have mask widths of W_i and W_{i-1} respectively. For the waveguides on our substrates $W_i = i/2 + 1$ (μm) and the waveguide nearest to cut off corresponds to $i = 0$. Special care must be taken at the discontinuity at $-\pi$ radians in Eq. 3 to assure proper calculation of $\Delta\phi_i$ from ϕ_i .

If the lengths of the two waveguides are not the same because the polished end faces are not parallel, the phase difference may be corrected by

$$\Delta\phi_i (\text{corrected}) = \Delta\phi_i (\text{measured}) \pm \frac{2\pi}{\lambda} (1 - N_i) \Delta L_i \quad (4)$$

where N_i represents the mode index of the guide i and λ is the source wavelength. In this equation, the substrate index, n_s , may be used in place of the mode index of the i^{th} waveguide since $N_i \approx n_s$.

The phase difference between two consecutive waveguides, then, is given by

$$\Delta\phi_i = \frac{2\pi}{\lambda} (N_i - N_{i-1}) L \quad (5)$$

Fig. 2 shows the results of four separate measurements of the fundamental mode of three bands of $\text{Ag}^+ - \text{Na}^+$ ion-exchanged glass waveguides [5] on the same substrate. At the first glance, the data looks unrecognizably erratic. This is caused by small, low-frequency fluctuations in one or both branches of the interferometer. From Eq. 5, the mode index N_n of the n^{th} guide is given by

$$N_n - n_s = \frac{\lambda}{2\pi L} \sum_{i=1}^n \Delta\phi_i \quad (6)$$

where we have assumed that the mode index of the guide $i = 0$ approaches the substrate index value n_s .

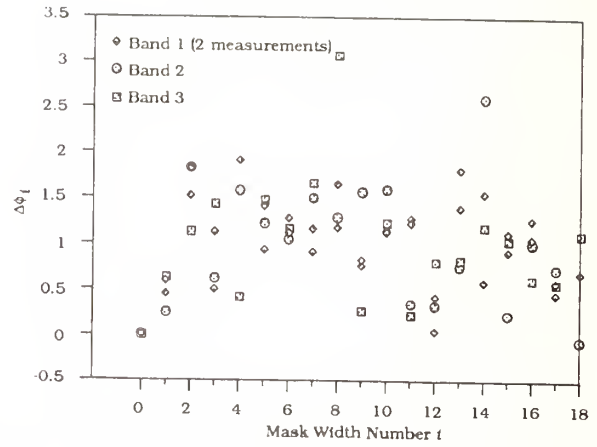


Fig. 2 Measured phase differences in radians between consecutive waveguides.

Fig. 3 presents the results of using Eq. 6 on the data of Fig. 2 along with the data of the first higher-order mode. Note that the errors caused by the low-frequency fluctuations in the interferometer do not add up and the error in each N_n is limited by the maximum phase fluctuation $\Delta\phi_e$ which depends on the stability of the system. Therefore, the error in mode index is determined by the error in relative phase difference $\Delta\phi_e$ by

$$N_e = \Delta\phi_e \frac{\lambda}{2\pi L} \quad (7)$$

Using the data in Fig. 2 for $\lambda = 1.3 \mu\text{m}$ and $L = 2.3 \text{ mm}$ and for the same band of waveguides, we see that in the worst case ($i = 14$) $\Delta\phi_e \sim \pi/3$. This gives an approximate maximum mode index error of $N_e = 1.0 \times 10^{-4}$. This value is comparable to the prism coupler accuracy.

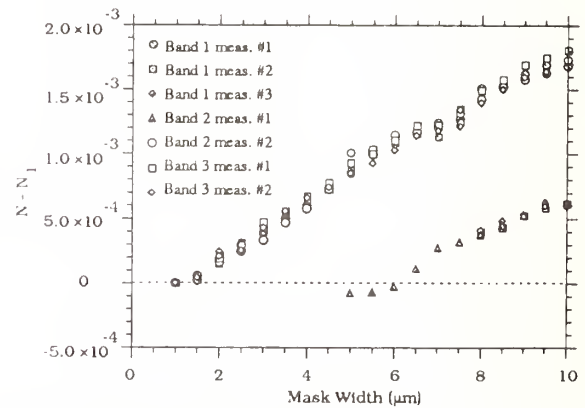


Fig. 3 Mode index values for waveguides of different mask widths.

Fig. 4 shows the comparison between the prism coupler data and the average values of the

measurements shown in Fig. 3 using the interferometer. Note that there is no significant difference in the mode indices for the two orthogonal polarizations of the guided modes in our waveguides. This is due to negligible birefringence in the $\text{Ag}^+ - \text{Na}^+$ exchanged waveguides. The data from Fig. 3 were shifted up by 2.3×10^{-4} to account for the difference between the substrate index and the mode index of the $1\mu\text{m}$ channel. An excellent agreement between the two is observed for both modes. However, an error is produced in the fundamental mode measurement when the first higher-order mode becomes well guided. This is due to the fact that in our measurement, we did not excite only the fundamental mode and a net fringe shift resulted from the overlap of the fringes of both modes. If, however, only one mode can be exclusively excited at a time, more accurate results within this regime should be obtained. The measurement of the first higher-order mode did not experience such a fringe overlap because the data window was taken from the edge of the fringe pattern where the field due to the first higher-order mode is much larger than that of the fundamental mode.

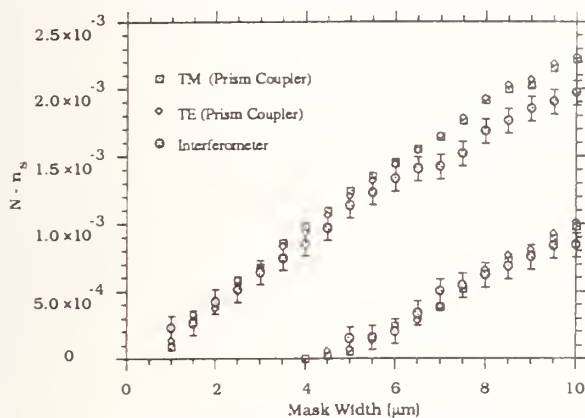


Fig. 4 Comparison between the interferometric and prism coupler techniques.

Unlike the prism coupler, the interferometric technique presented here can be applied to buried waveguides and optical fibers. In the case of fibers, one can monitor the uniformity along the longitudinal direction by embedding successively cut 2-3 mm fiber pieces in silicon grooves and polishing them on both ends. Measurements may be performed in the same fashion as presented above. For birefringence measurements, the guide may be inserted in the interferometer and the fringe pattern recorded for the two orthogonal polarizations (parallel and perpendicular to the substrate plane). In order to obtain mode index differences, only two or more waveguides with similar indices that satisfy Eq. 1 are required. However, to obtain the mode index of an individual waveguide, a series of channels from near-cutoff that satisfy Eq. 1 between each consecutive pair is required. This may be

impossible with fibers, but may generally be obtained with buried waveguides on planar substrates.

In conclusion, we have presented an interferometric technique for measurement of small differences in the propagation constants and birefringence of channel waveguides with an accuracy comparable to that of the prism coupler. Absolute values of the mode index in buried channel waveguides and waveguides of high index materials can also be measured.

We thank Mr. Huo Zhenguang for assistance in waveguide fabrication. Financial support from MICROFABRITECH Program at the University of Florida is also acknowledged.

REFERENCES

- [1] H. Yajima, "Dielectric thin film optical branching waveguide," *Appl. Phys. Lett.*, vol. 22, pp. 647-649, 1973.
- [2] M. Izutsu, A. Enokihara and T. Sueta, "Optical-waveguide hybrid coupler," *Opt. Lett.*, vol. 7, pp. 549-551, 1982.
- [3] Y. Silberberg, P. Perlmutter and J. E. Baran, "Digital optical switch," *Appl. Phys. Lett.*, vol. 51, pp. 1230-1232, 1987.
- [4] C. P. Hussell, H. C. Cheng, R. Srivastava, R. V. Ramaswamy, and J. L. Jackel, "Single-mode cross-coupler 3dB power dividers by ion exchange," MOC/GRIN conference, Tokyo, Japan, July 1989.
- [5] H. Zhenguang, R. Srivastava, and R. V. Ramaswamy, "Low-loss small-mode passive waveguides and near-adiabatic tapers in BK7 glass," *J. Lightwave Tech.*, vol. 7, pp. 1590-1596, 1989.

COMPARISON OF TIME AND FREQUENCY DOMAIN MEASUREMENT METHODS FOR HIGH SPEED OPTICAL MODULATORS

W. Charczenko, D.R. Hjelme, and A.R. Mickelson

MIMICAD Center
Department of Electrical & Computer Engineering
University of Colorado
Boulder, Colorado 80309-0425

Introduction:

The development of wideband fiber optical systems has created a need for simple and reliable test methods for high speed optoelectronic components. Time and/or frequency response characteristics of integrated optical modulators are important for determining the modulators contribution to the overall system performance. Practical measurement systems must be concerned with effective measurement bandwidth, signal to noise ratio, linearity, dynamic range, accuracy, and reproducibility. In this paper, after a brief description of the narrowband modulator used in the measurements, we outline and compare four different measurement techniques used in measuring the high frequency modulation characteristics of electro-optic modulators.

Microwave Narrowband Electro-Optical Modulator:

A proton exchange Mach-Zehnder integrated optical modulator with a resonant coplanar waveguide electrode structure is used in comparing the various measurement techniques. An illustration of the modulation scheme is shown in Figure 1. The transfer function relating the modulated output optical signal to the input signal can be written as

$$\langle I_o \rangle = \frac{I_i}{2} \{ 1 + \cos[\Phi_0 + M(\omega_m)\Phi(\omega_m t)] \} \quad (1)$$

where I_i is the input optical signal, $\langle I_o \rangle$ is the time average modulated optical output corresponding to the current output of a square law photodetector, $M(\omega_m)$ is the electro-optical depth of modulation, $\Phi(\omega_m t)$ is the microwave signal applied to the electrodes of the electro-optic modulator, and ω_m is the microwave frequency. The term Φ_0 in expression (1) is the DC optical phase shift that is present either intentionally through an electro-optical bias or optical path length difference, or, unintentionally through the fabrication variations between the two arms of the modulator. In the resonant electrode structure the optical phase bias Φ_0 is only due to the asymmetry in the Mach-Zehnder and cannot be changed. The frequency response of the narrowband electro-optical modulator is as shown in Figure 2.

High Speed Modulator Measurement Techniques:

The goal of the measurement techniques is to extract the frequency response of the optical depth of modulation $M(\omega_m)$. For large applied microwave

signals the modulator response is strongly nonlinear. Therefore, only small signal modulation is used in all of the measurement techniques.

Swept Frequency Method[1]

A block diagram of the swept frequency technique is as shown in Figure 3. In the swept frequency measurement technique, the microwave signal is amplitude modulated prior to application to the electro-optic modulator such that

$$\Phi(\omega_m t) = [1 + \sin(\omega_{IF} t)] \sin(\omega_m t) \quad . \quad (2)$$

Using a low speed photodetector the output of the modulator can be written as

$$I(t) \equiv I_i \left\{ \frac{1}{2}(1 + \cos \Phi_0 - \sin \Phi_0) + \frac{M^2(\omega_m)}{8}(\cos \Phi_0 - \sin \Phi_0) \sin(\omega_{IF} t) \right\}. \quad (3)$$

The main advantage in this technique is in that the bandwidth of the photodetector and the subsequent receiver need only be higher than the frequency of the IF envelope of the microwave signal and not the microwave frequency of the carrier itself.

Subpicosecond Optical Sampling Method [2]

A block diagram of the subpicosecond optical sampling technique is given in Figure 4. Optical pulses from a Nd:YAG laser are frequency doubled and compressed in a dual jet gain/absorption dye system resulting in a 76 MHz pulse train of subpicosecond pulses. The convolution of the optical pulse train with the system response of the modulator results in a modulation spectrum that is downconverted and centered around a baseband frequency. The output signal from the detector corresponding to the first two harmonics can be written as

$$I(t) \equiv I_i \left\{ \frac{1}{2}(1 + \cos \Phi_0 - \sin \Phi_0) - \frac{M(\omega_m)}{2} \sin \Phi_0 \sin(\Delta \omega t) + \frac{M^2(\omega_m)}{8} \cos \Phi_0 \cos(2\Delta \omega t) \right\}, \quad (4)$$

where $\Delta \omega$ is the difference frequency between a multiple of the pulse train repetition rate (76 MHz) and microwave signal (ω_m).

Optical Heterodyne Measurement Technique [3]

The optical heterodyne (also known as two tone) method uses two ND:YAG lasers as is illustrated in Figure 5. The optical signal from one laser is modulated by the electro-optic modulator and mixed with the reference signal (local oscillator) from the other laser in a photodetector such that

$$I(t) \equiv I_i \cos^2 \left(\frac{\Phi_0}{2} \right) + I_{l0} + \frac{M(\omega_m) \sqrt{I_i I_{l0}}}{2} \cos(\Delta \omega t + \Phi_0) \quad , \quad (5)$$

where I_{l0} is the optical intensity of the second laser used as a frequency shifted $\Delta \omega$ local oscillator.

Fabry-Perot Optical Spectrum Analyzer Method [4]

A Fabry-Perot cavity can be used as an optical spectrum analyzer as is shown in Figure 6. In this technique a CW laser diode source is directly applied to the device being tested while a sinusoidal microwave frequency is applied to the electrode structure. As the length of the Fabry-Perot is changed, the output intensity of the signal corresponds to the frequency spectrum of the modulated optical signal given as

$$I(\omega) \cong I_i \left\{ \cos^2\left(\frac{\Phi_0}{2}\right) \delta(\omega) + \frac{M^2(\omega_m)}{16} [\delta(\omega - \omega_m) + \delta(\omega + \omega_m)] \right\}. \quad (6)$$

Discussions and Conclusions:

In comparing the sensitivity of the above techniques, the optical depth of modulation shows up as a linear term in the output of the sampling and heterodyne techniques and as a quadratic term in the outputs of the swept frequency and Fabry-Perot techniques. Therefore, the sampling and heterodyne techniques are more sensitive than swept frequency and Fabry-Perot techniques. The heterodyne system with its use of the second laser as a local oscillator is the most sensitive of the measurement techniques. However, the heterodyne measurement technique is not able to separate the phase bias component from the depth of modulation. The optical sampling technique, while not as sensitive as the heterodyne method can extract both the optical depth of modulation and phase bias by measuring the amplitudes of the $\Delta\omega$ and $2\Delta\omega$ frequency components.

In general the Fabry-Perot and swept frequency techniques, with their dependence on $M^2(\omega_m)$, can be thought of as direct detection systems which are not as sensitive as the heterodyne and sampling techniques. Also, the accuracy of the swept frequency technique is dependent on the amount of optical bias Φ_0 . At the symposium, measurements using optical sampling and Fabry-Perot techniques will be presented and compared to the swept frequency results of the narrowband modulator given in Figure 2.

References:

- [1] S. Uehara, "Calibration of optical modulator frequency response with application to signal level control," *Appl. Opt.*, **17**(1), pp. 68-71, (Jan. 1978).
- [2] R.C. Alfemess, N.P. Economou, and L.L. Buhl, "Picosecond optical sampling technique for measuring the speed of fast electro-optic switch/modulators," *Appl. Phys. Lett.*, **37**(7), pp. 597-599, (Oct. 1980).
- [3] T.S. Tan, R.L. Jungerman, and S.S. Elliott, "Calibration of optical receivers and modulators using an optical heterodyne technique," *IEEE MTT-S Digest Vol. II*, Paper OO-2, pp. 1067-1070, New York, (May 25-27, 1988).
- [4] M. Izutsu, Y. Yamane, and T. Sueta, "Broad-band traveling-wave modulator using a LiNbO₃ optical waveguide," *IEEE J. Quantum Electron.*, **QE-13**(4), pp. 287-290, (April 1977).

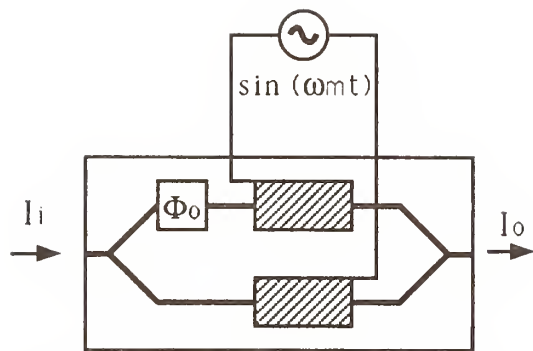


Figure 1: Mach-Zehnder modulator

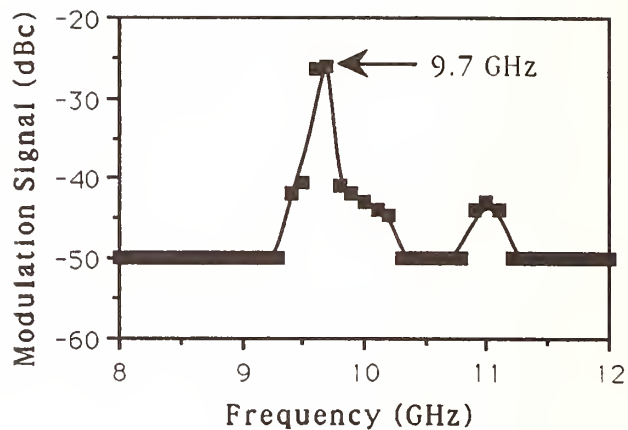


Figure 2: Swept Frequency Modulator Response

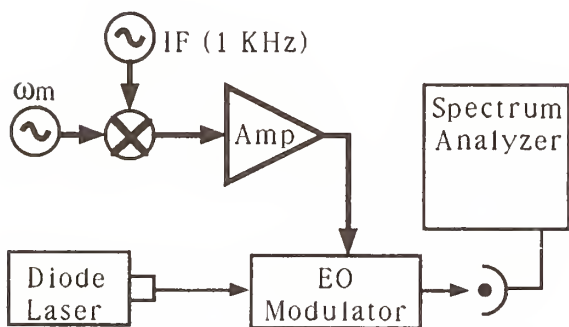


Figure 3: Swept frequency technique

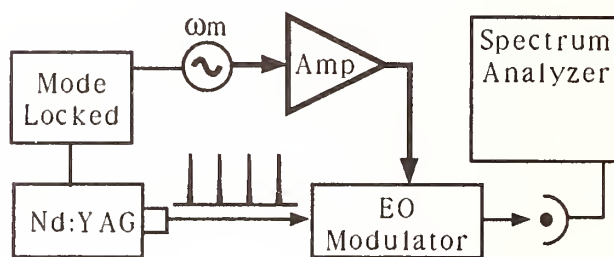


Figure 4: Subpicosecond sampling technique

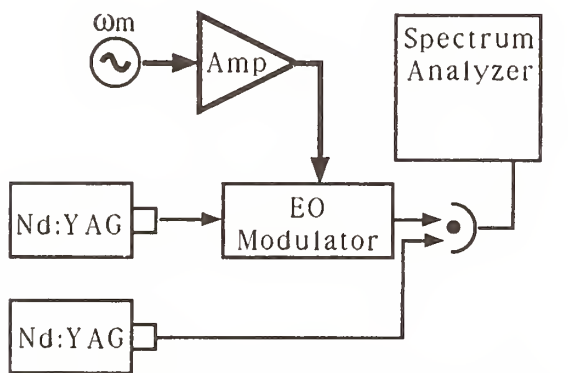


Figure 5: Optical heterodyne technique

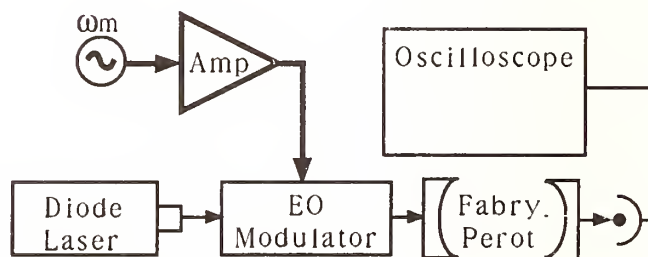


Figure 6: Fabry-Perot optical spectrum analyzer

CHARACTERIZATION OF THE DYNAMIC RESPONSE OF A WAVEGUIDE PHASE MODULATOR BY MEANS OF AN OPTICAL FREQUENCY DISCRIMINATOR

N. Caponio, P. Gambini, M. Puleo

CSELT – Centro Studi E Laboratori Telecomunicazioni S.p.A.
Via G. Reiss Romoli, 274 – 10148 Torino – Italy

Abstract

A simple method for the characterization of the frequency response of high speed waveguide phase modulators is proposed and demonstrated. The method, which is based on the use of a Fabry-Perot interferometer as an optical frequency discriminator, allows a fast and accurate evaluation of the dynamic performance of the device under test.

1. Introduction

Coherent lightwave transmission systems are gaining increasing interest in research laboratories due to their higher sensitivity, with respect to direct detection systems, and intrinsic wavelength selectivity, which allows the implementation of the so called Optical Frequency Division Multiplexed (OFDM) networks. Among possible modulation formats, PSK (Phase Shift Keying) and DPSK (Differential PSK) seem to be good candidates due to their high inherent sensitivity and spectral compactness. To attain the required phase modulation of the optical carrier, a LiNbO₃ waveguide modulator is usually employed. An accurate knowledge of the frequency response of the device is mandatory, particularly for high bit-rate applications, to optimize the system performance. In this paper we present a novel (at least to our knowledge) measurement technique which allows an accurate and simple characterization of the frequency response of high speed waveguide phase modulators.

2. Measurement principle

The optical field of the lightwave carrier undergoing phase modulation can be written as:

$$E(t) = E_0 \cos[2\pi f_c t + \phi(t)] \quad (1)$$

where f_c is the optical carrier frequency ($f_c \approx 200$ THz for a $1.5 \mu\text{m}$ source) and $\phi(t)$ is the phase modulation introduced by the device. Characteristic of the phase modulator is the relationship between the phase introduced and the applied voltage and its capability to follow fast changes of the driving voltage. If a sinusoidal voltage is applied, $\phi(t)$ changes with time according to the law:

$$\phi(t) = \beta \sin(2\pi f_m t) \quad (2)$$

where β is the modulation index (the maximum phase deviation) and f_m is the modulation frequency [1]. The resulting optical spectrum is composed by the carrier and a number of sidebands, spaced by the modulation frequency and with power content proportional to $J_n^2(\beta)$ (i.e. the square of the Bessel function of order n , the order of the sideband). The analysis of the modulated spectrum at several frequencies allows the frequency response characterization of the phase modulator by measuring the relative magnitude of the sidebands with respect to the carrier, once the peak to peak voltage (V_{pp}) applied to the device is known. This method easily permits to obtain the V_π voltage, i.e. the voltage required for a phase shift of π as a function of modulation frequency according to: $V_\pi = \pi V_{pp}/(2\beta)$;

this has been done in [2], but requires a rather long measurement time to fully investigate the frequency behaviour.

Due to sinusoidal phase modulation, the instantaneous frequency deviation from f_c is sinusoidal in time, too, with a maximum deviation given by:

$$\Delta f = f_m \beta \quad (3)$$

Therefore it is possible to obtain the phase deviation, β , by measuring the frequency deviation Δf as a function of the modulating frequency f_m , and dividing it by f_m :

$$\beta(f_m) = \frac{\Delta f(f_m)}{f_m} \quad (4)$$

The frequency deviation $\Delta f(f_m)$ can be obtained by using a Fabry-Perot interferometer as an optical frequency discriminator, and detecting the frequency-to-amplitude converted signal by means of a photodiode. A Network Analyzer (N.A.) is used to sinusoidally modulate the phase modulator and to synchronously detect the frequency-to-amplitude converted signal, as shown in fig. 1. The measurement procedure is similar to the one that is used to characterize the frequency modulation (FM) response of single frequency laser diodes [3]. The use of a N.A. allows to carry out a high resolution measurement (several hundred frequency values) in a few seconds.

3. Measurement set-up and experimental results

With reference to fig. 1, the measurement set-up is organized as follows: the CW emission of a single mode and narrow linewidth source (a 1.54 μm DFB laser diode) is coupled to the phase modulator through a polarization maintaining (PM) fiber. An optical isolator ensures that no backreflections disturb the laser emission. The RF signal (up to 3 GHz) from the output port of an HP8753 Network Analyzer is amplified and fed to the phase modulator. The phase modulator output is coupled to a PM fiber; the light is collimated and sent through a plane mirror Fabry-Perot interferometer (F.P.), having a free spectral range of ≈ 600 GHz and a finesse of ≈ 30 . The transmission resonance of the Fabry-Perot is fine tuned by adjusting (with piezo-electric transducers) the F.P. length, such that the optical carrier frequency, f_c , is set to the middle of one flank of the F.P. transmission curve, where the maximum frequency-to-amplitude conversion linearity can be obtained. The useful frequency deviation range and frequency response extend up to several GHz [3]. The frequency-to-amplitude converted optical signal is detected by a wide bandwidth PIN photodiode and sent to the input port of the N.A.. The frequency response of the PIN has been proved to be much higher than the present upper frequency limit of the measurement set-up in a separate test. A sweep of the N.A. provides $\Delta f(f_m)$; to obtain the phase modulation efficiency (in rad/V) two further steps are required: the division of $\Delta f(f_m)$ by f_m , which is readily performed by a computer, and the scaling of the measured response; this latter is performed by observing the optical spectrum (with a scanning confocal Fabry-Perot interferometer) at one fixed modulation frequency (usually 1 GHz) thus obtaining the phase modulation efficiency $\Delta\phi/\Delta V|_{f_m=1 \text{ GHz}}$; all other acquired points are then correspondingly scaled.

As the modulating RF power is kept constant during the sweep, the frequency deviation tends to vanish at very low frequencies. This results in conflicting effects: on one hand the presence of noise prevents from carrying out a correct measurement at these frequencies; on the other hand, as the result of the measurement must tend to zero with frequency, it is possible to know and then to subtract the noise contribution, imposing that the result be zero at zero frequency. It should be noted that the low frequency characterization may be quite difficult also with the measurement technique used in [2], unless a very narrow linewidth source (and high resolution spectrum analyzer) is used, as the tails of the carrier and sidebands tend to overlap preventing the correct evaluation of their magnitude.

Another very interesting feature of our measurement technique is given by the possibility of getting rid of spurious amplitude modulation which can be caused by an unwanted phase-to-amplitude modulation conversion by spurious Fabry-Perot cavities in the measurement set-up or especially by the LiNbO₃ chip itself. This spurious effect causes a skewness in the optical spectrum hindering an accurate conventional measurement. On the other hand, as described in [3], an optical frequency discriminator allows to perform two measurements, on the two flanks of the F.P. transmission curve: taking the difference between the two results, the undesired term cancels out while the true frequency (or phase)-to-amplitude converted signal is doubled (the two frequency modulation contributions have opposite sign, due to the opposite slope of the F.P. flanks, while the spurious amplitude modulation, that does not undergo conversion, has the same sign, cancelling out).

Figure 2 shows the result of a measurement performed on a commercial 1.55 μm LiNbO₃ phase modulator. The continuous curve is the frequency response as measured with the optical frequency discriminator, while the crosses represent the response as measured observing the sideband amplitudes in the optical spectrum. The two measurements are in very good agreement, showing a phase modulation efficiency of about 0.3 rad/V at low frequency and a bandwidth of about 2.5 GHz. The usefulness of performing a measurement over several hundred frequencies is stressed in fig. 3; a ripple in the frequency response, due to the poor impedance matching of the device, connected to the driver by a relatively long coaxial cable (not present in the previous measurement), is clearly visible. The limited number of points resulting, for practical reasons, from conventional measurement techniques, would not have allowed to evidence this effect.

4. Conclusions

A measurement set-up for the characterization of the dynamic response of integrated optics phase modulators has been developed. The method, which relies on a Fabry-Perot interferometer used as an optical frequency discriminator, allows a simple, accurate and fast evaluation of the frequency response of the device under test. The present upper frequency limit is 3 GHz, and is due to the Network Analyzer; the method can be easily extended to higher modulation frequencies, possibly making use of a different type of optical frequency discriminator, having a larger frequency range, like a piece of high birefringence fiber followed by a polarization analyzer [4]. The dynamic characterization of a commercial 1.55 μm LiNbO₃ phase modulator has been performed, thus demonstrating the feasibility of the proposed measurement technique. The usefulness of a high resolution measurement was clearly pointed out by showing a pronounced ripple in the frequency response due to the poor impedance matching of the device.

References

- [1] H. Taub and D. L. Schilling, *Principles of Communication Systems*. New York: Mc Graw-Hill Book Company, 1986, chapter 4.
- [2] R. E. Tench, *et al.*, "Performance evaluation of waveguide phase modulators for coherent systems at 1.3 and 1.5 μm ," *Journal of Lightwave Technology*, vol. LT-5, pp. 492-501, April 1987.
- [3] P. Gambini, N. P. Caponio, M. Puleo, and E. Vezzoni, "Accurate measurement of the FM response in magnitude and phase of different DFB laser structures," in *SPIE OE/FIBERS*, (Boston), vol. 1175, pp. 12-23, September 1989.
- [4] R. S. Vodhanel and S. Tsuji, "12 GHz FM bandwidth for a 1530 nm DFB laser," *Electronics Letters*, vol. 24, pp. 1359-1361, October 1988.

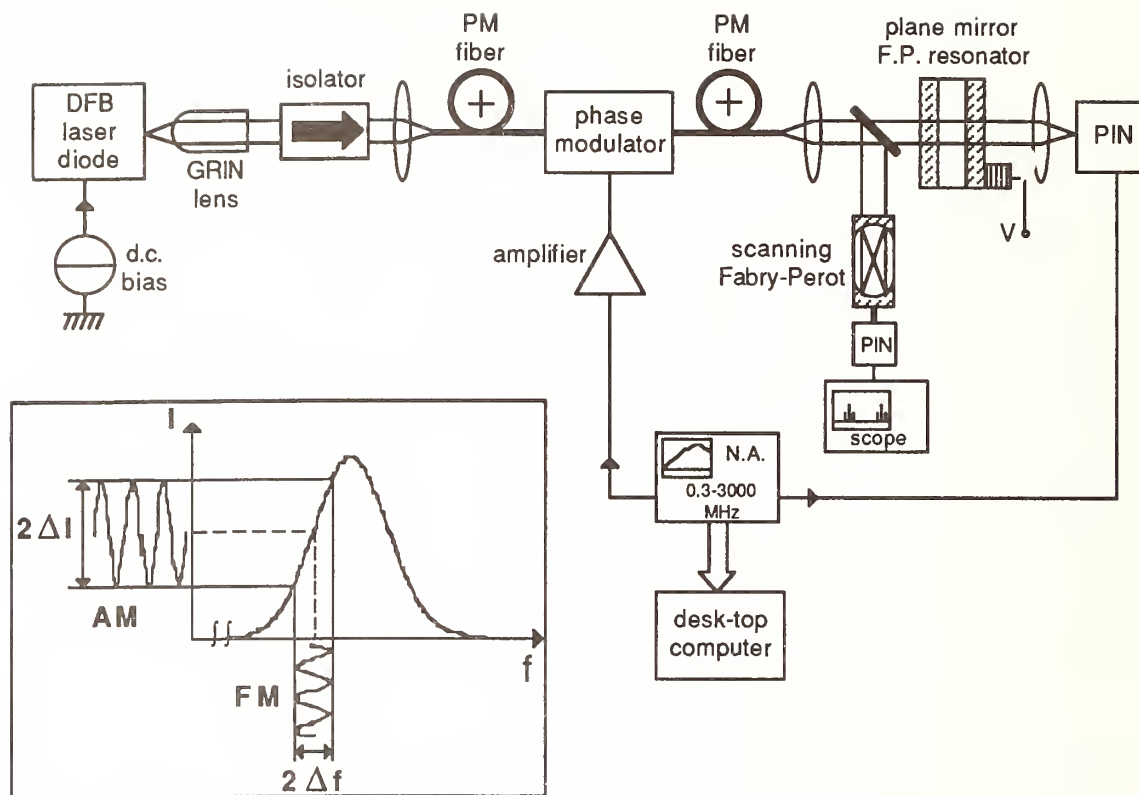


Fig. 1 – Schematic of the experimental set-up used for the phase modulator characterization. The inset shows the principle of the FM to AM conversion performed by the Fabry-Perot interferometer.

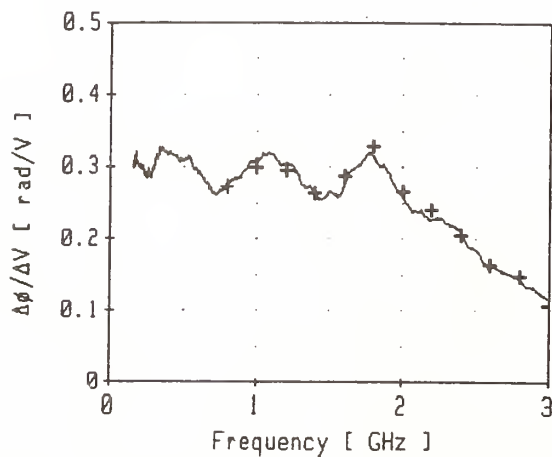


Fig. 2 – Frequency response of a waveguide phase modulator. Proposed measurement technique (optical frequency discriminator): continuous curve. Conventional technique: crosses.

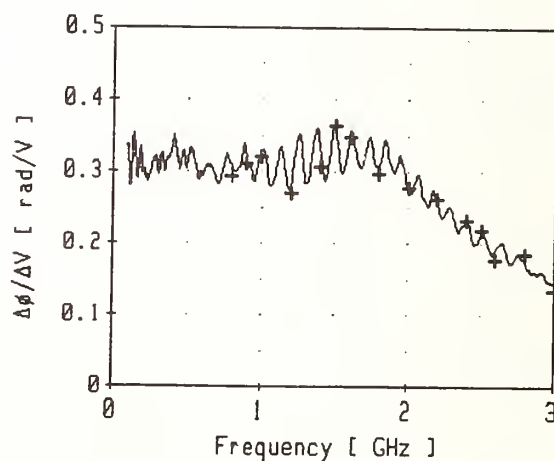


Fig. 3 – Same as fig. 2, except for the presence of a 1 m long coaxial cable between the driver and the phase modulator: the high resolution of the proposed technique is evidenced.

Fiber Discriminator Measurements of Phase Modulation in an Integrated Mach-Zehnder Intensity Modulator

Kok Wai Chang¹, Geraldine Conrad² and Wayne V. Sorin¹

¹ Hewlett-Packard Laboratories, Palo Alto, Ca 94303

² Network Measurements Division, Hewlett-Packard Company, Santa Rosa , Ca 95401

Summary

A fiber-optic Mach-Zehnder delay-line discriminator¹ can be used to measure small amounts of residual phase modulation impressed on amplitude modulated optical signals. This paper presents two separate methods that were used to measure residual phase modulation at the output of a LiNbO₃ Mach-Zehnder intensity modulator.

The delay-line discriminator used in this work was a single mode fiber Mach-Zehnder interferometer which could be locked at the quadrature point of its sinusoidal transfer function by feeding the appropriate control voltage to a cylindrical piezoelectric stretcher in one of its arms. When biased at this point, phase or frequency fluctuations of an input optical signal are converted to intensity fluctuations which may be detected at either of the discriminator outputs.

In these experiments, the test signal was the output of an integrated LiNbO₃ intensity modulator having a push-pull electrode configuration. Ideally, the output of such a modulator should only contain pure amplitude modulation sidebands. In practice, however, a small amount of phase modulation is superimposed on top of the amplitude modulated output, due to unequal phase shifts in each arm of the interferometer, or due to unequal power splitting/combining at the Y-junctions. It is this residual phase modulation that can be measured using either of the two methods described in this paper.

Fig.1 shows the first experimental arrangement used to measure the phase modulation component of the LiNbO₃ modulator output. In this case, the modulator was part of the lightwave test set of a commercially available lightwave component analyzer (HP8703A).² This method consists of two separate measurements made with different bias conditions on the modulator. With the discriminator locked in quadrature, the modulator is itself biased at quadrature and its output is measured and analyzed. At the quadrature bias point, the output optical signal consists of a strong AM and a weak PM component. The measured frequency response is dominated by the AM component which has a frequency dependence proportional to $mP_0|\cos(\pi f_m \tau)|$, where m is the intensity modulation index, f_m is the modulation frequency, P_0 is the average optical power, and τ is the differential delay between the two arms of the fiber interferometer.

When the bias point of the modulator is adjusted to maximize the output power, no intensity modulation is produced at the fundamental modulation frequency f_m (although a small amount of second harmonic is present). However, any phase modulation at f_m , will be converted to intensity modulation at the fundamental modulation frequency f_m , due to the PM to AM conversion of the fiber delay-line discriminator. Since the component

analyzer only measures the response at the modulation frequency, it will only measure the PM to AM conversion caused by the delay-line discriminator, which is proportional to $2\beta P_0 |\sin(\pi f_m \tau)|$, where 2β is the phase modulation index.

Fig. 2 shows the measured frequency responses of the above two measurements. The ratio of the peak PM to AM is $R_{PM-AM} = \frac{2\beta}{m} = 10^{-\frac{11.0}{10}} = 0.079$. Independent measurement of the AM modulation index was found to be $m = 0.25$. The residual phase modulation index 2β of the intensity modulator is then calculated to be 0.02 rad.

Although the above measurement method provides a good estimation of the residual PM in the LiNbO₃ Mach-Zehnder intensity modulator, one has to make an assumption that the PM response of the modulator is independent of its DC bias (the phase modulation index 2β is not measured at its normal operating point). Therefore, a second measurement method is developed with the bias condition of the modulator fixed at its normal operating point (i.e. quadrature). The large AM term and the small PM term are measured by taking two separate frequency response measurements with the fiber delay-line discriminator locked at quadrature phase on opposite slopes of its sinusoidal transfer curve ³ (see Fig. 3) . This function is accomplished by changing the polarity of the applied voltage to the piezoelectric fiber stretcher.

From the theoretical analysis of the fiber delay-line interferometer locked at phase quadrature, the frequency response of the output optical signal consists of the filtered AM and PM terms. Changing the locking slope causes the PM term to change phase by 180 degrees. Therefore, the summation of the frequency responses of the above two measurements contains only the AM term with the PM term being removed , and the difference consists of only the PM term with the AM term being removed. As shown in Fig. 4, the response of the AM term has a frequency dependence proportional to $2P_0 m |\cos(\pi f_m \tau)|$ (upper curve), and the PM term has a frequency dependence proportional to $4P_0 \beta |\sin(\pi f_m \tau)|(1 + \epsilon)$ (lower curve), where $\epsilon = -\frac{1}{16}m^2(1 - \sin(\omega_m \tau)) + 0.05m^4$ is the amount of fractional error correction due to the presence of the intensity modulation⁴. This fractional error ϵ is very small even for large intensity modulation. For example, the value of ϵ in the cross product term is $\leq 5\%$ for a intensity modulation index of $m \leq 0.63$.

From the ratio of the PM response to AM response (R_{PM-AM}) obtained from the above calculations and the known modulation index m , the amount of PM in the LiNbO₃ balanced intensity modulator is obtained. This measurement gives $2\beta = 0.022$ rad which agrees within experimental error with measurements made using the first method.

In summary, two methods, both using a fiber optic FM delay-line discriminator , were successfully used to measure the amount of residual phase modulation at the output of a balanced LiNbO₃ Mach-Zehnder intensity modulator. These techniques represent new and unique tools for the precise measurement of modulation characteristics of optical signals.

References:

1. K.J. Williams, A. Dandridge, A.D. Kersey, J.F. Weller, A.M. Yurek, and A.B. Tveten, 'Interferometric measurement of low-frequency phase noise characteristics of diode laser-pumped Nd:YAG ring laser ', Electronics letters , Vol. 25, No.12, pp. 774-775, 1989.

2. P. Hernday, R. Wong, and R.L. Jungerman, '20-GHz lightwave component analysis instrumentation using an integrated optical modulator ', Technical Digest, Vol. 1, OFC, pp. 125, 1990.
3. R.S. Vodhanel, 'Optoelectronic and integrated-optic devices and components ', Technical Digest, Vol. 1, OFC, pp.114, 1989.
4. W.V. Sorin, K.W. Chang, G. Conrad, and P. Hernday, 'Frequency domain analysis of an optical FM discriminator ', to be published.

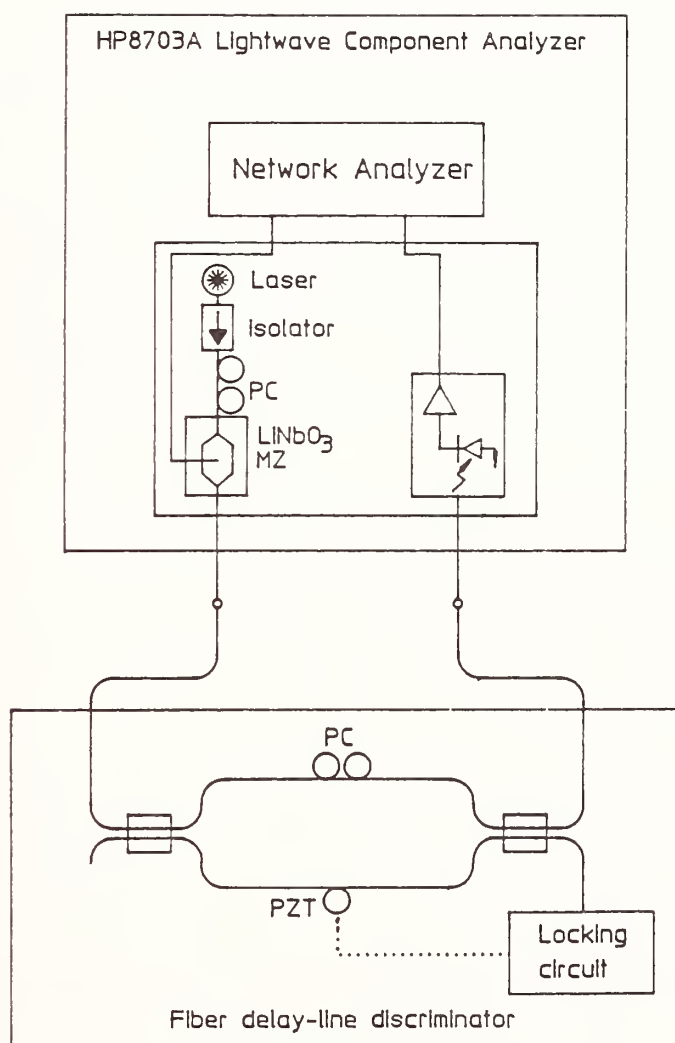


Fig. 1: Measurement arrangement showing the HP8703A lightwave test set with LiNbO₃ intensity modulator, receiver and the fiber delay-line discriminator.



Fig. 2: Frequency response of the AM and PM modulation of the LiNbO₃ Mach-Zehnder interferometer biased at quadrature (upper curve) and maximum output (lower curve).

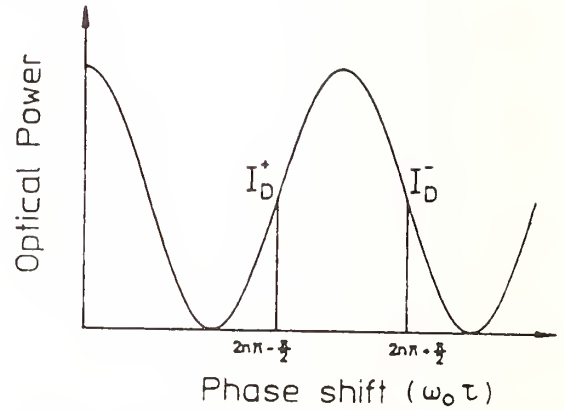


Fig. 3: Locking the fiber delay-line discriminator on its opposite slopes ($\omega_0\tau = 2n\pi \pm \frac{\pi}{2}$).

$$I_D^+ = \text{AM} + \text{PM} \text{ (locked on positive slope)}$$

$$I_D^- = \text{AM} - \text{PM} \text{ (locked on negative slope)}$$

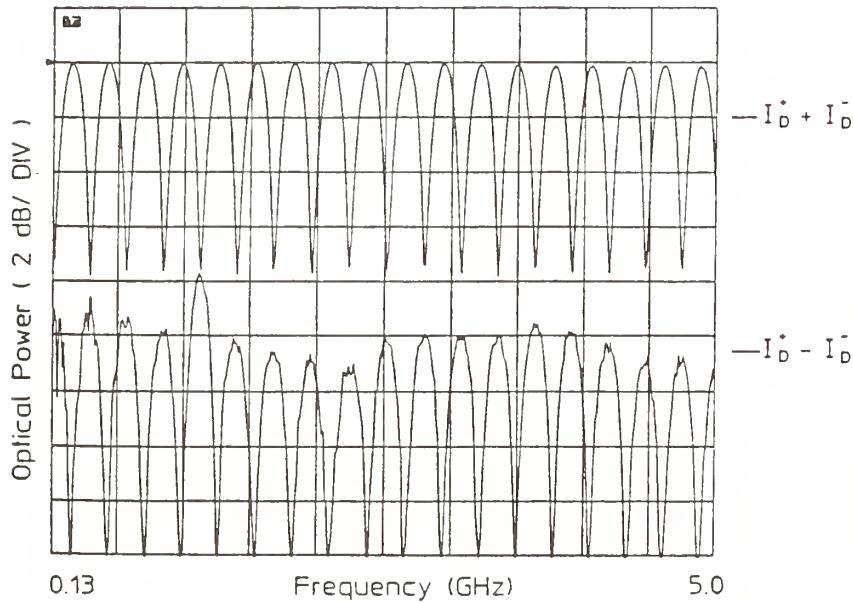


Fig. 4: The summation and the difference of the two frequency responses measured by locking the fiber delay-line discriminator on its opposite slopes at phase quadrature.

CHARACTERISATION OF ERBIUM-DOPED FIBRE AMPLIFIERS
R.I. LAMING
OPTOELECTRONICS RESEARCH CENTRE, THE UNIVERSITY, SOUTHAMPTON,
S09 5NH, UNITED KINGDOM

ABSTRACT

Experimental techniques necessary to characterise, and thus to optimise the design of both erbium-doped fibres and erbium fibre amplifiers are described.

I INTRODUCTION

Erbium-doped fibre amplifiers (EDFA) have recently attracted considerable attention in the field of optical fibre communications since they conveniently operate in the preferred telecommunications spectral-window located around $1.55\mu\text{m}^{1-7}$. It has been demonstrated that an EDFA can be optically pumped at a number of wavelengths (514nm^2 , 532nm^3 , 665nm^1 , 800nm^8 , $980\text{nm}^{3,4,9}$ and $1.49\mu\text{m}^{5,10,11}$), with high-gain¹⁰, efficient diode-pumped operation being demonstrated at pump wavelengths of $980\text{nm}^{4,9}$ and $1.49\mu\text{m}^{5,10}$. In addition the EDFA has been shown to exhibit polarisation-insensitive gain, low crosstalk¹²⁻¹⁶ between signals at different wavelengths, a high saturation output power and noise figure close to the quantum limit¹⁷⁻²⁰. A variety of host glasses and fibre designs are being investigated with a view to optimising amplifier characteristics such as pump efficiency or spectral bandwidth^{21,22}.

Measurement of a wide range of parameters of erbium-doped fibre are described. From these amplifier performance may be inferred. Subsequent techniques for detailed analysis of EDFA performance are presented.

II FIBRE CHARACTERISATION

A. **Spectral Absorption.** Measurement of spectral loss in Er^{3+} -doped fibres is complicated by the intense absorption caused by electronic transitions in the ions, combined with losses approaching those of telecommunications fibres away from the bands²³⁻²⁵. A typical spectrum is shown in Figure 1 for a fibre doped with around 300ppm Er^{3+} ($\lambda_c \approx 1250\text{nm}$). Intense bands (60,000dB/km) are recorded adjacent to a baseline loss of 7dB/km. A multiple cutback technique²³ of high spectral resolution is employed to determine loss peaks. For very short lengths (<5cm) cladding modes are removed by the photon bucket method²⁶. Average dopant concentrations can be estimated from attenuation plots if the overlap of the optical field with the fibre core is considered.

B. **Excited-State Absorption (ESA).** ESA is the absorption by an already excited ion of additional energy, so reducing amplifier efficiency by wasting signal or pump photons²⁷⁻²⁹. Signal ESA is negligible in Er^{3+} -doped SiO_2 -based fibre²⁹ but pump ESA limits choice of pump sources, and may be quantified by using the configuration²⁷ of Figure 2. Chopped white light is launched into a short section of doped fibre. The throughput is spectrally analysed with the fibre unpumped, and in the presence of counter-propagating pump light. Thus the difference between the ESA and ground-state absorption (GSA) is obtained. A cutback measurement then allows the unpumped loss i.e. GSA to be extracted.

A typical ESA spectrum is shown in Figure 3 for an Er^{3+} -doped $\text{Al}_2\text{O}_3/\text{SiO}_2$ core fibre. It may be seen that ESA extends across the potentially diode pumpable band around 807nm indicating that much of the pump energy will be dissipated non-radiatively. However no ESA is observed on the 980nm transition, emphasising the importance of ESA measurements for identification of ideal pump bands. The ratio of ESA and GSA cross-sections, $\sigma_{\text{ESA}}/\sigma_{\text{GSA}}$ at any wavelength indicates the degree of pump ESA and is listed in Table 1 for several host glasses.

C. **Fluorescence Measurements.** Emission spectra and decay time data allow the estimation of emission cross-section for the fibre under test^{24,30-34}. Hence information on the gain profile and eventual amplifier efficiency is obtained³⁵.

C1. **Spectral Characteristics.** A typical fluorescence measurement configuration is shown in Figure 4. In the three-level Er^{3+} system both pump wavelength and fibre length are important. In-band pumping (1490nm) is avoided since residual pump energy will mask the weak fluorescence. Further, both amplified spontaneous emission (ASE) and reabsorption distorts the output³⁴, however their effect is reduced by monitoring side-light emission or by employing a

short length of fibre such that stimulated emission and absorption are negligible (<0.1dB loss). Fluorescence spectra for two Er³⁺-doped fibres of different core glasses are shown in Figure 5, where the host is seen to alter the spectral profile. Identification of the Stark splitting responsible for the irregular profile can be obtained from fluorescence line-narrowing data³⁶. Note also the broad bandwidth (>200nm) of the emission, thus the measurement system must be carefully calibrated.

C2. Time-Dependent Characteristics. To determine emission decay-time characteristics, the Er³⁺-doped fibre is excited by a pulsed source and the exponential decay in fluorescence emission monitored directly. Short sample lengths are employed to ensure that the stimulated emission rate due to ASE is significantly weaker than the spontaneous rate. Alternatively, if sufficient signal is available, side-scattered light should be measured.

Typical Er³⁺-doped fibres exhibit truly exponential emission decay times, τ_n , of 10-12ms, dependent on host glass. Non-exponential decay is evidence of detrimental effects such as concentration quenching or co-operative upconversion²⁹.

Short initial decay components (<10 μ s) have been observed in clustered fibres²⁹. Ideally these should be resolved by pumping with a pulsed source (<1 μ s), directly into the metastable manifold. This is because long-lived (5 μ s) non-radiative decay from higher energy bands to the metastable level will mask these components for other pump wavelengths.

D. Dopant Distribution. Since erbium is a three-level system, improvements in amplifier performance can be obtained by localising the dopant in regions of high pump intensity^{4,37,38}. This has the effect of maximising the population inversion for a given pump power and thus minimises re-absorption due to unexcited ions. Typical amplifiers, pumped at either 980nm or 1.49 μ m, are designed such that only the fundamental pump and signal modes propagate and thus it can be desirable to localise the dopant in the centre of the fibre core.

A quantitative measure of the dopant concentration and distribution is obtained using either dispersive electron probe microanalysis (EPMA)³⁸, or secondary ion mass spectroscopy (SIMS). For both measurements, the dopant distribution is determined from preform samples or large core fibres owing to the limited resolution (typically 2 μ m) of the measurement systems (see Figure 6). Knowledge of the dopant distribution may then be used to modify the fabrication process and hence optimise the radial dopant profile for device applications³⁸.

E. Saturation Measurements. A qualitative measure of the dopant distribution in the fibre can be obtained by measuring the pump threshold, P_{TH} , the power required to bleach an infinitesimally-short section of fibre. For a given fibre NA and cutoff wavelength, a lower value of P_{TH} implies a higher degree of dopant confinement and a more efficient overlap, η_p , between the pump field and dopant³⁵.

P_{TH} is determined experimentally by monitoring side-scattered fluorescence from a short section of fibre as a function of pump power; the pump wavelengths being chosen to be free from ESA (e.g. 980nm). Figure 7 shows a typical measurement. P_{TH} is defined as the pump power at which the fluorescence attains half its maximum value and can be expressed:

$$P_{TH} = \frac{h\nu_p}{\sigma_p \tau_n} \frac{a}{\eta_p}$$

where $h\nu_p$ is the pump photon energy, a the core area and σ_p the pump absorption cross-section. For fibres of similar core composition, NA and λ_{cutoff} such that σ_p , τ_n and a are constant, P_{TH} gives a qualitative measure of the dopant confinement η_p . Generally, the higher the value of η_p the better the fibre. Alternatively, if the fibre parameters and dopant distribution are known accurately, the overlap parameter η_p can be evaluated numerically and thus the absorption cross-section, σ_p determined from such a measurement³¹.

III. AMPLIFIER CHARACTERISATION

A. Gain Characterisation. A typical configuration for the measurement of amplifier gain is shown in Figure 8. The input signal from a DFB laser, wavelength selected to match the peak gain of the fibre under test, is combined with the pump light via a dichroic coupler and input to the amplifier fibre. At the output the residual pump light is filtered. Direct modulation of the input signal at -20kHz and monitoring of the amplified output with lock-in techniques allows the output signal to be separated from the unmodulated ASE¹². Optical feedback is prevented by angle polishing the fibre ends.

The gain of an EDFA depends on the input signal, pump power and fibre length. Thus it is impossible to design an amplifier which is optimised for all operating conditions. For example, Figure 9 shows the dependence of amplifier output on fibre length for a range of input signals and a constant pump power of 6.2mW. It is clear that the optimum length decreases with increasing input signal. In addition, the optimum length is known to increase with pump power². Thus the intended operating conditions must be considered when characterising an EDFA.

Once the optimum fibre length has been determined the dependence of amplifier gain on input power can be established. Figure 10 shows such curves where the amplifier length is optimised for small signal gain⁴. It is noted that, for these high gain amplifiers, gain compression occurs at low (-35dBm) input signal powers.

The gain per unit pump power³ (dB/mW) is a useful figure of merit for EDFA's, and can be determined from the previous curves. Alternatively, small signal amplifier gain is measured as a function of pump power for a given fibre length (typically equivalent to 50dB signal absorption) and the maximum of their ratio quoted. Care must be taken in interpreting these figures since they depend on fibre parameters such as NA and λ_{cutoff} .

B. Spectral Gain Bandwidth. The gain bandwidth is an important parameter for system design, particularly when several amplifiers are concatenated. However, the EDFA bandwidth is influenced by the method of determination.

The small-signal gain bandwidth is easily determined using either a broadband, low-power ELED as the input and monochromator at the output²², or via a wavelength-scanned tunable laser diode with output attenuated to give a small-signal input (<100nW). However if the large signal spectral gain is determined with a single, large (-100μW) tunable input, a relatively flat gain spectrum is obtained. This is due to the near homogeneous line-broadening in erbium which allows near constant power extraction and thus gain, for a wide range of input signals³⁹. This result would be significantly different if several lasers covering the gain spectrum were employed simultaneously⁴⁰.

C. Homogeneous Linewidth. Knowledge of the homogeneous and inhomogeneous components in the spectral gain profile allows optimisation of the amplifier saturation characteristics and hence the determination of glass host most suited to multichannel operation. Two methods have been employed. First, cross-saturation of the gain from two closely-spaced (-0.75nm) signal wavelengths is monitored at room temperature¹². Alternatively, spectral gain hole burning at reduced temperatures is measured from which the room temperature homogeneous and inhomogeneous linewidths are inferred⁴¹.

D. Phase Noise. Spectral broadening due to phase noise introduced by chained erbium-doped-fibre amplifiers may limit the number of amplifiers which can be concatenated in an optical link. Spectral broadening in an EDFA has been measured using a novel Mach-Zehnder interferometer containing the amplifier in one arm⁴². Provided that the optical paths in the interferometer are matched in length such that the propagation time difference between the light passing through the two arms is much less than the coherence time of the DFB laser source, the technique effectively deconvolves the DFB laser spectrum from the amplifier spectral broadening. The interferometer thus provides an output which consists solely of the amplifier spectral broadening response to a zero-linewidth input spectrum.

A typical measured power spectral density (PSD) is shown in Figure 11. This shows an

approximately Lorentzian lineshape, with a half-power spectral width of less than 20kHz and indicates the signal broadening.

E. Noise Measurements. The output from an optical fibre amplifier is a combination of amplified signal and broad-spectrum ASE. If the input signal is coherent, its noise contribution is the usual shot noise associated with the amplified signal level. There is also a shot noise associated with the level of the ASE. Additional noise terms are introduced by the mixing on the detector of the amplified signal and spectral components of the ASE to give signal-spontaneous (sig-sp) beat noise and spontaneous-spontaneous (sp-sp) beat noise⁴³.

The ASE spectral density of a three-level system and thus the power spectral density (PSD) of both the sig-sp and sp-sp beat noises are a direct function of the amplifier inversion parameter, μ . μ is defined by $N_2/(N_2-N_1)$, where N_1 and N_2 are the population densities of the ground and metastable states respectively. Thus the EDFA noise characteristics depend on pump power and wavelength as well as fibre parameters such as NA and λ_{cutoff} . The PSD of the sig-sp beat noise is proportional to input signal and independent of optical bandwidth, conversely, sp-sp beat-noise is independent of input signal but a direct function of optical bandwidth. Thus for weak input signals and/or a large optical bandwidth, the noise is dominated by sp-sp beat-noise whereas for higher input signals and/or reduced optical bandwidth, sig-sp beat-noise dominates. In the latter the amplifier NF reduces to 2μ , the minimum NF possible being 3dB¹⁷.

Several techniques have been employed to characterise amplifier noise¹⁸⁻²⁰ of which RF spectral analysis of the detected amplifier output is the most widely used^{18,20}. The PSD is recorded for a wide range of input signals allowing identification of the contribution from individual noise components. Thus the amplifier inversion parameter μ and NF are determined¹⁸. Alternative techniques include heterodyne measurement⁴⁴ of the NF or direct optical measurement of the ASE spectral density²⁰.

IV CONCLUSIONS

Key experimental techniques for the characterisation and optimisation of erbium-doped fibres and EDFAs have been outlined.

V ACKNOWLEDGEMENTS

The collaboration of J.E. Townsend, P.R. Morkel, W.L. Barnes, G.J. Cowle, N.J. Payne and D.N. Payne is greatly appreciated. Thanks are also due to Pirelli General plc for the provision of a Senior Research Fellowship.

VI REFERENCES

1. R.J. Mears et al., *Elect. Lett.*, Vol. 23, pp. 1026-1028, 1987.
2. E. Desurvire et al., *Opt. Lett.*, Vol. 12, pp. 888-890, 1987.
3. R.I. Laming et al., *Elect. Lett.*, Vol. 25, pp. 12-14, 1989.
4. R.S. Vodhanel et al., *Elect. Lett.*, Vol. 25, pp. 1386-1387, 1989.
5. M. Nakazawa et al., *Appl. Phys. Lett.*, Vol. 54, pp. 295-297, 1989.
6. N. Edagawa et al., *Proc. ECOC*, Paper PDA-8, Gothenburg, 1989.
7. S. Saito et al., *Proc. OFC*, Paper PD2, San Francisco, 1990.
8. M. Nakazawa et al., *Elect. Lett.*, Vol. 26, pp. 548-549, 1990.
9. M. Yamada et al., *IEEE Photonics Tech. Lett.*, Vol. 1, pp. 422-424, 1989.
10. M. Nakazawa et al., *Elect. Lett.*, Vol. 25, pp. 1656-1657, 1989.
11. E. Desurvire et al., *Opt. Lett.*, Vol. 14, pp. 1266-1268, 1989.
12. R.I. Laming et al., *Elect. Lett.*, Vol. 25, pp. 455-456, 1989.
13. K. Inoue et al., *Elect. Lett.*, Vol. 25, pp. 594-595, 1989.
14. M.J. Pettitt et al., *Elect. Lett.*, Vol. 25, pp. 416-417, 1989.
15. C.R. Giles et al., *Opt. Lett.*, Vol. 14, pp. 880-882, 1989.
16. W.I. Way et al., *Proc. IOOC*, Paper 20PDA-10, Kobe, Japan, 1989.
17. R. Olshansky, *Elect. Lett.*, Vol. 24, pp. 1363-1365, 1988.
18. R.I. Laming & D.N. Payne, "Noise characteristics of erbium-doped fibre amplifier pumped at 980nm", to be published in *IEEE Photonics Tech. Letts.*
19. M.J. Pettitt et al., *Elect. Lett.*, Vol. 25, pp. 273-275, 1989.

20. C.R. Giles et al., IEEE Photonics Tech. Lett., Vol. 11, pp. 367-369, 1989.
21. C.G. Atkins et al., Elect. Lett., Vol. 25, pp. 910-911, 1989.
22. M. Tachibana et al., "Gain-shaped erbium-doped fibre amplifier (EDFA) with broad spectral bandwidth", Proc. Topical Meeting on Optical Amplifiers & their Applications, Monterey, California, 6-8 August 1990.
23. S.B. Poole et al., J. Lightwave Tech., Vol. 4, pp. 870-876, 1986.
24. B.J. Ainslie et al., J. Lightwave Tech., Vol. 16, pp. 287-293, 1988.
25. S.P. Craig-Ryan et al., Elect. Lett., Vol. 26, pp. 185-186, 1990.
26. W.C. Young, in Tech. Digest, Symp. Opt. Fib. Meas., Boulder, Colorado, 1986.
27. R.I. Laming et al., Opt. Lett., Vol. 13, pp. 1084, 1988.
28. C.G. Atkins et al., Opt. Comms., Vol. 73, pp. 217-222, 1989.
29. R. Wyatt, Proc. SPIE Fibre Laser Sources & Amplifiers, Vol. 1171, pp. 54-64, 1989.
30. W.L. Barnes et al., Proc. CLEO, Paper JTua3, Anaheim, California, 1990.
31. W.L. Barnes et al., "Absorption and emission cross-section of Er^{3+} -doped silica fibres", Submitted to IEEE J. Quantum Electron. April 1990.
32. J.N. Sandoe et al., J. Phys. D: Appl. Phys., Vol. 5, pp. 1788-1799, 1972.
33. W.J. Miniscalco et al. Proc. SPIE Fibre Laser Sources & Amplifiers, Vol. 1171, pp. 92-102, 1989.
34. E. Desurvire et al., J. Lightwave Tech., Vol. 7, pp. 835-845, 1989.
35. P.R. Morkel et al., Opt. Lett., pp. 1062-1064, 1989.
36. S. Zemon, Proc. SPIE Fibre Laser Sources & Amplifiers, Vol. 1171, pp. 219-236, 1989.
37. J.R. Armitage, Appl. Opt., Vol. 27, pp. 4831-4835, 1988.
38. B.J. Ainslie et al., Proc. ECOC, Vol. IEE 292, Pt II, pp. 62-65, Brighton, 1988.
39. R.I. Laming et al., "Highly-saturated erbium-doped-fibre power amplifiers", Proc. Topical Meeting on Optical Amplifiers & their Applications, Monterey, California, 6-8 August 1990.
40. W.I. Way, Proc. OFC, Paper PD21, San Francisco, 1990.
41. E. Desurvire et al., Proc. CLEO, Paper CFD2, Anaheim, California, 1990.
42. G.J. Cowle et al., Elect. Lett., Vol. 26, pp. 424-425, 1990.
43. T. Mukai et al., IEEE Trans. Microwave Theory & Tech., Vol. MTT-30, p. 1548, 1982.
44. R.S. Vodhanel et al., Proc. OFC, Paper WL4, San Francisco, 1990.

Fibre type Wavelength (nm)	GeO_2	$\text{GeO}_2/\text{P}_2\text{O}_5$	Al_2O_3
488	2.9	1.86	1.74
514.5	0.95	0.55	0.5
655	0.26	0.13	0.14
810	2.0	1.0	1.0
960			0

Table 1 Ratio of excited-state and ground-state cross-sections $\sigma_{\text{ESA}}/\sigma_{\text{GND}}$ as a function of wavelength.

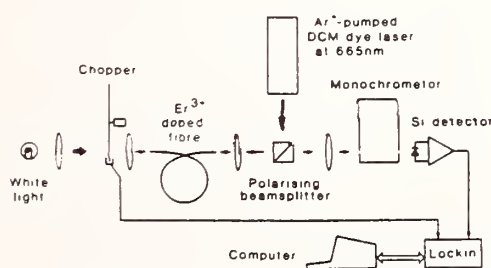


Figure 2 Experimental configuration for the measurement of pump ESA²⁷

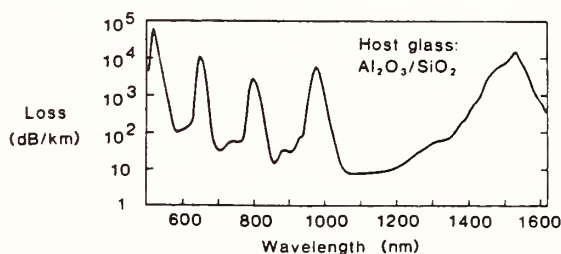


Figure 1 Spectral attenuation of fibre containing around 300ppm Er^{3+}

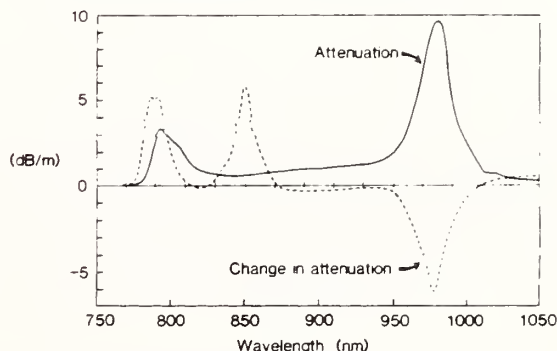


Figure 3 Spectral characteristics of pump ESA in an Er^{3+} -doped fibre with an Al_2O_3 - SiO_2 core²⁷

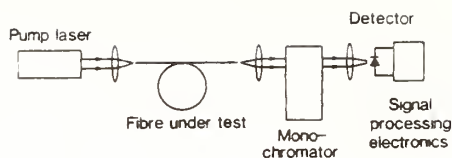


Figure 4 Experimental configuration for measurement of fluorescence²³

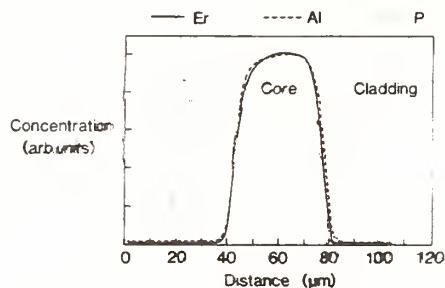


Figure 6 A typical elemental distribution of Er^{3+} , Al and P across an Er^{3+} -doped Al_2O_3 - P_2O_5 - SiO_2 fibre core³⁸

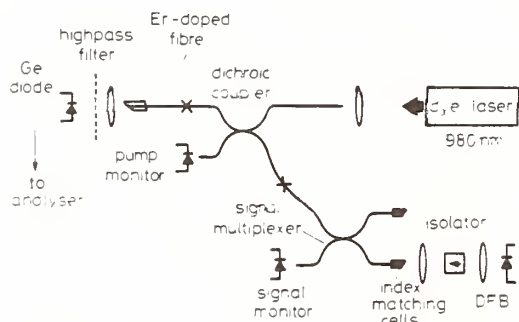


Figure 8 Typical configuration for the measurement of amplifier gain¹²

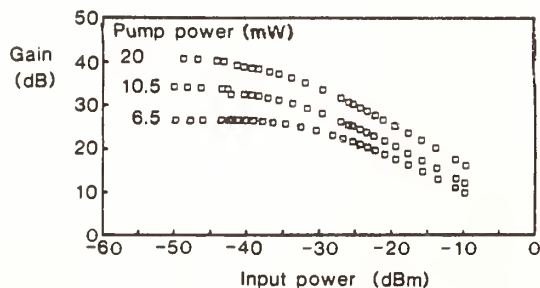


Figure 10 Dependence of amplifier gain on input power⁴. (Germanosilicate erbium-doped fibre, $\text{NA} \approx 0.2$, $\lambda_{\text{cutoff}} \approx 955\text{nm}$, pump power = 6.2mW)

Figure 11 Measured spectral broadening induced by phase noise in an EDFA

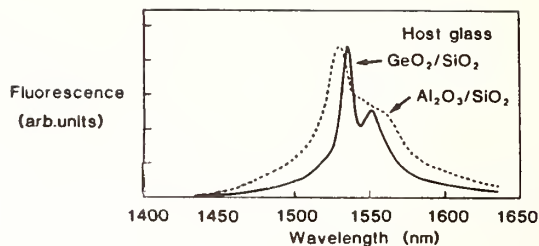


Figure 5 Fluorescence spectra

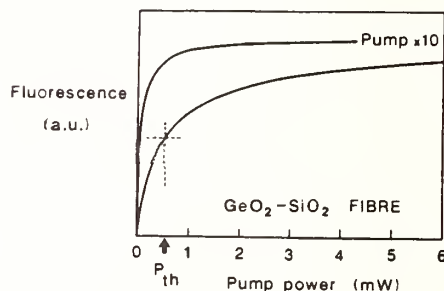


Figure 7 Typical saturation measurement showing the dependence of side-scattered fluorescence on pump power and determination of P_{TH}

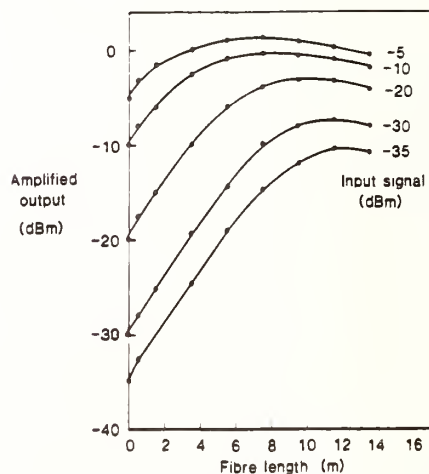
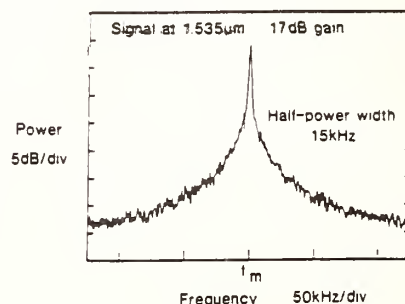


Figure 9 Dependence of amplifier output on fibre length. (Germanosilicate erbium-doped fibre, $\text{NA} \approx 0.2$, $\lambda_{\text{cutoff}} \approx 955\text{nm}$, pump power = 6.2mW)



Measurement of the Spectral Dependence of Absorption Cross Section for Erbium-Doped Single-Mode Optical Fiber

M.P. Singh, D.W. Oblas, J.O. Reese, W.J. Miniscalco and T. Wei
GTE Laboratories Incorporated, 40 Sylvan Road, Waltham, MA 02254

1. Introduction

Recently erbium-doped single-mode fiber has been demonstrated to be very promising in amplifying optical signals near 1.53 μm [1,2]. Er-fiber amplifiers offer advantages of high gain [3], low noise [4], high efficiency [5], large optical bandwidth [6], and polarization independence. Er^{3+} -doped fiber has absorption bands of interest near 800 nm, 980 nm and 1.53 μm , corresponding to $^4\text{I}_{15/2} \rightarrow ^4\text{I}_{9/2}$, $^4\text{I}_{15/2} \rightarrow ^4\text{I}_{11/2}$ and $^4\text{I}_{15/2} \rightarrow ^4\text{I}_{13/2}$ transitions, respectively. All three bands are potentially useful for pumping the 1.53- μm fluorescence band of Er ions.

The efficiency, gain and noise performance of three-level Er^{3+} -doped fiber amplifiers are quite sensitive to the absorption cross sections of these bands, which, in turn, depend on the compositions of the host glass. Knowledge of the absorption cross sections is therefore essential to modeling fiber amplifier for predicting signal gain and amplified spontaneous emission power. Experimental results of absorption cross section for the $^4\text{I}_{15/2} \rightarrow ^4\text{I}_{13/2}$ transition at 1.53 μm have been reported [6,7]. Absorption cross sections in previous experiments were determined indirectly from measurements of the absorption coefficient and fluorescence decay of the $^4\text{I}_{13/2}$ level.

We report here the first attempt to determine absorption cross section spectra for all three absorption bands in Er-doped silica fibers from measurements of the absorption spectra, the Er concentration profile in the core, and the optical mode field power distribution. The absorption cross section can then be obtained directly by calculating the overlap between the Er distribution and the optical power distribution.

2. Experiments

Absorption cross section spectra of Er^{3+} were measured for two $\text{Al}_2\text{O}_3/\text{P}_2\text{O}_5$ doped silica fibers. These fibers were prepared by the modified chemical vapor deposition process and the solution doping technique [8]. Both fibers of the matched-clad design were drawn from the same preform. Table 1 lists properties of these fibers.

Table 1. Optical and physical properties of Er-doped fibers

Fiber	NA	Core Dia. (μm)	MFD (μm)	λ_c (nm)
A	0.13	6.7	8.5	1085
B	0.13	4.0	-	645

2.1 Er Dopant Concentration

The Er dopant concentration and its distribution were determined in slices of the necked-down preform using secondary ion mass spectrometry (SIMS) [9]. To quantify the Er concentration, specially prepared Er-doped alumino-silicate glass standards were used to establish the calibration curve. We measured an ion density of $N_0 = 1.03 \times 10^{19}/\text{cm}^3$ at the center of the core of the fiber sample, equivalent to about 1200 ppm (wt). We estimated that the accuracy of current SIMS measurements was about 18%, due to calibration error introduced by different glass matrices and scan variability, and concentration fluctuations within the preform and the fiber.

2.2 Spectral Attenuation

The measurement of spectral loss in rare-earth doped fibers requires particular care owing to the presence of very intense absorption bands caused by the electronic transitions of the rare-earth

ions, and low-loss regions away from the absorption bands. A multiple cutback technique was used to overcome these difficulties. The input was provided by a white-light source with a scanning double monochromator having a spectral bandpass of 2 nm, while the output power was measured using either an Si or, for longer wavelengths, a liquid-N₂ cooled Ge detector. The above method allowed a dynamic range of up to 15,000 dB/km to be achieved.

2.3 Optical Mode Field Power Distribution

The mode field distribution in the fiber was determined using the far-field angular axial scanning method [10]. A computer-controlled rotation stage moved the detector in a circular arc centered on the fiber end face. A small area detector (0.5 mm dia.) was used to improve the angular resolution. To measure the mode field distributions at several wavelengths within the three widely separated absorption bands, different light sources were required. Tunable Ti:sapphire lasers were used to cover the 800-nm and 980-nm bands. A distributed-feedback laser provided the probe near 1532 nm; however, the fiber-coupled power had to be boosted from ~0.5 mW to >20 mW by an Er³⁺ fiber amplifier due to the strong absorption by Er³⁺ at the probe wavelength. The near fields of the fiber were then computed from the measured far fields with inverse Hankel transforms.

3. Calculation of Absorption Cross Section

The observed absorption by Er³⁺ ions in a fiber depends upon the overlap between the distributions of Er³⁺ ions and optical mode field power in the fiber. The absorption coefficient α at a particular wavelength can be calculated by:

$$\alpha = \frac{2\pi N_0 \sigma \int_0^\infty \rho(r) E^2(r) r dr}{2\pi \int_0^\infty E^2(r) r dr}, \quad (1)$$

where N_0 is the Er ion concentration at the core center; σ is the absorption cross section; $\rho(r)$ is the normalized Er ion distribution as a function of the radial distance r ; and $E^2(r)$ is the normalized mode field power distribution in the fiber.

4. Results and Discussion

Figures 1(a), 1(b), and 1(c) show the respective attenuation spectra of Er-doped silica fibers in the following absorption bands: 800 nm, 980 nm, and 1532 nm. The normalized Er dopant concentration profile in the fiber taken from SIMS measurements is given in Figure 2. The mode field power distributions in Er-doped fibers were measured at four, five, and two selected wavelengths within the 800-nm, 980-nm, and 1532-nm bands, respectively. As an example, Figure 2 illustrates the radial distribution of the mode field intensity at 1532 nm.

From the mode field distribution result at each selected wavelength, the absorption cross section was calculated from Equation (1) using the attenuation data and the corresponding Er dopant concentration profile. Figures 3(a), 3(b), and 3(c) illustrate the calculated absorption cross sections (denoted by cross marks) within the absorption bands at 800 nm, 980 nm, and 1532 nm, respectively. The absorption cross section values at other wavelengths within each band were determined by scaling the peak cross section according to the absorption spectrum, i.e., multiplying the peak cross section by the ratio of the absorption coefficient at each wavelength to the peak absorption coefficient. The solid curves in Figure 3 show the scaled cross section spectra for all three bands. They were found to be in excellent agreement with the cross sections calculated at those selected wavelengths.

Table 2 lists peak absorption cross sections for those three absorption bands, wavelengths at the peaks, and the full-widths at half-maximum (FWHM). The peak absorption cross section at 1532 nm was found to be $6.44 \times 10^{-21} \text{ cm}^2$, which is about twice that at 978 nm. This value falls within the reported range of $(4.3\text{-}7.3) \times 10^{-21} \text{ cm}^2$ at 1531 nm or 1532 nm for an Er^{3+} -doped silica fiber [6,7,11,12]. Nevertheless, the absorption cross section at a pump wavelength between 1470 nm and 1490 nm is somewhat smaller than that at the 980-nm pump wavelength. The peak cross section of $3.25 \times 10^{-21} \text{ cm}^2$ at 978 nm is about 3.5 times larger than that at 793 nm. This result is consistent with the excellent amplifier performance achieved by pumping Er-doped silica fiber amplifiers at 980 nm [3,5]. The FWHM for the 978-nm absorption band is close to that of 793-nm band and less than a half of the value at 1532 nm.

Table 2. Peak absorption cross sections of Er-doped fibers

Fiber	Peak σ (cm^2)	Peak λ (nm)	FWHM (nm)
A	6.44×10^{-21}	1532.0	38.3
B	3.25×10^{-21}	978.2	16.0
B	9.19×10^{-22}	793.2	21.3

5. Conclusion

Absorption cross sections for Er^{3+} -doped single-mode fibers were determined directly for three principal pump bands using measured absorption spectra, Er doping profiles and optical mode field power distributions. The absorption cross section for the 980-nm pump band was found to be larger than those at 800 nm or 1480 nm, which is partly responsible for the achieved excellent performance in pump efficiency and amplifier gain for Er-doped silica fibers pumped at 980 nm. To further improve this measurement technique, an analytical method providing a more accurate determination of the Er concentration in optical fiber has to be developed.

Acknowledgements

The authors are grateful to Dr. L.J. Andrews for helpful discussions, and J. Connolly, B. Hall, J. McCabe and B. Thompson for technical assistance.

References

- [1] R.J. Mears, L. Reekie, I.M. Jauncey and D.N. Payne, OFC '87, Tech. Digest, p. 167 (1987).
- [2] E. Desurvire, J.R. Simpson and P.C. Becker, Opt. Lett. 12, 888 (1987).
- [3] W.J. Miniscalco, B.A. Thompson, E. Eichen and T. Wei, OFC '90, Tech. Digest, p. 192 (1990).
- [4] C.R. Giles, E. Desurvire, J.L. Zyskind and J.R. Simpson, IEEE Photonics Technol. Lett. 1, 367 (1989).
- [5] M. Shimizu, M. Horiguchi, M. Yamada, I. Nishi, S. Uehara, J. Noda and E. Sugita, OFC '90, Postdeadline Paper PD17 (1990).
- [6] C.J. Atkins, J.F. Massicott, J.R. Armitage, R. Wyatt, B.J. Ainslie and S.P. Craig-Ryan, Electron. Lett. 25, 910 (1989).
- [7] E. Desurvire, IEEE Photonics Technol. Lett. 1, 293 (1989).
- [8] J. E. Townsend, S. B. Poole, and D. N. Payne, Electron. Lett. 23, 329 (1987).
- [9] D.W. Oblas, T. Wei, W.J. Miniscalco, and B. T. Hall, Material Research Society Symp. Proc. 172, 315 (1990).
- [10] W.T. Anderson and D.L. Philen, J. Lightwave Technol. LT-1, 20 (1983).
- [11] E. Desurvire, C.R. Giles and J.R. Simpson, Proc. SPIE 1171, 103 (1990).
- [12] K. Dybdal, N. Bjerre, J. Engholm Pedersen and C.C. Larsen, Proc. SPIE 1171, 209 (1990).

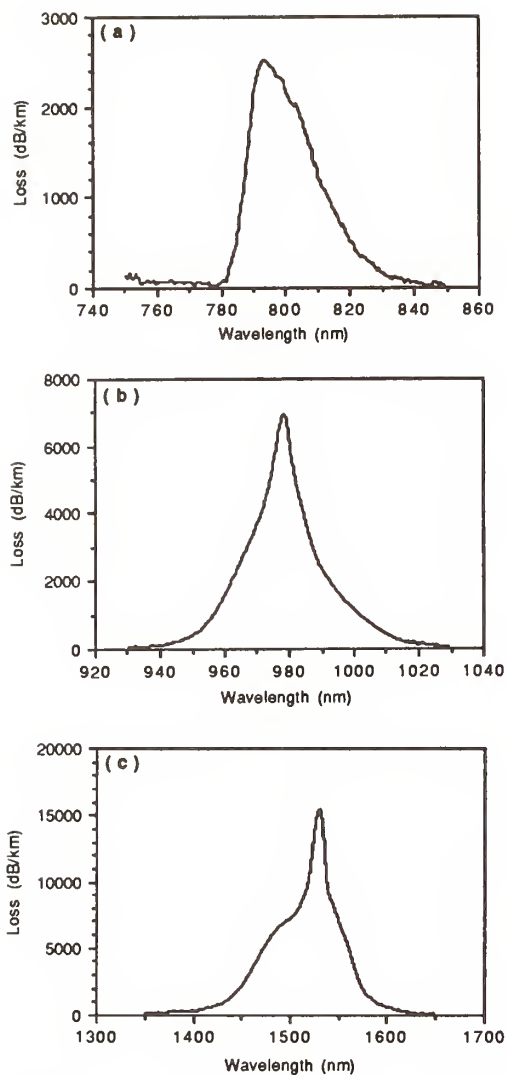


Figure 1. Attenuation spectra of Er-doped silica fibers near three absorption bands: (a) 800 nm, (b) 980 nm, and (c) 1530 nm.

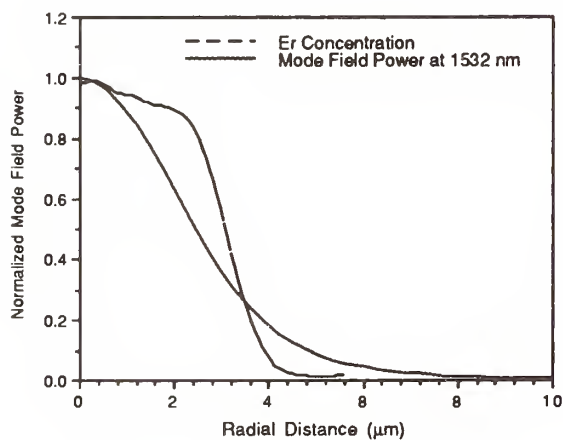


Figure 2. Normalized mode field power distribution at 1532 nm for Fiber A. The dashed curve shows the Er distribution.

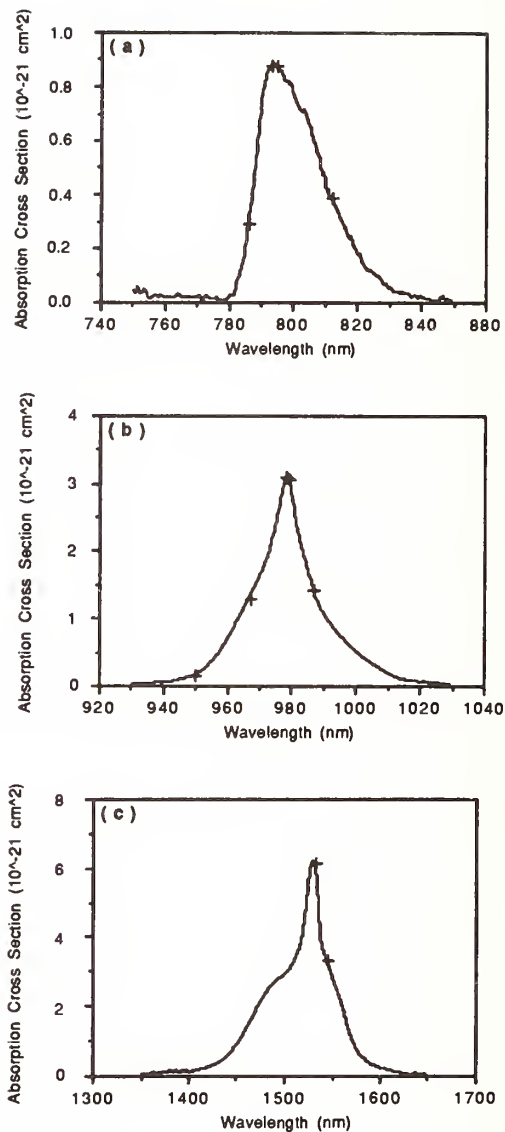


Figure 3. Absorption cross section spectra of Er-doped silica fibers within absorption bands near: (a) 800 nm, (b) 980 nm, and (c) 1530 nm.

Wavelength Characterisation of Components for Optical Networking Applications in the 1.5 μ m Transmission Window

P J Chidgey, B P Cavanagh, P D D Kilkelly and H J Westlake
British Telecommunications Research Laboratories, Martlesham Heath, Ipswich,
Suffolk, IP5 7RE, U.K.

and
J Lyle

University of Nottingham, Department of Electrical and Electronic Engineering, University Park,
Nottingham, NG7 2RD, U.K.

Abstract : *The use of a high power broadband edge emitting diode at 1.5 μ m for the rapid assessment of the wavelength dependent transmission of optical components is discussed. The extension of the technique to measure the gain of optical amplifiers is demonstrated and measurements of the evolution with pump power of the gain of an aluminium co-doped erbium fibre amplifier are reported. The results are compared with measurements made at spot wavelengths using a long external cavity controlled semiconductor laser.*

Introduction : Monomode optical transmission technology has revolutionised networks design for telecommunications, cable TV, computing and data distribution [1]. In telecommunications it has enabled increased data rates and transmission distances in the main (inter-office) network and is beginning to influence the design of local (subscriber) networks [2]. Currently, however, the inherently large bandwidth of the transmission medium is not exploited. Increased traffic arising from growth in demand for existing services, new service provision and new markets will ultimately require efficient utilisation of this bandwidth. Use of the wavelength domain will enable new planning strategies to be developed to provide, for example, flexible network growth in response to changes in traffic, improved capacity utilisation and simple network restoration in the event of terminal or cable failure. The key to the future exploitation of bandwidth is to retain optical transparency by using components and networking solutions which place few constraints on the transmitted signals. Wavelength routed networks [3] to a large extent fulfil this requirement and the use of rare earth doped fibre amplifiers [4,5] allow these networking principles to be tailored to meet a wide variety of network constraints such as geography, traffic and reliability [6]. The complex optical networks which may evolve require careful management of the spectral domain and it is therefore necessary to develop at an early stage a rational approach to spectrum management. An agreement on standards is needed to ensure component and equipment compatibility which takes into account intrinsic limitations in device technologies as well as system and fibre capabilities. Ideally wavelength standards should be common for all network applications allowing interworking and retaining optical transparency between applications. The wavelength characterisation of optical components and systems is therefore essential to allow for this future exploitation.

The paper demonstrates the use of a high power, broadband, unpolarised optical signal from an edge emitting diode for the routine characterisation of optical components. The method is shown to be a powerful tool for measuring amplifier mean gain-bandwidth and the evolution of mean gain with pump power. The system is compared with point wavelength gain measurements using a real-time chopped signal technique and a long external cavity controlled semiconductor laser (LEC) [7]. Advantages and limitations of the system are discussed.

Measurement Technique : Conventional techniques for determining the transmission of optical components utilise either broadband sources or tunable sources by comparing the incident and transmitted power as a function of wavelength using, for example, a monochromator. A common source used employs a halogen lamp to give a broad spectral coverage from 0.6 - 1.6 μ m but the spectral power density of this source is small being ~ 55 dBm/nm. Broadband light emitting diodes are available with typical spectral bandwidths of ~ 150 - 200 nm FWHM and total output powers of ~ 23 dBm in the 1.5 μ m region. The most attractive sources are superluminescent and edge emitting diodes operating in the 1.5 μ m region with powers in excess of -16 dBm into a typical bandwidth of ~ 60 nm FWHM. The increased spectral power density of these sources make them ideal for component characterisation in the 1.5 - 1.6 μ m window.

A schematic of a typical component measurement scheme is shown in Fig. 1. The wavelength dependent performance of the coupler and splice losses are measured and corrected for using a cut back technique. Typical

measurements of the wavelength dependent transmission of a grating-based wavelength division multiplexer and the effects of bandwidth concatenation are shown in Fig. 2 [8]. This basic measurement technique was modified to allow measurements on optical amplifiers, Fig. 3. Reflections were minimised using 'Super' PC connectors and an isolator common to both the input and amplified signal measurements. Three spectral measurements were taken: the quiescent spontaneous emission from the amplifier; the spontaneous emission plus the amplified signal; and the input signal. The data was transferred from the optical spectrum analyser to the computer over the interface bus. Using software the data was converted from dBm to linear form and the spontaneous emission subtracted to give the amplified signal; the gain, as a function of wavelength, was then computed. A key point in this measurement technique is the assumption that the amplifier spontaneous emission with and without the input signal power has the same output power and spectral distribution. This assumption will only be true for small input signals where the amplifier output is not saturated. Resolution bandwidth is determined by the optical spectrum analyser. The measurement time is less than five minutes for the gain at 501 discrete wavelengths determined by the optical spectrum analyser range and start wavelength.

Measurements have been made on numerous erbium doped fibre amplifiers having a range of fibre lengths and pump powers. Fig. 4 shows the evolution of gain with pump power for 7m of an erbium doped aluminium silica based fibre [9]. This was reverse pumped using a packaged multiple quantum well semiconductor laser diode, emitting at $1.48\mu\text{m}$, having a maximum output power of 45mW [10]. The pump power was injected using a fused, tapered fibre wavelength division multiplexer (WDM) with passbands centred at $1.48\mu\text{m}$ and $1.57\mu\text{m}$. The pump power was adjusted by varying the drive current to the semiconductor pump laser. All the measurements were made in <30 minutes using the ELED system and demonstrate the power of the technique. An equivalent point by point measurement made using a tunable source would take several hours to perform. The curves are in good agreement with published results [11]. On analysis, their interpretation is complicated by the following: The gain profile is a function of pump wavelength [11] and the semiconductor pump source spectral density is current dependent. As the pump current is decreased, the available pump power decreases and the pump wavelength shortens. The amplifier becomes less well pumped, tending to suppress the peak at $1.53\mu\text{m}$, but at shorter pump wavelengths the peaking at $1.53\mu\text{m}$ tends to increase. Thus we have two competing effects. In the gain saturation region, the gain at $1.53\mu\text{m}$ is suppressed more than at longer wavelengths. Compounded with this, the measurements were taken with a constant input power of -22dBm which has the effect of driving the device more into saturation at lower gain. Measured gain curves at -32dBm and -22dBm were identical indicating no saturation at a pump power of 35mW with 10mW residual pump power after the erbium fibre. Amplifier spontaneous emission became of the same order as the amplified signal for input power levels below -32dBm resulting in large errors in determining the gain.

For comparison gain measurements were also made using a narrow linewidth, tunable LEC. The signal was chopped at 270Hz and split, using a 3dB coupler, into the amplifier fibre and a monitor arm; corrections were made for the wavelength dependence of the splitter. Real-time measurements of amplifier gain were made by detecting the chopped signal at the monitor and amplifier outputs using a dual head power meter. Gain saturation measurements were possible over a wider range of input powers compared to the ELED system described above. Input signal powers varied from -30dBm, limited by residual pump power reflections masking the chopped signal, to -6dBm. Fig. 5 shows amplifier gain saturation results in the wavelength range $1.53 - 1.56\mu\text{m}$ made using the LEC; ELED results are shown for comparison at an assumed effective input power of -25.6dBm, obtained from Fig. 4 for a pump power of 35mW. This effective input power was arrived at by considering what happens to the broadband signal in the fibre amplifier. This signal is filtered by both the amplifier gain profile and the wavelength response of the WDM. The 3dB bandwidth of the ELED signal is 61nm ($1.511 - 1.572\mu\text{m}$) while the Erbium doped fibre has a 3dB bandwidth of 38nm ($1.527 - 1.569\mu\text{m}$), hence the signal will be amplified in the overlap region and attenuated in the lobes. The input signal that is absorbed contributes to the population inversion, but this power is some 4 orders of magnitude less than pump power. We therefore have an effective input signal power which is less than the total power. If we assume that the effective input signal is given by the ELED power falling within the 3dB amplifier gain profile, then the input signal, seen by the amplifier, is reduced by 3.6 dB compared to the total ELED power. The exact effective input signal power will be a function of amplifier gain and ELED spectral profiles. The amplified, bandwidth-restricted ELED signal is then further filtered by the WDM transmission characteristic. If the amplifier is forward pumped then filtering occurs before the gain medium and the effective input signal power is lower, cf. reverse pumping. This implies that if the amplifier is in saturation then the gain profiles observed for forward and backward pumping will be different. This effect will also occur for a narrow linewidth source, such as an

LEC. Where Fig. 5 is in the plateau region, i.e. no saturation, the agreement between the LEC and ELED measurements is within 0.2dB. At 1.53 μ m, however, the discrepancy is 0.7dB, but at this wavelength, an input signal power of -25.6dBm does not lie on the plateau. It is possible that the 'true' effective ELED input power is less than that estimated from a simple 3dB filter bandwidth model due to 'shaping' effects of the gain. The gain measured using the ELED system is close to the expected plateau gain inferred from the trend seen in the LEC measurements. Gain measurements on other erbium doped aluminium silica based fibre amplifiers are shown in Fig.6 for various fibre lengths and pump powers. Gain measurements have also been made on semiconductor laser amplifiers where the use of an unpolarised ELED source results in the measurement of the mean gain of the optical amplifier.

Conclusion : We conclude that high spectral power densities available from superluminescent and edge emitting diodes provide an ideal source for the rapid characterisation of both active and passive optical components for use in optical networks. The combination of the ELED and LEC measurements provides a rapid technique for fully characterising optical amplifiers; the ELED system measuring the wavelength dependent gain information and the LEC gain saturation measurements for specific wavelengths. The wavelength characterisation of optical components, networks and systems is essential if the full potential of the available bandwidth of monomode optical fibre is to be realised. An agreement on wavelength standards is needed to ensure component and equipment compatibility which takes into account intrinsic limitations in device technologies as well as system and fibre capabilities and enables future optical systems upgrade.

Acknowledgements : Acknowledgement is made to Graham Walker for his work on the chopped LEC measurement system for amplifier assessment and to Sue Craig-Ryan for supply of the erbium-doped fibre.

References :

- 1 : BRACKETT, C. A. : 'Dense WDM Networks', Proc. ECOC 88, Brighton, U.K., 11th - 15th September 1988, pp. 533 - 540.
- 2 : See for example the Proceedings of IEEE Workshop on Passive Optical Networks for the Local Loop, Heathrow Penta Hotel, London, 8th - 9th May 1990.
- 3 : HILL, G. R.: "A wavelength routing approach to optical communications networks", Br. Telecom Technol. J., 1988, 6, pp. 24-31.
- 4 : URQUHART, P. : 'Review of rare earth doped fibre lasers and amplifiers', IEE Proc. J, 1988, 135, pp. 385-407.
- 5 : SAITO, S., IMAI, T., SUGIE, T., OHKAWA, M., ICHIGASHI, Y., and ITO, T. : 'An over 2,200km coherent transmission experiment at 2.5Gbit/s using erbium-doped-fibre amplifiers', Postdeadline Paper PD-2, OFC '90, San Francisco, 22nd - 26th January 1990.
- 6 : HILL, G. R., HAWKER, I. and CHIDGEY, P. J.: "Applications of wavelength routing in a core telecommunications network". Accepted for publication at IEE Conference on Integrated Broadband Services and Networks, London, U.K., 15th - 18th October 1990.
- 7 : WYATT, R., CAMERON, K.H. and MATTHEWS, M.R. : 'Tunable narrow line external cavity lasers for coherent optical systems', Br. Telecom Technol. J., 1985, 3, pp. 5-12.
- 8 : CHIDGEY, P. J. and HILL, G. R.: "Experimental demonstration of wavelength routed optical networks over 52km of monomode optical fibre". Paper MoA1-5, ECOC'89, Gothenberg.
- 9 : AINSLIE, B. J., CRAIG, S. P., DAVEY, S. T. and WAKEFIELD, B. : 'The fabrication, assessment and optical properties of high-concentration Nd³⁺ and Er³⁺ - doped silica based fibres', Materials Lett., 1988, 6, pp.139-144.
- 10 : COOPER, D. M., SELTZER, C. P., AYLETT, M., ELTON, D. J., HARLOW, M., WICKES, H. and MURRELL, D. L. : 'High-power 1.5 μ m all-MOVPE buried heterostructure graded index separate confinement multiple quantum well lasers', IEE Elect. Lett., 1989, 25, pp. 1635-1637.
- 11 : ATKINS, C. G., MASSICOTT, J. F., ARMITAGE, J. R., WYATT, R., AINSLIE, B. J. and CRAIG-RYAN, S. P. : 'High-gain, broad spectral bandwidth erbium-doped fibre amplifier pumped near 1.5 μ m', IEE Elect. Lett., 1989, 25, pp.910-911.

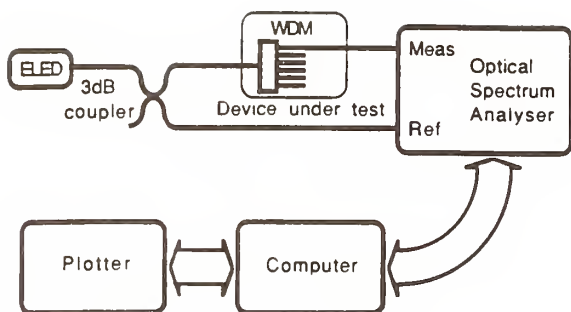


Figure 1 : Optical component assessment using ELED

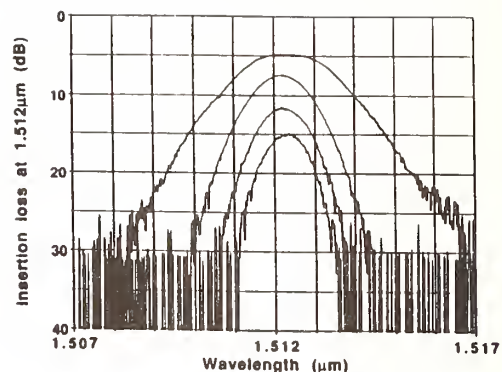


Figure 2 : Bandwidth and concatenation effects of grating based wavelength division multiplexers

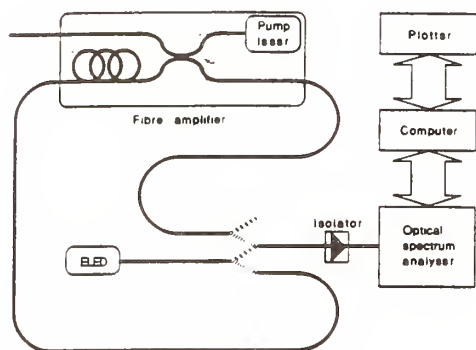


Figure 3 : Optical amplifier assessment using ELED

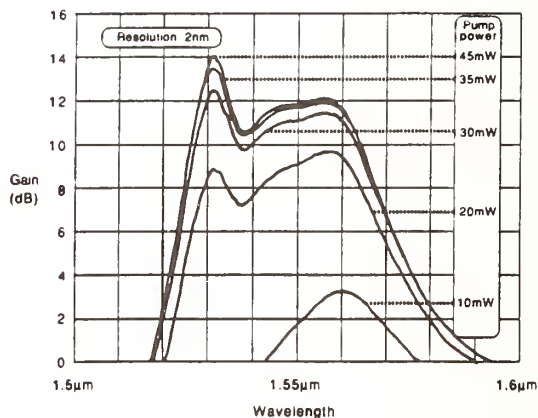


Figure 4 : Amplifier gain evolution with pump power.

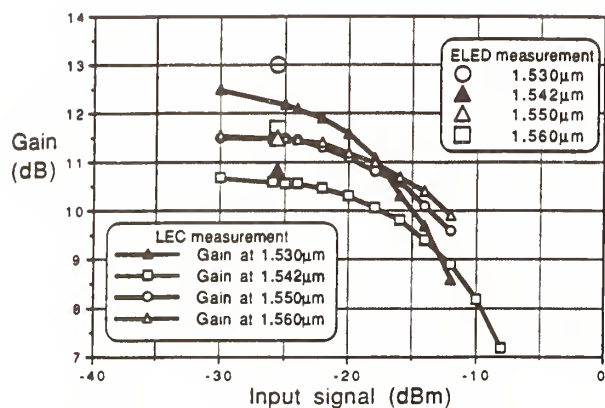


Figure 5 : LEC measurement of amplifier gain saturation at spot wavelengths

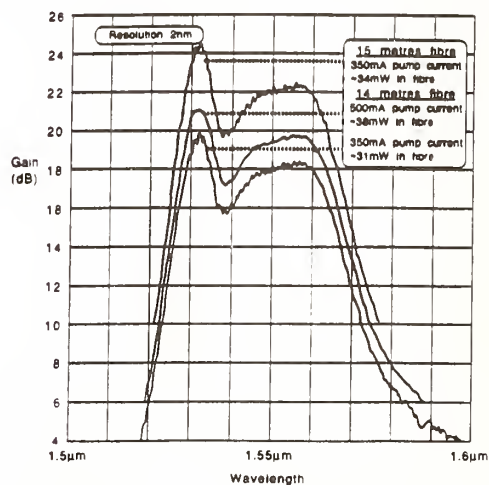


Figure 6 : Erbium doped aluminium silica based fibre amplifier gain measurements

MEASUREMENT OF LASER DIODE INTENSITY NOISE BELOW THE SHOT NOISE LIMIT

C. M. MILLER and L. F. STOKES

HEWLETT-PACKARD COMPANY
ROHNERT PARK, CALIFORNIA

Introduction

The intensity noise of laser diodes used to transmit information on optical fiber has improved dramatically the past several years. This excess laser noise component is often the limiting factor in the signal-to-noise ratio in a lightwave transmission system. Measurements of intensity noise can become difficult as the noise level approaches the detection shot noise and the thermal noise limit of the receiver. However, careful measurement and subtraction of these noise components using a calibrated lightwave signal analyzer, with no extraneous measurement instrumentation, can result in a computed excess laser noise component below the shot noise limit.

Background

The source of laser intensity noise is the unavoidable spontaneous emission in the laser gain medium. The frequency dependence of the intensity noise can be analyzed by adding Langevin noise sources to the rate equations.¹ This frequency dependence has exactly the same denominator as the laser's intrinsic modulation response, which can be obtained from a small signal analysis of the rate equations.² Typically, the intensity noise has a damped resonance at the relaxation-oscillation frequency, which increases in frequency and becomes increasingly damped as the bias current is increased.

An important quantity related to intensity noise and signal-to-noise ratio is relative intensity noise (RIN). It has been historically defined as the ratio of the mean square intensity fluctuation spectral density of the optical output $(\Delta P)^2$, to the square of the average optical power, $(P_{av})^2$. This quantity indicates the maximum possible signal-to-noise ratio in a lightwave transmission system, where the dominant noise source is the laser intensity noise. For a laser biased at a given power level, and modulated by a sinusoidal signal with 100% modulation index, the signal-to-noise ratio is 3 dB less than the magnitude of RIN.³

Traditionally, RIN has been measured by using a photodiode to detect the laser output. The photodiode's electrical output can be amplified and displayed on an electrical spectrum analyzer. This measurement, P_n (measured), corresponds to an amplified electrical equivalent of $(\Delta P)^2$. Simultaneously, the DC photocurrent must be monitored. The DC photocurrent squared, multiplied by 50 ohms and the amplifier power gain, results in P_{av} (electrical), the corresponding electrical equivalent of $(P_{av})^2$. Care must be used in this measurement technique to obtain accurate results. The photodiode, amplifier, and spectrum analyzer frequency responses, as well as the mismatch losses between them, must be well characterized.

Thus,

$$I_{av} = 1.6 \text{ mA}$$

$$2e/I_{av} = 2.0 \times 10^{-16}/\text{Hz}$$

Finally, using equation (II)

$$\begin{aligned} \text{REN} &= 5.01 \times 10^{-16}/\text{Hz} - 2.0 \times 10^{-16}/\text{Hz} - 1.99 \times 10^{-16}/\text{Hz} \\ &= 1.02 \times 10^{-16}/\text{Hz} = -159.9 \text{ dB/Hz} \end{aligned}$$

Subtracting shot noise and thermal noise from the measured RIN, yields a REN value that improves by 6.9 dB; a result that is less than the shot noise. Figure 4 shows a plot of calculated REN (laser) as a function of the measured RIN and P_{av} (optical), using the values of P_n (thermal), and r_v in the example. Clearly, the correction to the measured RIN becomes more significant when this noise is close either to the shot noise limit or the thermal noise floor.

The previous measurement example was made with 0 dB input attenuation, for maximum sensitivity. However, for high power lasers attenuation is often required to avoid compression effects. Since adding attenuation modifies the effective photocurrent being detected, I_{av} must be reduced by $10^{-\text{atten}/20}$, where atten is the electrical value of attenuation. P_n (thermal) would also increase linearly with the attenuation value. A comparison of the calculated values for two equivalent measured RIN values at different optical power levels is shown in Table 1.

Table 1

P_{av} (optical)	P_{av} (electr.)	RIN (measured)	ATTEN	P_n (thermal)	I_{av}	REN
2 mW	23 dBm	-153 dB/Hz	0 dB	-134 dBm	1.6 mA	-160 dB/Hz
20 mW	43 dBm	-153 dB/Hz	20 dB	-114 dBm	1.6 mA	-160 dB/Hz

Summary

A simple, but effective technique for determining the excess laser noise in the presence of shot noise and thermal noise using a lightwave signal analyzer has been described. A laser with a 2 mW optical average power has been measured to have a REN of -160 dB, several dB below the shot noise limit.

References

1. M. Huag, "Quantum mechanical rate equations for semiconductor lasers," Phys. Rev., 184, pp. 338-348, 1969.
2. J. Bowers, "High speed semiconductor laser design and performance," Solid State Electron. 30, pp. 1-11, 1986.
3. K. Lau and A Yariv, "Ultra-high-speed semiconductor lasers," IEEE J. Quantum Electron, QE-21, pp. 121-138, 1985.

Measurements and Computations

The measurement of excess laser noise and the RIN solely due to the laser is often limited by several factors. First, there is the detector shot noise current i_n , where $(i_n)^2 = 2eI_{av}$ for a 1 Hz-bandwidth, I_{av} is the average photocurrent and e is the electronic charge. This shot noise power is proportional to the square root of the detected laser power. For shot noise limited detection, the measureable RIN can be shown to be equal to $2e/I_{av}$, and it increases 10 dB per decade increase in photocurrent. Second, the measureable RIN range can be limited by the electrical spectrum analyzer sensitivity, or thermal noise. With the addition of a broadband, low-noise preamplifier, the shot noise limited detection can be achieved at lower optical power levels. These receiver limitations are shown graphically in figure 1.

In some cases, the desired excess laser noise component, which is proportional to the detected laser power, can be less than one or both of the measured receiver noise components. The excess noise component, P_n (laser), can be determined from the measured value using the following relationship:

$$P_n \text{ (laser)} = P_n \text{ (measured)} - P_n \text{ (shot)} - P_n \text{ (thermal)} \quad (\text{I})$$

where P_n (thermal) is the measured noise floor of the lightwave signal analyzer in a 1 Hz bandwidth. Dividing by P_{av} (electrical), results in a relationship for the relative excess noise of the laser or REN:

$$\text{REN} = \text{RIN (measured)} - \frac{2e}{I_{av}} - \frac{P_n \text{ (thermal)}}{P_{av} \text{ (electrical)}} \quad (\text{II})$$

where P_n (electrical) is the displayed average electrical power on the lightwave signal analyzer. The detected photocurrent I_{av} can be determined from either the average optical power or the average electrical power, both of which can be displayed on the lightwave signal analyzer:

$$I_{av} = rP_{av} \text{ (optical)} \quad \text{or} \quad r[P_{av} \text{ (electrical)} * 50]^{1/2}/r_v$$

where r is the diode responsivity in A/W (typically .75 to .8), and r_v = voltage responsivity in V/W (typically 1500 to 1600).

Shown in figure 2 is a RIN measurement on a Nd:YAG laser. The measurement set-up is shown in figure 3. The following values can be determined from the measurement:

$$\begin{aligned} P_{av} \text{ (electrical)} &= 23.0 \text{ dBm} = .200 \text{ watts (equivalent to 2.0 mW} \\ &\quad \text{optical power)} \\ \text{RIN (measured)} &= -153.0 \text{ dB/Hz} = 5.01 \times 10^{-16}/\text{Hz} \\ P_n \text{ (thermal)} &= -134.0 \text{ dBm/Hz} = 3.98 \times 10^{-17} \text{ W/Hz} \\ r_v &= 1604 \text{ V/W} \\ r &= .8 \text{ A/W} \end{aligned}$$

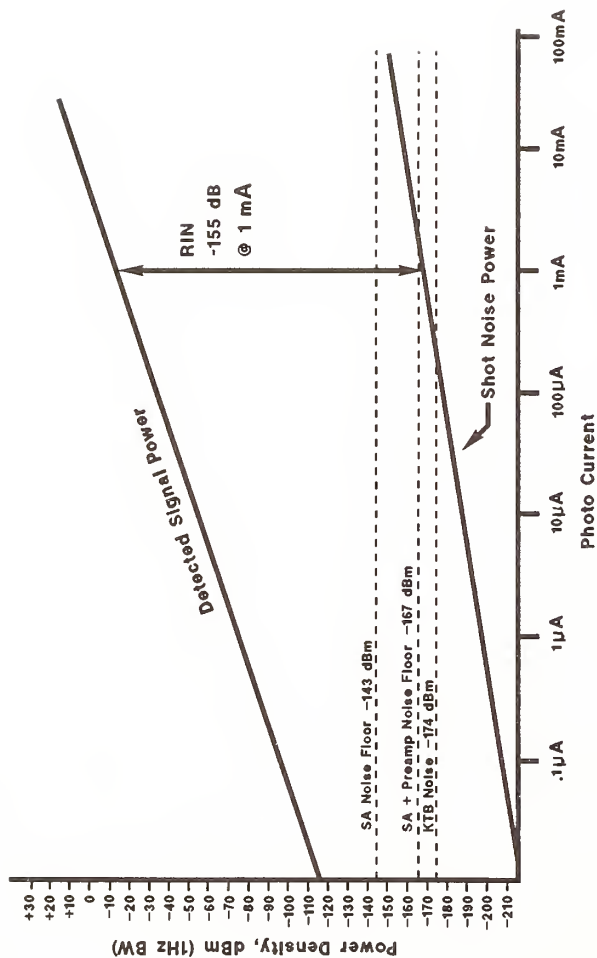


Fig. 1. RIN limits imposed by receiver sensitivity.

Fig. 2. Measured RIN of -153 dB/Hz.

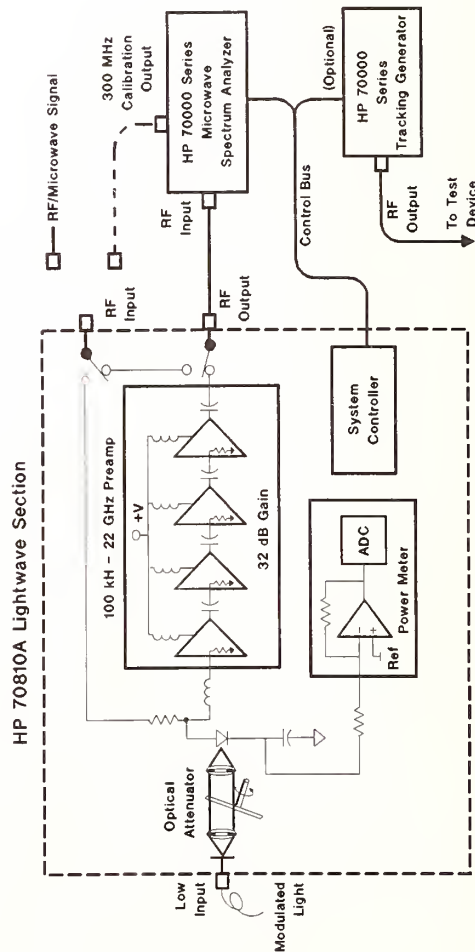
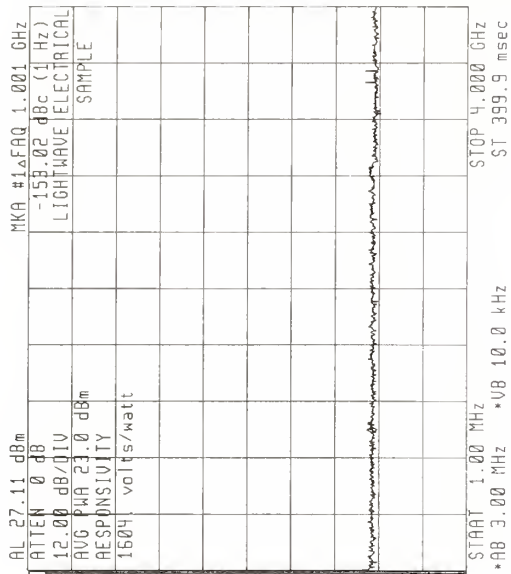
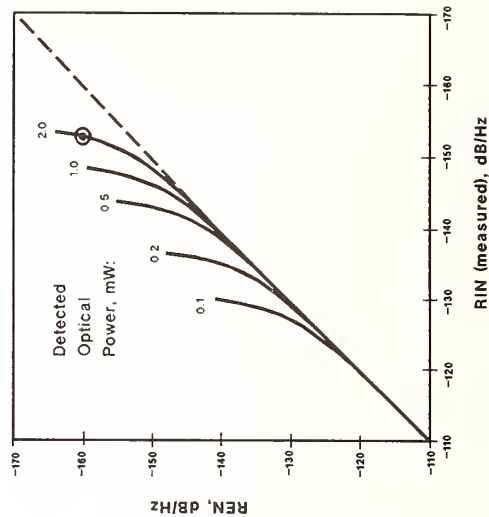


Fig. 3. Lightwave signal analyzer block diagram.

Fig. 4. REN calculated from RIN (measured).



AN OPTICAL SYNTHESIZER WITH SINUSOIDAL-MODULATED MICHELSON INTERFEROMETER FOR GENERATION OF AN ABSOLUTELY STABILIZED CARRIER FREQUENCY COMB

A. Mattheus, L. Giehmann and M. Rocks

Research Institute of Deutsche Bundespost TELEKOM
Berlin Branch
Ringbahnstr. 130, D-1000 Berlin 42

ABSTRACT

A theory, a preliminary experimental setup and first measurement results of an optical synthesizer consisting of a He-Ne laser, a semiconductor laser and a Michelson interferometer are reported. The synthesizer frequencies are absolutely stabilized and can be generated by any tunable single mode laser in the region between 1.2 μm and 1.6 μm . The number of accessible synthesizer frequencies is only limited by the tuning range of the semiconductor laser and the free spectral range (FSR) of the interferometer. In our experimental setup with a FSR of 5 GHz up to 16 frequencies can be generated with the available DFB laser. The complete set of frequencies can be tuned continuously by an offset voltage. This setup can be used for multichannel communication systems.

THEORY

A comb of absolutely stabilized carrier frequencies is a major element in the conceptional design of multichannel coherent transmission systems /1-3/. These frequencies may be generated by using an optical synthesizer /4, 5/.

In this paper we present our proposal for the synthesizer which is realized by a Michelson interferometer with the geometrical path difference L (fig. 1). The output intensity P_1 of the He-Ne laser is given by

$$(1) \quad P_1(t) = d_1 \cdot I_1(t) \cdot [1 - \sin(4\pi \frac{n_1}{\lambda_1} \cdot (\Delta l + \Delta L(t) + y_0 \cdot \sin(\omega_m \cdot t)))]$$

with the constant d_1 , the input intensity $I_1(t)$, the refractive index n_1 , the vacuum wavelength $\lambda_1 = c/f_1 \approx 633 \text{ nm}$, a constant length offset Δl and a noise component $\Delta L(t)$ resp.. The modulation component $y_0 \cdot \sin(\omega_m \cdot t)$ with the frequency $f_m = \omega_m / 2\pi = 181 \text{ Hz}$ is induced via a.c. Coupling (fig. 1). By means of the first control loop, comprising the optoelectronic receiver D_1 , the lock-in detector (tuned to $2 \cdot f_m$), amplifier units, a transmitter (Tr) and the piezoelectric transducer, Δl is kept constant and $\Delta L(t)$ is controlled to zero.

In an analogue control loop the frequency of the DFB laser is set and stabilized to a well-defined value of the equispaced set

$$(2) \quad f'_2 = (p + 0.25) \cdot \nu_0, \quad p \in \mathbb{N}$$

with the FSR $\nu_0 = c/(2 \cdot n_2 \cdot L_0) = 5 \text{ GHz}$, using the injection current $I_{\text{DFB}} = I_0 + \Delta I_s$ as the control value (fig. 1). The amount I_0 defines a certain value of p . The additional current ΔI_s increases or decreases p stepwise by ± 1 . The complete set of frequencies can be detuned continuously by scanning the FSR via the length component ΔL .

According to $f_2(t) = f'_2 + \Delta f_2(t)$ the actual frequency $f_2(t)$ of the DFB laser differs from the desired one by the frequency fluctuation $\Delta f_2(t)$. The output signal of this laser

$$(3) P_2(t) = d_2 \cdot I_2(t) \cdot \left\{ 1 - \sin \left[2\pi \frac{\Delta f_2(t)}{\nu_0} + 4\pi \frac{n_2 \cdot f'_2}{c} \cdot (\Delta L(t) + y_0 \cdot \sin(\omega_m t)) \right] \right\}$$

with the constant d_2 , the input intensity $I_2(t)$ and the refractive index n_2 is used to control the frequency fluctuation $\Delta f_2(t)$ to zero. However the noise component $\Delta L(t)$ causes an additional deviation $\Delta f_2 = -2 \cdot n_2 \cdot f'_2 \cdot \nu_0 \cdot \Delta L(t) / c$ from the desired frequency f'_2 .

EXPERIMENTAL

The synthesizer was developed as an easy-to-transport device for multichannel coherent transmission systems. As illustrated in fig. 1 the light of the DFB laser is coupled into the interferometer via a monomode fibre. As a consequence, the DFB laser can be replaced easily without readjustment of the interferometer. Care was taken to prevent interfering reflections by means of an optical isolator and by obliquely positioning the beam splitter cube BS_B .

The first control loop was optimized by the measures described below. Special beam splitters and triple prisms which might allow an extreme high interferometric accuracy [6] were not used, since a mirror with a low mass has favourable influence on the control behaviour of this loop. The hysteresis curve of the piezoelement with the expansion coefficient of 6 nm/V is considerably narrowed by a defined compressive stress. The noise of a specially developed piezo amplifier ($50 \text{ } \mu\text{V}$) is negligible as compared with the noise of the receiver unit SS_D and the lock-in detector. Taken altogether the maximum length deviation $\Delta L(t)$ measured in the first control loop does not exceed 100 pm .

In a separate experiment DFB detuning values of 20 GHz/K and 930 MHz/mA and a linewidth of 20 MHz were measured. At present residual current fluctuations of $5 \text{ } \mu\text{A}$ in the whole second control loop limits the accuracy of the DFB laser emission frequency down to 5 MHz .

In fig. 2 the measured intensity curve of the He-Ne radiation (solid line) was compared with the calculated values $P_1(t)$, using eqn. 1 with the values $\Delta L = -2.43 \text{ nm}$ and $y_0 = 153.6 \text{ nm}$ (circles). The good agreement between measurement and calculation shows that modulation of the piezoelectric transducer does not give rise to major distortions. The latter could, in principle, be caused by hysteresis effects in the piezo element or

by nonlinear transmission of the modulation voltage to the piezo element.

APPLICATIONS

The synthesizer described in this paper can be used to generate an absolutely stabilized carrier frequency comb. To achieve this one may lock each transmitter laser to a preselected frequency of the synthesizer by means of a heterodyne technique including an AFC control loop /7/. The synthesizer frequencies have to be identified once. This can be done by using a precise wavemeter /8/ or a built-in absorption cell /9/.

REFERENCES

- /1/ M.W. Maeda, J.R. Barry, T. Kumazawa, and R.E. Wagner, "Absolute frequency identification and stabilisation of DFB lasers in 1.5 μ m region". Electron. Lett., 1989, 25, pp. 9-11
- /2/ Y.C. Chung, K.J. Pollock, P.J. Fitzgerald, B. Glance, R.W. Tkach, and A.R. Chraplyvy, "WDM coherent star network with absolute frequency reference", Electron. Lett., 1988, 24, pp. 1313 - 1314
- /3/ R.A. Valenzuela, L.J. Cimini, R.W. Wilson, K.C. Reichmann, A. Grot, "Frequency stabilisation of AlGaAs lasers to absorption spectrum of Rubidium using Zeeman effect", Electron. Lett., 1988, 24, pp. 725-726
- /4/ K. Kuboki, C.H. Shin, T. Kato and M. Ohtsu, "Performance and its evaluation of optical tracking generator/ optical frequency synthesizer by semiconductor lasers", CPEM'88 DIGEST, pp. 24-25
- /5/ B. Glance, O. Scaramucci, T.L. Koch, J. Stone, "Optical frequency synthesiser", Electron. Lett., 1989, 25, pp. 1193-1195
- /6/ A. Valentin, C. Nicolas, L. Henry, and A.W. Mantz, "Tunable diode laser control by a stepping Michelson interferometer", Appl. Opt. 26, 41-46 (1987)
- /7/ T. Okoshi and K. Kikuchi, "Frequency stabilisation of semiconductor lasers for heterodyne-type optical communication systems", Electron. Lett., 1980, 16, pp. 179-181
- /8/ A. Fischer, R. Kullmer and W. Demtröder, "Computer controlled fabry-perot wavemeter", Opt. Commun. 39, 277-282 (1981)
- /9/ H. Furuta and M. Ohtsu, "Evaluations of frequency shift and stability in rubidium vapor stabilized semiconductor lasers", Appl. Opt. 28, 3737-3743 (1989)

Fig. 1 Schematic diagram of the synthesizer

PZT: piezoelectric transducer, BS_A and BS_B : beam splitters, Tr: transmitter, M: fixed mirror, WDM: wavelength division multiplexer, D_1 and D_2 : detector units. The synthesizer output may be used to lock transmitter lasers to the synthesizer frequencies.

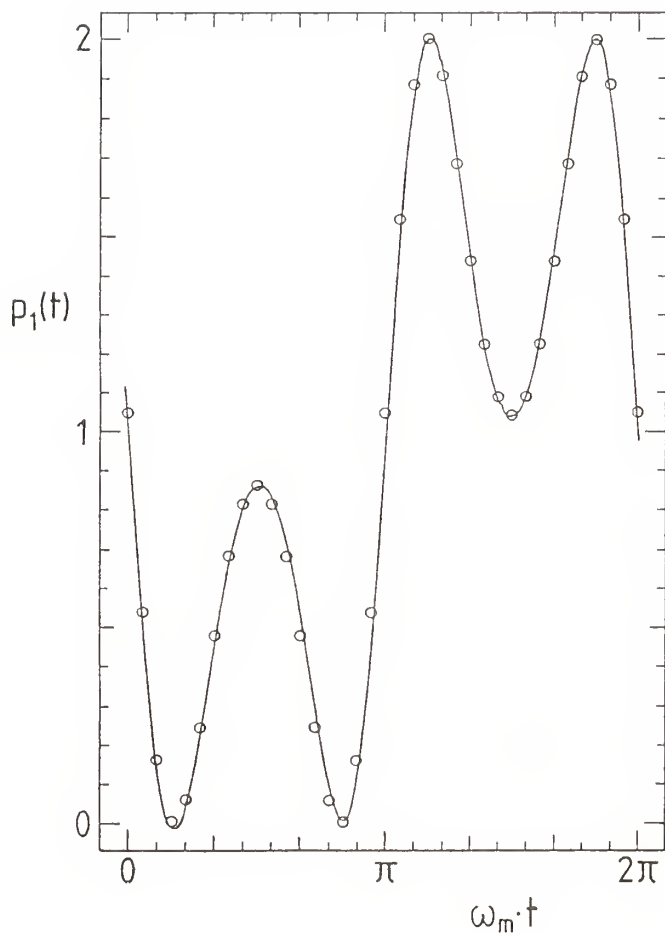
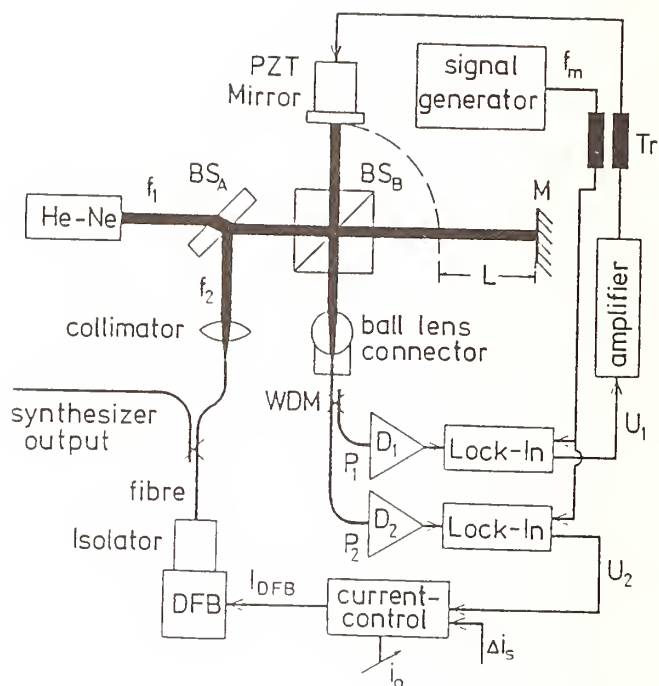


Fig. 2 The measured normalized intensity $p_1(t) = P_1(t)/(d_1 * I_1(t))$ (solid line) versus $\omega_m * t$ in comparison with the theoretical result (circles) with $\Delta l = -2,43 \text{ nm}$, $\Delta L(t) = 0$ and $y_0 = 153,6 \text{ nm}$ (eqn. 1). The input intensity $I_1(t)$ did not change during the measurement.

Characterization of High Birefringence Fiber for Sensor Applications

John Feth and James Blake
Honeywell
P.O. Box 21111 Phoenix, Arizona 85036-1111

ABSTRACT

In this paper we define a test station and several test procedures we have developed for characterization of incoming polarization maintaining fiber used in the production of fiber optic sensors and for signal processing applications.

All fiber optic sensors are constructed from an optical circuit. Circuit performance is governed by the character of the components, and can be optimized only if the components are well defined. At present, the burden of characterization is born by the optical circuit manufacturer who is driven by both necessity and practicality. In order to characterize the most basic optical component, the waveguide, and other more sophisticated components such as polarizers, couplers, and phase modulators, a test station capable of supplying and maintaining well polarized light at the operational wavelength must be available.

The optical source in the test station (figure 1) is a 15 nm wide multimode laser diode. In order to provide linearly polarized light of constant power at all azimuths, a polarizer and quarter wave plate are introduced immediately after the collimating lens. The polarizer, which need not be of high quality, is set at the azimuth which passes the most power, and the quarter wave plate, which need not be of great precision, is rotated relative to the polarizer until the collimated beam is isotropic within 1 dB when checked with a rotating polarizer.

The polarizer and analyzer used for characterization are high quality Glan-Thompson polarizers capable of extinguishing the collimated beam produced above to -50 dB or better. The coupling lenses are set up to focus and recollimate the beam between the polarizers and tested at various input azimuths first in one order and then with the focussing and recollimating lenses exchanged. The lens pair must be able to maintain an extinction ratio of -43 dB or better at any input azimuth in either order for use in the test station.

The test station detector is a precision device capable of measuring light levels from 0 to -90 dBm, and the test area is capable of darkening so that all power measurements are at least 10 dB above the ambient light level. We at Honeywell use

a test station boot strapped as described above to provide reliable and consistent data on all incoming fiber and fiber components with confidence that the data are not artifacts of the test system.

h-PARAMETER MEASUREMENT

In principle, well polarized light coupled into either axis of a birefringent fiber will remain in that axis during its transit through the fiber. In actuality, light is coupled from one axis to the other because of scattering in the fiber or local application of stress. In long coiled lengths small stresses applied as the fibers cross each other perturb the disposition of the axes enough to couple small amounts of light between axes.

A measure of the fiber capacity to maintain polarization is the h-parameter. An exact expression for the h-parameter is:

$$h = \tanh^{-1}(P_y/P_x)/L \quad (1)$$

An excellent approximation for $P_y \ll P_x$ is:

$$h = (P_y/P_x)/L \quad (2)$$

where P_x is the power exiting the fiber in the axis initially coupled to, P_y is the power coupled from the x axis and exiting the fiber in the y axis, and L is the fiber length, typically measured in meters.

An incoming h-parameter test is performed on fiber at the test station as wound on the shipping spool. Light is first coupled into the fiber with both polarizer and analyzer at arbitrary azimuths, and power maximized by translation of the fiber input end orthogonal to the direction of transmission. The polarizer and analyzer are then rotated sequentially to minimize the power on the detector, a condition recognized when rotation of the polarizer or analyzer in either direction increases the power. The output power of both axes is measured with the analyzer and the ratio P_y/P_x calculated and divided by the fiber length. The polarizer is rotated 90° and the process is repeated for the other axis.

Since all of the extrinsic causes for coupling between axes are potentially made available in coil winding, the h-parameter as measured on the shipping spool can easily degrade when the fiber is wound on a smaller diameter. Additionally, large temperature changes stress the coil and further degrade h-parameter performance so that, without careful attention to process, the h-parameter can increase by several orders of magnitude. Because of this, further testing of the fiber in its final coil form may be necessary for a true representation of h-parameter performance.

POLARIZER TEST PROCEDURE

A polarizer may be constructed from specially optimized highly birefringent fiber which not only maintains a single linear input polarization, but also severely attenuates any other polarization state when formed into a 2.5 to 3 cm coil. Measurement of a fiber polarizer presents the test station with an interesting challenge. The test procedure however, is straightforward and consists of four power measurements in units of dBm for simple calculation (figure 2).

Light is coupled into the fiber polarizer and the power is maximized by translation of the fiber end as above and further maximized by rotation of the input polarizer and analyzer. After the power is maximized, the analyzer is rotated 90° to the reject axis of the fiber polarizer and the power is measured as P_1 . The analyzer is returned 90° to the pass axis of the fiber polarizer the power is measured as P_2 . Next, the polarizer is rotated 90° to minimize the power, a condition recognized when rotation of the polarizer in either direction increases the power, and the power is measured as P_3 . Finally, the analyzer is rotated 90° to the reject axis of the fiber polarizer and the power measured as P_4 .

The extinction ratio of the fiber polarizer is found immediately as

$$\varepsilon = P_4 - P_2 \quad (3)$$

and the extinction ratio maintained by the coupling lens in the test station and the fiber lead to the coiled fiber polarizer is found as

$$k_1 = P_3 - P_2 \quad (4)$$

Similarly, the extinction ratio maintained by the fiber lead exiting from the coil of the fiber polarizer and the collimating lens is found as

$$k_2 = P_1 - P_2 \quad (5)$$

An analysis of the Jones matrices describing the test station and the fiber polarizer shows that the fiber polarizer extinction ratio can be measured accurately to $(k_1 + k_2)$ dB. The fiber leads to the coil of the polarizer are observed to degrade the -40 dB extinction ratio maintained by the coupling and collimating lenses to a nominal -35 dB. This yields $k_1 + k_2 = -70$ dB, or 20 dB better than the Glan-Thompson polarizer and analyzer pair in the test set up, with a precision of 1 dB.

BEAT LENGTH MEASUREMENT

Currently, fiber manufacturers characterize beat length by two methods, scattering and wavelength scanning. In the scattering method coherent light is coupled into both fiber axes and the beat length is observed directly as the separation of regions where light scatters from the fiber when the electric vectors in both axes are in phase. The wavelength scanning method couples narrow band light from a scanning monochromator into both axes and observes intensity fluctuation in the light exiting the fiber and passing through a polarizer at 45° to each axis.

Each of these methods has practical draw backs. Scattering varies inversely as the fourth power of wavelength, and to observe the effect in low loss polarization maintaining fiber would require a high power dye laser tuned to our operational wavelength in the infrared. The scanning method, while useful in the infrared, in practice, uses relatively few cycles of the intensity vs. wavelength curve to determine the beat length and consequently may not be of high accuracy.

An approximate scaling of beat length, L_B , with wavelength λ ,

$$L_B/\lambda = \text{constant} \quad (6)$$

is often used to estimate beat lengths in the infrared from those measured by the scattering method in the visible. This scaling relationship is useful for rough estimates of beat lengths, but breaks down when accuracies of a few percent are required.

Our new and very accurate beat length measurement method makes use of a well characterized partially coherent source, such as a laser diode. Consider a multimode laser diode having a coherence function $\gamma(T)$ depicted in figure 3. A high degree of coherence is established in a two beam interferometer when the two legs experience a differential path delay τ . If a polarization interferometer is built using birefringent fiber (figure 4) an interference signal will be established when the propagation delays in the two polarizations differ by τ .

The beat length of the fiber can be determined experimentally by finding the fiber length, ξ , through a series of cutbacks such that coherent interference between the two polarizations is observed. The expression

$$L_B \sim \xi\lambda/c\tau \quad (7)$$

relates fiber beat length to ξ . Here c is the free space propagation velocity of light and λ is the free space mean wavelength. This relationship is in fact only approximate because beat length is related to the phase velocities of the two polarizations whereas coherence is related to the group velocities of the two polarizations.

A more accurate expression relating the fiber length, ξ , to its beat length is given by taking dispersion into account giving

$$L_g^2/\lambda(dL_g/d\lambda) = \xi\lambda/c\tau \quad (8)$$

which is equivalent to eq. (7) if eq. (6) is assumed. The beat lengths measured with the group velocity approximation are common to both our method and the scanning wavelength method.¹ We have found that using this approximation yields results that differ from the scaled results of the scattering method by up to 10%. In interferometric sensors it is fringe visibility, which depends on the group delay, that determines sensor sensitivity. Because of this dependence, the useful definition of beat length often becomes the right hand side of eq. (8).

The polarization interferometer in figure 4 is used for beat length measurement of all incoming fibers. The interferometer is swept simply by stretching the fiber slightly and the degree of coherence, as measured by the normalized depth of modulation, is plotted as a function of fiber length in figure 5. The length required in eq. (7) is obtained as the length at which the depth of modulation is greatest.

The results of three typical fibers are compared with manufacturer's data scaled using eq. (6). The source used was a multimode laser diode having a mean wavelength of 818 nm and a coherence function peak corresponding to $c\tau = 2.00$ mm measured in a Mach-Zehnder setup. The fiber lengths required to establish coherence between the two polarizations were several meters measured to an accuracy of 1 cm. Thus the beat lengths are determined to an accuracy better than 1%. Table 1 shows beat lengths for the two fibers compared to the manufacturer's data scaled to our wavelength. Figure 5 shows a plot of the degree of coherence observed as the York II fiber was cut back.

The manufacturer's data for York was scaled from a value at 633 nm obtained with the scattering method, and the manufacturer's data for Fujikura was scaled from a measured value at 850 nm obtained with the wavelength scanning method. That the scaled beat lengths of the York fibers exhibit larger differences from our results than does the Fujikura fiber is due to the difference in beat length measurement techniques of the two vendors.

Reference:

- 1) S. C. Rashleigh, Optics Letters 6, 336 (1982)

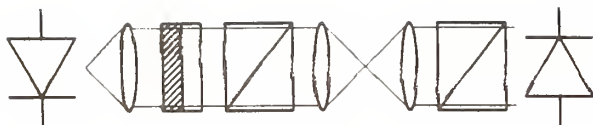


Fig. 1. Test Station. From left to right, source, collimating lens, polarizer, wave plate, Glan-Thompson polarizer, focussing lens, collimating lens, Glan-Thompson analyzer, detector.

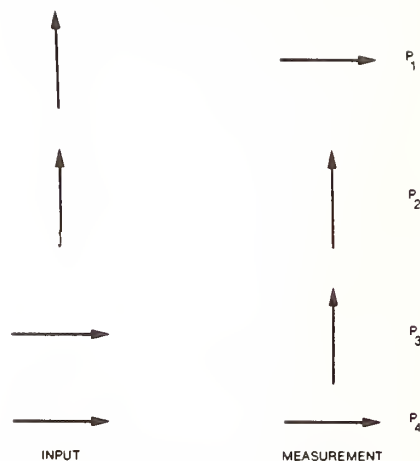


Fig. 2. Polarizer Test States. Fiber polarizer pass axis is vertical, reject axis horizontal.

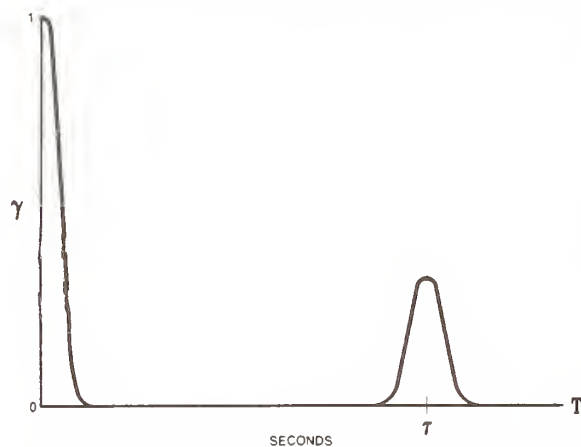


Fig. 3. Coherence function of a multimode laser diode.

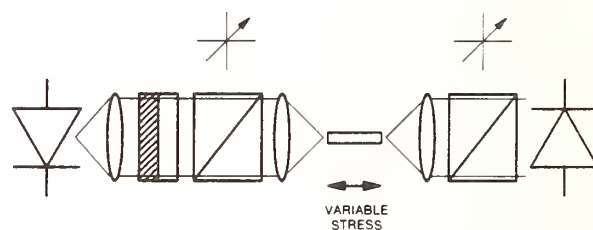


Fig. 4. Polarization interferometer for beat length test. Polarizer and analyzer alignment is at 45° relative to fiber axes.

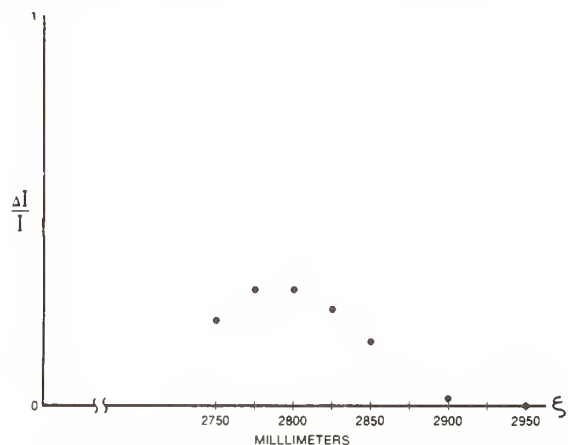


Fig. 5. Degree of coherence vs. fiber length for York II.

MANUFACTURER	MANUFACTURER'S SCALED L_B (MM)	COHERENCE FUNCTION L_B (MM)	DIFFERENCE (%)
YORK I	1.29	1.17	-10
YORK II	1.16	1.13	-2.5
FUJIKURA	1.635	1.61	-1.5

Table 1

Interpretation of Polarization Dispersion in a Single-Mode Fiber

Makoto TSUBOKAWA and Masaharu OHASHI
NTT Transmission Systems Laboratories
Tokai, Ibaraki-ken, 319-11 Japan
phone: +81 292 87 7312, facsimile: +81 292 87 7866

I. Introduction

In a weak birefringent fiber such as a typical single-mode fiber, the group delay difference between two eigen modes decays due to the mode conversion effect.^{1,2} It tends to saturate with distance, and its second moments, contributing to the pulse broadening, increases at a constant rate.¹⁻⁵ However, strictly speaking, no polarization mode is defined for a fiber having birefringence perturbation along a fiber axis. Thus, polarization dispersion experimentally evaluated for a real fiber is not yet clear. Recently, Poole suggested a phenomenological approach⁶ to this problem, and suggested that 'the principal state' corresponding to two orthogonal polarization states independent on a wavelength to the first order, exists in a fiber with birefringence perturbation. Using the model, polarization dispersion has already been experimentally evaluated as the group delay difference between the two states, in the same manner as for an ideal fiber having uniform birefringence.⁷⁻⁹ Although the principal state model enables an explanation of the group delay characteristics of a fiber, it is not always clearly determined for a fiber with extensive mode conversion. In these reports, moreover, the group delay difference is merely treated as the accumulation of random variables with zero mean regardless of mode conversion. Therefore, it is significant to reconsider the group delay characteristics through evolution of the SOP (state of polarization) of light. This paper shows a new interpretation of polarization dispersion of a long single-mode fiber. The group delay difference is evaluated through the evolution of SOP on the Poincaré sphere, and its length dependence is briefly estimated.

II. Polarization dispersion resulting from the SOP of light

In a general single-mode fiber, the eigen polarization modes can be locally defined along the fiber for a short length range. Here, we consider a tandem fiber model consisting of short fiber pieces in which the eigen modes are determined. (The principal state can also be used in place of the eigen mode.) The eigen modes in the fiber pieces are different each other, and mode couplings occur at fiber connections. A typical example of evolution of SOP's along a fiber piece is shown in Fig. 1, using the Poincaré sphere representation. In Figs. 1(a) and 1(b), $\mathbf{S}(\omega, z)$ is a unit Stokes vector specifying the SOP at ω and z . \mathbf{P}_{j1} and \mathbf{P}_{j2} are unit vectors representing eigen modes assumed from SOP of input ($j = i$) or output ($j = o$) light, and Ω_j describes rotation. \mathbf{P}' are a unit vector defined in a fiber piece and Ω' describes rotation which governs real change of SOP with z . Symbols A and C indicate coordinates of the Stokes vectors $\mathbf{S}(\omega, z)$ and $\mathbf{S}(\omega + \Delta\omega, z)$, where $\Delta\omega$ is the small frequency deviation, and B and D indicate coordinates of $\mathbf{S}(\omega, z + \Delta z)$ and $\mathbf{S}(\omega + \Delta\omega, z + \Delta z)$, respectively. The SOP changes from A to B and from C to D on the sphere as light propagates from z to $z + \Delta z$. Here, Δz is assumed to be much less than the correlation length of modal birefringence of a fiber. As shown in Fig. 1, vector $\Omega \times \mathbf{S}$, which is oriented along distance z , is not always parallel to the direction of $\partial \mathbf{S}(\omega, z) / \partial \omega$ if mode conversion occurs. In other words, the Stokes vector did not always trace a complete arc on the sphere as a function of

wavelength. In Fig. 1, the angles AOC and BOD are respectively written as

$$\psi(\omega, z) = |\partial \mathbf{S}(\omega, z)/\partial \omega|, \quad \psi(\omega, z + \Delta z) = |\partial \mathbf{S}(\omega, z + \Delta z)/\partial \omega|. \quad (1)$$

If the locus drawn through the points A and C (or B and D) is an arc on the sphere, the input (or output) lights are completely represented by two eigen modes. In this case, the phase differences between two modes are

$$\begin{aligned} \phi(\omega, z) &\approx \psi(\omega, z)/\cos \theta_i, & \text{for input light,} \\ \phi(\omega, z + \Delta z) &\approx \psi(\omega, z + \Delta z)/\cos \theta_o, & \text{for output light,} \end{aligned} \quad (2)$$

with

$$\theta_j = \frac{q_{j1} - q_{j2}}{q_{j1} + q_{j2}}, \quad (j = i, o). \quad (3)$$

Here, θ_j is the latitude of an arc against two poles \mathbf{P}_{j1} and \mathbf{P}_{j2} , and q_{j1}/q_{j2} corresponds to the power distribution ratio of two eigen modes. As described above, in general, the Stokes vector of input and output light did not draw circular loci. It is therefore difficult to determine the phase difference ϕ over the wavelength bandwidth. On the other hand, ψ defined in Eq.(1) is determined regardless of such a restriction. ψ is given as the product of ϕ between modes optionally assumed and $(1/\cos \theta_i)$ depending on the power ratio. Both ψ and ϕ are identical when the locus of the Stokes vector is the meridian on the sphere.

Let us consider what the locus of the Stokes vector of output light means. From Fig. 1(b), the increment $\Delta\psi(\omega, z) \{ \equiv |\psi(\omega, z + \Delta z) - \psi(\omega, z)| \}$ per short distance Δz satisfies the relation:

$$\begin{aligned} \Delta\psi(\omega, z) &\simeq \left| \frac{\partial \mathbf{S}(\omega, z + \Delta z)}{\partial z} \right|^{-1} \left(\frac{\partial \mathbf{S}(\omega, z + \Delta z)}{\partial \omega} \cdot \frac{\partial \mathbf{S}(\omega, z + \Delta z)}{\partial z} \right) \\ &\quad - \left| \frac{\partial \mathbf{S}(\omega, z)}{\partial z} \right|^{-1} \left(\frac{\partial \mathbf{S}(\omega, z)}{\partial \omega} \cdot \frac{\partial \mathbf{S}(\omega, z)}{\partial z} \right). \end{aligned} \quad (4)$$

It is apparent from Eq.(4) that the increment $\Delta\psi$ is approximately equivalent to the difference between the $\psi(\omega, z)$ and $\psi(\omega, z + \Delta z)$ projected on the circular locus of the Stokes vectors. That is, $\psi(\omega, L)$ observed at a fiber output end contains information on $\Delta\psi$'s locally determined along a fiber with length L . It is here noted that $\psi(\omega, L)$ is not expressed as a sum of all $\Delta\psi$'s, but as a result of vector summation describing the mode conversion effect. In other words, $\psi(\omega, L)$ is regarded as a sum of $\Delta\psi$'s considering the weight of mode power distributions locally fluctuating along the fiber.

III. Brief Estimation of Length Dependence of Polarization Dispersion

When modal birefringence perturbation is governed by the random distribution function, it has been considered that the group delay difference tends to saturate as fiber length increases. Consequently, a pulse width, which is generally estimated as a standard deviation for random values with zero mean, increases with fiber length at a constant rate as a function of the mode coupling coefficient. In some experimental reports, however, the group delay difference still increases over hundred kilometer lengths, which is much longer than the correlation length of birefringence fluctuation. It implies that $\partial\psi/\partial\omega$ is not regarded as the conventional group delay difference.

We now consider the length dependence of $\psi(\omega, z)$ using the above described model. Let us assume that angle $\alpha(\omega, z)$ between $\partial \mathbf{S}/\partial \omega$ and $\boldsymbol{\Omega} \times \mathbf{S}$ obeys probability density function $p(\alpha)$. α is equivalent to the relative angle change between birefringent axes of adjoining

fiber pieces. For geometrical simplicity, the difference between ψ_{AB} and ψ_{CD} is considered. Assuming $\psi_{AB} - \psi_{CD} = \psi_{AB}$ and $\psi_{CD}=0$, ψ_{BD} is approximately written as

$$\psi_{BD} \approx \frac{1}{\pi} \int_0^\pi p(\alpha) [\psi_{AB}^2 + \psi_{AC}^2 - 2\psi_{AB}\psi_{AC} \cos \alpha] d\alpha, \quad (5)$$

for $|\psi_{AB}|, |\psi_{AC}| \ll \pi$. Here, subscripts of ψ stand for coordinates on the sphere shown in Fig. 1. From Eq.(5), as an example, when α obeys uniform random values for $[0, \pi]$, we can find that the increment $\Delta\psi (= \psi_{BD} - \psi_{AC})$ per unit bandwidth is always greater than zero. As ψ_{AB}/ψ_{AC} decrease, increment $\Delta\psi$ decays. (In this case, $\Delta\psi \propto (\psi_{AB}/\psi_{AC})^2$ is approximately valid.) Thereby, we can roughly estimate that the ψ is proportional to z^x , where $0 < x < 1$. To clear this problem, the length dependence of $\partial\psi/\partial\omega$ is investigated by calculating the SOP of light propagating through a single-mode fiber with birefringence fluctuation.¹⁰ In this calculation, a fiber piece length Δz is 10 m, modal birefringence B is fixed to be 1×10^{-7} , which corresponds to that in a fiber with core ellipticity of about 0.5 %, and angle α of birefringent axes obeys the random distribution functions. $\psi(\omega, L)$ is obtained by iterative calculation¹⁰ for all fiber pieces. Calculated results are shown in Figs. 2(a) and (b). Curves A, B, and C indicate the ψ when α obeys the gaussian random deviation with variance σ of 0, $\pi/18$, and $\pi/3$ about the initial values α_0 , and curve D when α obeys uniform random distribution for $[0, \pi]$. It is seen from Figs. 2(a) and (b) that $\partial\psi/\partial\omega$ shown by curves B, C, and D roughly increases with increasing z at an almost constant rate of $\sim \sqrt{z}$ over a 1000 km-length. Note that it can not be precisely estimated at a distance z because of the length dependence accompanying fluctuation. This result well explains the above discussion and the results in previous reports⁷. Polarization dispersion, $\psi(\omega, z)$ per unit bandwidth, evaluated from the SOP measurement, should be interpreted as a value like a pulse width in the case of extensive mode coupling.^{1,5}

IV. Conclusion

Polarization dispersion evaluated from the SOP of light was specified for a single-mode fiber with birefringence perturbation. The group delay difference observed at a fiber end contains information of the power distribution ratios at local parts of a fiber, and it grows with distance, like a pulse width. As a result, the evaluated group delay difference is expected to increase with distance at an almost constant ratio over a 1000 km-length. Evaluation of polarization dispersion is noted as a potential limitation in long-haul transmission systems.

The authors wish to thank T. Imai for his useful comments, and Drs. S. Shimada, K. Ishihara, and M. Kawase for guidance and encouragement.

References

1. S. D. Personick, Bell Syst. Tech. J., **50**, 843 (1971).
2. S. Kawakami and M. Ikeda, IEEE J. Quantum Electron., **QE-14**, 608 (1978).
3. M. Tsubokawa, N. Shibata, and S. Seikai, J. Lightwave Technol., **LT-3**, 850 (1985).
4. M. Tsubokawa and Y. Sasaki, Electron. Lett., **24**, 350 (1988).
5. C. D. Poole, Opt. Lett., **13**, 844 (1988).
6. C. D. Poole and R. E. Wagner, Electron. Lett., **22**, 1029 (1986).
7. N. S. Bergano, C. D. Poole, and R. E. Wagner, J. Lightwave Technol., **LT-5**, 1618 (1987).
8. D. Andresciani, F. Culti, F. Matera, and B. Daino, Opt. Lett., **13**, 844 (1987).
9. C. D. Poole, N. S. Bergano, R. E. Wagner, and H. J. Schulte, J. Lightwave Technol., **6**, 1185 (1988).
10. M. Tsubokawa and Y. Sasaki, Trans. IEICE Japan, **E 73**, 519 (1990).

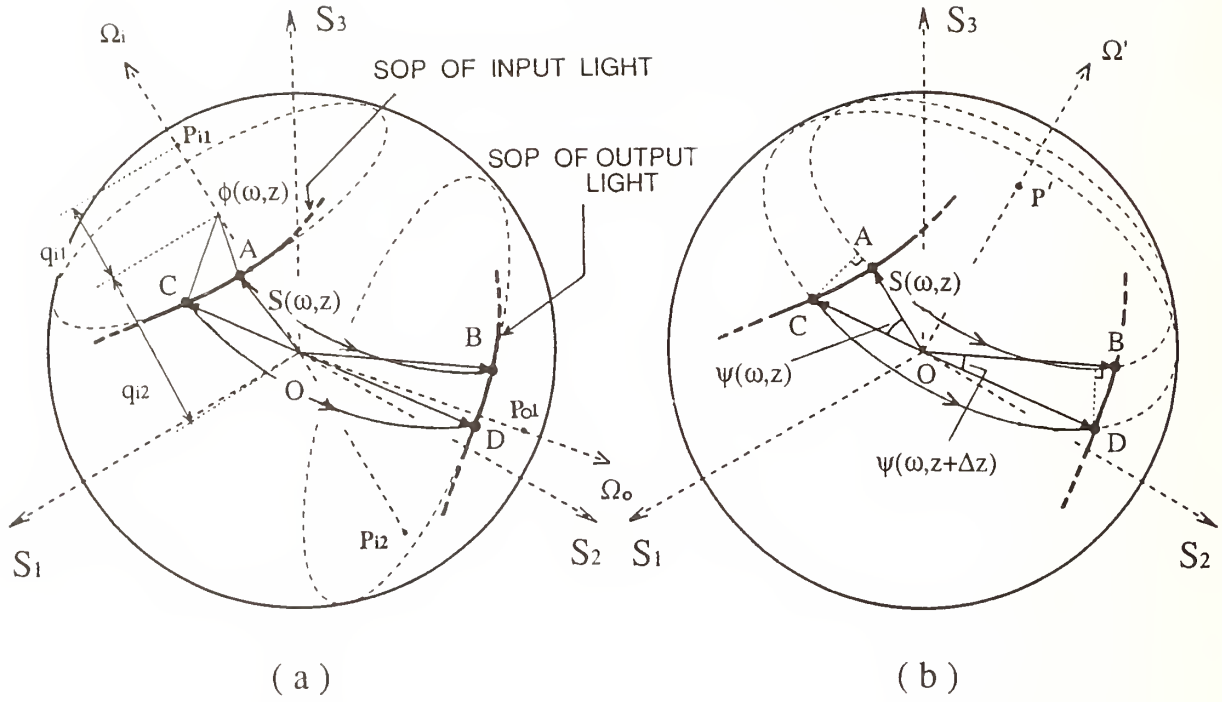


Fig. 1 SOP change on the Poincaré sphere for light propagating through a fiber piece. Both (a) and (b) explain identical SOP situations. Bold lines indicate the locus of Stokes vectors at z and $z + \Delta z$. The coordinates A and C, indicating SOP's of input light, change to B and C, respectively, as light propagates distance Δz .

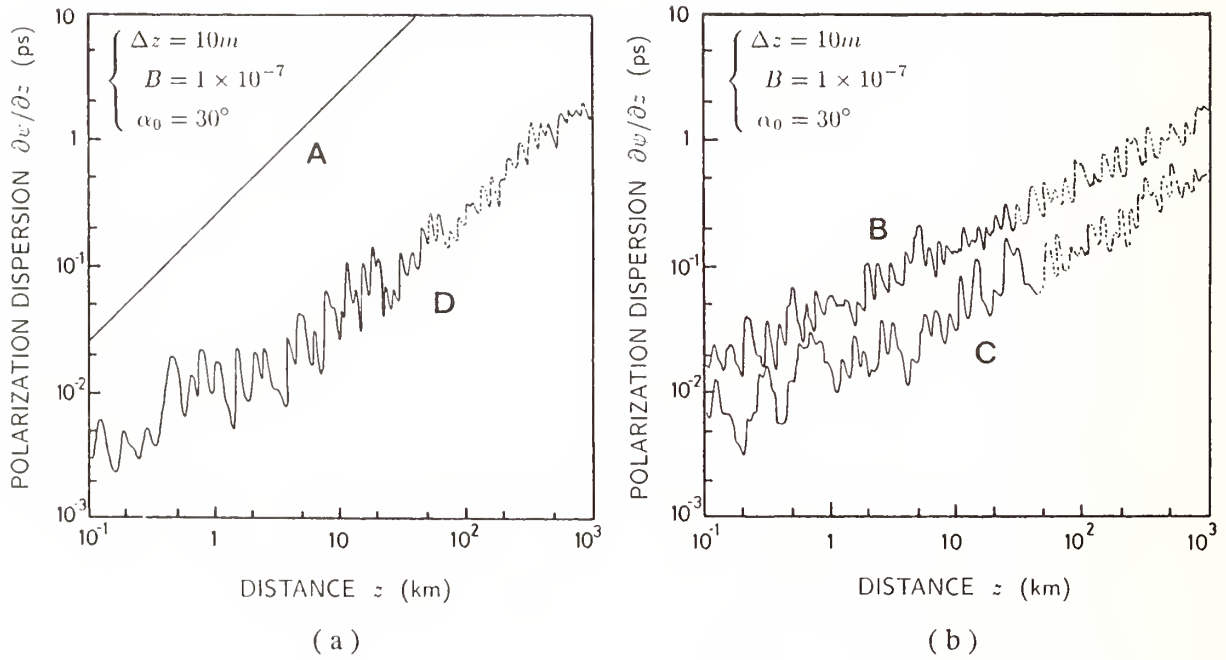


Fig. 2 Length dependence of polarization dispersion given by $\partial\psi/\partial\omega$. Curves A~D are calculated for different birefringence perturbation. Fine fluctuation are not fully resolved in the region of dotted curves.

Polarization Mode Dispersion of short and long single-mode fibers

Nicolas Gisin, J.P. Pellaux,
Group of Applied Physics
University of Geneva
1211 Geneva 4
Switzerland

Jean-Pierre Von der Weid
Physics department
Pontificia Universidade Catholica
C.P. 38071
Rio de Janeiro 22452, Brazil

Abstract

We present the analysis of the polarization mode delays at the exit of the test fiber by a Michelson interferometer made out of a polarization maintaining fiber coupler. This technique is applied to the measurement of short fiber samples as well as to long fibers, the length of the test fiber no longer being a limitation of the method. A statistical model for polarization mode dispersion with random mode coupling is presented and compared to actual measurements.

Polarization maintaining interferometry.

When partially coherent light is directly launched at a Michelson interferometer, the fringes envelop gives the Fourier transform of the input light spectrum, centered at the position corresponding to equal group delays between the two arms of the interferometer^{1..3}. When the birefringence of the interferometer arms is considered, each polarization mode gives rise to its own group delay, so that a double structure can be observed^{1..3} (Fig 1). In order to avoid the inconvenient wings of the sinc function corresponding to the in-focus square spectrum, a gaussian spectrum is obtained by appropriately filtering high spatial frequencies by means of an apodization mechanism consisting in moving the endface of the launching fiber away from the focal plane of the monochromator's optics.

Because the fast and slow modes of the interferometer are completely separated, the system can be considered as a polarization analyzer. A single polarization can be selected by an appropriate choice of the time delay in the variable air path. Therefore, the interferometer can be used to analyze the polarization mode delays of a single mode fiber placed between the launching fiber and the interferometer, without making use of discrete optics and polarizers^{1..5}. The polarization maintaining interferometer can thus be used to analyze the autocorrelation function of the input light after passing through a birefringent fiber. If more than one piece of birefringent fiber are concatenated with some coupling probability between fast and slow modes, the input light at the interferometer can be described as series of coherence peaks, each one corresponding to a different time of flight along the whole concatenated input fiber. The interferometer's output is then the autocorrelation function of these coherence peaks, whose intensities are determined by the coupling probabilities between the birefringent pieces and the projections onto the interferometer's polarization eigenmodes. Let us emphasize that the concept of principal states of polarization is not appropriate for the spectral width of ≈ 20 nm as we used.

Let us briefly introduce our theoretical model. We consider a single mode optical fiber with birefringence too weak to maintain the polarization, so that the fast mode and the slow mode easily couple. The existence of some birefringence implies that there are two group velocities, the fast one and the slow one; and the random coupling implies that at random positions along the fiber some of the energy in one mode couples to the other mode. We are interested in the distribution of time of flight τ after traveling a fiber length ℓ . Let v denote the mean group velocity, and $v \pm \delta v$ the fast and slow group velocities. We first introduce our model with discrete coupling positions. Assume that the light travels a distance $\delta\ell$, then couples with probability p to another mode. After a distance $m\delta\ell$ there are clearly m possibilities: the light moved n times between the two modes, with $n=0, \dots, m-1$. Let $\delta\ell/h$ be the probability of coupling over the length $\delta\ell$, i.e. h = mean coupling length, and let ϵ_i be independent random variables:

$$\epsilon_i = \begin{cases} +1 & \text{with probability } 1 - \delta\ell/h \\ -1 & \text{with probability } \delta\ell/h \end{cases}$$

The time τ_m^\pm at which the position $m\delta\ell$ is reached reads:

$$\tau_m^\pm = m\delta\ell \frac{1}{v} \pm \Delta\delta\ell(1 + \epsilon_1 + \epsilon_1\epsilon_2 + \dots + \epsilon_1\epsilon_2 \dots \epsilon_{m-1})$$

where the sign \pm depends on the fast or slow mode at position $m\delta\ell$ and $\Delta = -\delta v(1/v)^2$. This model has a continuous limit⁵ which leads to the following eq. for the time of flight distribution:

$$\frac{\partial^2 \rho_\ell(\tau)}{\partial \ell^2} = \Delta^2 \frac{\partial^2 \rho_\ell(\tau)}{\partial \tau^2} - \frac{2}{h} \frac{\partial \rho_\ell(\tau)}{\partial \ell}$$

This equation is well known from the early days of telegraphy^{7,8} and is called the *telegrapher's equation*. Its solution is known analytically⁸:

$$\rho_\ell(\tau) = \frac{1}{2} e^{-\ell/h} \left\{ \delta(\tau - \Delta\ell) + \delta(\tau + \Delta\ell) + \frac{\epsilon(\Delta\ell - |\tau|)}{h\Delta} \left[I_0\left(\sqrt{\frac{\ell^2 - \tau^2}{h^2 - \Delta^2 h^2}}\right) + \frac{\ell}{h} \frac{1}{\sqrt{\frac{\ell^2 - \tau^2}{h^2 - \Delta^2 h^2}}} I_1\left(\sqrt{\frac{\ell^2 - \tau^2}{h^2 - \Delta^2 h^2}}\right) \right] \right\}$$

where ϵ is the step function: $\epsilon(x)=1$ for $x>0$, $\epsilon(x)=0$ for $x\leq 0$. The mean square deviation of the distribution $\rho_\ell(\tau)$ can be computed explicitly:

$$(\Delta\tau)^2 \equiv E\{\tau^2\} - E\{\tau\}^2 = \frac{1}{2} \Delta^2 h^2 \left[2\ell/h - 1 + e^{-2\ell/h} \right] \quad (1)$$

This expression is identical to the one found by C.D. Poole⁹.

The table 2 presents the experimental results for three commercially available fibers, labeled A, B and C. After subtraction of the central peak and of the noise in the wings, the polarization mode dispersion is computed as the second moment. All fibers have also been measured on a short sample, using the technique described in ref. 3.

The figure 3, fiber A, shows clearly some additional fringes. The corresponding birefringence is due to the bending on the drum, as has been

checked by rotating the drum axes with respect to the interferometer: for some angle the side peaks disappear, and at 90 degrees they are maximum. The drum radius was 140 mm and the measured induced polarization mode dispersion 0.11 ps/km. If we compare this value to the 30.5 ps/km that we obtained¹⁰ for the much smaller radius of 7.5 mm, we find a remarkable agreement with Ulrich's law¹¹: The bend induced polarization mode dispersion is proportional to the square of the inverse of the radius.

The fibers B and C have a relatively large polarization mode dispersion. The figure 4 is essentially independent of the drum's orientation. This indicates that the complete random state is achieved and the polarization mode delay increases with the square root of the fiber length, in accordance with eq. (1). The measurements on some meters long samples confirm the existence of accidental birefringence in these two fibers. On a sample, however, one can only measure the difference of speed Δ , and not the mean coupling length h . One can thus not compare the results on a sample with the measurements on the full length fiber. However, using both results and equation (1), one can estimate the value of the mean coupling length: ≈ 30 meters for fiber B and ≈ 20 meters for fiber C.

Interferometry in polarized light is an easy to implement method applicable to the measurement of residual birefringence in single-mode fibers. The time range from 0.1 to 80 ps is sufficient to characterize the standard single-mode fibers. Our results show that some standard commercial single-mode fibers have a non negligible polarization mode dispersion due to residual or accidental birefringence induced during fiber manufacturing. In the case of small residual birefringence, the bend induced polarization mode dispersion remains the only source of polarization dispersion, even for a drum as large as 28 cm diameter.

Acknowledgment

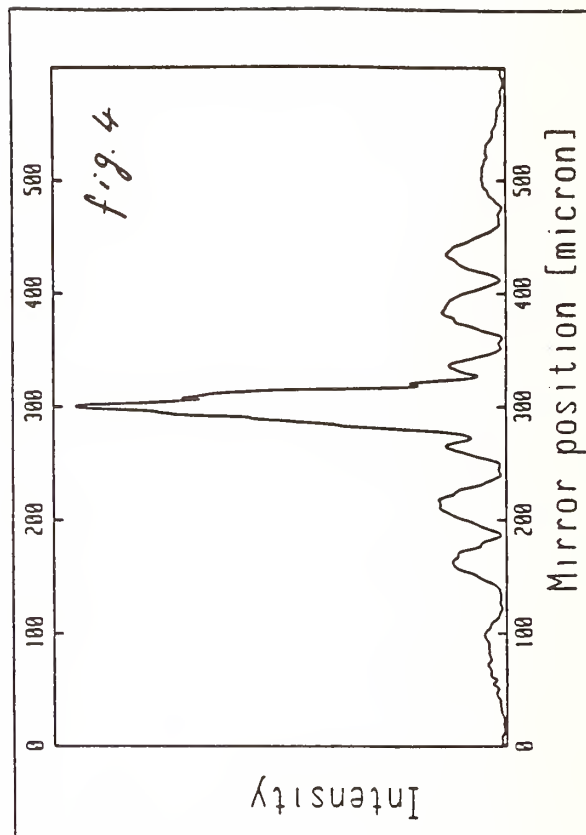
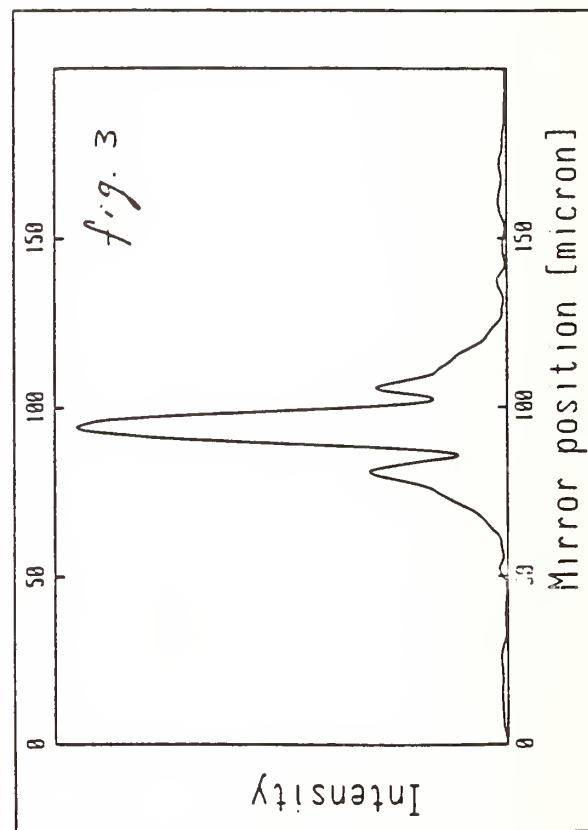
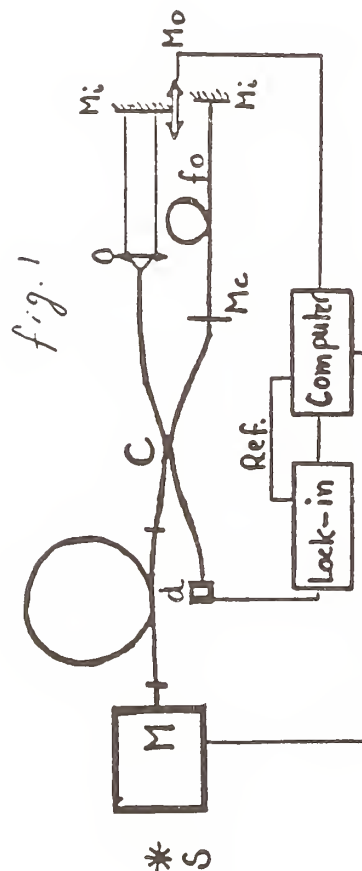
It is a pleasure to acknowledge financial support from the Swiss PTT.

References

1. JP. Von der Weid, L. Thévenaz and JP. Pellaux, *Electron. Lett.*, **23**, pp 151-152, 1987.
2. PL. Francois, M. Monerie, C. Vassallo, Y Durteste and FR. Alard, *J. Lightwave Technol.* vol LT-7, pp 500-513, 1989.
3. L. Thévenaz, JP. Pellaux, N. Gisin and JP. Von der Weid, *J. Lightwave Technol.* vol LT-7, pp 1207-1212, 1989.
4. C. Edge, W.J. Stewart and I. Bennion, *ECOC'86*, pp 271-274, 1986.
5. J. Pelayo, F. Lopez and F. Villuendas, *ECOC'89*, pp 510-513, 1989.
6. M. Kac, *Rocky Mountain J. Math.*, **4**, 497, 1974.
7. W. Thomson (Lord Kelvin), *Proc. Roy. Soc.* **VII**, 382, 1855; G. Kirchhoff, *Ann. der Phys.* **193C**, 25, 1857.0; Heaviside, *Phil. Mag.* **II**, 135, 1876.
8. J.A. Stratton, "Electromagnetic theory", chapter 9, McGraw-Hill, New-York, 1941.
9. C.D. Poole, *Opt. Lett.* **13**, pp 687 689, 1988.
10. R. Passy, JP. Von der Weid, L. Thévenaz, N. Gisin and JP. Pellaux, "devices", to appear in the proceedings of SPIE "Interferometry'89, 100 years after Michelson. State of the art and applications", 1989.
11. R. Ulrich, S.C. Rashleigh and W. Eickhoft, *Optics Lett.* **5**, 273, 1980.

Fiber	Type	PHD on sample	PHD on boblin	ø boblin
A	matched cladding	$< 1 \frac{\text{fs}}{\text{m}}$	$0.17 \frac{\text{ps}}{\text{km}} \xrightarrow{\ell} 0.11 \frac{\text{ps}}{\text{km}}$	28 cm
B	matched cladding	$112 \frac{\text{fs}}{\text{m}} \xrightarrow{\ell} 3.5 \frac{\text{fs}}{\text{m}}$	$0.3 \frac{\text{ps}}{\text{km}} \xrightarrow{\sqrt{\ell}} 0.30 \frac{\text{ps}}{\text{km}}$	15 cm
C	depressed cladding	$89 \frac{\text{fs}}{\text{m}} \xrightarrow{\ell} 24.1 \frac{\text{fs}}{\text{m}}$	$2.3 \frac{\text{ps}}{\text{km}} \xrightarrow{\sqrt{\ell}} 1.73 \frac{\text{ps}}{\text{km}}$	28 cm

Table 2 Polarization Mode Dispersion for 3 commercial single-mode fibers, measured on a meters long sample and kilometer long fibers on a drum. The exact lengths of the samples and the drums are indicated, the results are then normalized to one kilometer using either a linear (ℓ) or square root law ($\sqrt{\ell}$) as indicated, depending on the absence or presence of random polarization mode coupling. The wavelength is 1300 nm. Fiber A and B are matched cladding single-mode fibers, Fiber C is a depressed cladding single-mode fiber.



Distributed Strain Measurements in Optical Fibers Using Brillouin Optical-Fiber Time Domain Analysis

Tsuneo Horiguchi, Mitsuhiro Tateda and Toshio Kurashima

NTT Transmission Systems Laboratories

Tokai, Ibaraki-ken, 319-11, Japan

1. INTRODUCTION

Accurate measurement of strain induced by fiber manufacturing, cabling and installation is necessary to assure the long-term reliability of optical fibers. The strain has been evaluated by measuring the fiber elongation using optical pulse or phase delay [1][2]. This technique can measure average strain over the full length of the fiber. However, it cannot accurately estimate the distributed strain along the fiber length, which is of great importance for the prediction of fiber lifetime [3]. By using distributed strain sensors [4]-[7], the strain in an optical fiber cable may be evaluated, if the sensors are attached to the cable. However, it is a very expensive procedure for long optical fiber cables.

This paper describes a recently developed technique for the distributed strain measurements. With this technique, the strain in optical fibers can be evaluated by accessing the test fiber itself without using the above-mentioned sensors. This paper also reviews recent applications of the technique.

2. PRINCIPLES

The Brillouin frequency shift ν_b for silica optical fibers has been found to be very sensitive to the strain ϵ , and can be expressed as follows [8]:

$$\nu_b(\epsilon) = \nu_b(0) + M\epsilon$$

where M is the proportional constant. The developed technique relies on the strain dependence of the Brillouin frequency shift, which is analyzed in a time domain. Therefore, this technique is called Brillouin optical-fiber time domain analysis (BOTDA) [9][10]. The basic configuration of BOTDA and its signal waveform is schematically shown in Fig. 1. In BOTDA, the pump pulse and the probe continuous wave lights counterpropagate in a test fiber. The probe light is detected at the fiber end from which the pump pulse is launched. If the frequency difference $\Delta\nu = \nu_p - \nu_{cw}$ between the pump and probe waves is tuned to the Brillouin frequency shift ν_b at

some location along the fiber, the probe signal is amplified there due to stimulated Brillouin scattering between the pump and probe lights. Therefore, a distributed strain measurement is made possible by measuring the time-dependent probe light power for various $\Delta\nu$, and by obtaining the Brillouin frequency shift ν_b anywhere along the fiber length. The measured Brillouin frequency shift at some location, which is a center frequency of the Brillouin gain spectrum, corresponds to the strain ϵ which is averaged around that location over the fiber length of spatial resolution in BOTDA. Assuming that the stimulated Brillouin scattering is fast enough to respond to the pump light pulse, the spatial resolution in BOTDA is given by [9]

$$\delta z = vw/2$$

where v is the light velocity in the fiber, and w is pump pulse width. Strain measurement accuracy of BOTDA is given by [9]

$$\delta\epsilon = (\Delta\nu_b/M)/\sqrt{2}(\text{SNR})^{1/4}$$

where $\Delta\nu_b$ is the Brillouin gain bandwidth and SNR is the signal-to-noise ratio of the detected BOTDA signal. For $\Delta\nu_b=50$ MHz, $M=581$ MHz/% [11] at 1319 nm wavelength, and $\text{SNR}=100$, then $\delta\epsilon=0.02$ % is expected.

When the strain is not uniform within the spatial resolution, the Brillouin gain bandwidth there is greater than that for a uniformly elongated fiber. Therefore, the magnitude of the strain variation within the spatial resolution can be evaluated from the increase in the Brillouin gain bandwidth [12].

An experimental arrangement for testing the BOTDA performance is shown in Fig. 2 [9]. A Nd:YAG laser and a distributed feedback laser diode (DFB-LD) were used as the pump and probe light sources, the wavelength of which was 1319 nm. A 1 μ s pulse was generated from the Nd:YAG laser by means of an acoustooptic modulator (AO). The frequency difference between the two lasers was monitored by an RF-spectrum analyzer, which is not shown in the figure, and was changed with an interval of 12 MHz. The power coupled into a single-mode fiber was 0.5 mW from each laser. The fiber was a standard single-mode fiber composed of three portions A to C. The intermediate portion B was intentionally elongated.

In Fig. 3, the BOTDA signal waveforms for various frequency differences $\Delta\nu$ are displayed in three dimensions. The small and large peaks at the fiber ends are Fresnel reflections of the pump pulse. These Fresnel reflections could be minimized by using an optical filter in front of the detector. By tracing the BOTDA signal power versus $\Delta\nu$ at any location along the test fiber, the Brillouin gain spectrum there was obtained. In turn, the frequency difference at which the Brillouin gain spectrum reaches its maximum was obtained as a function of the distance along the test fiber. The results are shown in Fig. 4, where the Brillouin frequency shift was transformed into the strain ϵ using the ν_b - ϵ relationship. The strain, intentionally applied in portion B of the fiber, was clearly measured with the spatial resolution of 100 m, and was estimated at 0.16 %. It was found that the measured value closely agrees with that measured by mechanical tension meter of 0.18 %.

3. APPLICATIONS

3.1 RESIDUAL STRAIN AFTER CABLE INSTALLATION

A technique for continuous optical fiber strain measurement during cable installation has been reported [1]. However, residual strain distribution after the installation, which is of primary importance for long-term reliability of the cable, is not thoroughly understood yet. Recently the measurement has been performed for a field-installed fiber using BOTDA [13]. The conduit route of the installation and the measurement results are shown in Fig. 5. The installed cable was a 24-fiber slotted-core type single-mode optical fiber cable. It can be seen in Fig. 5 that about 0.06 % strain occurs in the conduit section between the corners marked D and E. These results confirm that BOTDA is a powerful tool for evaluating cable installation technology.

3.2 FIBER STRAIN IN A BENT CABLE

When a fiber cable is bent, the fibers in the cable experience tensile and compressive strain at a period of fiber stranding pitch. The stranding pitch is usually so short (less than 1 m) that it is very difficult to estimate this strain through the time-resolved measurement of the center frequency of the Brillouin gain spectra. However, as explained in 2, the magnitude of the strain variation can be evaluated from the increase of the Brillouin gain bandwidth $\Delta\nu_b$. In Fig. 6, the relative center frequency and bandwidth of Brillouin gain spectra versus distance along the fiber for a bent cable are shown. The origin of the relative center frequency in Fig. 6 is the Brillouin frequency shift ν_{bs} for the straight cable. A 300 m fiber cable is wound on a drum of 0.2 m radius, and is segmented into two layers, inner and outer, each 150 m in length. Lead fibers 20 m in length were spliced at both ends of the cable. It can be seen in Fig. 6 that the cable bending increased the Brillouin gain bandwidth by as much as 150 MHz, while having virtually no effect on the center frequency of the Brillouin gain spectra. In Fig. 6, we can also see a little difference in the Brillouin gain bandwidth between the inner and outer layers due to a small difference in the bending radius. The strain amplitude ϵ_a due to the cable bending, which is obtained from the BOTDA measurements, has been found to be in good agreement with that calculated from the cable structure [12].

3.3 RESIDUAL STRESS BY FIBER DRAWING

SiO₂ core/F-SiO₂ clad single-mode optical fibers are expected to have low optical loss because Rayleigh scattering loss can be reduced by avoiding dopants in the core. However, in these fibers, relatively large residual stress is induced by the fiber drawing tension. This is due to the thermal property difference between the core and cladding [14]. The residual stress influences the cutoff wavelength of the fiber. Therefore, it is very important to evaluate the residual stress by fiber drawing. The relationships between the normalized change in the Brillouin frequency shift and the drawing tension for fibers with refractive index differences of 0.27 and 0.45 % [15] are shown in Fig. 7. We can see that the normalized change in the Brillouin frequency shift is proportional to the drawing tension. On the other hand, it is known that the residual stress is proportional to the drawing tension [16]. Thus, the distribution of the residual stress along the fiber length can be evaluated by BOTDA. This will contribute to improve fiber manufacturing technology.

4. SUMMARY

A promising technique for distributed strain measurement in optical fibers has been developed. The technique is based on time-resolved measurement of Brillouin gain spectra which depends on the strain. The technique will contribute to the improvement of technologies for fiber manufacturing, cabling, and cable installation, and also make it possible to accurately predict the lifetime of optical fibers in service.

The reviewed technique accesses both ends of the test fiber. In some applications, however, single-ended measurement is required. This will be made possible by measuring backward spontaneous Brillouin scattering (SPBS) from a forward travelling pulse light, instead of stimulated Brillouin scattering (SBS) as in the reviewed technique. However, SPBS is about 20 dB lower than Rayleigh scattering [17]. Therefore, it may be necessary for that purpose to increase the pulse energy by using, for example, an Er³⁺ doped fiber amplifier [18], and to improve the receiver sensitivity by using, for example, heterodyne detection [19][20]. Both techniques have been found to be effective for optical time domain reflectometry using backward Rayleigh scattering [21]-[23].

REFERENCES

- [1] M. H. Reeve, R. Kashyap, S. Hornung and S. A. Cassidy, Proceedings of 30th IWCS, 406, 1981.
- [2] M. Tateda, S. Tanaka and Y. Sugawara, Appl. Opt., 19, 770, 1980.
- [3] Y. Mitsunaga, Y. Katsuyama, H. Kobayashi and Y. Ishida, Trans. IECE Japan, J66-B, 829, 1983.

- [4] A. J. A. Bruinsma, P. van Zuylen, C. W. Lamberts and A. J. T. de Krijger, Technical Digest of OFS'84, 399, 1984.
- [5] T. Abe, Y. Mitsunaga and H. Koga, J. Lightwave Technol., 7, 525, 1989.
- [6] G. Meltz, W. W. Morey and W. H. Glenn, Opt. Lett., 14, 823, 1989.
- [7] B. Zimmerman, D. Kapp, R. Claus and K. Murphy, Technical Digest of OFC'90, WA2, 45, 1990.
- [8] T. Horiguchi, T. Kurashima and M. Tateda, IEEE Photon. Technol. Lett., 1, 107, 1989.
- [9] T. Horiguchi, T. Kurashima and M. Tateda, Trans. IEICE Japan, J73-B-I, 144, 1990.
- [10] T. Horiguchi, T. Kurashima and M. Tateda, IEEE Photon. Technol. Lett., May issue, 1990.
- [11] T. Kurashima, T. Horiguchi and M. Tateda, Technical Digest of IOOC'89, 4, 21C4-2, 70, 1989.
- [12] T. Horiguchi, T. Kurashima and M. Tateda, Submitted to ECOC'90.
- [13] M. Tateda, T. Horiguchi and T. Kurashima, Technical Digest of OFC'90, PD15-1, 1990.
- [14] U. C. Paek and C. R. Kurkjian, J. Am. Ceram. Soc., 58, 330, 1975.
- [15] Y. Hibino, T. Edahiro, T. Horiguchi, Y. Azuma and N. Shibata, J. Appl. Phys., 66, 4049, 1989.
- [16] Y. Hibino, F. Hanawa, T. Abe and S. Shibata, Appl. Phys. Lett., 50, 1565, 1987.
- [17] T. C. Rich and D. A. Pinnow, Appl. Opt., 13, 1376, 1974.
- [18] A. Takada, K. Iwatsuki and M. Saruwatari, IEEE Photon. Technol. Lett., 2, 122, 1990.
- [19] Y. Ichihashi, T. Imai, N. Ohkawa, T. Sugie and T. Ito, Technical Digest of IOOC'89, 5, 20PDA-12, 34, 1989.
- [20] R. W. Tkach, A. R. Chraplyvy and R. M. Derosier, Electron. Lett., 22, 1011, 1986.
- [21] L. C. Blank and D. M. Spirit, Technical Digest of OFC'90, WM27, 126, 1990.
- [22] J. P. King, D. F. Smith, K. Richards, P. Timson, R. E. Epworth and S. Wright, IEEE J. Lightwave Technol., LT-5, 616, 1987.
- [23] Y. Koyamada, H. Nakamoto, Electron. Lett., 26, 573, 1990.

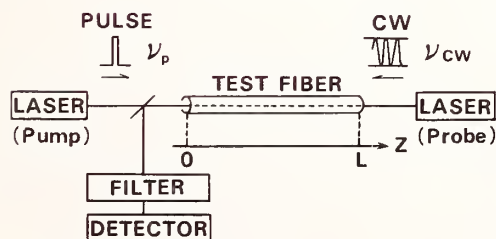


Fig. 1 Basic configuration of BOTDA

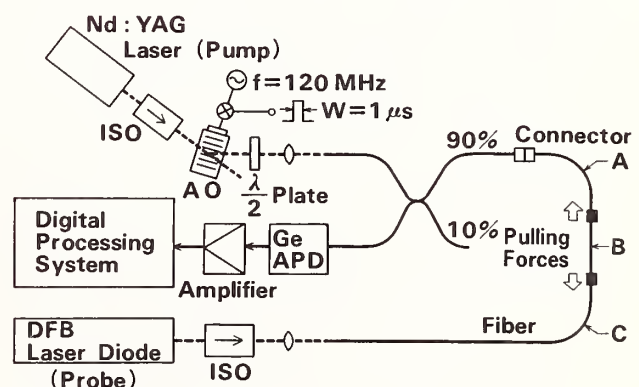


Fig. 2 Experimental arrangement of BOTDA

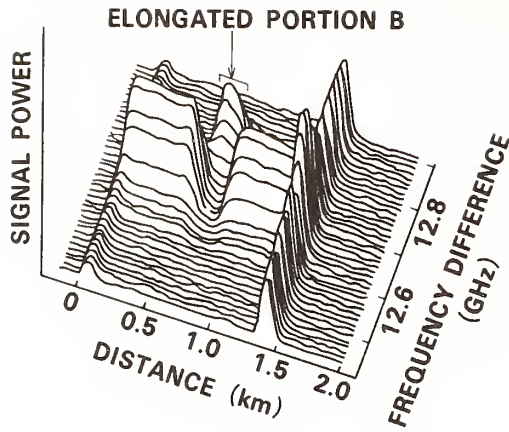


Fig. 3 Measured laser frequency difference dependence of BOTDA signal

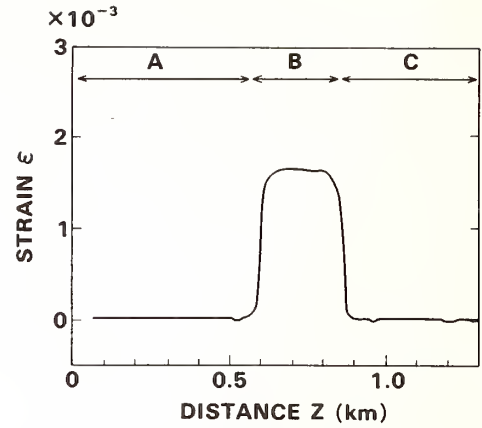


Fig. 4 Measured strain distribution

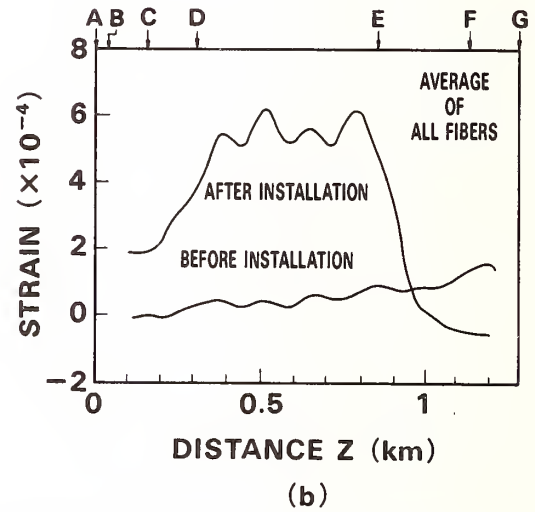
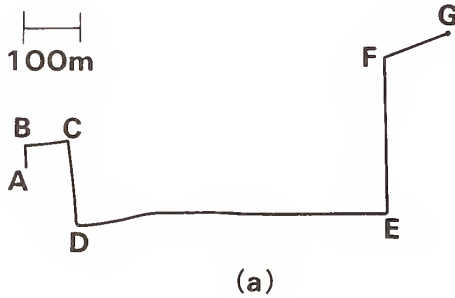


Fig. 5 (a) Conduit route for installation, (b) Strain distribution before and after installation

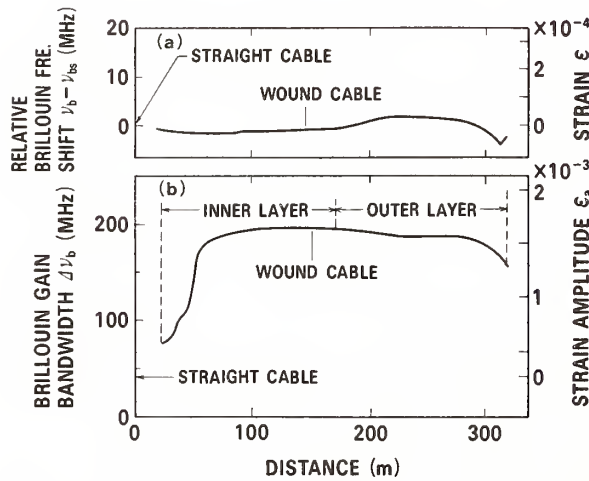


Fig. 6 Distribution of (a) relative Brillouin frequency shift $\nu_b - \nu_{bs}$, and (b) gain bandwidth $\Delta \nu_b$.

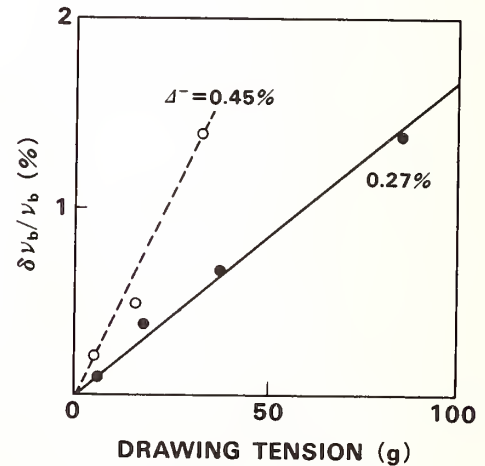


Fig. 7 Relationships between normalized change in Brillouin frequency shift and drawing tension

Standards for optical fiber geometry measurements

Matt Young

National Institute of Standards and Technology
Electromagnetic Technology Division
325 Broadway, Boulder, Colorado 80303

Although the Telecommunications Industry Association is adopting the gray scale method¹ for measuring fiber geometry, precisely how to calibrate a gray scale system remains a problem: some would say a nagging problem. A bit over a year ago, industry representatives contacted us at NIST and asked for our assistance. Specifically, they wanted a calibrated fiber whose cladding diameter was traceable to NIST. During the Fall of 1989 and the Winter of 1990, we held several meetings with what you might call an *ad hoc* committee of fiber and equipment manufacturers; this paper is a progress report.

The committee was reluctant to accept a chrome mask as an artifact standard because the criterion you use to locate an edge depends on the illumination of the sample. For example, in one application of the gray scale method, the fiber is backlighted so that its end is silhouetted against a bright background. Any point along the circumference of the fiber's end face is therefore illuminated by bundles of rays that originate in only a half-space, whereas a chrome mask is illuminated from nearly all directions. For this reason alone, there can be no guarantee that a chrome-on-glass disk will give the same image as a fiber end that has the same diameter. Similarly, if you calibrate the distance scale of your system, with either a well characterized reticle or chrome-on-glass annulus, you have no guarantee that width measurements are accurate; indeed, they most likely suffer from a systematic error of a fraction of 1 micrometer. Frontlighting the fiber and the disk can lead to similar errors, if only because the disk is deposited on a glass substrate and the fiber is not.

In addition, the committee wanted the artifact standard to be calibrated accurately with uncertainty $\pm 0.1 \mu\text{m}$ or less, so that they could be confident that subsequent measurements based on the fiber standards would be accurate with uncertainty less than $\pm 1 \mu\text{m}$. It was easy, therefore, to decide that any measurement would have to rely on interferometry to determine position precisely. We considered several methods: white light interferometry;² scanning confocal microscopy; a form of electron microscopy, where the fiber sample is scanned across a stationary electron beam; contact micrometry; and Fizeau fringes. We ruled out electron microscopy because we projected a long development time and finally fixed on contact micrometry and scanning confocal microscopy.

Contact micrometry. My colleague, Ted Doiron of NIST, Gaithersburg, has designed and built a contact micrometer that has two hardened steel surfaces, one moveable and one stationary. The moving surface is flat, and the stationary surface is cylindrical. The fiber is positioned between the two surfaces, and with its axis perpendicular to the axis of the cylindrical surface. The moving part presses it against the stationary part with a force of about 0.1 N (the weight of a 10 g mass). The greatest force that will not crush the fiber is very low, so the moving part slides in an air bearing to reduce friction. The formulas for the deformation of the fiber and the steel bearing surfaces are known and involve the geometry and the elastic constants of the materials. These deformations are between 0.1 and 0.25 μm , depending on the force, and the measurement can be corrected with the formulas. The position of the moving part is measured with a commercial interferometer that can interpolate between fringes with an uncertainty of 5 nm or so. So far, preliminary tests on steel wires have revealed an overall uncertainty of about 0.1 μm ; the best micrometers at NIST are about equally accurate, so it will take some effort to determine just how accurate the new micrometer is.

Scanning confocal microscopy. Because the gray scale method may not be accurate enough, even with a calculable correction, we decided to find a second accurate method whose

results we could compare with those of the micrometer. For the second, we chose scanning confocal microscopy, partly because this method should produce a precise result without the need for modeling nor for a correction.

In a scanning confocal microscope, the object is illuminated point by point by a laser beam as the object scans past the focal point of a microscope objective. That point is imaged onto a pinhole, behind which lies a detector. Our microscope actually works in reflection, so the beam goes through the same objective twice, but the principle is the same. My colleague, Greg Obarski, and I are building it from scratch because, when we last checked, the scanning confocal microscopes that were available commercially no longer translated the object physically but rather used a Nipkow disk to perform the scans optically.³ Although these commercial systems could probably be calibrated like any other video microscope, we decided to go to first principles and devise a microscope that we could scan under interferometric control.

The (amplitude) impulse response of a confocal microscope is the square of the usual coherent impulse response, $2J_1(r)/r$, where $J_1(r)$ is the first-order Bessel function. Symmetry dictates that the geometrical image of an edge is located at the half-amplitude point of the (amplitude) edge response, or the quarter-intensity point of the measured (intensity) profile. Because the light is highly coherent and the edge-finding intensity is known, there ought to be no significant systematic error in a scanning confocal microscope as there is in almost all partially coherent microscopes; one of our tasks is to verify this theoretical result experimentally. Our experience with video microscopy suggests that we will be able to measure the outside diameter of the fiber with an uncertainty of several tens of nanometers.

Video microscopy. Why don't we just set up a video microscope, calibrate it, and implement the gray scale method? My colleague, Steve Mechels, and I set up just such a microscope, which used an ordinary 40X, 0.65-NA objective, a CCD video camera, and a computer with frame digitizing electronics.⁴ We purchased a chrome-on-glass reticle (or stage

micrometer) that has 21, 2 μm wide lines about 10 μm apart and sent it to Bill Penzes at NIST, Gaithersburg, for calibration; the result is an estimated uncertainty of about 40 nm over the 200 μm length of the reticle. We used this reticle to calibrate our video microscope and found that we can measure a distance of 125 μm with uncertainty of 50 nm or so (3 standard deviations). Roughly half the error comes from the length standard we used and half from the uncertainties of our own measurements.

Next, we used a linewidth standard called SRM 475 to investigate the measurement of width as opposed to distance. This standard includes several chrome-on-glass lines that are approximately 10 μm wide and whose widths are known with an uncertainty of ± 60 nm. Since the widths of these lines are many times the resolution limit of the system, we can consider the image of each edge to be isolated from the other; consequently, any systematic error in the width measurement is independent of width and should be the same for a 125 μm line as for a 10 μm line.

It will come as no surprise to anyone here that the width measurements suffered from a systematic error between 0.1 and 0.2 μm , depending on the criterion we used to locate the edge and on the numerical aperture of the illumination. This error may well be different for a fiber than it is for a chrome line, but we can expect it to have the same order of magnitude. If the microscope is set up properly and the algorithms are robust, I doubt that the systematic error will exceed, let us say, half a resolution limit, or about 0.25 μm . That precision is adequate to calculate cladding ovality and the decentering between core and cladding accurately, but it is not adequate as a standard for diameter measurements that must be precise within ± 1 μm . For this reason, we are attempting to develop a fiber standard whose diameter is known more accurately than ± 0.1 μm and which can be used to determine the systematic error and correct for it.

References

1. Fiberoptics Test Procedure FOTP-176, "Measurement method for optical fiber geometry by automated gray-scale analysis," Telecommunications Industry Association--Electronic Industries Association, 2001 Eye Street, N.W., Washington, D.C. 20006.
2. M.J. Saunders, "Noncontact, interferometric determination of the outside diameter of optical fibers," in Technical digest—Symposium on optical fiber measurements, 1988, G.W. Day and D.L. Franzen, eds., Nat. Bur. Stand. (U.S.) Spec. Publ. 748 (1988), pp. 149-152.
3. But see Th. Zapf and R.W. Wijnaendts-van-Resandt, "VLSI metrology using an automatic beam-scanning confocal laser microscope," *Scanning* 10, 157-162 (1988). Commercial scanning confocal microscopes that use a laser source are becoming available. Such systems probably eliminate the systematic error that arises from partial coherence. Measurements made with such scanning confocal microscopes may therefore yield width measurements as accurate as our distance measurements with the video microscope but which are very precise and need little or no correction.
4. Steven Mechels and Matt Young, "Video microscope with sub-micrometer resolution," submitted to *Appl. Opt.*, May, 1990.

A COMPARISON OF INTERFEROMETRIC TECHNIQUES FOR FIBER CLADDING DIAMETER MEASUREMENTS

K.A. Emig
Corning, Inc.

Abstract

Two interferometric techniques have been proposed as reference test methods for the measurement of fiber cladding diameter. These techniques derive their calibration accuracy from interferometric fundamentals instead of calibration artifacts. Prototypes of these systems are evaluated and contrasted for accuracy, precision, simplicity of construction, cost and ease of use.

Introduction

As optical fibers achieve deeper penetration into the telephony loop, issues of low-cost connectorization become increasingly more important. One approach to reducing the high cost of connectorizing single-mode fibers is to tighten the geometrical specifications for the fiber. This requires reevaluation of the accuracy tolerances and methodologies of measurement system calibration.

Calibration of optical fiber glass geometry measurement systems typically involves the use of calibration devices such as chrome-on-glass artifacts or wire gauges. Unfortunately, the use of these devices to calibrate optical microscope systems, such as Grey-scale analyzers, often requires different lighting conditions compared to that used for the test fibers. This causes degradation of calibration accuracies at levels below the optical diffraction limit of the measurement system.

One alternative is the use of interferometric measurement systems that develop their calibration accuracy from the wavelength of light, instead of a calibration artifact. Such devices can be used to measure test fibers directly, or used to characterize calibration fibers for non-interferometric measurement systems. Two such interferometric techniques have been proposed [1],[2] utilizing Fizeau and Michelson Interferometry. Work recently completed at Corning's Waveguide Product Engineering Laboratory involved the construction of prototypes of both interferometric systems for the purpose of evaluating and contrasting the two designs with regard to their accuracy, precision and operational characteristics.

System Designs

Fizeau Interferometer

The Fizeau Interferometer, shown schematically in Figure 1, is a simple device consisting of two optical flats resting together at one end, and separated by the test fiber at the other end. The inner surfaces of the flats create a wedge-shaped air gap sufficient to generate optical interference from a monochromatic laser beam. The optical flat assembly is mounted on a linear scanning stage capable of moving the assembly through the laser beam along the axis of the flats. Interference fringes are generated between the flats and recorded by the fringe counting detector and recording device. A complete fringe cycle is created for every $\lambda/2$ separation of the flats. By recording the number of cycles generated as the beam is scanned from the contact point of the two flats (zero reference) to the center of the test fiber, the exact separation of the flats at the point of contact with the fiber can be determined, thereby yielding the diameter of the fiber.

Michelson Interferometric Microscope

The Michelson Interferometric Microscope is a more complex design than the Fizeau, incorporating two optical interferometer systems. This design, shown in Figure 2, uses a Michelson white-light interferometer attached to a common optical microscope to view the fiber transversely. By properly adjusting the reference mirror of the interferometer, white-light interference fringes are generated when the surface of the fiber is placed at the focal point of the microscope. Location of the central, white-light fringe allows for very precise focusing on the surface of interest. A second, Distance-Measuring Interferometer (DMI) is used to measure the relative vertical movement of the test fiber as the focus is moved from one surface to the other.

Two measurement methods are available with this technique, single-surface contact and non-contact. In the single-surface contact method, the measurement is performed from the top surface of the fiber to the top surface of the optical flat on which the fiber lies. The fiber diameter then is calculated as the difference in the DMI positions of the two surfaces. In the non-contact method, the fiber is located over a hole in the optical flat, and the measurement is performed from the top surface of the fiber to the bottom surface by viewing the bottom surface through the fiber. In this case, the difference in the DMI positions must be compensated by dividing by the effective refractive index of the fiber's cross section.

Test Results

A five-fiber comparison was made between the Fizeau Interferometer and the Michelson Interferometric Microscope using the single-surface contact method. The data, shown here in Table I, indicates cladding diameter agreement between the devices to less than $0.1\ \mu\text{m}$ on average. A further comparison made to an Image-shearing Microscope having an established calibration bias in the CCITT round robin [3] predicts performance of both systems to within $0.1\ \mu\text{m}$ of the industry mean for cladding diameter.

Advantages/Disadvantages

Fizeau Interferometer

The simplicity of design is a clear cost and maintainability advantage of the Fizeau design. Data interpretation is relatively straightforward once the determination of the start and stop points for fringe counting has been accomplished. Several viable algorithms have been developed for this purpose, and data analysis by computer greatly simplifies the fringe counting task, and can reduce measurement inaccuracies to well below meaningful levels.

The primary disadvantages of the Fizeau design result from the fact that it requires physical contact between the flats and the test fiber over some axial fiber distance, usually 3 to 4 mm. First, there are three contacting surfaces in the Fizeau design, making the device susceptible to inaccuracies due to foreign matter (dirt and dust) at the contact points. Second, the relatively long contact area with the fiber, usually 3 to 4 mm, makes this technique completely insensitive to axial diameter fluctuations having periodicities less than the fiber contact distance.

Michelson Interferometric Microscope

An inherent advantage of the Interferometric Microscope design is the ability to perform non-contact or single-surface contact measurements on the same device. As a single-surface contact measurement, the measurement easily can be performed manually, and works equally well on transparent or opaque fibers, such as those with hermetic coatings. As a non-contact measurement, inaccuracies due to particulate matter easily can be eliminated. Additionally, the non-contacting measurement is sensitive to axial diameter variations, with axial resolutions of a few micrometers achievable with the appropriate optical magnification. This also permits a transverse measurement

to be made very close to the fiber endface, making it more useful as a calibrator for end-view systems. By properly locating the test sample in the microscope field of view, measurements can be made by both methods, permitting the effective refractive index values for the test fiber to be measured directly.

The primary disadvantages of this technique are the higher level of design complexity (higher cost) and the need for image analysis equipment in the non-contact measurement. During location of fringes on the bottom surface of the fiber, the fiber itself acts like a lens, causing spatial compression of the fringe pattern image. This makes it difficult to determine the central fringe location without the aid of image analysis equipment, which further increases system cost.

Conclusions

Both interferometric techniques provide viable options to obtaining cladding diameter accuracies of $0.1\ \mu\text{m}$ or less, making them useful for the calibration of end-view microscope systems. Clear tradeoffs exist between the designs for complexity, cost, ease of use and physical measurement limitations. Neither design lends itself to the measurement of fiber parameters involving the core, such as concentricity error, core diameter, or core non-circularity. Cladding non-circularity measurement is possible with both techniques by repeated diameter measurements with controlled incremental rotation.

Acknowledgements

The author would like to acknowledge the efforts of J.E. Brarens for his work in the construction of the systems and fiber measurements, and C. Saravanos and B. Wong of Northern Telecom Canada Ltd. and M.J. Saunders of AT&T Bell Labs for helpful discussions.

References

- [1] M.S. O'Sullivan and D.W. Grandsen, "A fizeau fringe interferometer for fiber outside diameter measurements," SPIE Conf. Proceedings, Vol. 841, Paper 39, p. 287-290, 1987.
- [2] M.J. Saunders, "Non-contact, interferometric determination of the outside diameter of optical fibers," Symp. Optical Fiber Measurements, NBS SP 748, p. 149, 1988.
- [3] British Telecom and N.I.S.T., Study Group XY - Contribution, CCITT, September 1989.

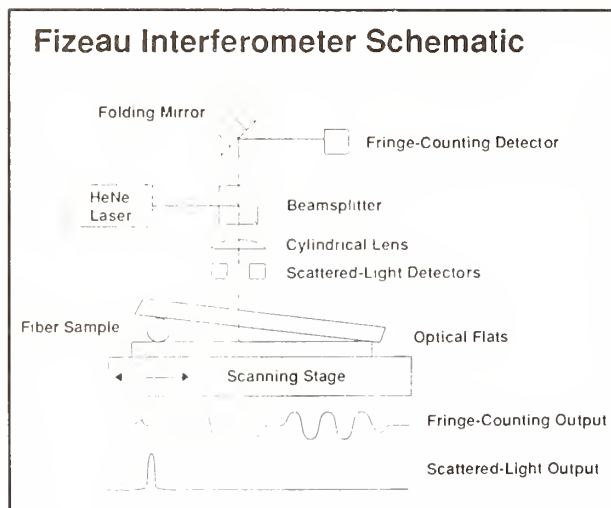


Figure 1

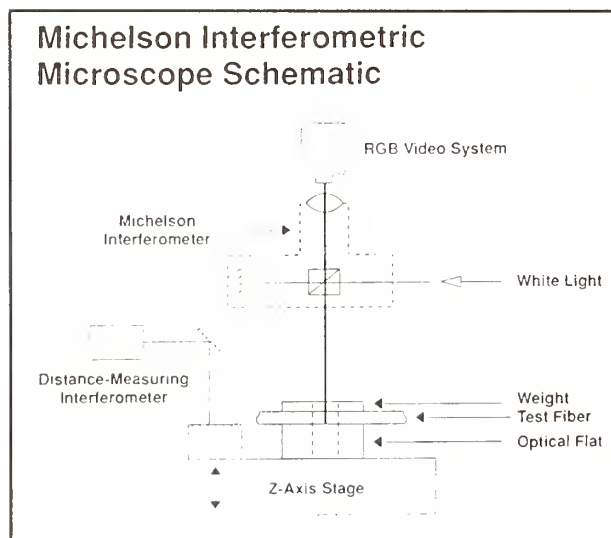


Figure 2

Cladding Diameter Comparison

Fiber	Fiz	MIM	Fiz-MIM
1	125.70	125.89	-0.19
2	125.47	125.43	+0.04
3	125.71	125.86	-0.15
4	125.06	125.06	0.00
5	124.86	124.91	-0.05
		\bar{x}	-0.07
		s	0.10

Where Fiz = Fizeau Interferometer
MIM = Michelson Interferometric Microscope

Table I

ACCURATE DETERMINATION OF CLADDING DIAMETER AND NONCIRCULARITY OF OPTICAL FIBERS

Bennett Wong, Costas Saravanos
Northern Telecom Canada Limited
Optical Cables Division
Saskatoon, Saskatchewan, Canada S7K-3L7

ABSTRACT

The conventional data fitting algorithm used for grayscale fiber geometry measurements can lead to large variations in test results. To improve repeatability, a Fourier transform and an elliptical fitting algorithm are developed. As well, a technique for identifying and eliminating spurious data is introduced. A comparison of the two methods show similar repeatability performance. However, with commercially available fibers, the Fourier method gives more reliable results.

1.0 INTRODUCTION

The accurate measurement of fiber geometry parameters is crucial in the areas of splicing and connectorization. The future success of the fiber-to-the-home concept will depend strongly on the availability of high quality yet economical interconnections. For connectors, one key step to manufacturing a high-performance device is to precisely match the fiber cladding diameter and noncircularity to the ferrule microhole. For fusion splicing and other field-installable connections, low loss is achieved by using fibers made with consistent geometric parameters.

One popular method for measuring fiber geometric parameters is the Grayscale^[1] technique. However, the task of reducing a digital image to useful geometric parameters is far from trivial. Conventional methods describe the fiber cladding using a best-fit-circle definition, without any provision for eliminating noisy data. This can often lead to variations of up to 0.5 μm in diameter results. Here, two new fitting methods for improving measurement repeatability are presented and compared.

2.0 TEST METHOD DESCRIPTION

A schematic of the Grayscale test station is shown in Figure 1. A CCD camera acquires an image of the cleaved end of the test fiber. The image is then digitized by a digital framestore and transferred to the computer, where the fiber edge coordinates are located and stored into an edge table. The table entries are subsequently fitted with an appropriate algorithm to arrive at values for average cladding diameter (OD_{avg}), minimum cladding diameter (OD_{min}), maximum cladding diameter (OD_{max}), noncircularity (NC), and core-cladding concentricity error (CE). The system's accuracy is based on a reference fiber measured using a Fizeau interferometer^[2].

2.1 ELLIPTICAL FITTING ALGORITHM

This fitting method assumes that the shape of the fiber cladding is that of an ellipse. An ellipse oriented with its minor and major dimensions a and b on the x and y axes, and with horizontal and vertical offsets x_0 and y_0 , is given by the expression

$$[(x-x_0)/a]^2 + [(y-y_0)/b]^2 = 1$$

Values for the minor and major axes and center offset are obtained using least-squares fitting^[3]. Cladding noncircularity is expressed in percent, and is calculated by the difference between the minor and major axes, normalized with respect to the average diameter. Noncircularity in this case is more appropriately known as ellipticity.

2.2 FFT FITTING ALGORITHM

To perform the Fourier fit, the edge table in Cartesian coordinates is first converted to polar coordinates. The resulting radial function is then interpolated into points of equal angular spacing. As this data is periodic with θ , it can be represented by a Fourier series of the form

$$R(\theta) = \sum_{n=-\infty}^{\infty} c_n \exp(in\pi\theta/T)$$

where c_n are the Fourier coefficients, and T is the function period.

The Fourier coefficients are easily computed using FFT algorithms^[4]. These components have physical significance in that they represent the degree of each order's contribution to the overall cladding shape. For example, the zero-th order is the average radius; the first order term describes the offset between the assumed and true centers; the second order represents ovality; while the third order term translates to three-sidedness; and so on.

2.3 SPURIOUS DATA REJECTION

The presence of spurious data in the edge table is due to debris on the fiber surface or cleaving defects. If the cladding shape is in fact smooth, then its Fourier coefficients should decay rapidly. For small cleave defects, truncating the series of all high-order terms^[5] will effectively remove the noisy data. When large, continuous defects (such as a uniform cleave angle) are present, there will be non-trivial contributions to the low-order Fourier terms. A simple truncation in this instance will not eliminate the flawed data. Likewise, it will be equally difficult to exclude the erroneous data with the ellipse fitting method. An algorithm was therefore developed to evaluate the quality of each cleave, and to require a re-cleaving or re-cleaning of the fiber should the defect reach uncorrectable levels.

For a fiber endface containing dirt or cleaving defects, the contrast of the image at the flaw will be reduced. If a contrast table is maintained along with the edge table, it is possible to identify and eliminate edge table entries that correspond to low values in the contrast table. The decision threshold for excluding data is obtained experimentally by measuring cleaves of known angles and recording their contrast levels. The intensity profiles for a fiber with an optimum cleave and a hackled cleave are shown in Figures

2(a) and 2(b), respectively. Note the sharp reduction in contrast in the region of the hackle. In Figure 2(c), the edge and contrast table entries are plotted. Here, the questionable edge data is easily identified by matching to low contrast levels.

Restoration of deleted data can be performed by interpolation from adjacent data entries. This method works well for small numbers of problem data points. For larger defects, eliminating too many consecutive points will introduce greater uncertainty in the measurement. In these cases, it would be best simply to indicate that the fiber should be re-cleaned and/or re-cleaved.

3.0 DATA AND RESULTS

To determine whether noncircular fibers were simply oval or contained higher order shapes, seven fibers with various degrees of noncircularity were measured. Figure 3 summarizes the average relative magnitudes of the Fourier components for the fibers up to the fourth order. Since true ellipses do not contain terms higher than the second order, this implies that the fibers cannot be treated as simple ellipses.

A comparison of the difference between Fourier and ellipse fitting algorithms is given in Figure 4. The Fourier results were obtained using a fourth order truncation filter (a second order filter gives comparable values). The two methods show excellent agreement in determining cladding average diameter and noncircularity. A small bias in the noncircularity measurements exists because the ellipse fitting algorithm gives slightly optimistic results for the OD_{min} and OD_{max} measurements. Figure 5 is an example of the two fitting methods for the data of one particular fiber. The correlation coefficients for the Fourier and elliptical fits are 0.92 and 0.84, respectively. Here, it is evident that the Fourier algorithm gives a more reliable fit to the asymmetric data, as it allows for higher order shapes.

The sensitivity with respect to cleave angle for the two algorithms was investigated. Here, two fibers with noncircularity values of 0.42% and 1.18% were measured for cleave angles of up to 2 degrees. The test results of the experiment are depicted in Figure 6. For both fibers, the one-standard deviation values are less than 0.08%, using either algorithm. Furthermore, the relatively low values would indicate that the system's optics contain sufficient depth-of-field to compensate for the cleave angles.

4.0 SUMMARY AND CONCLUSIONS

Fourier transform and elliptical fitting algorithms have been developed to analyze and describe fiber cladding shape. Both methods have been successfully applied to grayscale testing, with similar improvements in repeatability over the best-fit-circle method. However, tests show that commercially available fibers can contain significant high order components, which are more accurately described by the Fourier transform method. This method is also suitable for filtering spurious data due to small cleaving defects. For larger flaws, a contrast table is used to determine the validity of each edge table entry.

REFERENCES

- [1] D.R. Briggs, Measurement Method For Optical Fiber Geometry By Automated Gray-Scale Analysis, EIA/TIA DRAFT FOTP-176, April, 1990.
- [2] M.S. O'Sullivan and D.W. Gransden, A Fizeau Fringe Interferometer For Fiber Outside Diameter Measurements, SPIE Conference Proceedings, Vol. 841, paper 39, p287-290 (1987).
- [3] R.W. Hornbeck, Numerical Methods, Quantum Publishers (1975).
- [4] For example, the HP98821A BASIC Numerical Analysis Library for HP Series 200/300 computers.
- [5] F. Scheid, Numerical Analysis, Schaum's Outline Series, McGraw-Hill (1968).

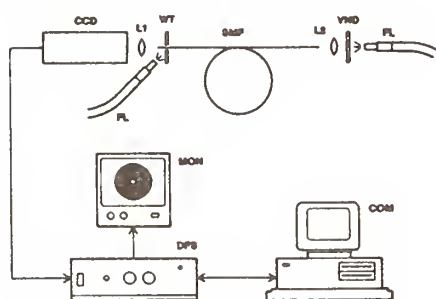


Fig. 1. Grayscale geometry test system. CCD: CCD camera, L1: 40x/0.65NA lens, L2: 20x/0.40NA lens, WT: white target, SMF: single mode fiber, VND: variable neutral density filter, FL: fiber optic illuminator, MON: video monitor, DFS: digital framestore, COM: computer.

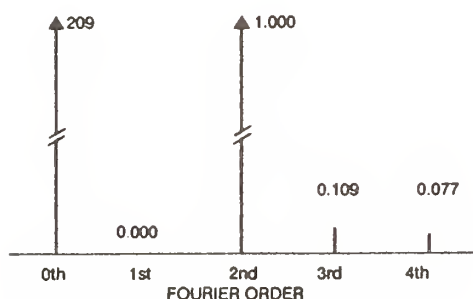


Fig. 3. Average magnitude of Fourier components for 7 fibers. Terms higher than second order indicate that the fibers are not simple ellipses.

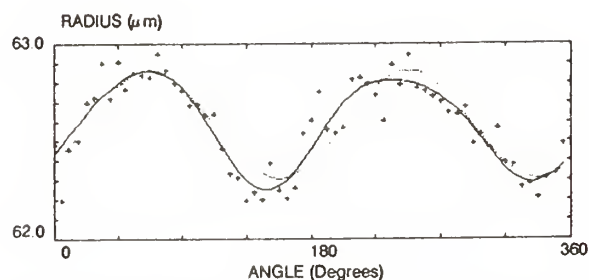


Fig. 5. A comparison of fitting methods for a fiber with asymmetric data. The Fourier method (solid line) gives a slightly more accurate fit than the ellipse method (dashed line).

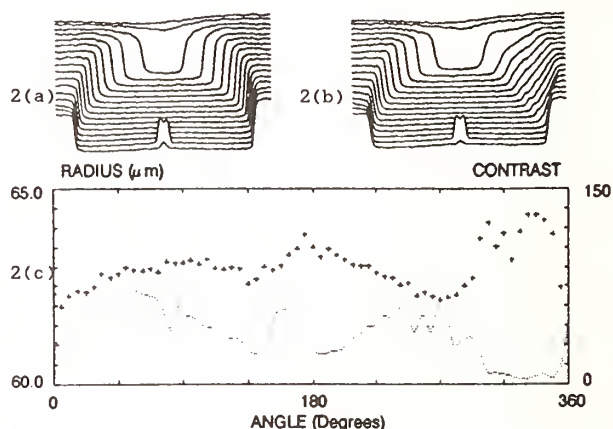


Fig. 2. 2(a), 2(b): Intensity profiles for near-perfect and hackled cleaves. Note the reduction in contrast in the defect region in 2(b). 2(c): Radial data of hackled cleave with corresponding contrast table values (dashed line).

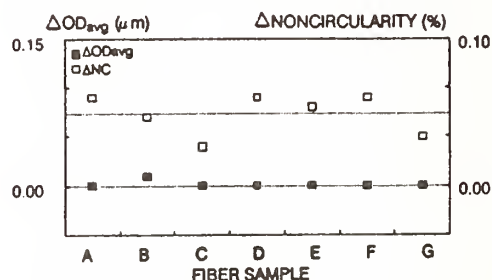


Fig. 4. A comparison between Fourier and ellipse fitting algorithms for 7 fibers. The ellipse method measures NC smaller by 0.06%, on the average.

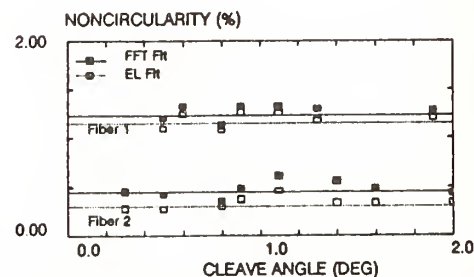


Fig. 6. Noncircularity repeatability as a function of cleave angle for two fibers, using Fourier and ellipse fitting algorithms.

CALIBRATION OF FIBER DIAMETER MEASUREMENTS

K.W. Raine⁽¹⁾, J.G.N. Baines⁽¹⁾, A.G. Hallam⁽²⁾, N.P. Turner⁽¹⁾

⁽¹⁾ Division of Mechanical and Optical Metrology,
National Physical Laboratory, Queens Road, Teddington,
Middlesex, UK. TW11 0LW

⁽²⁾ York Technology Ltd, York House, School Lane
Chandlers Ford, Hampshire, UK. SO5 3DG

A recent study of the calibration of fiber diameter measuring instruments [1] has highlighted various problems associated with some of the more commonly used measurement techniques.

The use of a cleaved fiber end as a transfer standard was considered unsatisfactory because of the difficulty in maintaining a good quality cleave over long periods of time and the effect of cleave quality on edge fitting algorithms. In order to establish a reliable reference standard we have measured the diameter of many samples of the same pure silica fiber by three independent techniques (white light interferometry, mechanical contact and image inverting microscopy) and the results had a total spread of $0.1\mu\text{m}$ [1]. This fiber was then used as a reference for the assessment of chromium-on-glass artefacts and of other measurement techniques under various conditions. Chromium masks were studied because they are mechanically robust, can be made with sharp edges and are already used as linewidth standards in microelectronics. We investigated the use of a linewidth standard and circular chromium-on-glass patterns (apertures, stops and annuli) which are more representative of a fiber end.

Measurements using imaging microscopy showed that the mean diameter of an annulus, or the line spacing of a linewidth photomask, is insensitive to experimental conditions. Such objects are therefore suitable for calibrating the transducers and detectors of many fiber diameter measuring instruments.

When measuring fibers and masks it is common practice to use the 50% intensity level of the image as the edge setting criterion. However, the true edge position normally occurs at or close to the 25% intensity for both fibers and opaque chromium masks when using a properly set up microscope [2]. Therefore to obtain the true diameter or linewidth, it is necessary for the 25%-50% offset to be accurately known and reproducible. We found that this could be determined from measurements of calibrated circular chromium masks or linewidth standards in transmitted light. Using a grey scale digitization system the offset was larger than expected ($0.8\mu\text{m}$) and instrument dependent. This has been further investigated. We showed that it was possible to obtain agreement with the reference methods to $\pm 0.15\mu\text{m}$ on grey scale and image shearing instruments.

USING CHROMIUM MASKS IN REFLECTED LIGHT

It is always advisable to measure opaque chromium masks in transmitted light (T) as this avoids the edge distortion due to the phase differences between the light reflected from each side of the boundary [2]. Thus when measuring with reflected light (R), the 25% intensity level which normally locates the true edge position can now lead to an error. Because some grey scale instruments are designed for use with reflected light only, we have measured a number of bright and dark chromium-on-glass lines in reflected light. Some masks were made with a single layer of chromium, others had anti-reflection coatings on the chromium. The measurements were carried out with an image shearing microscope using an objective with a numerical aperture (NA) of 0.65 (x40 magnification) and green filtered illuminating light. Additional magnification was used to make the TV scan linewidth correspond to $0.1\mu\text{m}$ in the

object plane. Surprisingly, we found that with both dark and bright lines the linewidth determined at the 50% intensity level, measured in R, were in the range 0.05 μ m to 0.15 μ m smaller than the value measured in transmission (corrected for the appropriate 25%-50% offset). This was contrary to expectation since the dark line, as viewed in R, should have measured larger than the corrected value. The measurements were found to be fairly insensitive to operating conditions. For example, a change in condenser NA of 0.6 to 0.1, or of the center wavelength of the illumination from 550nm to 633nm changed the value by no more than 0.05 μ m. The introduction of several wavelengths of spherical aberration (by placing a 170 μ m thick cover-slip between the objective and the mask) only led to small increases in linewidths of between 0.05 μ m and 0.1 μ m, in fact resulting in measurements closer to the correct value.

Thus whereas fibers, and chromium masks measured in T, have the same offset [1], the results show that the difference in the offset between fibers, and chromium masks measured in R, would be up to 0.15 μ m with this instrument. However, the 50% intensity level was found to be insensitive to experimental conditions, for example focus, when the ratio of the condenser NA to the objective NA (S) was about 0.7, thus it should be possible with good characterization to use chromium masks for calibration using reflected light.

THE 25%-50% OFFSET

In the earlier work [1] we noted that the 25%-50% offset seemed to be the appropriate correction, for a fiber in R, even if the value was increased by inadequate TV resolution. We have investigated this unexpected result further by measuring in T a calibrated clear linewidth under different conditions. We have found that the 25%-50% offset determined from photometric measurements can lead to errors. When this value was increased from the theoretical value of 0.2 μ m to 0.35 μ m (NA 0.65) by reducing the image size on the TV, repeated measurements showed an error of 0.1 μ m in the linewidth. The photometrically determined value of the 25%-50% offset also led to errors in the presence of spherical aberration or when the green filter was removed. However, if the offset was determined from the difference between the measured value and the calibrated linewidth, the correct value of the offset was obtained under a wide range of conditions. Measurements of fiber using this value then led to agreement with the diameter determined from other methods to 0.1 μ m. Applying the offset obtained in this way to our earlier measurements with inadequate TV resolution [1] led to a reduction in diameter of 0.1 μ m but we found the results to be still within the $\pm 0.15\mu$ m of the reference value.

Alternatively, the offset may be determined from measurements of a calibrated chromium aperture or incorporated into the calibration by setting the true diameter at the 50% intensity level. For this to be accurate the diameter of the chromium aperture must be close to the fiber diameter (125 μ m). Following a calibration by this method, diameter measurements made on the fiber agreed to $\pm 0.1\mu$ m with measurements made by other techniques. This affect would appear to be due to interaction of the curvature of the image with the TV resolution.

One of the reasons for measuring at the 50% level has often been its convenience and the insensitivity of this level to experimental conditions. However, if the condenser NA is reduced so that S is less than 0.2, leading to coherent illumination, we have found that the 25% intensity level is similarly insensitive to focus errors and the presence of large amounts of spherical aberration [3]. These conditions typically lead to errors of less than 0.05 μ m in linewidth values. Unfortunately we have not been able to try this with fiber measurements because low light levels caused signal to noise problems.

EFFECT OF CCD PIXEL SIZE AND PITCH IN GREY SCALE MEASUREMENTS

For the grey scale digitizer it was found that the 25%-50% offset depended on the pixel element size of the CCD camera. Offsets were determined by calculating the diameter of the reference fiber at different intensity levels. Previous work [4] showed the existence of

an offset of approximately $0.8\mu\text{m}$ for a 0.4 NA (x20) objective operating at a wavelength of 550nm. In this case the pixel pitch was $15.7\mu\text{m} \times 11.3\mu\text{m}$. However, using a different camera having a pixel pitch of $11.6\mu\text{m} \times 11.4\mu\text{m}$ resulted in an offset of $0.55\mu\text{m}$ under the same experimental conditions. This improvement was due the improved spatial sampling where the pixel pitch was about $0.5\mu\text{m}$ referred to the object plane.

It was found that when measuring a fiber edge a 0.65 NA (x40) objective gave an offset of $0.39\mu\text{m}$ (theoretical value about $0.25\mu\text{m}$) when the value of S was 0.7. The corresponding pixel size was $0.25\mu\text{m}$ in the object plane. The difference between the measured and theoretical offset was similar to that obtained with the image shearing microscope when the TV linewidth was also about $0.25\mu\text{m}$ in the object plane. It has been shown [1] that additional empty magnification leads to agreement between the theoretical and measured offsets and could be applied to this instrument with possible advantage. However this would require a camera with smaller pixel size.

To minimise processing time in grey scale analysis it is preferable not to use all the available pixels. To investigate the effect on the measured diameter of a fiber a series of measurements was made using different grid spacings. The smallest grid spacing corresponded to the pixel size of about $0.5\mu\text{m}$ in the object plane using a x20 objective. Larger grid spacings were generated by omitting pixels and were integer multiples of the pixel size. It was found that the fiber diameter was constant to within $0.1\mu\text{m}$ for grid spacings up to $1.5\mu\text{m}$. For larger grid spacing the computed fiber diameter was reduced. The 25%-50% offset was also found to be independent of grid spacing up to a value of $1.5\mu\text{m}$.

The insensitivity of the measurements to the grid spacing was a little surprising. It is probably due to the interaction of the image of the curved fiber edge with the square format of the CCD array, such that each part of the edge slope of the fiber is sampled at some point on the circumference.

In order to determine the offset by calibrating with a reference fiber, care must be taken to understand the interaction of the curve fitting algorithm with the actual form of the fiber edge. We have found that the presence of blade impact damage and hackle on the end of the fiber can result in an underestimation of the fiber diameter. Also, the effect of cleave damage on the fiber edge reduces the average edge slope. Thus for an imperfect edge the offset will be larger than the value expected from diffraction considerations. The use of a chromium artefact should therefore provide a more reliable means of determining the offset for grey scale instruments. If used in transmitted light, as in the image shearing measurements described above, a direct calibration incorporating the offset would also be possible.

CONCLUSIONS

We have shown that chromium-on-glass masks used with transmitted light are capable of calibrating transducers and determining offsets for imaging instruments designed for measuring the cladding diameter of optical fibers. Alternatively, they can be used to provide a calibration which includes the offset when the width of the chromium pattern has the same dimensions of the fiber. If the TV linewidth is less than $0.1\mu\text{m}$ in the object plane, the measured offsets have been found to agree with those evaluated from theory. Before reflected illumination is employed for calibration the characteristics of edge setting criteria need further investigation and characterization. If measurements are made at the 50% intensity level then the value of S should be about 0.7 but if direct measurement is made at the 25% intensity levels S should be less than 0.2. In each case the measurements are insensitive to experimental conditions and therefore more reproducible. Although we have only discussed the application of chromium masks for calibration and determining edge setting offsets, circular masks also have applications in calibrating for circularity, concentricity and assessing form fitting software and can be used to assess the orthogonality of scanning x-y stages.

REFERENCES

- [1] Baines, J.G.N., Raine, K.W., Hallam, A.G., Turner, N.P., "Fiber diameter measurements and their calibration," Accepted for publication by J. Lightwave Tech.
- [2] Reynolds, G.O., DeVellis, J.B., Parrent Jr., G.B., Thompson, B.J., "The new physical optics notebook: Tutorials in Fourier Optics," SPIE Optical Engineering Press, p 147, 1989.
- [3] Kirk, C.P., "Aberration effects in an optical measuring microscope," Appl. Optics, vol. 26, no. 16, pp 3417-3424, August 1987.
- [4] Hallam, A.G., Baines, J.G.N., Raine, K.W., Turner, N.P., "Towards a calibration standard for fiber geometry measurement", Optical Fiber Communication Conf. (OFC '90), Tech. Digest, 1990.

Fibre Geometry Measurement and Quality of Parameter Estimation

D.A.Svendsen, N.MacFarlane

York Technology, School Lane
Chandlers Ford, Hants, SO5 3DG, UK

Introduction

Currently, there is considerable activity in both the United States and Europe in developing and establishing appropriate standards for the routine estimation of the geometrical characteristics of optical fibers. This paper indicates the importance of the mathematical process used to derive the parameters and suggests a generalised approach which combines both the need for unambiguous standards definitions and the flexibility to accommodate future developments without continual revision of these standards. The discussion concentrates on the estimation of the fiber cladding boundary although it is also applicable to core parameter estimation.

Current Procedure

Since the fiber cladding boundary is very nearly circular, it has been conventional for this edge to be described as a circle with a diameter and a center, together with an additional "non-circularity" parameter which describes the degree to which the fiber edge deviates from an ideal circle. Until recently, the fiber edge was estimated by means of a few data points determined visually by an operator, and the circle diameter, centre, and non-circularity were obtained from these few points [1]. The availability of automated techniques of obtaining many more edge points around the cladding boundary, such as grey scale analysis of video images, has made it feasible to apply mathematical techniques and definitions which lead to more accurate and repeatable parameter estimation [2]. It seems to be widely accepted by the US and European standards organisations that the fibre cladding diameter and center should be obtained by applying a least-squares area minimisation algorithm to the edge point data set. It has been proposed that the minimisation should be with respect to a best-form circle and that non-circularity should be defined in relation to this best-fit circle.

Problems in Current Procedure

The quality of the edge points is clearly important; attention must be paid to grid and grey scale precision if acceptable accuracy is to be obtained. However, the constraints on the data points with respect to the algorithm used in parameter derivation are less well defined other than that the edge points should be approximately equally spaced in angle. The importance of this constraint can be seen by considering the practical situation where data points have been discarded from areas of damage to the fiber edge caused by fiber cleaving. If the fiber edge is essentially circular then the best-fit circle will interpolate across regions of rejected data in the optimal sense defined by the best-fit area minimisation criterion. However, if the fiber edge deviates significantly from a circle, then the best-fit circle does not correctly interpolate across the missing regions, giving errors in estimated diameter and center.

This is shown in Figures 1 and 2 where the diameter and center errors are plotted as a function of fiber edge ellipticity. The fiber edge has been modelled as an ideal ellipse and then regions of the edge have been removed. Even at the low ellipticities of a few percent which occur in the fiber industry, the errors caused by using a best-fit circle to approximate to a non-circular edge are significant given the levels of accuracy and repeatability currently required. Applying a best-fit ellipse, or higher order Fourier analysis, will give the correct diameter and center. As an approximate rule-of-thumb, the modelling suggests the following expression for the error, E, in both fiber diameter and center, with removal of a section of angular width W (degrees) from a fiber of diameter D (um) and ellipticity Ell (%):

$$E = 1.4E-5 * Ell * W * D \text{ (um)} \quad (1)$$

Further modelling has been performed, where the ideal ellipses have been used with the addition of randomly distributed noise in order to more closely match real measured data. This noise has little effect on the curves shown and does not change the conclusions reached.

These examples show that it is essential to apply a suitable best-form fit to the data, and also to be aware of the quality of the fit.

Choice of Best-Form

Since the shape of optical fibers varies, it may be that one functional form is appropriate for one type of fiber and another form may be more appropriate for another type. In practice, the difference may be significant for instrumentation costs and convenience of use. The problem of choice of best-form can be solved by quantification of the degree to which a chosen form actually matches the data points. This quantification can be used to judge the suitability of a particular form. Subsequently, the parameters obtained from the use of the best-form will then be a best description of the fiber edge.

Quality Index

The quality of the match of the best-form function to the edge points is probably best described by using the minimisation criterion itself. It is therefore suggested that a Quality Index, QI, be defined as follows :

$$QI = 1 - (E_{max} - E_{min}) / (D * D) \quad (2)$$

where D is the fitted diameter and E_{max} and E_{min} are the maximum and minimum of the deviations E_i in the minimisation algorithm. Each E_i is calculated from the distance, R_i, from the fitted center to the edge point and the fitted distance, R_{fit}, at the angle corresponding to the edge point :

$$E_i = R_{fit} * R_{fit} - R_i * R_i \quad (3)$$

This definition of the Quality Index is essentially independent of the best-form of the curve fitted and is therefore suitable as a measure of the appropriateness of the actual best-form chosen. In practice, the QI would be monitored to ensure that it was consistently above some threshold, still to be defined. If the QI were to fall below the threshold, this would indicate either, a poor set of edge points, or a fiber edge whose form deviated significantly from the form used in the parameter estimation algorithm. Hence the QI provides a warning that the parameters were potentially in error.

Summary

It is suggested that definitions on the estimation of fiber geometry patterns should be assessed using a Quality Index and that the choice of exact form of mathematical technique should depend on the requirements of the particular fiber type. This combines the rigour of the need to set standards with flexibility for future development.

Acknowledgements

The authors are grateful to the Directors of York Technology for their permission to publish this paper.

References

- [1] EIA FOTP 45 Microscope Method For Measuring Fiber Geometry Of Optical Wave guide Fibres, August 1988.
- [2] EIA FOTP 176 Measurement Method For Optical Fiber Geometry By Automated Grey-Scale Analysis, (draft) January 1990.

Figure 1 Variation of Diameter Error with Fiber Ellipticity

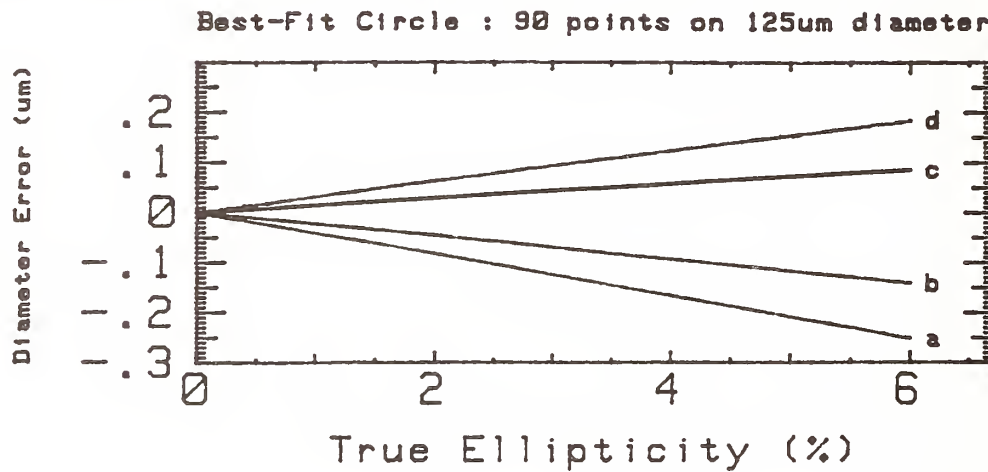
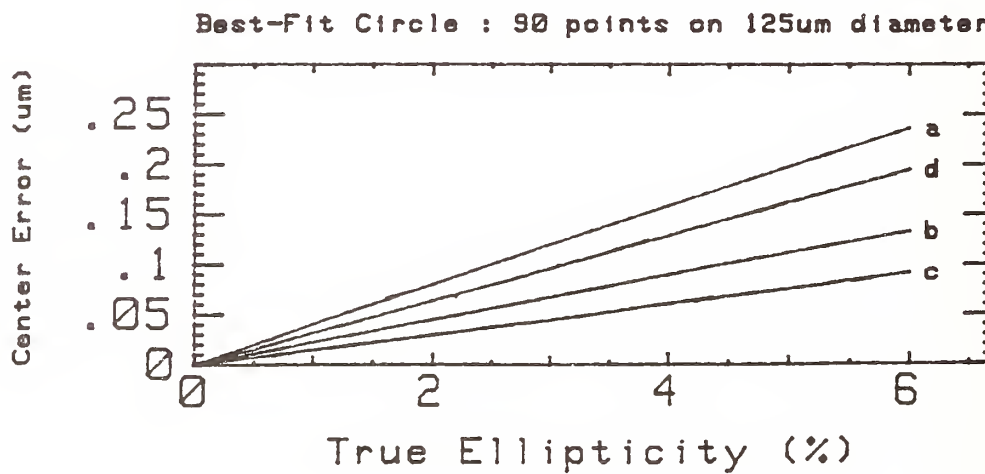


Figure 2 Variation of Center Error with Fiber Ellipticity



- a Missing Width of 20 degrees on major axis
- b Missing Width of 10 degrees on major axis
- c Missing Width of 10 degrees on minor axis
- d Missing Width of 20 degrees on minor axis

Pulse-Delay Measurement for Long Zero-Dispersion Fibers

Yoshiaki YAMABAYASHI and Hidehiko TAKARA

NTT Transmission Systems Laboratories

1-2356 Take Yokosuka 238, Japan

Introduction

Repeater spacing in an optical transmission system can be maximized if the transmission wavelength lies as close to the zero-dispersion and loss-minimum wavelength as possible. It is important to determine dispersion of full-length of transmission fibers at the transmission wavelength. Relative pulse-delay or phase-delay techniques as a function of wavelength are commonly used for fibers of longer than 10 km. Although the multiple-laser-source [1] method is able to avoid errors associated with ambient-temperature variations, the system should be costly. Because it requires at least two laser diodes which are carefully chosen and controlled in wavelength. Yamada has proposed a dispersion determination method making use of longitudinal-mode spacing of laser diodes [2]. This method has made a single laser diode enough to obtain the dispersion value at the wavelength, but needs some calculation. We propose a pulse-delay measurement technique to overcome all these problems. Our measurement system is nearly all-fiber and employs just one chirped-pulse laser, thus it is compact and easy to handle.

Experiment

Chirped light pulses were generated with a 1.55 μm distributed-feedback (DFB) laser diode, and compressed to about 13 ps duration (FWHM) with the linear compression method [3]. The wide-band pulses were launched into a test fiber. The pulses traversed the fiber and were decomposed with a variable band-pass-filter (BPF) having a 0.8 nm resolution. The filter used was a dielectric multilayer thin-film type packaged with a rotational stage. Since the test-fiber length may vary with time because of the ambient temperature variations, considerable errors may be incurred. One degree of temperature increase produces a 2 ps/km delay increase in silica fibers. Thus the arriving pulse is divided into two by a fiber coupler. One arm is connected to the wavelength filter and the other arm forms the time reference, as shown in Fig. 1. The filtered pulse component and the reference pulse, delayed slightly so as not to collide with the filtered one, are combined and then detected with an optical sampling system [4] or a *pin* detector followed by an electrical sampling oscilloscope. The temporal resolution of these systems was 26 and 30 ps, respectively.

Three single-mode fibers were tested: 5 km of normal fiber (dispersion unshifted), and 50 and 100 km of dispersion-shifted fibers. To overcome fiber loss, we placed fiber amplifiers at the

input and output ports of the fiber. The compressed pulse source was directly connected to the input splitter to determine base-delay and wavelength. Test fibers were individually connected to the test system and the BPF was switched over 9 wavelengths while the relative net delay was measured. Results are shown in Fig. 2. For the 5 km normal fiber, the dispersion is 18 ps/-nm which agrees well with typical data at 1.55 μm . On the other hand, the dispersion-shifted fibers exhibited serious anomalies. Especially for the 50 km fiber, the plots are quite different from the expected slope given by the manufacturer. To solve this discrepancy, we measured the filtered spectra at the output port of the test fibers. Down-chirp of the input pulses was transformed to up-chirp after travelling the 50 and 100 km dispersion-shifted fibers, as shown in Fig. 3 where the launching peak power for the fibers was 65 and 88 mW, respectively. The words "up" and "down" refer to instantaneous frequency increase and decrease during the pulse. Negligible chirp change was observed for the 5 km normal fiber. Significant deformation of the total spectrum was observed for both shifted fibers. The spectral deformation can result in multi-peak spectra by filtering; hence we use mean values of half-intensity wavelength for the abscissa of Fig. 3. The spectral deformation was power dependent, as shown in Fig. 4. A narrow spectral peak develops and moves toward shorter wavelengths as the intensity increases. Although spectral deformation was apparent, pulse-waveform distortion was not seen for pulses traversing the dispersion-shifted fibers.

The theory for nonlinear pulse distortion at the zero-dispersion wavelength has been summarized by Agrawal [5]. In the case where nonlinearity dominates transmission characteristics, the theory explains our results well. According to this theory, the spectral deformation, or chirp change, is attributed to self-phase modulation effect (SPM); pulse intensity modifies pulse phase because of nonlinear refractive index and long interaction length without walk-off. For Fourier transform-limited pulses, SPM produces oscillatory and widespread up-chirped spectrum. Quantitatively, the chirp change shown in Fig. 3 can be explained as follows. Input pulses were down-chirped. SPM eliminates the down-chirp, and then forces up-chirping. Chirping manipulation using cross-phase modulation has been experimentally reported [6]. High-power Nd-YAG laser pulses (5.5 W maximum) were used to control 1.3 μm laser-diode pulses. The second order dispersion, B3 in Ref. [5], is expected to cause slightly asymmetrical spectra and oscillatory decaying pulse tails. Indeed, the observed spectra were far from symmetric, but this was not caused mainly by the second order dispersion, but by nonuniform chirp. Characteristic pulse tails were not observed in our experiments.

Conclusion

Experiments proved that pulse-delay measurements based on the linear refractive-index assumption are valid only in the dispersive wavelength region, and invalid at zero-dispersion wavelength. This is because pulses travelling at the zero-dispersion wavelength change their wavelength due to SPM effect, even for pulses lower than 100 mW peak power and 13 ps duration. Second-order dispersion was not a problem in our experiment. We have found that it is impossible

to retain the original pulse spectrum at the zero-dispersion wavelength if the repeater spacing is longer than 50 km. This fact is important for designing pulse transmission systems that use the short pulses described here.

Acknowledgments

The authors thank Sadakuni Shimada and Hideki Ishio for their encouragement. We also thank Kiyoshi Nakagawa and Masatoshi Saruwatari for their helpful discussions.

References

- (1) M. Fujise, M. Kuwazuru, M. Nunokawa, and Y. Iwamoto, "Highly accurate long-span chromatic dispersion measurement system by a new phase-shift technique," *J. Lightwave Technol.*, LT-5, pp. 751-758 (1985).
- (2) J. Yamada, "Simple dispersion measurement of a long-span, single-mode fibre using the longitudinal mode spacing of a semiconductor laser," *Opt. Quantum Electron.*, vol. 14, pp. 183-187 (1982).
- (3) A. Takada, T. Sugie, M. Saruwatari, "Picosecond optical pulse compression from gain-switched 1.3 μm distributed-feedback laser diode through highly dispersive single-mode fibre," *Electron. Lett.*, vol. 21, pp. 969-971 (1985).
- (4) Y. Yamabayashi, A. Takada, and M. Saruwatari, "Picosecond optical sampling with LiNbO₃ waveguide and compressed laser diode pulses," *Integrated and Guided-Wave Optics*, WD-5 (1988).
- (5) G. P. Agrawal, *Nonlinear Fiber Optics*, Ch. 4, (Academic Press, 1989).
- (6) T. Morioka and M. Saruwatari, "Demonstration of chirping manipulation of laser diode chirped optical pulses utilising cross-phase modulation in optical fibers," *Electron. Lett.*, vol. 25, pp 646-648 (1989).

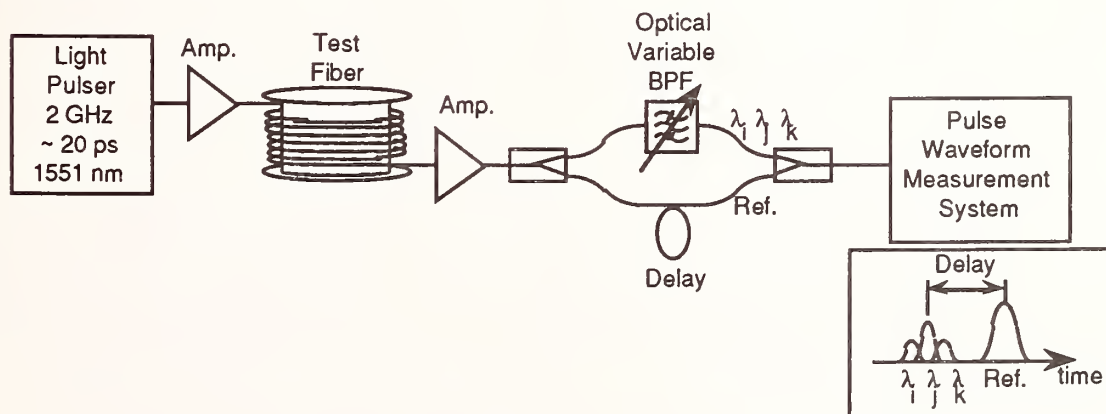


Fig. 1. Experimental setup for the relative-delay measurement; delay arm is for time reference, as shown in inset.

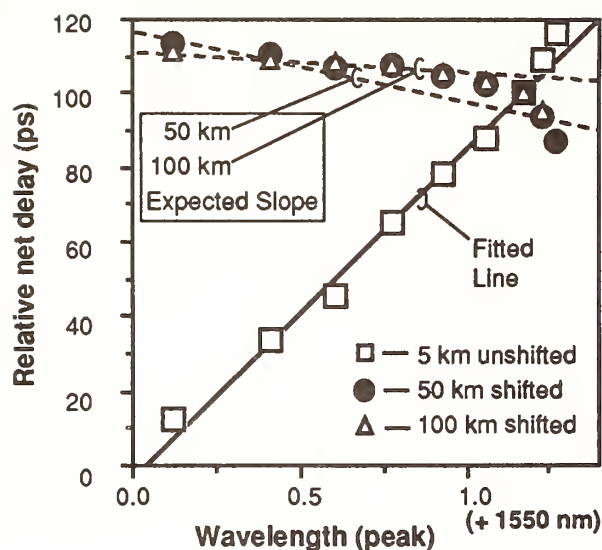


Fig. 2. Relative net delay as a function of peak wavelength. Fitted solid-line indicates 18 ps/(km nm) in agreement with the typical data for dispersion unshifted fibers. Plots for dispersion-shifted fibers do not fit with dashed lines calculated from manufacturer's dispersion data.

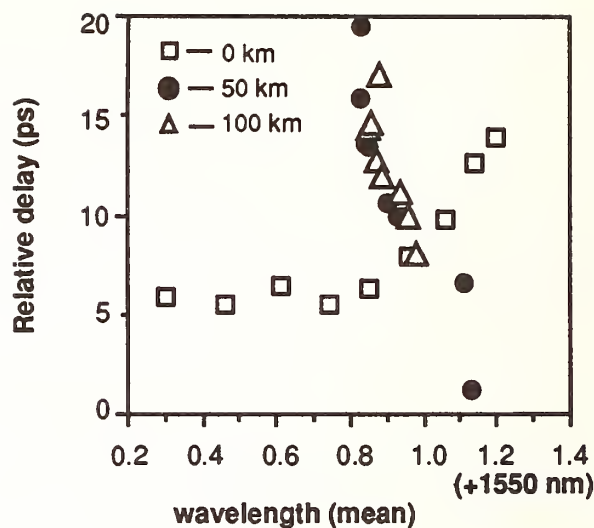


Fig. 3. Chirping before and after transmission through the dispersion-shifted fibers. Fiber input peak power was 65 and 88 mW for 50 and 100 km fiber, respectively. Mean values of half-intensity wavelength are used to reduce the effect of spectral deformation.

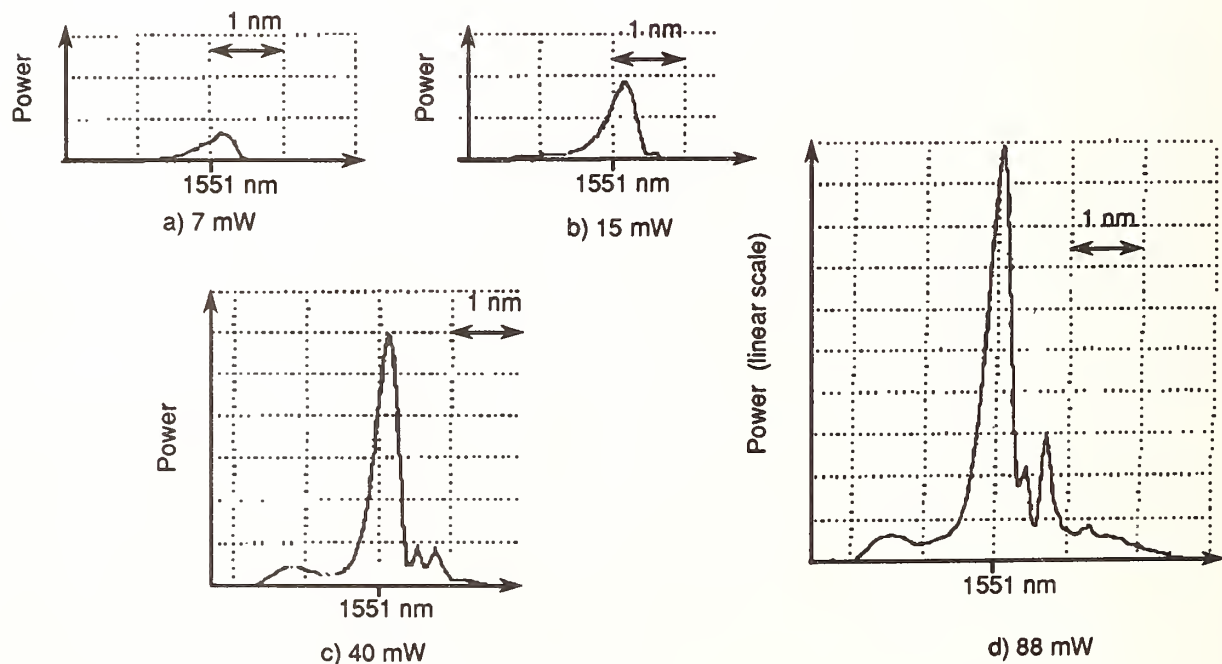


Fig. 4. Power dependent optical spectra after transmission through the 100 km dispersion-shifted fiber, ordinates in linear scale.

Measurement of Reduced Germania (GeO) Defect Levels in Optical Fibers by Fluorescence and Absorption Spectroscopy

R. M. Atkins
AT&T Bell Laboratories
Murray Hill, NJ 07974

Introduction

It is well known that germanosilicate optical fibers contain a reduced germania defect, often referred to as GeO^[1]. This defect absorbs strongly in the UV and is likely the defect responsible for the ability to write Bragg gratings into fibers (Hill gratings) using direct UV irradiation^[2] or by second harmonic generation from blue-green argon ion laser lines^[3]. GeO levels in preforms have also been shown to correlate with increased susceptibility in fibers to radiation and hydrogen induced loss^[4]. Two techniques for measuring GeO in optical fibers are presented here for the first time.

Experimental

The simplest method of GeO measurement in fibers is to measure the optical attenuation of the fibers at the wavelengths at which GeO is known to absorb, i.e. 240nm and 330nm. This can be accomplished using radiation from a Xe arc lamp, passed via a monochromator through the fiber and detected using a photomultiplier system. Problems associated with materials dispersion in refractive optics were avoided by placing the launch end of the fiber under test directly in the exit slit of the monochromator. To avoid problems caused by fiber fluorescence, a second monochromator was used ahead of the photomultiplier to select only the wavelength launched into the fiber and reject any fluorescence radiation. Light exiting the fiber under test was coupled to this second monochromator by placing the end of the fiber directly in the monochromator entry slits. As can be seen from figure 1, optical loss of the order of 20dB/meter is found at 330nm so measurements must be made on relatively short lengths of fiber in order to stay within the dynamic range of measurement instruments. Since the absorption coefficient at 240nm is approximately 1000 times greater^[1] than at 330nm, the direct measurement of attenuation at 240nm is impractical since it would require the use of cm lengths of fiber. Using absorption coefficients given by Schultz^[5] for GeO, it can be calculated that about 0.25% of the Ge in a typical fiber is in the form of GeO.

Loss values using this absorption measurement are calculated using the standard cut-back technique. In the course of making these absorption measurements it was noted that there was a periodic fluctuation in the intensity of the light exiting the fiber, as a function of input wavelength and the fiber length. It was also noted that the period of these fluctuations was proportional to the wavelength of illumination and inversely proportional to the fiber length. It is evident that the fluctuations are the result of interference between differently propagating modes. Though the fibers measured were single mode at 1.3 microns, in the short wavelength region they exhibit limited multimode propagation characteristics, with from 10 to 25 possible propagation modes in the 600 - 400nm region. The intensity of the fluctuations is somewhat dependent on launch conditions

(and hence the modes excited), but typical spectra are shown in figure 2. Fourier analysis of the more complex output fluctuations revealed several frequency components, corresponding to several propagation modes. While an analysis of these results may be of interest to those modeling propagation in optical waveguides, the fluctuations cause problems when measuring optical loss in a fiber particularly since they change position when a cut-back is performed. It was found that their amplitude could be reduced, or even eliminated, by a device which rapidly bent the fiber back and forth with a bend radius of ca. 1cm (mechanical mode averaging). The bending results in a different change in effective path length for each of the propagating modes and this change in effective length results in an averaging out of the interference effects provided the data collection time at a given wavelength is long compared to the period of fiber bending.

Though the absorption measurement of GeO is quite straightforward, it can be time consuming. A second, and perhaps easier, technique for GeO determination is based on the observation that GeO fluoresces when illuminated in the UV. GeO has two major UV absorption bands, centered near 240nm and 330nm and excitation at either wavelength results in fluorescence emission around 400nm. The 240nm band has approximately 1000x the absorption coefficient of the 330nm band. In this study the absorption of 254nm light, and the associated fluorescence emission in the 400nm region was used to make a quantitative determination of GeO in optical fibers. The experimental apparatus shown in figure 3 was developed for this purpose. A mercury lamp was used as the UV source and a 254nm interference filter was used to select a single intense mercury line. The polymer coating was stripped from a 1" section of a short (100cm) length of optical fiber. A fixed length of this uncoated section was then exposed from the side to the 254nm radiation from the filtered mercury lamp. The remote end of the fiber was coupled to a sensitive photodetector which measured the amount of fluorescence captured and guided by the fiber. The amount of fluorescence which is captured is dependent on the N.A. of the fiber. In the geometric ray model this corresponds to light whose angle of incidence on the core/cladding boundary is greater than the critical angle being lost from the fiber. Fluorescence emission will, of course, be guided along the fiber in both directions. Reflection of fluorescence emission from the excitation end of the fiber back to the photodetector can be minimized by the use of a drop of index matching oil on the excitation end of the fiber, though in these experiments it was found that this procedure was not necessary. Using data obtained from the absorption measurements, it can be calculated that the optical density of the material in a typical fiber core at 240nm is around 2200/meter. For a fiber core 8 microns in diameter, illuminated from the side, this would result in a maximum absorption of only about 3.5% of the incident radiation. Under these conditions fluorescence intensity is a linear function of fluorescing species concentration and the volume of material illuminated. Attenuation of the fluorescence emission along the fiber is not normally a problem since short ($< 100\text{cm}$) lengths of fiber are used, resulting in losses $< < 0.1\text{dB}$ at 400nm. In the case of special fibers with appreciable attenuation over a 100cm length at 400nm, measurements can be made on a number of fiber lengths, and results extrapolated to zero length (zero loss). Thus, in the general case, in comparing fluorescence from fibers of different structure, N.A., core size and fiber loss at the fluorescence wavelength must be taken into account. The relationship between fluorescence intensity and absolute GeO concentration requires the use of a fiber whose GeO content has previously been determined by absorption measurement as described earlier.

Conclusions

The GeO content of germanosilicate optical fibers can be determined quantitatively using absorption and fluorescence spectroscopy. These measurements may be useful in selecting fibers for special properties, such as the ability to easily form Hill gratings. Absorption spectroscopy measurements can be complicated by interference effects caused by multimode propagation in the fiber, but these effects can be overcome by mechanical mode averaging. An analysis of output intensity fluctuations due to interference between modes may be useful to those modeling optical propagation in fibers.

References

- 1 - M. Josephine Yuen, *Appl. Opt.*, **21**, 136 (1982).
- 2 - G. Meltz, W. W. Morey and W. H. Glenn, *Opt. Lett.*, **14**, 823 (1989).
- 3 - K. O. Hill, Y. Fujii, D. C. Johnson and B. S. Kawasaki, *Appl. Phys. Lett.* **32**, 647 (1978)
- 4 - K. T. Nelson, R. M. Atkins, P. J. Lemaire, J. R. Simpson, K. L. Walker, S. Wong and D. L. Philen, *Technical Digest, Optical Fiber Communications Conference*, San Francisco (1990), p6.
- 5 - P. C. Schultz, *Proceedings*, 11th Int. Cong. on Glass, Prague (1977).

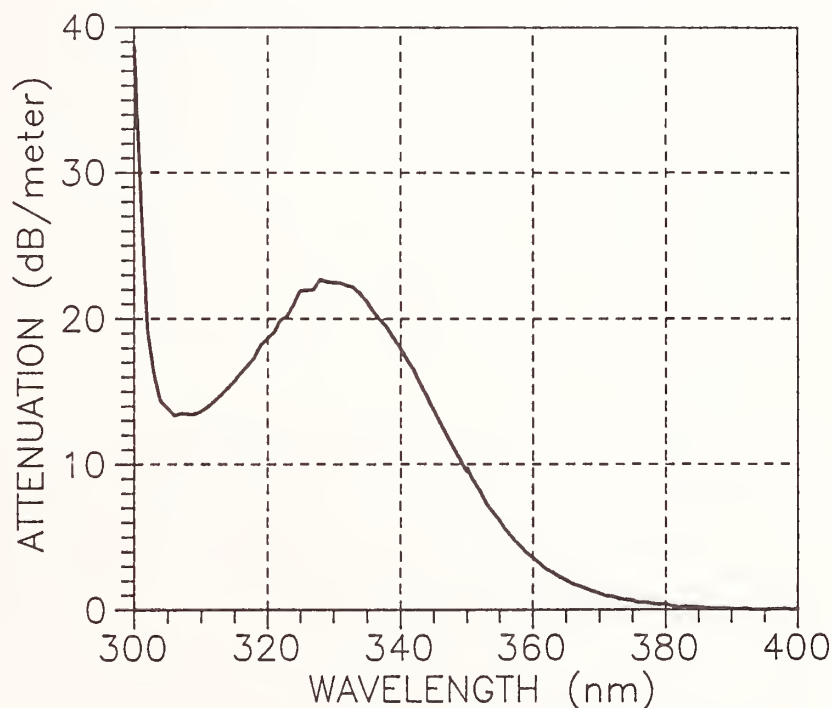


FIGURE 1 Short wavelength loss spectrum of a typical germanosilicate optical fiber. The absorption band at 330nm is due to an oxygen deficient germanium defect (GeO)

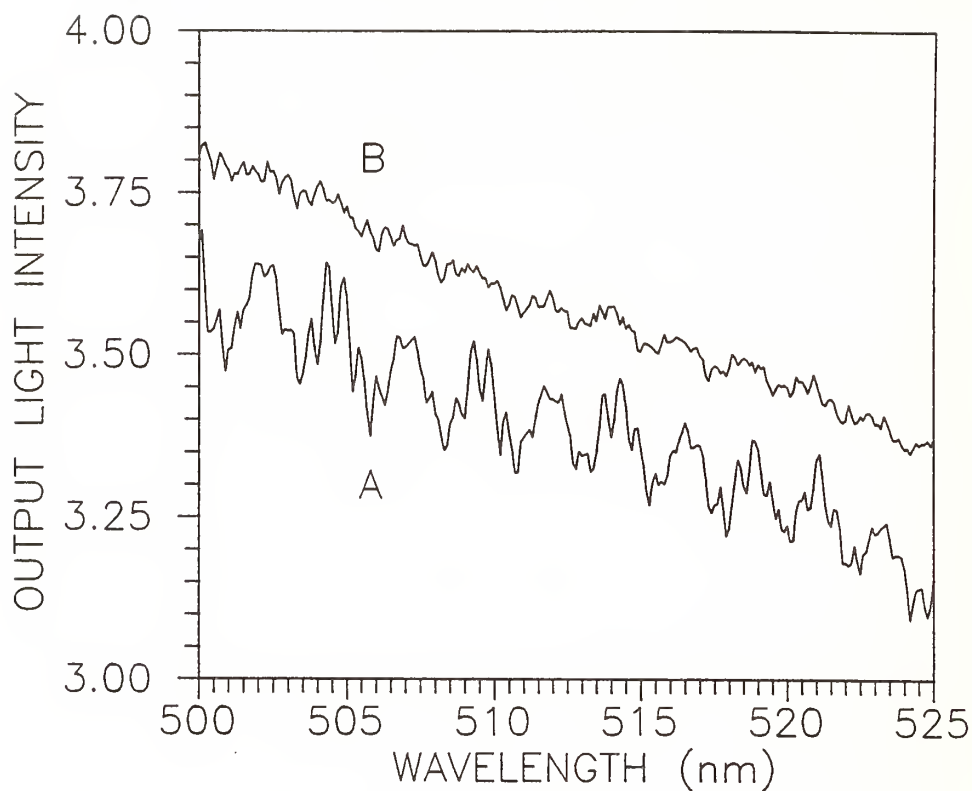


FIGURE 2 Output light intensity from a short (ca. 100cm) length of single mode optical fiber (cutoff at 1.25 microns). Trace **A** clearly shows the effects of interference between differently propagating modes. Trace **B** shows the effects of mechanical mode averaging (see text). Note that the trace **B** is offset for clarity - it actually approximates the mean of trace **A**.

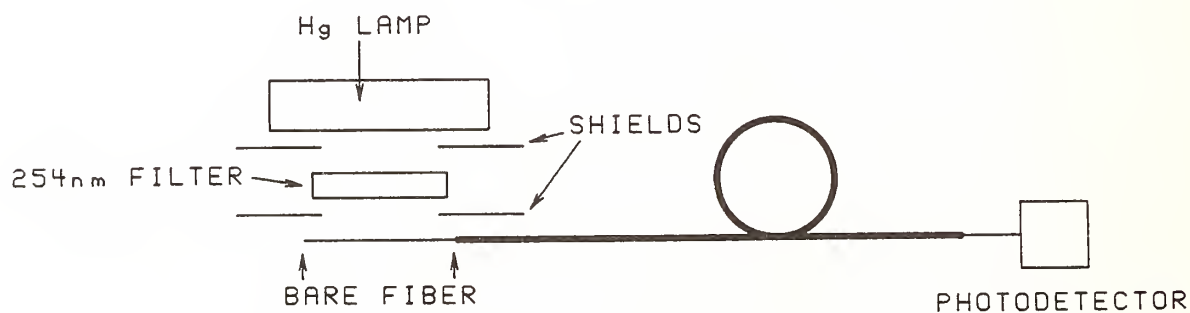


FIGURE 3 Schematic of the apparatus used for the fluorescence based measurement of the GeO content of optical fibers

STANDARDIZED MEASUREMENTS FOR DETERMINING THE RADIATION-INDUCED ATTENUATION IN OPTICAL FIBERS

E.W. Taylor,* E.J. Friebele** and P.B. Lyons***

*AFSC Weapons Laboratory, Kirtland AFB, NM 87117

**Naval Research Laboratory, Washington, DC 20375

***Los Alamos National Laboratory, Los Alamos, NM 87545

ABSTRACT

This paper summarizes the work of 14 laboratories in NATO Panel IV, Research Study Group 12, Nuclear Effects Task Group over a period of 5 years to obtain consistent measurements of the attenuation induced in optical fibers by steady state and transient radiation exposures. Critical parameters for standardized testing have been identified.

INTRODUCTION

Since optical fiber data links and fiber sensors may be deployed in applications which might be exposed to radiation, it is important to determine the change in optical attenuation in the fiber induced by the radiation environment. Steady state environments include space, fallout, delayed gamma, or nuclear reactors, while potential transient radiation sources are pulsed fusion reactors, pulsed laboratory facilities, or military radiation environments. The incremental loss can be measured by conventional transmission or reflection techniques, but it is of the utmost importance that these measurements be standardized, that the parameters critical for consistent, reliable results be identified, and that values for these parameters be adequately specified.

In particular, measurement of the response of fibers to steady state environments addresses the growth of the incremental loss during exposure and the recovery following the irradiation, while transient measurements are primarily concerned with the recovery of the incremental loss following a high dose rate-pulsed radiation exposures of ≤ 100 ns duration. This paper will summarize the results of interlaboratory comparisons of the responses of fibers exposed to ^{60}Co steady state and various pulsed electron and x-ray radiation sources performed by members of NATO Panel IV, Research Study Group 12 Nuclear Effects Task Group. Three papers have been published summarizing steady state measurements[1,2] and transient results.[3]

Over the 5 year time period during which the comparisons were made, the tests have progressed from step index silica core 100/140 multimode fibers at $0.85\ \mu\text{m}$ to $1.3\ \mu\text{m}$, followed by measurements of graded index fibers at $1.3\ \mu\text{m}$ and single mode waveguides at both 0.85 and $1.3\ \mu\text{m}$. The 14 laboratories involved in the tests were: the Air Force Systems Command Weapons Laboratory (WL), Aerospace Corporation, Boeing Aerospace Corporation, Commissariat à l'Energie Atomique (CEA) and Direction des Recherches, Etudes et Techniques-Etablissement Technique Central de l'Armement-Centre d'Etudes de Gramat (CEG) in France, EG&G Santa Barbara Operations, Fraunhofer-Institut für Naturwissenschaftlich-Technische Trendanalysen (F-INT) in W. Germany, Harry Diamond Laboratories (HDL), Lawrence Livermore National Laboratory (LLNL), Los Alamos National Laboratory (LANL), Messerschmidt-Bölkow-Blohm GmbH (MBB) in W. Germany, Naval Research Laboratory (NRL), and Royal Military College of Science (RMCS) and STC Technology Ltd. (STC) in the UK. Except as noted above, the laboratories were in the US.

STEADY STATE MEASUREMENTS

Initial measurements carried out by the participating laboratories using their own "standard" test conditions revealed a wide range of measured responses.[1] The first attempt at standardization was specification of 1 μW optical power in the fiber, a measurement wavelength near 0.85 μm , and specific combinations of dose rate and total dose shown in Table I. For the first set of measurements, the fibers were to be irradiated using combination A, i.e. a dose rate of 3 Gy/min to a total dose of 30 Gy. Fig. 1 shows the data reported by 4 laboratories who measured the 100/140 silica core fiber A nominally under the specified conditions. It is obvious that the agreement was not good--the average mean incremental loss at 20 Gy was 4.00 dB/km, but the standard deviation was 0.97 dB/km, i.e. approximately 25% of the induced loss. This wide variance was attributed in part to differences in source wavelengths from 0.828-0.850 μm , optical powers from 0.75-1.0 μW , dose rates from 1.92-3.04 Gy/min, sample coil diameters from 3.7-58 cm, and injection conditions.[1]

Table I Dose Rate and Total Dose Combinations Specified for Steady State Tests.		
Combination	Dose Rate (Gy/min)	Total Dose (Gy)
A	3	30
B	13	100
C	13	1000
D	100	10000

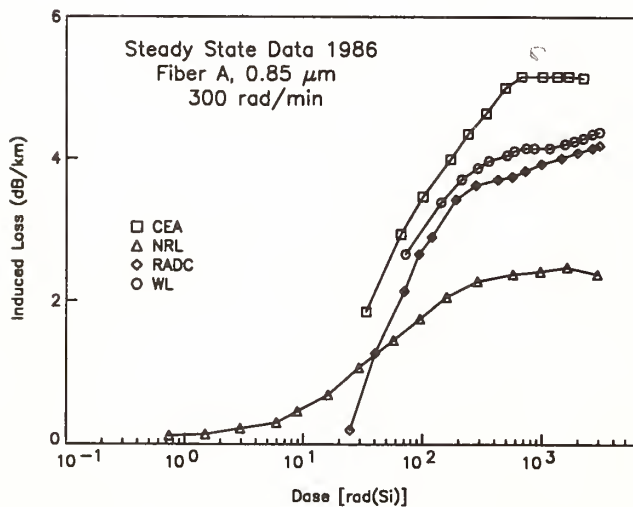


Figure 1. Growth of the radiation-induced optical absorption at 0.85 μm in a 100/140 silica core multimode fiber during nominally 3 Gy/min steady state exposures to 30 Gy. The lines connect the data points. Note that 1 Gy = 100 rad.

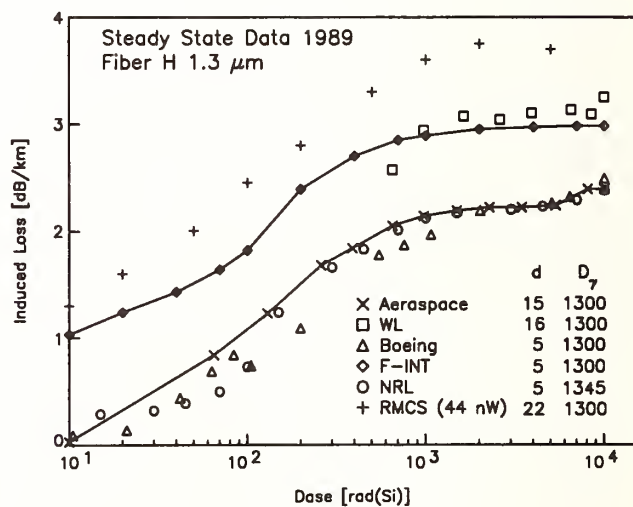


Figure 2. Growth of the radiation-induced optical absorption in a single mode silica core fiber during 13 Gy/min steady state exposures to 100 Gy. Note the different sample coil diameters d (cm) used by the laboratories. The two lines connect data sets of the two groups of laboratories reporting similar radiation responses (see ref. 2).

Additional specification was thus implemented in later tests.[2] In particular, identical fiber-pigtailed LED's were distributed to participants, and a test protocol for assuring 1 μ W of *injected* power in the fibers was established. It was found that the presence or absence of mode scrambling and mode stripping had little effect on the measured loss, and an experiment conducted to compare the measured incremental loss using 70/70 limited phase space injection conditions[4,5] vs. simple fusion splicing demonstrated equivalent results.

Results typical of the improved agreement are shown in Fig. 2 for a 1.3 μ m silica core single mode fiber.[2] The mean peak incremental loss is 2.70 dB/km, and the standard deviation is only 0.35 dB/km. (The RMCS data was excluded from this calculation because it was obtained with an optical power level significantly lower than specification, which inhibited any photobleaching that occurred during exposure and made comparison with the other data meaningless.) Note that because of increased radiation hardness and longer wavelength of measurement, it was necessary to expose this fiber was exposed to dose-dose rate combination B to obtain sufficient induced loss for significant comparison. Under the tighter specifications, standard deviations of 7-17% of the peak induced loss are routinely achieved.

These comparisons of steady state fiber responses have demonstrated that for consistent measurements it is essential to adhere to specified total dose-dose rate combinations and optical powers to minimize photobleaching differences, while variations in injection conditions do not appear to contribute significantly to variations in measured response. Although improvements have been achieved in interlaboratory results, there remain variances in reported measurements which may arise from factors such as differences in sample coil diameter, source spectrum due to moderation by either water or air between the source and sample, and the effect of dose build-up layers. Dose buildup occurs where the dose experienced by subsequent layers of fiber increases due to the enhanced stopping power for low energy electrons ionized from the air surrounding the fiber and the low energy component of the γ -ray source spectrum.

TRANSIENT MEASUREMENTS

An example of the lack of agreement at the beginning of the study is shown in Fig. 3.[3] Since the 3 reporting laboratories used doses varying from 440 to 1200 Gy, the data have been normalized to 450 Gy. The LLNL spectral data were extrapolated to 0.84 μ m, while LANL and MBB/F-INT used 0.84 μ m LED's. Optical powers in the fiber varied from 0.2 to 300 μ W. Note also the lack of temporal overlap between the data sets, precluding detailed comparisons.

To minimize the variations in test conditions among the laboratories, the level of specification of radiation and optical parameters was increased throughout the period.[3] Dose levels of 5, 100 and 1000 Gy were to be used, optical sources at 0.84 and 1.3 μ m with powers of 1 μ W were suggested, and significant efforts to improve dosimetry were undertaken.

An example of the excellent agreement obtained among 6 laboratories testing a silica core single mode fiber in 1989 is shown in Fig. 4.[3] The experimental parameters were quite consistent: almost all laboratories used a dose of 100 Gy; the optical source wavelengths varied only from 0.83-0.85 μ m, and all but two laboratories used 1 μ W optical power. This adherence to specified conditions, together with close attention to the dosimetry, resulted in excellent agreement in spite of significant differences in radiation source energy (0.5-25 MeV) and pulse length (1.5-9000 nsec) used by the laboratories.[3]

CONCLUSIONS

This study has demonstrated that consistent, standardized testing of the incremental loss induced in optical fibers by radiation exposure is achievable, provided the test parameters are properly specified and implemented.[2,3] As a result, an improved test procedure for measuring the response of optical fibers to environmental and adverse nuclear environments has been

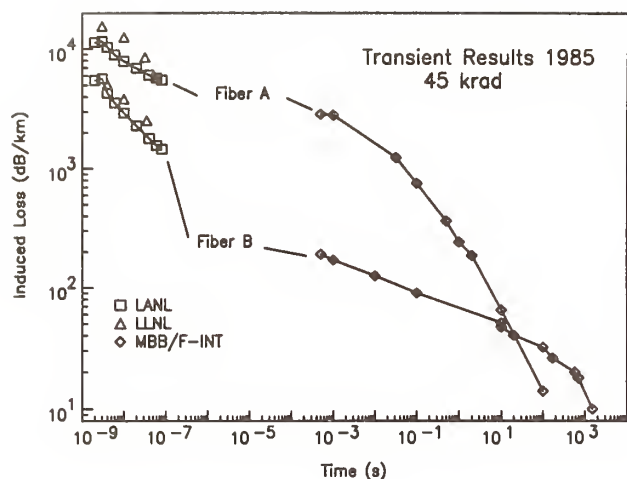


Figure 3. Transient radiation-induced absorption near $0.85 \mu\text{m}$ reported by 3 laboratories in 1985 on 100/140 low- and high-OH silica core fibers A and B, respectively. The lines connect the LANL and MBB/F-INT data sets.

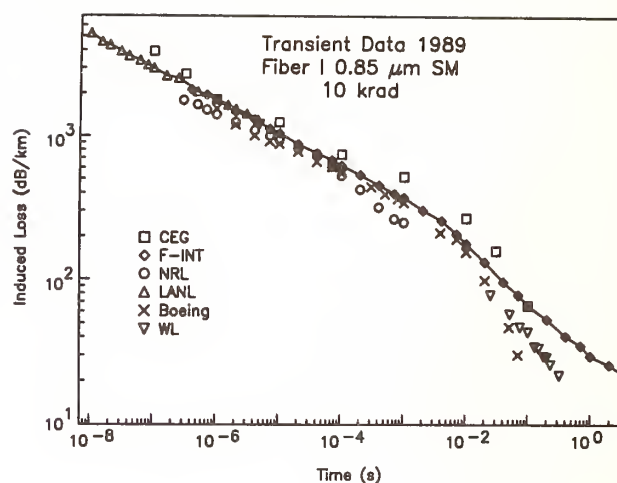


Figure 4. Transient radiation-induced absorption reported by 6 laboratories in 1989 on a silica core single mode fiber at $0.85 \mu\text{m}$ following an exposure of 100 Gy. A line has been drawn through the LANL and F-INT data sets to aid the eye.

completed and is being submitted to NATO Panel IV for consideration. The details of this document will be discussed at the meeting. In addition, a procedure for standardized measurement of the transient radiation response of fibers is being drafted.

REFERENCES

1. E.J. Friebele, E.W. Taylor, G. Turquet de Beauregard, J.A. Wall and C.E. Barnes, "Interlaboratory comparison of radiation-induced attenuation in optical fibers I. Steady state exposures," *J. Lightwave Tech.* **6** (1989) 165-171.
2. E.W. Taylor, E.J. Friebele, H. Henschel, R.H. West, J.A. Krinsky and C.E. Barnes, "Interlaboratory comparison of radiation-induced attenuation in optical fibers. Part II: Steady state exposures," *J. Lightwave Tech.* **8** (1990) 967-976.
3. E.J. Friebele, P.B. Lyons, J.C. Blackburn, H. Henschel, A. Johan, J.A. Krinsky, A. Robinson, W. Schneider, D. Smith, E.W. Taylor, G. Turquet de Beauregard, R.H. West, and P. Zagarino, "Interlaboratory comparison of radiation-induced attenuation in optical fibers. Part III: Transient exposures," *J. Lightwave Tech.* **8** (1990) 977-989.
4. P.R. Reitz, "Measuring optical waveguide attenuation: The LPS method," *Optical Spectra*, August 1981, pp. 48-52.
5. EIA-RS-455-FOTP 46: "Spectral attenuation measurement for long length, graded index optical fibers," FOTP 50: "Light launch conditions for long length graded index optical fiber spectral attenuation measurements." Electronic Industries Association, Washington, DC.

Test Method for Fiber Optic Connector Parameters Directly Affecting Return Loss

Z. Pasturczyk^{*}, T. Chepyha⁺, C. Saravanos^{*}, H. Wood⁺

^{*} *Optical Cable Division, Northern Telecom Canada Ltd.,
Saskatoon, Saskatchewan, S7K 3L7*

⁺ *Department of Electrical Engineering, University of
Saskatchewan, Saskatoon, Saskatchewan, S7N 0W0*

1.0 Introduction

The return loss of a fiber optic connector is an important parameter for determining the amount of light reflected at the connection point. Reflected light is detrimental to high bit rate fiber optic transmission systems and must be minimized by using low return loss connectors, otherwise:

- a. Light reflected back into the laser may cause system instability and degradation of signal to noise ratio [1].
- b. Multiple connection from several connectors may create constructive or destructive interference of the incoming signal causing large power fluctuations [1].

The most common way to achieve a low return loss without compromising insertion loss is to form a convex shape at the end face of the connector. This is known as PC polishing. The idea behind the PC connector is to maintain polished fiber ends in Physical Contact. The final return loss of a PC connector is highly dependant on the shape of the ferrule end face. Deviation from the specified geometrical shape will result in an undesirable air gap between fibers. Presence of an air gap can degrade return loss by up to three orders of magnitude. Physical shape of the connector end face in terms of surface quality is also important. Scratches on the fiber and/or the higher refractive index at the end face due to surface damage during polishing can alter the return loss by one order of magnitude.

It is common practice for connector manufacturers to measure the return loss of fiber optic connectors according to FOTP-107 [2]. The limitations of this test method made it necessary to develop a supplementary test method so that good return loss is guaranteed for even the most unfavorable circumstances in the field. This paper describes a novel automated test station for measuring the geometrical parameters of connector end faces using a non-contacting optical method, in which a personal computer is used to analyze interferometric images of the connector end face.

2.0 Limitations of FOTP-107 [2]

FOTP-107 is the industry standard test method for measuring return loss of fiber optic connectors. The connector under test is mated with a reference quality connector and the return loss of the mated pair is measured. The typical acceptable return loss of a connector is -40 dB.

The problem with the existing method is that it does not give any information about the geometrical shape of the ferrule end face. Connector end faces with slight imperfections usually make PC contact when mated with a perfectly shaped reference connector, giving an acceptable return loss. However, if two imperfect connectors are mated with each other, there will be a high probability that the fiber ends will be separated by an air gap, resulting in very poor return loss. Figure 1 shows how an air gap between two similarly shaped PC connectors is created. The end face of both connectors deviates from the ideal case, where the center of the convex shaped end face coincides with the fiber center.

Return loss degradation can introduce noise due to interference, causing an entire fiber optic communication link to fail. Therefore, for systems requiring low reflections, it is dangerous to accept connectors based exclusively on measurements performed according to FOTP-107, because connectors that exhibit low reflections in production may fail in the field.

3.0 Proposed Test Method

The main purpose of the proposed test method is to analyze the geometrical shape of the ferrule end face. The objective is to guarantee contact between fibers in the worst possible combination of two out-of-shape connectors. Three parameters of the PC shaped ferrules are tightly controlled:

- a. **Vertex offset**, defined as the distance between the center of the fiber and the highest point of the convex surface of the ferrule end face.
- b. **Radius of curvature**, defined as the radius of a best fit spherical surface into the convex shape over the area within 100 microns from the ferrule center.
- c. **Overpolishing/Underpolishing**, defined as the average distance between the fiber end surface and the best fit spherical surface.

The acceptance or rejection criteria of a connector is based on a combination of these parameters.

3.1 Test Equipment

The proposed test station is shown in Figure 2. The connector under test becomes an element of a Michelson interferometer^[3] once the ferrule is inserted into the holder. The holder locks the ferrule in a repeatable position that is precisely aligned to the axis of the interferometer. A Helium-Neon laser beam is also aligned to the interferometer axis. Light reflected from the ferrule end face, combined with the light reflected from a flat mirror inside the Michelson interferometer, produce an interference pattern. Since the connector end face is convex, the interference fringes form a set of concentric rings. The magnified ring pattern is imaged onto a CCD camera, which is then digitized by an image capture device and sent to the computer for analysis.

3.2 Test Procedure

For each connector tested, the parameters listed in Section 3.0 are calculated from the fringe pattern.

- a. **Vertex offset** is the distance between the center of concentric rings and the fiber center.
- b. **Radius of curvature** is calculated from the distance between adjacent fringes. The wider spaced the rings, the larger the radius.

- c. **Overpolishing/Underpolishing** is determined from the deviation of the fringe pattern from circular shape. Only the portion of the fringes that goes through the fiber area is taken into account. The larger the deviation, the higher the degree of overpolishing/ underpolishing.

The test station is fully automated and takes less than 10 seconds to perform all the required calculations. The operator only inserts new connectors and adjusts focus.

4.0 Test Results

A number of connectors were tested to determine interrelation between the ferrule geometry and return loss. Parameters such as vertex offset and radius of curvature were varied while overpolishing was minimized. The polishing procedure was optimized to minimize the number of scratches and to eliminate the high refractive index layer from the fiber end face.

A number of connector pairs were selected by mating connectors with the same end face characteristics. The return loss of each pair was measured and the results are shown in Figure 3. For vertex offsets below a threshold value, the connector return loss remains constant and better than -40 dB. When the vertex offset exceeds the critical value, the return loss increases rapidly to approximately -10 dB. This sharp increase is caused by the separation of the fiber ends and the resultant air gap between the fiber end faces. Connectors with larger radii of curvature maintain low return loss over wider range of vertex offset. Overpolishing would result in loss of PC contact even sooner than those shown in Figure 3. Further data, including measurement repeatability and accuracy, will be presented at the conference.

5.0 Conclusions

A novel instrument for the precise measurement of fiber optic connector parameters that directly affect its return loss performance has been developed. The measurement technique is fully automated, therefore eliminating subjective operator input.

The proposed test method measures connectors for their worst case performance, thereby guaranteeing low return loss performance in the field. The technique also eliminates the need for a reference connector, which results in improved measurement repeatability.

6.0 References

- [1] V. Shah, W.C. Young, L. Curtis, "Large Fluctuations in Transmitted Power at Fiber Joints with Polished Endfaces: OFC/IOOC'87 TUF4, (1987)
- [2] FOTP-107 "Return Loss For Fiber Optic Components", ANSI/EIA/TIA-455-107-1989
- [3] A.A Michelson, E. W. Morley, "On the Relative Motion of the Earth and the Luminiferous Ether". The American Journal Of Science [Third Series], Vol. XXXVI, No. 203, Nov. 1887.

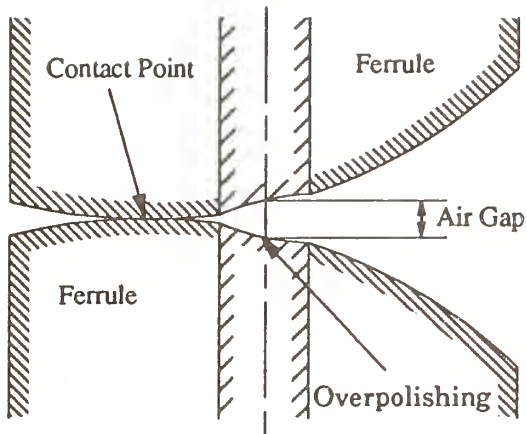


Figure 1.0 Air Gap Due to Contact Point Offset

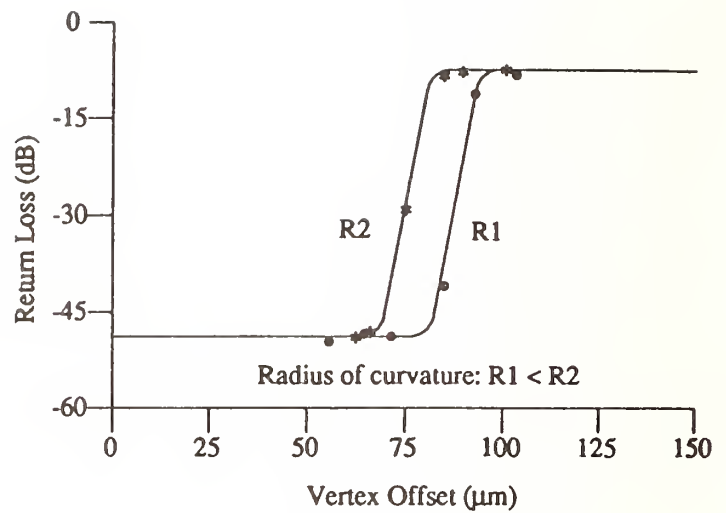


Figure 3.0 Effect of Radius of Curvature and Vertex Offset on Return Loss

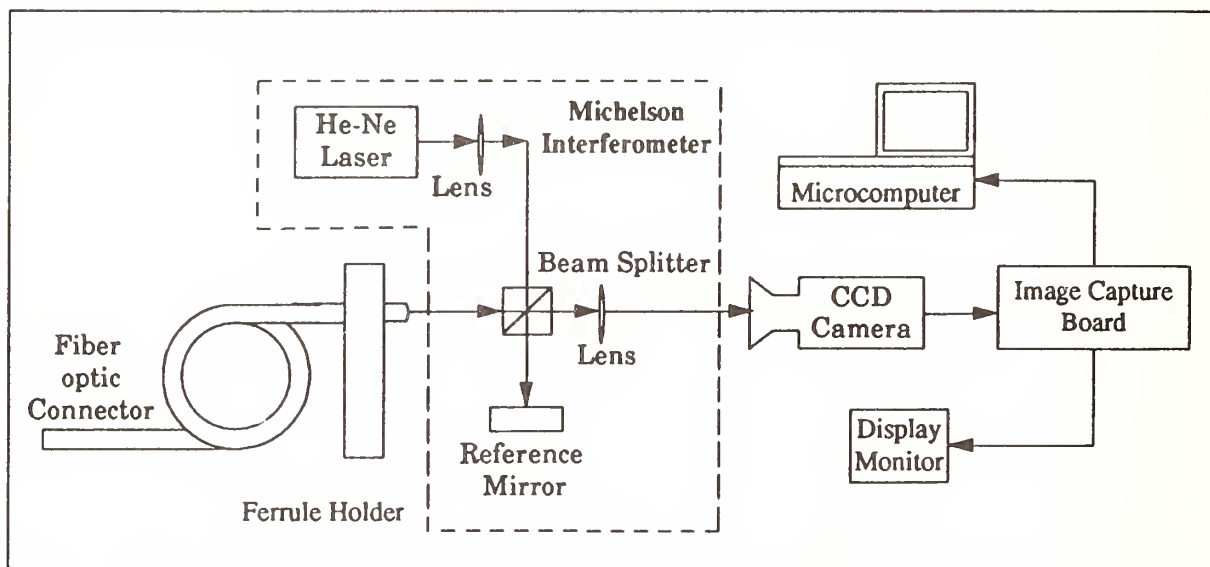


Figure 2.0 - Test Station Block Diagram

DIFFERENTIATING CORE AND CLADDING LOSS CONTRIBUTIONS IN SINGLE MODE FIBER ATTENUATION MEASUREMENTS

W. LIESE, R. KERSLAKE, K. KOWALIUK, P. PILON

NORTHERN TELECOM CANADA LTD
OPTICAL CABLE DIVISION
SASKATOON, SASKATCHEWAN

ABSTRACT

The measured attenuation of single mode fibers is affected by loss contributions from both the core and the cladding. These regions can have different attenuation characteristics. In such a case a shift in the ratio of core to cladding power of the LP₀₁ mode, due to a change in the cutoff wavelength, will result in a change of the measured attenuation spectrum. We have developed a technique to separate core and cladding attenuations and by way of example, use the individual effects of radiation, hydrogen and impurities on the core and cladding region of single mode fibers to highlight the usefulness of the technique.

1.0 INTRODUCTION

The optimization of fiber processing steps for single mode telecommunication fibers can benefit from the ability to discriminate between core and cladding attenuations. At present this is particularly important for the development of fibers with high resistance to radiation damage [1] and hydrogen damage, as well as for research on new fiber materials such as plastics, sol gel and ZBLAN glasses. However, a well developed method does not currently exist. The standard cutback method for spectral attenuation provides no information on attenuation taper over the fiber length. The introduction of dual wavelength, bidirectional OTDR measurements [2] eliminates the guesswork on fiber taper by obtaining attenuation, relative cutoff and relative modefield diameter along the fiber length. For multimode fibers the method of selected excitation of distinct fiber modes has been used in the UV to obtain information on radial attenuation distributions [3]. This paper describes a method to discriminate between core and cladding attenuation in single mode fibers with applications for process optimization and fiber material selections.

2.0 THEORETICAL BACKGROUND

Attenuation spectra of single mode fibers are affected by contributions from the core and the cladding region since the LP₀₁ mode radius (which depends on the cutoff wavelength) extends beyond the core into the cladding. Therefore, the significance of the cladding attenuation increases in any measured attenuation spectrum from short to long wavelengths.

The power fraction of the LP₀₁ mode travelling in the cladding (Pf_{clad}) can be calculated with (1a). Using the Gaussian approximation [4], Pf_{clad} can be approximated to better than 1% accuracy with (1b).

$$Pf_{\text{clad(a)}} = \frac{\int_a^\infty r P(r) dr}{\int_0^\infty r P(r) dr} \quad (1a)$$

$$Pf_{\text{clad}} = e^{-2(a/w_0)^2} \quad (1b)$$

$$\frac{w_o}{a} = 0.65 + 0.434 \left(\frac{\lambda}{\lambda_c} \right)^{3/2} + 0.0149 \left(\frac{\lambda}{\lambda_c} \right)^6 \quad (2)$$

Where "a" is the fiber core radius, "w_o" is the LP₀₁ modefield radius and "λ_c" is the LP₁₁ cutoff wavelength.

The fiber cutoff wavelength can be controlled during the drawing operation. Simply changing the fiber outer diameter leads to a change of the cutoff wavelength according to :

$$\lambda_c = \frac{2\pi a NA}{V} \quad (3)$$

where V is the normalized frequency and NA is the numerical aperture.

Core and cladding attenuations contribute to the measured attenuation α_m in a good approximation according to the respective power fractions Pf:

$$\alpha_m = \alpha_{core} Pf_{core} + \alpha_{clad} Pf_{clad} \quad (4)$$

where

$$1 = Pf_{core} + Pf_{clad} \quad (5)$$

and the approximation αL << 1, with the fiber length L.

Spectral attenuation measurements carried out at different cutoff wavelengths permit us to solve a set of linear equations for core and cladding attenuations. Graphically this is represented in Fig.2 where attenuations α₁ and α₂ measured at a fixed wavelength but different cutoff wavelengths, are plotted versus their cladding power fractions Pf_{clad}. Linear regression is used to obtain core and cladding attenuations by extrapolation of the power fraction to 0% and 100%. Repeating this procedure for different wavelengths leads to the construction of core and cladding attenuation spectra, α_{core}(λ) and α_{clad}(λ).

For the applications reported below we have varied the cutoff between 1000 and 1500 nm. For typical communications fibers, this leads to a variation of the power launched into the cladding between 10% and 30%. From this discussion it is obvious that an extrapolation technique can lead to serious errors. The method is therefore most suitable to situations, where large differences in the launched powers exist and attenuation measurement errors are minimized. The accurate knowledge of the launched power is of little significance. It is assumed with this method that all power measured and attenuated is from the LP₀₁ mode. This requires a careful removal of all higher modes by a careful fiber layout [5] at the low end of the spectrum. Bending losses (in the low cutoff case) set the limit at the long end of the spectrum, and can be minimized by appropriate winding conditions.

3.0 APPLICATIONS

In order to demonstrate the effectiveness of this technique, we have manufactured a fiber preform with a Ge doped core and P/F doped depressed cladding, and pulled it at three cutoff wavelengths (1120, 1240, 1350 nm) by varying the fiber diameter. The measured spectral attenuation characteristics of the three fiber pieces were identical within .03 dB/km over the entire spectral range indicating no significant differences between core and cladding attenuation. The results of separating the core and cladding components are shown in FIG.3a. The OH peak at 1385 nm is slightly increased for the cladding region and a long wavelength tail is present due to the P-content in the cladding. The fiber was used for the following experiments.

Radiation Testing: After ⁶⁰Co - γ irradiation with a dose of 1050 rad (35 rad/min;30 min) there is a significant change in attenuation for the three fibers (FIG.3b). The fiber with the lowest cutoff shows the most significant loss increase. This is expected from PI-defects in the

cladding region leading to a broad absorption tail in the vicinity of 1550 nm [6]. Separating core and cladding attenuation (FIG.3c) clearly demonstrates that the loss increases in FIG.3b are indeed caused by the cladding contribution with a loss of 7 dB/km at 1.55 μ m.

Hydrogen Testing: Similarly, we have exposed three lengths of fiber from the above preform to H_2 at 1 atm; $T=125^\circ C$ for 3h and dry N_2 at $T=125^\circ C$ for 18h to allow time for the interstitial H_2 to leave the glass matrix. Separating core and cladding loss for these fibers reveals a significant increase in the OH peaks for both core and cladding as well as a long wavelength attenuation tail in the cladding region (FIG.4). A broad peak at 1400 nm is very noticeable in the core region and attributed to Ge OH, which has been clearly isolated here.

Impurities: The method can also be used to trace impurities to the core or cladding region of the fiber. FIG 5 gives an example showing minor OH contamination of the core region only.

5.0 CONCLUSION

We have demonstrated a method which discriminates between core and cladding attenuation in step index single mode fibers by combining attenuation measurements from fibers drawn with different cutoff wavelengths. The standard cutback test method was used, requiring only modifications of the existing test software. The suggested test method is not limited to core and cladding separation but can also be applied to probe any radial region of a fiber by imposing suitable integration limits on equation (1a). Altogether this leads to a powerful new tool with applications to future developments in fiber process and materials.

6.0 ACKNOWLEDGEMENT

This work would neither have been fun nor possible without the support of D. Lambert, B. Bachewich, D. Paquin, D. Hyde, and S. Gransden. Their contributions are gratefully acknowledged.

7.0 REFERENCES

- [1] E.J. Friebele, "Radiation Response Prediction of Single Mode Fiber", NCC Technical Inf. Bull. 88-1, Optical Science Div. Naval Res. Labs, Washington, DC 20375, March 1988
- [2] K. Kowaliuk, J. Ferner, "A Technique to Estimate the Cutoff Wavelength Profile in Singlemode Fibers Using a Switchable Dual Wavelength OTDR", Techn. Digest, Symp. on Optical Fiber Measurements" Boulder, Col., NBS Special Publ. 748, 1988
- [3] K.F. Klein, A. Muehlich, K.H. Worner, "Reduction of drawing induced UV-absorption band in undoped silica core fibers", paper WQ15, Technical Digest, Optical Fiber Communications Conf., New Orleans, 1988.
- [4] L.B. Jeunhomme, "Single-Mode Fiber Optics" Marcel Dekker Inc, New York, p.18, 1983.
- [5] Z. Pasturczyk, C. Saravanos, R.S. Lowe, "Measurement of Single Mode Fiber Attenuation over an Extended Spectral Range" "Technical Digest, Symp. on Optical Fiber Measurements" Boulder, Col, NBS Special Publication 748, 1988.
- [6] E.J. Friebele, D.L. Griscom, "Color Centers in Glass Optical Fiber Waveguides", in "Defects in Glasses", F.L. Galeener et al, Mat. Res. Soc. Proceedings, Vol. 61, Pittsburgh, 1986.

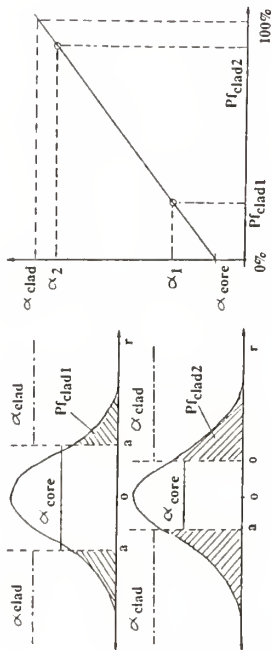


Figure 1 Power distribution of LP01 mode in core/cladding for different core diameters (cutoff wavelength).

Figure 2 Attenuation vs. cladding power fraction at a fixed wavelength (here $\alpha_{clad} > \alpha_{core}$).

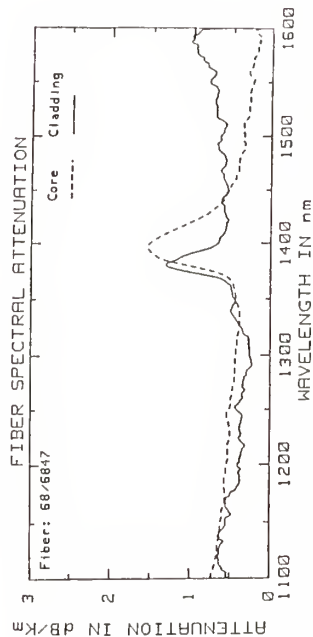


Figure 3a Core and cladding attenuation after hydrogen exposure of a fiber (3a shows attenuation before hydrogen exposure). Note the shift in the core attenuation peak at 1400 nm.

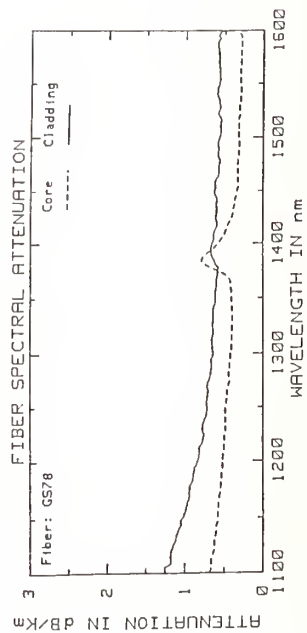


Figure 3b Spectral attenuation of a fiber with low level OH impurities in the core region. Note the absence of OH in the cladding.

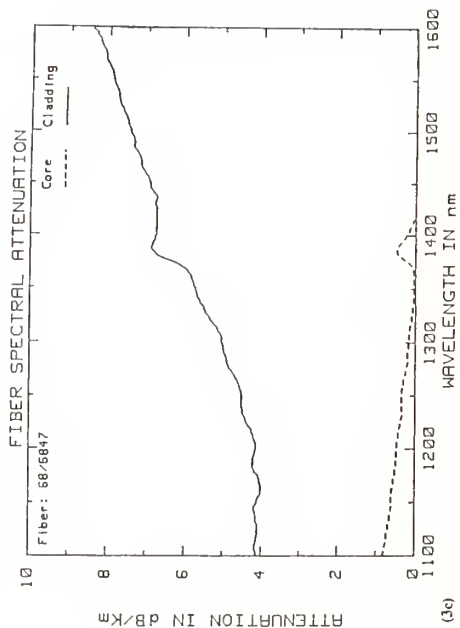
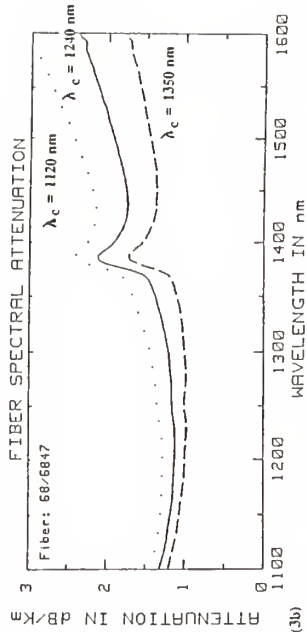
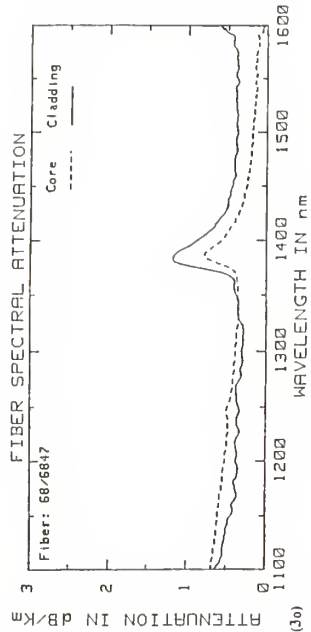


Figure 3 Radiation effect on fiber with P/F doped cladding and Ge doped core.
(3a) Core/cladding attenuation before C_{60} gamma irradiation.
(3b) Spectral attenuation of fiber pulled at different diameters after irradiation.
(3c) Core/cladding attenuation of fiber (3a) after irradiation.

A Single Launch Technique to Determine Loss and Dispersion in Multimode Fiber Systems

Michael Yadlowsky
Alan Mickelson
University of Colorado
Department of ECE
Boulder, CO 80309

June 4, 1990

1 Introduction

Because of mode dependent propagation effects, the bandwidth of a section of multimode fiber depends of its excitation. Therefore, the dispersion penalties for "short" components such as connectors and splices can vary considerably from system to system. The ambiguity of simple bandwidth measurements can be partially overcome through the use of pulse transition matrices (PTM's) [1], an extension of the mode transition matrices. This technique, however, requires n^2 steady-state loss measurements and n^2 dispersion measurements made using n different launches to generate the three $n \times n$ matrices needed to characterize distributed components. There are also inaccuracies inherent in the matrices because it is not possible to excite completely independent launches [2,3] or detect only specific portions of the output power [1]. Finally, the matrices only provide information regarding the broadening and delay of pulses resembling those used in the actual measurements.

Transfer function theory, on the other hand, offers a means of simplifying fiber measurements and calculations because a component can be characterized by measurements made with a single launch [3,4]. This is made possible by including a physical model of a component's operation into its mathematical description. Thus, even a distributed component such as a fiber can be characterized by a pair (full length and cut-back) of steady-state near-field measurements and a similar set of dispersion measurements. By reducing the number of launches needed for dispersion measurements and avoiding the launch dependence of PTM's, the transfer function technique has the potential to both simplify the dispersion measurement process and improve the accuracy of system models. Furthermore, once determined, the transfer function of a system can be used to calculate its time domain response to any specified input.

The ultimate goal of applying transfer functions to dispersion is to develop a comprehensive theory that can be used to produce an automated CAD package for multimode fiber systems design. This would make it possible to accurately evaluate complicated system designs using only a few simple measurements.

2 Theory

The use of broad-band sources such as LED's and multimode laser diodes with multimode fibers leads to the presence of a continuum of modes propagating within a fiber [5]. Thus, while mode coupling only occurs between modes of a given wavelength, external quantities such as the fiber

near-field intensity profile and impulse response are continuous functions because of the combined effects of all wavelengths present in the source linewidth. It is therefore possible to index the fiber modes with a continuous parameter R^2 which can be related to both the propagation constant of the mode and the ray tracing variables of the ray congruences associated with a mode [6].

The transfer function for short components can be defined by its effect on the time dependent power distribution function $P(z, t, R^2)$ (the total power in modes R^2 to $R^2 + d(R^2)$) according to

$$P_{av}(z^+, t, R^2) = \int_0^1 dR'^2 T(R^2, R'^2) P(z^-, t, R'^2), \quad (1)$$

whereas for distributed components it is necessary to solve the time dependent equation of transfer,

$$\left(\frac{\partial}{\partial z} + \frac{1}{v_g(R^2)} \frac{\partial}{\partial t} \right) P(z, t, R^2) = \int_0^1 d(R'^2) K(R^2, R'^2) P(z, t, R'^2). \quad (2)$$

The first order solution of equation (2) is given by

$$P_1(z = l, t, R^2) = v_g(R^2) \int_{-\infty}^t dt' \int_0^1 d(R'^2) K(R^2, R'^2) P(0, t' - \frac{l - v_g(R^2)(t - t')}{V_g(R'^2)}, R'^2) \quad (3)$$

The function $v_g(R^2)$ is the group velocity of the modes designated by R^2 and is assumed to have the form

$$v_g(R^2) = v_{g0} + v_{g1} R^2. \quad (4)$$

The power redistribution function $K(R^2, R'^2)$ is related to the time independent transfer function of the device and contains all of the mode coupling effects and differential mode attenuation (DMA). Mode coupling is assumed only to take place between adjacent degenerated mode groups (in a single scattering event) and to obey the mode coupling model of reference [7], leaving only one overall strength parameter to be measured. Olshansky's [8] linear DMA model provides two additional parameters to be experimentally determined. The next section describes how these parameters are obtained from near-field and dispersion measurements using curve fitting techniques.

3 Measurement/Fitting Procedure

The test setup used to make the needed measurements is shown in Fig. 1. The procedure used to measure and characterize short components has been described previously [4,2]. To measure a long piece of fiber, the full length fiber is excited with an overfilled launch (or any other launch which excites all modes), and the pulse response is measured using an pulses whose duration is short compared to the anticipated broadening of the fiber. The steady-state transmitted power and the near-field intensity are also measured. The fiber is then cut back, and the above measurements are repeated. The steady-state measurements are used to calculate the total loss of the fiber. The near-field profiles are normalized so that the ratio of their total powers is consistent with the loss measurement. The input (cutback) and output (full length fiber) mode group power distributions are calculated from Chebyshev polynomial fits to the fiber near-field according to the relation

$$P(z, t, R^2) = -\frac{\pi R}{2} \frac{d}{ds} I_z(s)|_{s=R} \quad (5)$$

where s is the normalized radial coordinate of the fiber, $s = r/a$ and $I_z(s)$ is the fiber near-field intensity at position $z = l$.

The mode coupling and DMA parameters are then used to fit the input power distribution function to the output power distribution using equation (1) and the relation

$$T(R^2, (R')^2) = e^{K(R^2, (R')^2)}. \quad (6)$$

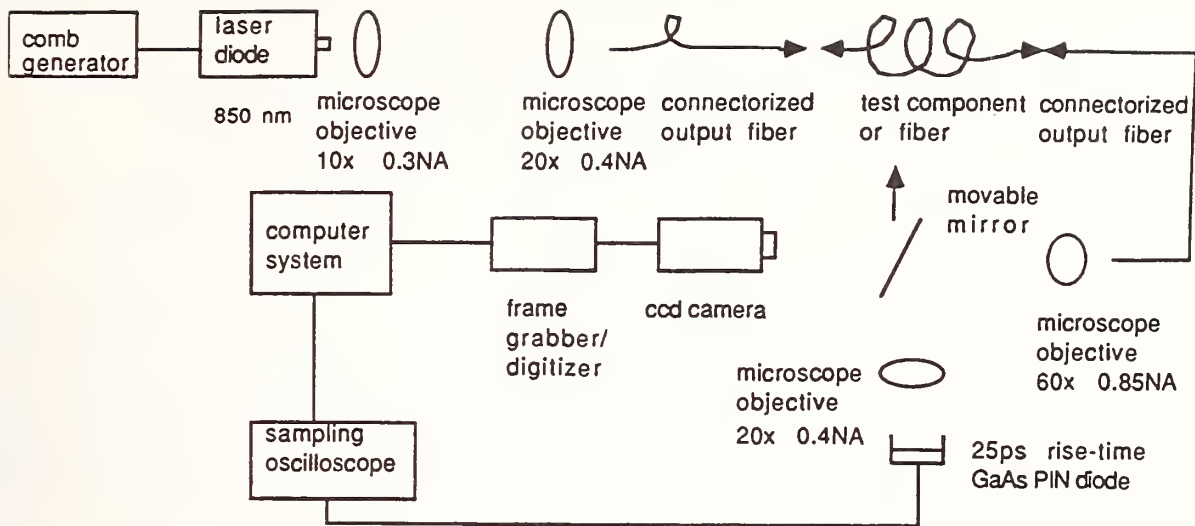


Figure 1: Measurement Set-up

These parameters are then substituted into equation (3), and this is integrated over R^2 and fit to the measured pulse response of the fiber using the parameters v_{g0} and v_{g1} .

This set of parameters then provides a complete model of the fiber which can be used to predict the loss, dispersion and mode coupling effects found in any length of the test fiber. This model can be used in conjunction with the short component models for splices and connectors as well as the power splitter model under development, to perform complex system calculations.

4 Results

As a first test of the validity of the theory, equation (3) has been used to calculate the evolution of pulses with propagation length down a fiber. This has made it possible to generate dispersion curves showing the length dependence of pulse dispersion in the presence of mode coupling, DMA and random profile fluctuations. These results show qualitative agreement between equation (3) and previously published experimental data [9] and also demonstrate that all three of these effects are capable of causing sub-linear dispersion for certain parameter values.

A more thorough test of the theory is underway in the form of a concatenation experiment. In order to demonstrate the utility of the theory to predict fiber system performance from component models, a test system consisting of splices, connectors, power splitters and fiber sections is being measured. Because power splitters have a significant effect on the modal power distribution of a fiber, this test should provide an accurate appraisal of the above theory.

5 Conclusion

By including a model of the basic operation of fiber components into their mathematical description, it is possible to greatly reduce the complexity of the measurements needed to characterize them. Previous work has demonstrated the efficacy of transfer function theory for describing systems containing "short" components. The work presented here describes how the theory can be extended to distributed components such as long fiber links. While complete experimental verification of the theory is still underway, preliminary results show qualitative agreement between some of the

theory's predictions and experimental results already in the literature. When fully developed, transfer function theory provides the opportunity to produce a complete CAD package that can do loss and dispersion simulations of complicated fiber systems.

References

- [1] G. Evers, F. Henze and U. Unrau, "Mode Transition Matrices for DMA and DMD Characterisation of Optical Fibers and Components," *Proc. of SPIE*, v.559, pp.176-180, 1985.
- [2] S. Yang, I. P. Vayshenker, D. R. Hjelme, and A. R. Mickelson, "A Transfer Function Analysis of Measured Transfer Matrices," to appear in *Applied Optics*.
- [3] S. Yang, D. R. Hjelme, I. P. Januar, I. P. Vayshenker and A. R. Mickelson, "A Single Launch Technique for the Determination of Mode Transfer Matrices," in *Technical Digest of the Symposium of Optical Fiber Measurements*, sponsored by the National Bureau of Standards, NBS special publication 748, pp.103-106, 1988.
- [4] S. Yang, D. R. Hjelme, I. P. Januar, I. P. Vayshenker, and A. R. Mickelson, "A Transfer Function Approach to the Experimental Determination of Mode Transfer Matrices," *Applied Optics*, v.28, pp.3148-3157, August 1, 1989.
- [5] A. R. Mickelson and M. Eriksrud, "Mode Continuum Approximation in Optical Fibers," *Optics Letters*, vol.7, pp.572-574, 1982.
- [6] S. Piazzola and G. de Marchis, "Analytic Relation between Modal Power Distribution and Near-field Intensity in Graded Index Fibers," *Electronics Letters*, vol.15, pp.721-722, 1979.
- [7] A. R. Mickelson, O. Klevhus, and M. Eriksrud, "Backscatter Readout from Serial Microbending Sensors," *Journal of Lightwave technology*, LT-2, pp.700-709, 1984.
- [8] R. Olshansky and S. M. Oaks, "Differential Mode Attenuation Measurement in Graded Index Fiber," *Applied Optics*, vol.17, pp.1830-1835, 1978.
- [9] M. Eriksrud, A. Mickelson, N. Ryen, "Length Dependence of Optical Fibre Bandwidth", *Electronics Letters*, vol. 19, pp.994-996, Nov. 10, 1983.

Measurement of Fiber Coating Geometry Using a Transversely Scanning Laser Beam

Gregory E. Smith
Corning Incorporated
Wilmington, NC

Introduction

During the manufacture of optical fiber one or more layers of protective polymer coating(s) are applied to the fiber. This coating is important in maintaining the optical performance of the cabled fiber and in providing needed protection to the fiber. Multiple coating layers are commonly applied to the fiber to provide optimum performance. A measurement is required to assure that the required thickness of coating is applied uniformly around the circumference of the fiber. The measurement should be capable of characterizing all of the individual layers as well as the combination if multiple layers are used. A quality measurement will provide manufacturing process feedback as well as agreement throughout the industry.

The current predominant technique in use today is a manual technique using a microscope equipped with a filar gauge. In this technique an operator inserts a coated fiber into a special microscope slide so that the fiber is immersed in index fluid. Using various techniques to secure the fiber, the operator rotates the fiber until the point of minimum coating thickness is observed. The operator then uses the filar gauge to measure this minimum coating thickness and the thickness of the coating opposite the minimum. The coating concentricity is then calculated. For multiple coating layers, this procedure is repeated for each layer. Coating concentricity is calculated according to the following formula :

$$\text{Concentricity}(\%) = \left(\frac{\text{Minimum Wall Thickness}}{\text{Wall Thickness Opposite Minimum}} \right) \times 100\% \quad (1)$$

Studies into the accuracy and repeatability of various operators using this manual technique showed repeatabilities as low as $\pm 8\%$. The error is most noticeable as concentricities approach 100% and locating the actual point of minimum coating thickness becomes more difficult. In addition to this unrepeatability, additional errors up to 2 % can be predicted from the virtual imaging caused by light refraction inside the coatings as the operator performs the filar measurements. Given the ever tightening specification on minimum allowable coating concentricity, an improvement over the current manual technique seems necessary.

After reviewing the forward scattering model developed by Watkins¹ for single layers of coatings, the model was extended to multiple coating layers. It was observed that a measurement would be possible if a light beam were focused to a relatively fine spot and scanned transversely across the coated fiber. As the beam is traversed across the fiber it is deflected by the coating layers based on the position of the incoming beam with respect to the axis of the fiber. The deflection function has several key inflection points whose location is based on the geometry of the coating and fiber. The easiest type of inflection point to describe mathematically from the theory and to locate experimentally is the point of first derivative equalling zero. This deflection function and the major inflection points can be described theoretically using ray optics. Once the deflection of the beam is measured as the beam is traversed across the fiber, these key inflection point locations can be determined. After the inflection points have been determined, the coating geometry can be calculated by solving the theoretical equations. The magnitude of the deflection at the point of inflection is not needed for the calculation of coating

¹ L.S. Watkins, "Scattering from Side-Illuminated Clad Glass Fibers for Determination of Fiber Parameters", Journal of the Optical Society of America, V.64, No.6, June 1974

geometry, only the beam position. This insensitivity to magnitude makes the measurement dependant only on the accuracy with which the scanning beam position is known as the deflection is measured. Position is an easily measured and controlled parameter with commercially available equipment. A similar technique was used by Watkins² on fiber preforms to determine index profile, but in that case it was the magnitude of the deflection that was key in the measurement.

Equipment and Setup

The basic overview of the optical setup can be seen in Figure #1. Here a fiber is inserted vertically into an oil filled cell. The refractive index of the oil has been chosen to optimize the measurement with the type of coating used. For all the coatings currently in use by Corning, a single oil is used. On two sides of the cell, optically flat glass plates are used to contain the oil yet allow a light beam to pass through the cell. A laser beam is expanded, spatially filtered, collimated, then refocused down to approximately a $5\ \mu\text{M}$ spot. The focal point of the beam is centered on the fiber that is immersed in the oil cell, through the flat cell window. A linear lateral effect cell is then mounted on the opposite side of the oil cell to measure the position of the focused beam with respect to the cell after it has been deflected by the fiber. A rotating magnetic clamp is mounted on the top of the oil cell to hold the fiber and rotate the fiber for the measurement. An extension of the clamp is a specially designed holder which maintains the fiber position at the focal plane of the laser beam while allowing it to rotate and the beam to traverse the fiber. The entire oil cell, detector, and fiber clamp assembly is mounted on a linear air bearing slide. As the cell is traversed, it has the effect of traversing the focused beam laterally across the fiber. The deflection of the laser beam is measured at very small increments of fiber traverse. A computer is used to gather the deflection data and locate the inflection points. An example of this deflection function can be seen in

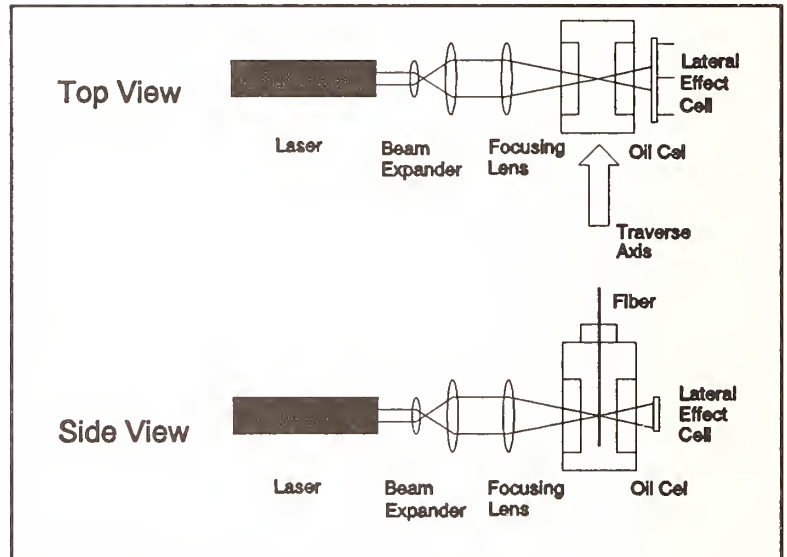


Figure 1 Basic Optical Setup

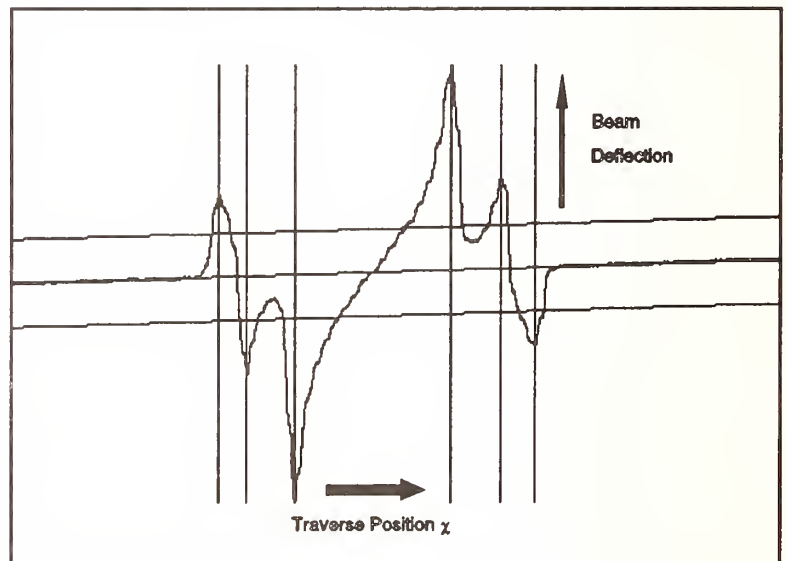


Figure 2 Beam Deflection

²L.S. Watkins, "Laser Beam Refraction Traversely Through a Graded-Index Preform to Determine Refractive Index Ratio and Gradient Profile", Applied Optics, Vol. 18, No. 13, July 1979

Figure #2 for a two layer coating system. In this figure the inflection points are indicated by vertical lines. The computer automatically controls the fiber traverse and data collection, and then controls fiber rotation. The fiber is rotated to gather multiple scans of data for the final determination of all the coating geometry characteristics.

Calculations

For every layer of coating applied to the fiber, there are three key parameters that describe the geometry of the layer with respect to its center medium, whether that be a fiber or another coating layer. The three key parameters are:

- ω = Radius of Inner Medium; Overall Radius ω_0 equals 1.0
- ϵ = Offset Distance of Coating Center to Inner Medium Center
- θ = Angle of Concentricity with Respect to Viewing Angle

The additional characteristic of the coating necessary to perform the calculations is:

- η = Index of Refraction of Coating Layer

The nomenclature is illustrated in Figure #3. As stated earlier the complete model describes the deflection of the beam as it passes through the fiber and exits at a certain angle. A measured deflection function as a function of entering ray position was shown in Figure #2 for a two coating layer system. The main inflection peaks in this function physically occur due to points of maximum reflection or refraction, depending on the refractive indices of the coating layers. For the case of up to two coating layers the following equations apply:

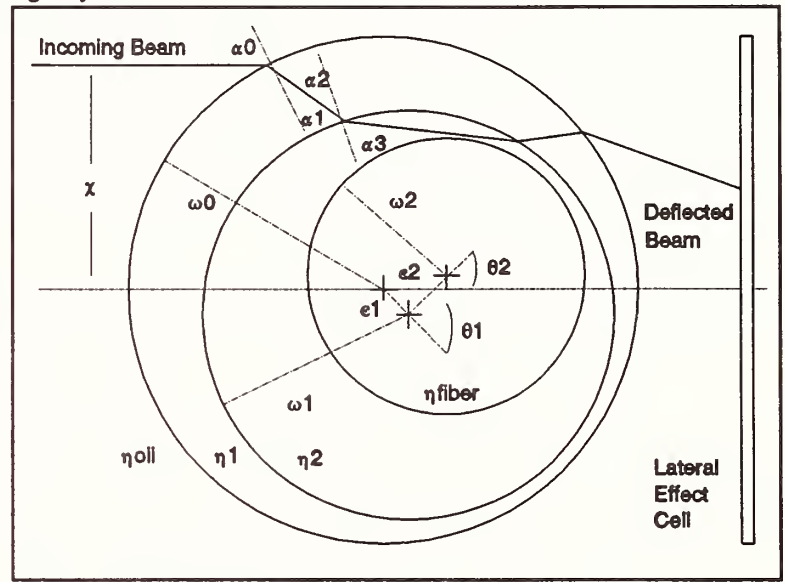


Figure 3 Nomenclature

$$\alpha_0 = \arcsin(\chi) \quad (2)$$

$$\alpha_1 = \arcsin(\sin(\alpha_0) \times \frac{\eta_{oil}}{\eta_1}) \quad (3)$$

$$\delta_1 = \alpha_0 - \alpha_1 + \theta_1 + (2\pi - \phi) \quad (4)$$

$$\gamma_1 = \left(\frac{\sin(\alpha_1)}{\omega_1} \right) - \left(\sin(\delta_1) \times \left(\frac{\epsilon_1}{\omega_1} \right) \right) \quad (5)$$

$$\gamma_2 = \gamma_1 \times \left(\frac{\eta_1}{\eta_2} \right) \quad (6)$$

$$\alpha_2 = \arcsin(\gamma_1) \quad (7)$$

$$\alpha_3 = \arcsin(\gamma_2) \quad (8)$$

$$\delta_2 = \alpha_0 - \alpha_1 + \alpha_2 - \alpha_3 + \theta_2 + 2\pi - \phi \quad (9)$$

$$\gamma_3 = \sin(\alpha_3) \times \left(\frac{\omega_1}{\omega_2} \right) - \sin(\delta_2) \times \left(\frac{\epsilon_2}{\omega_2} \right) \quad (10)$$

$$\gamma_4 = \gamma_3 \times \left(\frac{\eta_2}{\eta_{fiber}} \right) \quad (11)$$

The angle ϕ is the angle of the entire system with respect to the initial view, for situations where the fiber is rotated between scans. For the case where the index of the secondary layer, η_1 , is greater than that of the primary, η_2 , a point of maximum reflection will occur when γ_2 is equal to 1.0. For the opposing condition when the primary layer index is greater than the secondary layer index, a point of maximum refraction will occur when γ_1 is equal to 1.0. Similarly, when the index of the fiber cladding is less than that of the primary layer, then a point of maximum reflection will occur when γ_4 is equal to 1.0. Finally, when the index of the fiber cladding is greater than that of the primary layer a point of maximum refraction will occur when γ_3 is equal to 1.0. By observing the direction of beam deflection, the software can determine which case applies when solving for the geometry parameters.

The calculation involves solving equations 2 through 11 depending on the relative indexes of the coatings, and the number of layers. Since η_{oil} and η_{fiber} are known, there are eight unknowns in the system of equations for two layers of coatings, ω_1 , ω_2 , ϵ_1 , ϵ_2 , θ_1 , θ_2 , and η_1 , η_2 . At each inflection the entering ray position χ was measured. Additionally, the dependency of equations 2 through 11 on η_1 and η_2 is very small and constants accurate to within ± 0.05 are used in the solution of the equations. To solve for the remaining six unknowns, six unique inflection locations are required. Each scan of the beam across the fiber yields four inflections for the current case of two coating layers. Therefore only two scans of data at different rotational views, ϕ , are required for a solution. To improve accuracy, 12 scans are taken at 30° rotational intervals of ϕ and a least squares solution is performed. Once the individual concentricities of each of the coating layers is calculated, the overall combined concentricity is calculated as the geometrical combination of the individual layers.

Summary and Results

Repeatability tests were performed on the device with a variety of fiber types with successful results. For the standard fiber configuration with a fiber diameter of $125 \mu\text{m}$, primary coating layer of $205 \mu\text{m}$, and a secondary coating diameter of $250 \mu\text{m}$, the repeatability (one Sigma) measured was 0.3%. The repeatability of diameter measurements for all layers was $0.15 \mu\text{m}$, with an accuracy of $\pm 0.3 \mu\text{m}$. Since ray theory forms the basis of the measurement, no virtual imaging problems exist as in the manual method.

These results indicate an increase in repeatability over the current manual method of more than an order of magnitude. In addition, the measurement time of approximately 30 seconds is much faster than the current technique and becomes an advantage when a high number of measurements are being performed.

Acknowledgements

I would like to acknowledge H.A. Spicer and R.A. Fanning for their contributions to all phases of this project and without whom the successful results would not have been possible.

RELIABILITY TESTING OF A FIBER OPTIC SYSTEM FOR SUBSCRIBER LOOP APPLICATIONS

T. S. Frank Lee

Bellcore
Transmission Quality & Reliability Division
331 Newman Springs Road
Red Bank, NJ 07701

This paper describes the techniques and results of reliability testing of a fiber optic transmission system. During these reliability tests, various measurements were performed to monitor the system's performance, including optical spectral characteristics, power, and other parameters related to the optical transmitter/receiver. The reliability tests performed, temperature cycling and temperature/humidity aging, were designed to investigate the impact of the uncontrolled subscriber loop environment on fiber optic equipment.

Ensuring the reliability of fiber optic equipment is important in reducing equipment life-cycle costs and maintaining customer satisfaction. It also has an important role in the successful realization of a future all-fiber telecommunication network. Lab reliability testing and measurements at an early stage represent a critical step toward these ends.

As fiber optic and digital technologies are introduced into the subscriber loop, relatively new equipment designs and state-of-the-art components may be housed in above-ground cabinets or aerial enclosures, whose inside environments are uncontrolled. Relative humidity can vary between extremes. Temperatures can range from -40°C to $+65^{\circ}\text{C}$. Until recently, most fiber optic transmission systems have not been designed or tested for operation for these wide temperature and humidity extremes. The challenge to loop equipment suppliers is not just to demonstrate proper equipment operation at these extremes one time, but to assure long-term endurance of their equipment operating for many years under these hostile conditions.

The system under study is a combined fiber optic transport and digital multiplex system that is designed for uncontrolled environment applications in the loop. It is a SONET-based system transmitting at the SONET OC-3 signal level (155.52 Mb/s). The optical transmitter and receiver are combined into a single optical plug-in card, which utilizes a laser diode with a 1310-nm wavelength as the light source and an avalanche photodiode as the detector. The system has 84 DS1 (1.544 Mb/s) low-speed interface channels, and can transmit 2016 VF channels over a single-mode fiber pair.

The test setup is illustrated in Figure 1. The fiber optic system was first placed in an environmental chamber and temperature cycled between -40°C and $+65^{\circ}\text{C}$ for 100 cycles. The ramp time in each direction was 30 minutes, resulting in a ramp rate of

3.5 °C/min. The dwell time at either temperature extreme was 60 minutes. Various measurements (Table 1) monitored the system's performance before, during and after temperature cycling. Following this, the system was subjected to high temperature/humidity aging at 65 °C and 95% RH for 1000 hours. Similar measurements were performed on the system in this second test.

Results indicate that the system's optical characteristics, bit error and jitter performance, and other measured parameters remained relatively constant throughout the 100 temperature cycles. [Table 2 shows the optical measurement results.] This outcome suggests that the test did not cause long-term performance degradation of the system, and consequently implies that a "good" fiber loop system should be able to endure the conditions of a test like this. Thus, there appears justification for customers to require a temperature cycle endurance test as part of the equipment supplier's system qualification and reliability test programs.

However, a potential quality and performance problem was discovered, which was associated with the dynamic ramping of temperature. During temperature ramp-down from about 0 °C to -40 °C, a bit error rate (BER) exceeding the Bellcore requirement (10^{-9}) was consistently observed throughout the temperature cycle test. [Figure 2 shows ramp-induced BER as a function of cycle number.] This BER disappeared after the system stabilized at -40 °C for about 15 minutes, indicating that it was not a steady-state problem. When the ramp-down rate was decreased from the original 3.5 °C/min to 0.9 °C/min, the BER was still present, although slightly smaller. Further investigation on this problem is underway, and the results will be reported at the Symposium.

Table 1. Parametric Measurements

Measurement Type	Parameters
Optical Characteristics	Laser Output Power Central Wavelength (λ_c) Spectral Line Width ($\Delta\lambda$) Received Optical Power Receiver Sensitivity
Transmission Characteristics	Bit Error Rate (BER) % Error-Free Seconds (%EFS) Burst Errored Seconds (BES) Jitter Generation Jitter Tolerance
Other Characteristics	Laser Module Temperature Test Point DC Voltages Input Voltage Tolerance Protection & Alarms System Start-Up

Table 2. Optical Characteristics in Temperature Cycling

Operating Temperature	Parameter	Before Cycling	After 5 Cycles	After 10 Cycles	After 50 Cycles	After 100 Cycles
-40 °C	Output Power (dBm)	-15.5	-15.4	-15.4	---	15.4
	λ_c (nm)	1284.5	1284.5	1284.5	---	1284.5
	$\Delta\lambda_{RMS}$ (nm)	0.5	0.5	0.5	---	0.5
	$\Delta\lambda_{MSTM}$ (nm)	1.3	1.2	1.2	---	1.2
	Rx Sensitivity (dBm)	-39.6	-39.5	-39.9	---	-39.7
+20 °C	Output Power (dBm)	-15.2	-15.3	-15.3	-15.2	-15.4
	λ_c (nm)	1303.5	---	1303.4	1303.8	1304.0
	$\Delta\lambda_{RMS}$ (nm)	1.4	---	1.4	1.5	1.5
	$\Delta\lambda_{MSTM}$ (nm)	4.5	---	3.7	4.5	4.3
	Rx Sensitivity (dBm)	-40.0	---	-40.1	-40.0	-39.9
+65 °C	Output Power (dBm)	-15.1	-15.1	-15.2	-15.3	-15.3
	λ_c (nm)	1318.2	1318.0	1318.1	1318.6	1318.1
	$\Delta\lambda_{RMS}$ (nm)	1.2	1.1	1.2	1.1	1.2
	$\Delta\lambda_{MSTM}$ (nm)	4.0	3.3	3.3	3.8	3.4
	Rx Sensitivity (dBm)	-37.5	-37.5	-37.6	-37.6	-37.6

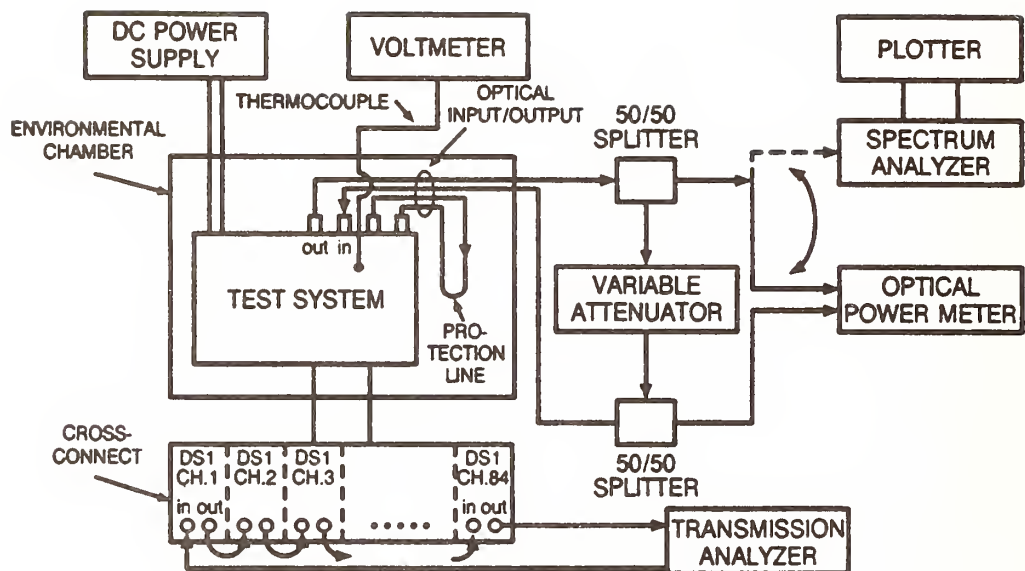


Figure 1. Equipment Set-Up

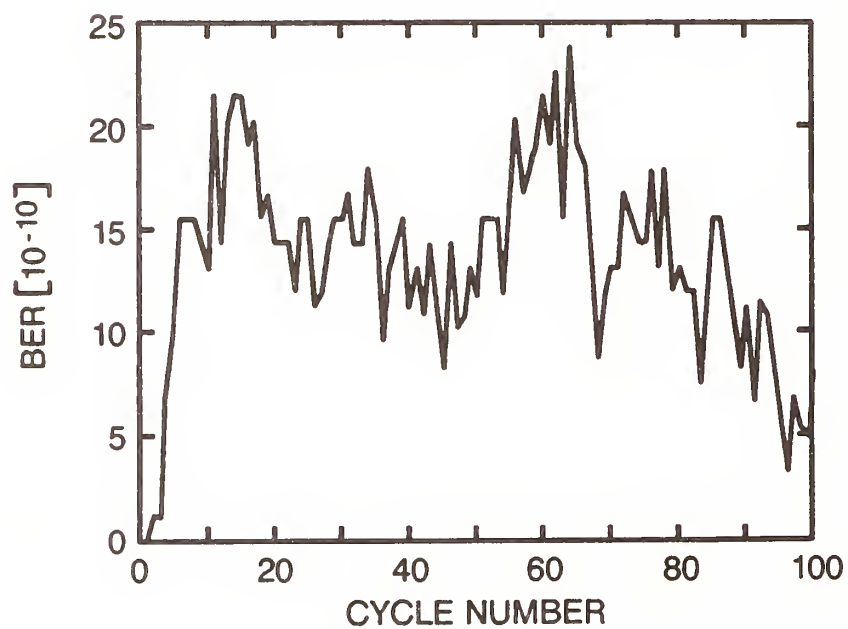


Figure 2. Temperature-Ramp-Induced BER

ACCURATE MODAL CHARACTERIZATION OF PASSIVE COMPONENTS BASED ON SELECTIVE EXCITATION OF OPTICAL FIBERS

D. PAGNOUX, P. FACQ, J-F. SEIGNOLE, J-M. BLONDY
Institut de Recherches en Communications Optiques et Microondes
123, avenue A. Thomas - 87 060 Limoges - FRANCE

INTRODUCTION

It is well known that modal phenomena (differential mode delays, mode coupling and modal attenuations) in multimode fibers and components complicate the predictions of multimode communications performances, by significantly modifying their bandwidth and by changing the nominal value of the received power level. Multimode passive components are typically characterized when the modal equilibrium is realized in the component input fiber. But their characteristics are largely dependent on the incident modal population. On the other hand, the equilibrium of the incident modal population is destroyed after passing through a number of these components, such as fused tapered couplers, misaligned connectors and a wide variety of variable attenuators. These last two considerations show that a mode-by-mode excitation, associated with the modal analysis of the emergent field is absolutely necessary in order to accurately characterize multimode passive components and provide link budget.

In the first section of this paper, we describe a laser source emitting in a tunable wavelength range, between 700 and 900 nm. Into this laser cavity, the selection and switching of pure Laguerre-Gaussian transverse modes of different orders is possible, before launching them in the input fiber of the component under test. Photographs of modes selected in this operational mode generator are shown. The wavelength tunability of the laser is necessary to take into account the wide range of operating wavelengths of the emitting sources used in optical communication systems. For example, the mode generator may be efficiently used to evaluate modal effects in monomode 1300 nm networks operating at 780 nm. The use of 780 nm lasers transmitters and silicon receivers is motivated by their low cost due to their large production for the compact-disc industry [1-4]. The modal behaviour of some passive components, observed in the laboratory, is reported. In section 2, it is shown that the LP_{11} excitation coefficient exhibits a strong azimuthal dependence versus misalignment. Based on this special property, a new accurate source alignment technique is proposed. Experimental results are presented.

I - SELECTIVE MODAL EXCITATION OF OPTICAL FIBERS

Various methods to selectively excite optical fibers have been previously reported. The excitation with a shifted Gaussian spot is very easy to realize. Nevertheless, this method cannot present a good selectivity of the modes in the fiber [5,6]. On the contrary, propagation of pure modes is obtained with side launch excitation of the fiber [7]. An alternate method consists of launching previously synthesized mode structures by means of holography [8], or outer spatial filtering [9]. All these last techniques are difficult to set up, and none of them provides easy modes tunability.

In this paper, the similarity between the transverse modes of a cylindrical laser cavity, and the modes of a graded-index fiber, is used to build a tunable pure mode generator by internally filtering transverse modes of a laser cavity. In order to make possible further modal characterization of passive multimode components, with selected exact Laguerre-Gaussian modes of low and high orders, the cavity must satisfy a number of conditions: 1/ its operating bandwidth must be within the operating wavelength range of optical fibers; 2/ the cavity must exhibit a perfect symmetry of revolution, homogeneous pumping and strong gain; 3/ it should emit a large diameter and high divergence beam.

For these reasons a Ti:sapphire laser cavity pumped by a pulsed YAG laser is chosen to realize the mode generator, as shown in Fig.1. Inside the cavity, a tunable mode filter assigns lines of zeros of the desired mode, using for example networks of fine movable metallic threads. Tubular modes $LP_{\mu 1}$ of different orders have been selected, up to $LP_{15,1}$ mode. Some of them are shown in Fig. 2. A Lyot filter inserted in the cavity allows one to set the operating wavelength from 700 nm to 900 pm. Finally, the selected mode is launched into the input fiber through an optical device which matches the beam size to the size of the mode guided by the fiber.

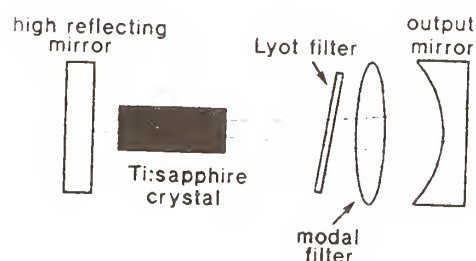


Figure 1: mode generator

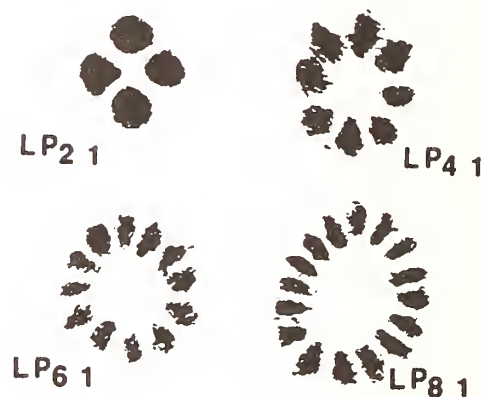


Figure 2: selected Laguerre-Gaussian modes

We have evaluated performances of different kinds of multimode bidirectional Y couplers, nominally 50/50, as well as optical attenuators, when excited by LP_{01} , rotating LP_{11} , and $LP_{\mu 1}$ modes of different orders. Surprising results have been observed, that will be discussed in detail during the conference. For example, nominally 50/50 multimode Y couplers, using Y waveguides in integrated optics, show no significant modal dependencies and a good splitting uniformity. On the other hand, the splitting ratio of Y couplers designed using waveform division depends upon the mode launched into the input fiber, and also strongly depends on the azimuth of the LP_{11} when launched. We have verified that nominally 50/50 fused tapered multimode couplers keep more than 99% of the power in the direct fiber, when excited by very low order modes. Modal effects have been observed and measured in 1300 nm monomode couplers operating at 780 nm, and induced modal noise has been evaluated.

Two multimode optical attenuators (one with 3 dB and the other with 6 dB nominal attenuation) exhibit attenuations lower than respectively 0.7 dB and 2 dB when low order modes are launched. Measured attenuations strongly increase with the order of the input mode.

II - SPECIAL PROPERTIES OF THE LP_{11} MODE : APPLICATION TO A NEW ALIGNMENT TECHNIQUE

In this section, we describe a new application of optical fiber selective excitation, based on azimuthal properties of LP_{11} family. Let us consider the excitation of a parabolic-index fiber by a slightly offset LP_{11} mode. In this case, it can be shown that the injection loss $A(x, \phi)$, expressed in decibels, sinusoidally depends on the mode azimuth [10]:

$$A(x, \phi) = \frac{KV}{a^2} [2 + \cos(2\phi)] x^2 \quad (1)$$

x is the offset amplitude

ϕ is the mode azimuth referenced to the offset direction

$V = k a$ ON, is the normalized spatial frequency of the fiber

a is the core radius

$K = 5 \log_{10}(e) = 2.1715$

$A(x, \phi)$, expressed in decibels, is proportional to x^2 , as established by formula (1). We define a modulation ratio $R = 10 \log_{10}(b/B)$, where b and B respectively are the variation amplitude and the mean value of $P(\phi)$, $P(\phi)$ being the coupled power under rotating LP_{11} excitation.

Considering the observation made above, we can note a linear dependence between R and $\log_{10}x$. Figure 3 shows this dependance for various fiber core radii. A modulation ratio of -30dB corresponds to a residual alignment defect lower than $0,1 \mu m$. Taking advantage of the rotating LP_{11} mode properties, a new alignment technique has been designed for selective modal excitation and for fiber splicing and connecting [11]. This technique consists of minimizing the modulation ratio R measured at the output of the system to be aligned, when excited by a rotating LP_{11} mode. Fig. 4 shows results in an experimental implementation of the method. The rotating LP_{11} mode is generated according to the technique described in section 1, by internal filtering into a continuous HeNe laser cavity.

This measurement method leads to accurate source alignment as well as multimode splices and connectors centering. Being self-referenced, the modulation ratio R is independent of source power level and detector sensitivity drifts.

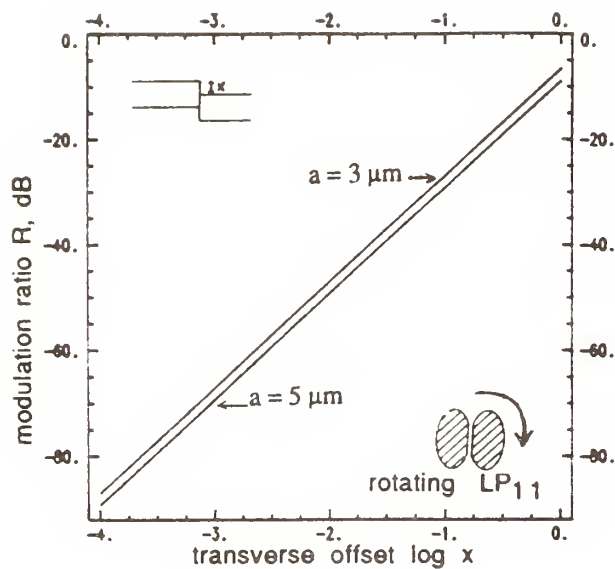


Figure 3: Theoretical dependence of modulation ratio R versus $\log x$; (x : transverse offset in micrometers; nominal monomode fibers used in bimodal regime)

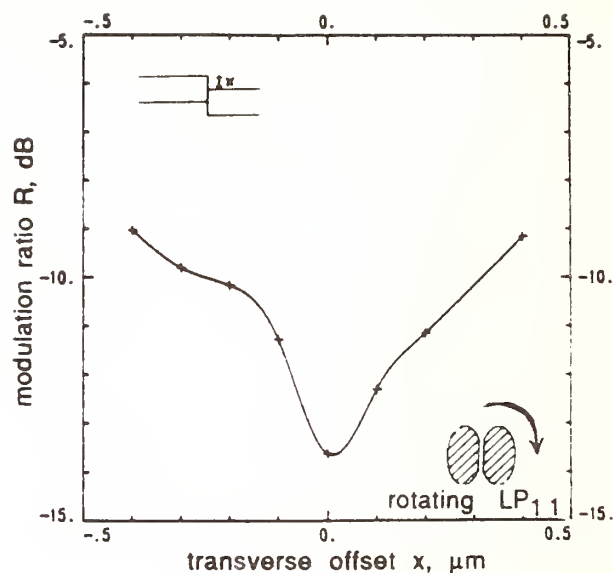


Figure 4: Experimental dependence of modulation ratio R versus transverse offset x . [Monomode fiber ($\lambda_c = 870$ nm) used in bimodal regime ($\lambda = 633$ nm)]

References

- [1] J.L. Mc NAUGHTON, "Fiber to home: an analysis of three alternatives in the united telephone system," SPIE, vol 991, p 246, 1988
- [2] R.L. SODERSTROM et al., "CO laser as a fiber optic source for computer data links," SPIE vol 991, p 179, 1988
- [3] S.J. GILLHAM, O. CAMPBELL, M. CORK, O.W. STOWE, "Single-mode fiber optic transceiver using short wavelength active devices in long wavelength fibers," Proceedings of SPIE, Boston, Sept. 1989
- [4] A. GRAVES "Digital video on fiber: the Heathrow system," Proceedings of OFC, p 164, San Francisco, 1990
- [5] L. JEUNHOMME, J.P. POCHOLLE, "Selective mode excitation of graded-index optical fibers," Applied Optics, vol 17, n° 3, 1978
- [6] M. CALZAVARA, R. CAPONI, F. CISTERNINO, "Selective excitation of annular zones in a graded-index multimode fiber," Journal of Optical Communication, vol5, p82, 1984
- [7] P. SZCZEPANEK, J.W. BERTHOLD III, "Side launch excitation of selected modes in graded-index optical fibers," Applied Optics, vol 17, n° 20, 1978
- [8] S.G. KRIVOSHLYKOV, private communication
- [9] P. FACQ, P. FOURNET, J. ARNAUD, "Observation of tubular modes in multimode graded-index optical fibers," Electronics Letters, vol 16, n° 17, 1980
- [10] P. FACQ, internal report, IRCOM, 1990
- [11] P. FACQ, G. FRESSY, D. PAGNOUX, J-M. BLONDY, J-F. SEIGNOLE, "Dispositif pour le controle et l'ajustement de l'alignement modal des fibres optiques," Patent n° 89 02221

THE MTF FOR COUPLING COMPONENTS

Shao Yang and Alan R. Mickelson
Department of Electrical & Computer Engineering
Campus Box 425
University of Colorado
Boulder, Colorado 80303-0425

Introduction

Component intensive multimode fiber systems such as LANs are not adequately described by simple loss and bandwidth measurements because of the mode selective behavior of the fiber components. Since the performance of individual components is often highly dependent on the modal distribution of the incident power, the behavior of the complete system can exhibit a dependence on the arrangement of its constituent parts. An analytical tool to attempt to quantify some of these basic problems was the mode transmission matrix introduced by Holmes in 1981 [1]. These matrices are an empirical description of the effect of fiber components on 2 or 3 arbitrarily designated mode groups. The utility of the mode transfer matrices is, however, limited by the number of measurements ($n \times n$) required for their determination, as well as by their inherent inaccuracies [2].

The mode transfer function is a generalization of the MTM. By incorporating the basic physics of each device's operation into its mathematical description, it is possible to both improve the accuracy of the model and reduce the number of measurements needed [3]. The transfer function approach has been successfully applied to such components as connectors and splices [2]. In this work, the concept of MTF is extended to the more complicated components such as power splitters. Experiment results fit well the MTF for splitters, which is a modification of the MTF for connectors and splices. Better models are under discussion with more physical insight of the coupling mechanism.

Theory

The MTF is a mode continuum extension of the modal power coupling matrix (MPCM) concept put forward by Mickelson et al. [4]. In the MPCM model, the coupling of power is assumed to take place between adjacent modes and is proportional to the number of modes in each mode group involved. When the source spectrum is wide enough to satisfy [5]

$$\left. \frac{\delta \lambda}{\lambda} \right|_{\text{crit}} > \frac{\sqrt{2\Delta}}{kaN_1} \quad (1)$$

all the modes form a continuum and the coupling matrix transforms into a transfer function which takes the form:

$$T(R, R') = \delta(R - R') - \int dR'' m(R'') \alpha(R'', R) \delta(R - R') + m(R) \alpha(R, R') \quad (2)$$

where the coupling function $\alpha(R, R')$ is given by

$$\alpha(R, R') = \frac{1}{2} \alpha_0 e^{-R^2 - R'^2 / 2\tau} \quad (3)$$

which is assumed to be Gaussian because a large number of mechanisms are involved in the coupling process. Two free parameters τ and α_0 are to be determined by experiment. Measurements of loss and the variation of input and output modal power distributions under one launch condition, usually overfilled launch, are sufficient to determine τ and α_0 .

A 1x2 fused biconical power splitter has two output arms, one called the straight-through arm and the other the coupled arm. The cross section of the fused part of the splitter can be pictured as shown in Figure 1. According to this picture, the following assumptions can be made:

(1) The outer part of both arms is affected more than the inner part by fusion process.

(2) Coupling between higher order modes is stronger than between lower order modes.

(3) Power splitting between the two arms is more symmetrical for higher order modes than lower order modes. It varies from approximately 50/50 for the higher order modes to a much higher ratio for the lower order modes. The coupling function $\alpha(R, R')$ can thus be assumed to have the forms:

$$\alpha_1(R, R') = \alpha_0 S_1(R) e^{-R^2 - R'^2 / \tau(R')} \quad (4)$$

and

$$\alpha_2(R, R') = \alpha_0 S_2(R) e^{-R^2 - R'^2 / \tau(R')} \quad (5)$$

where $S_1(R) + S_2(R) = 1$ are the splitting coefficients and $\tau(R')$ reflects the dependence of coupling on mode order.

It is also possible to use the MPCM approach for power splitters. The matrix will now be a $2n \times 2n$ one. The key to this approach is to find coupling elements between the two arms using the same picture of coupling process as stated above. This approach is still under discussion at present.

Experiment Results

Measurements have been taken on a fused biconical power splitter. By fitting the output nearfield pattern, the free parameters in the coupling and splitting coefficients are determined. Figure 2 shows the fitting curves for both arms along with the output modal power distributions. The results show clearly that power in the lower order modes mostly remains in the straight-through arm and coupling occurs primarily between the higher order modes of the two arms. More results will be presented at the conference.

References

- [1] G. T. Holmes, "Estimation of Concatenated System Response Based on Measured Transfer Functions for Low and High Order Modes," Proc. Seventh European Conf. on Opt. Comm., Copenhagen, 3.4-1-3.4-4 (September 1981).
- [2] S. Yang, I. P. Vayshenker, D. R. Hjelm, and A. R. Mickelson, "A Transfer Function Analysis of Measured Transfer Matrices," Appl. Opt. 28, pp. 3148-3157 (1989).
- [3] S. Yang, D. R. Hjelm, I. P. Vayshenker, and A. R. Mickelson, "A Single Launch Technique for Determination of Mode Transfer Matrices," NIST Symposium on Optical Fiber Measurements 1988.
- [4] A. R. Mickelson, O. Klevhus, and M. Eriksrud, "Backscatter Readout from Serial Microbending Sensors," IEEE/OSA J. Lightwave Technol. LT-2, pp. 700-709 (1984).
- [5] A. R. Mickelson and M. Eriksrud, "Mode-Continuum Approximation in Optical Fibers," Opt. Lett. 7, pp. 572-574 (1982).

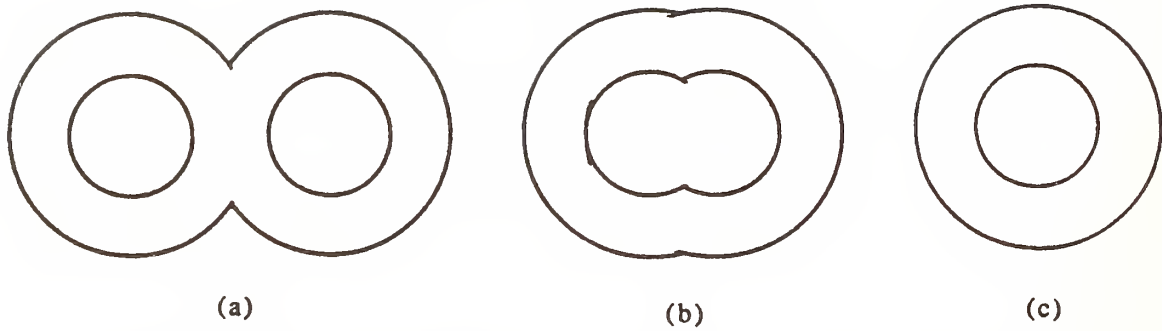


Fig. 1. Picture of fused part of the biconical power splitter. (a) weakly fused, very little coupling between the two arms; (b) moderately fused, coupling mainly between higher order modes, true for most practical case; (c) strongly fused, total overlapping.

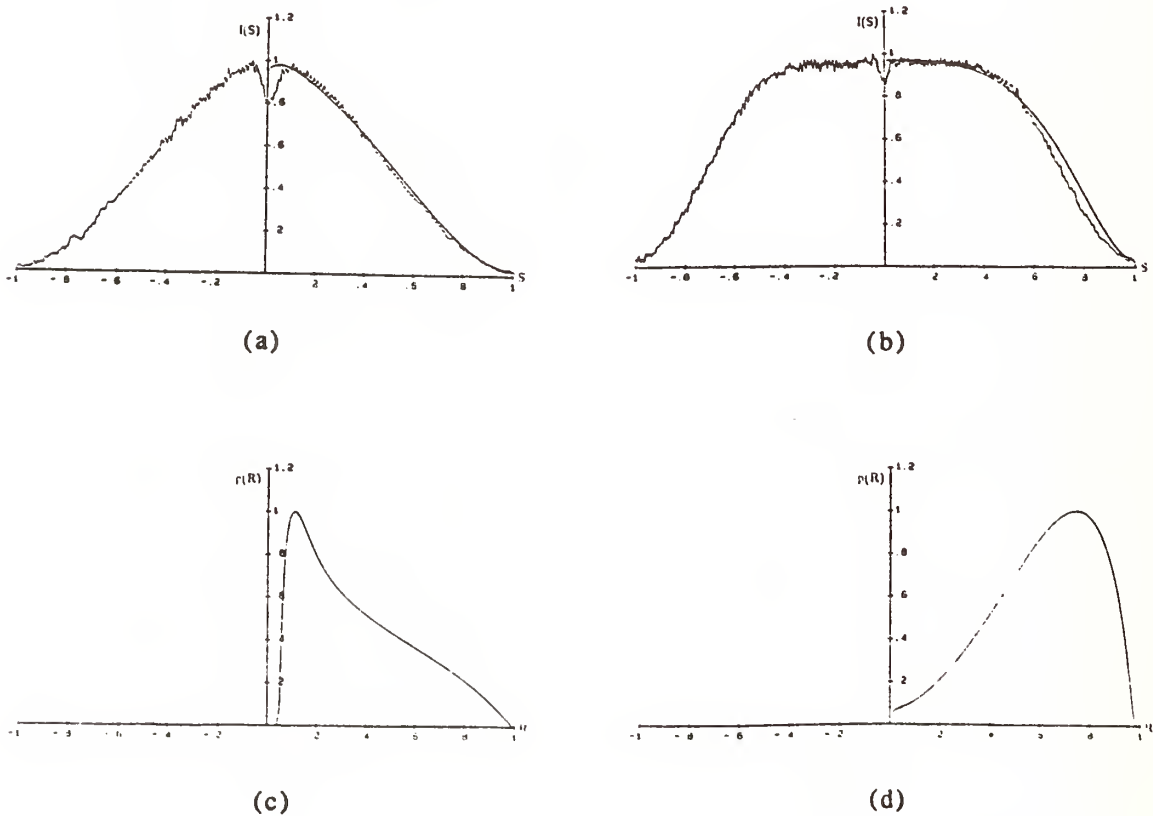


Fig. 2. Output nearfield of (a) arm one and (b) arm two and modal power distribution of (c) arm one and (d) arm two.

Low Reflectance, In-Line, Continuously Variable Attenuator for Lightwave Systems Characterization

V. Shah, L. Curtis, D. D. Mahoney, and W. C. Young

Bellcore

331 Newman Springs Road

Red Bank, NJ 07701

Introduction: Optical reflections from index discontinuities in the optical path can adversely affect the performance of direct-detection, coherent-detection, and analog lightwave communications systems. They can also affect the characterization of laser transmitters and optical amplifiers. Multiple reflections, may cause interferometric conversion of laser phase noise to intensity noise,^[1] resulting in systems degradations and/or measurement limitations. Optical feedback may also cause detrimental changes in the performance characteristics of active components, resulting in further systems degradations and measurement limitations. For example, optical feedback into the laser cavity can increase the mode-partition noise and can add noise due to reflection-induced power fluctuations.^[2] In optical amplifiers, reflections can cause lasing or multiple reflection noise^[3] severely affecting the measurement of amplifier characteristics and can drastically restrict the amounts of amplifier gain and/or reflectance that can be allowed in high-speed systems.

Thus, the characterization of laser transmitters and optical amplifiers, and the improvements in system performance, may require low reflectance connectors, splices, and other optical components. Until recently, most of the work on low reflectance components has been directed towards connectors and splices,^[4,5] but the interest in other low reflectance components is now growing.^[6] In this paper, we present the results of the characterization of a low reflectance, in-line, single-mode fiber, continuously variable attenuator (optical line build-out) with < -65 dB reflectance over the entire attenuation range (0 - 45 dB) and 0.28 dB insertion loss. Angular misalignment loss mechanism, used in a previously reported attenuator,^[7] provides the variable attenuation. However, the low reflectance is achieved by using oblique fiber endfaces appropriately aligned in a continuous V-groove that incorporates an index-matching material.

Principle of operation: Fig. 1 shows the geometry of the low reflectance variable attenuator. With fibers anchored some distance away from the joint, linear displacement of the V - groove in the vertical direction is translated into the angular misalignment at the fiber joint thereby providing continuously variable attenuation. The joint is filled with index-matching oil to provide lubrication

and to reduce the Fresnel reflection losses. To achieve low reflectance, the fiber endfaces at the joint in the attenuator V - groove are polished at an oblique angle $\alpha = 11^\circ$.

However, in contrast to the case of low reflectance splices,^[6] the relative orientation of the obliquely polished endfaces plays an important role in the reflectance performance of the variable attenuator. This is because the fiber axes are parallel, as in a splice, only in the zero attenuation position. In this case, the reflectance value can be shown to be independent of the relative orientation of endfaces at the joint. Away from the zero attenuation position (non-parallel axes), the reflectance depends on the relative orientation of the endfaces as discussed below.

The use of index-matching oil in the joint with obliquely polished endfaces reduces the deflection of the transmitted beam to a negligible value so that, for all practical purposes, transmission is transparent to the oblique angle. Thus, the attenuation performance of the attenuator is identical with or without the obliquely polished endfaces. However, to ensure excellent reflectance performance over the entire range of the attenuator, the relative orientation of endfaces must be carefully chosen. Fig. 2(a) shows the endfaces oriented parallel to each other while Fig. 2(b) shows the orientation corresponding to both endfaces making angle 2α with each other. The beam reflection from the transmitting fiber makes an angle 2α with the fiber axis in both cases. It can also be shown, for both cases, that in the zero attenuation position (solid lines), the beam reflection from the receiving fiber endface enters the transmitting fiber at an angle 2α with the transmitting fiber axis resulting in the excellent reflectance performance. Away from the zero attenuation position (dashed lines), the fiber axes are tilted as shown in Fig. 2. For the parallel orientation, Fig. 2(a), it is observed that the reflection from the receiving fiber endface may enter the transmitting fiber at an angle $< 2\alpha$ for a part of the attenuation range resulting in degraded reflectance performance. However, for the orientation in Fig. 2(b), it is observed that the reflection from the receiving fiber endface always enters the transmitting fiber at an angle $> 2\alpha$. Therefore, the reflectance performance is not degraded as the attenuation is increased. Thus, the orientation in Fig. 2(b) is the optimum one and is therefore used in the fabrication of the attenuator.

Results and Discussion: A variable attenuator with 11° oblique endface angle was fabricated with the endface orientation shown in Fig. 2(b). One fiber was polished with oblique angle extending slightly past the core with the remaining endface perpendicular to the fiber axis. The other fiber was polished at 11° well past the core and the remaining endface was polished at a reverse angle of 30° as shown in Fig. 1. This arrangement minimizes relative lateral motion between the endfaces during the displacement of the V - groove. Fig. 3 shows a theoretical plot (solid line) of the attenuation as a function of angular misalignment at 1540 nm wavelength. The crosses in the

figure represent the measured values of attenuation as a function of the displacement of the V - groove. Good agreement between the measured and the theoretical values suggests that angular misalignment is the major and determining attenuation mechanism. At a wavelength of 1540 nm, the measured insertion loss of the attenuator was 0.28 dB and the measured worst case reflectance, over the entire attenuation range, was < -65 dB.

Conclusion: Based on an angular misalignment loss mechanism, a low reflectance (< -65 dB), in-line, single-mode fiber continuously variable attenuator (0 - 45 dB range) with obliquely polished fiber endfaces was demonstrated. At a wavelength of 1540 nm, the insertion loss was 0.28 dB. The attenuator is a useful component in characterizing lightwave systems and optical amplifiers, and can also be used as a continuously variable optical line build-out.

References:

- [1]. Choy, M. M., et al, Electron. Lett., Vol. 23, p. 1151, (1987).
- [2]. Agrawal, G. et al, IEEE J. of Lightwave Tech., Vol. LT-4, p. 58, (1986).
- [3]. Gimlett, J. L., et al, IEEE Photon. Tech. Lett., Vol. 2, p. 211, (1990).
- [4]. Young, W. C., et al, IEEE Photon. Tech. Lett., Vol. 1, p. 461, (1989).
- [5]. Young, W. C., et al, Proc. 37th IWCS, Reno, Nevada, p. 395, Nov. 15-17, (1988).
- [6]. Benner, A. F., et al, NBS Symp. Opt. Fiber Meas., Boulder, CO, p. 43 (1988).
- [7]. Curtis, L., et al, US Patent No. 4,519,671.

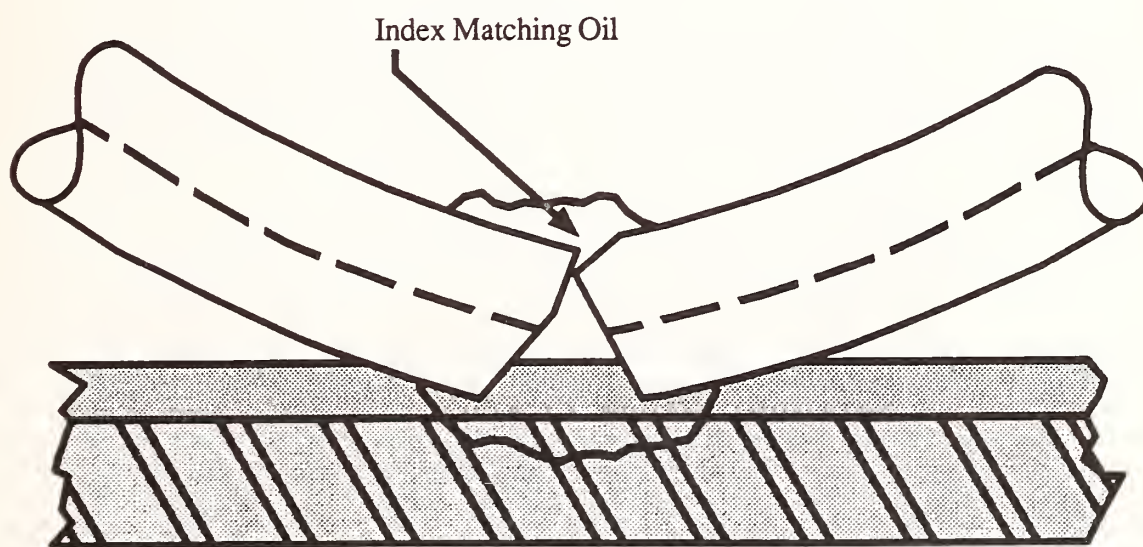


Fig. 1. Geometry of the variable attenuator with obliquely polished fiber endface.

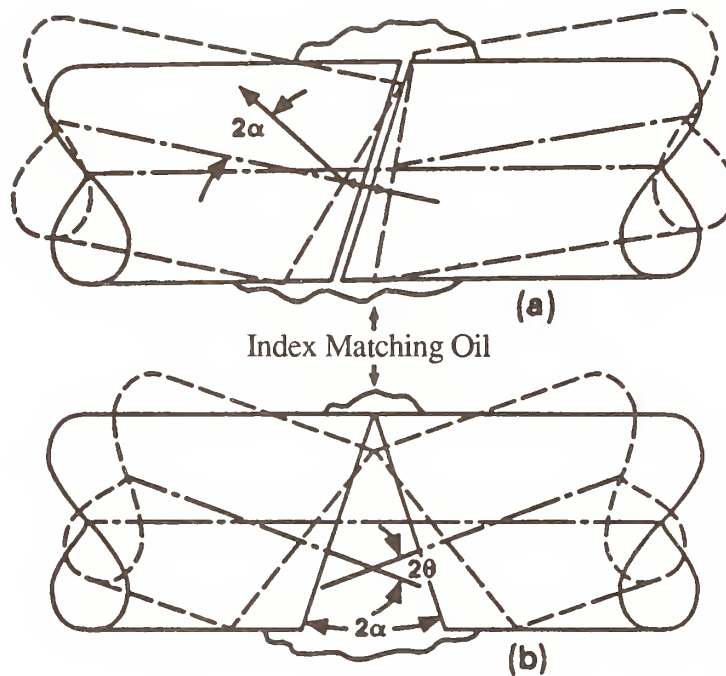


Fig. 2. Two extreme relative orientations of oblique endfaces with (dashed lines) and without (solid lines) angular misalignment between fiber axes. (a) Parallel orientation and (b) the orientation corresponding to the maximum included angle between fiber axes.

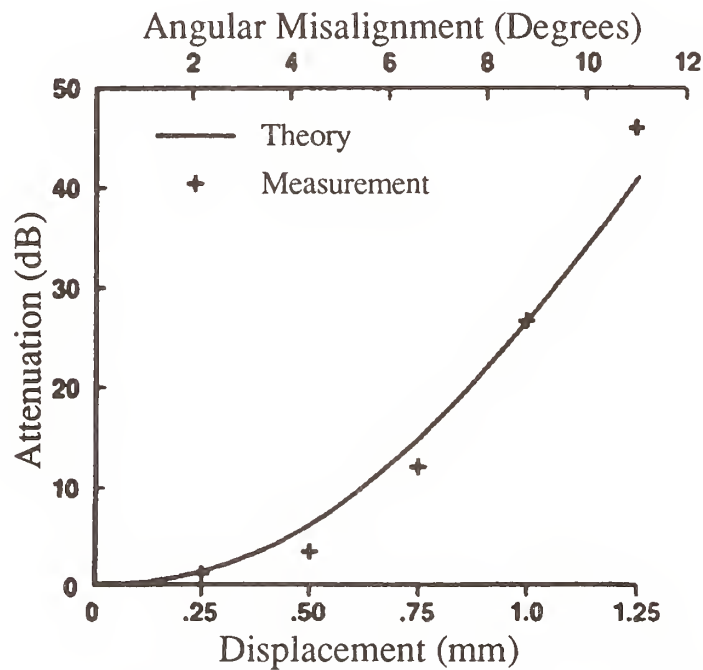


Fig. 3. Theoretical plot of attenuation as a function of the angular misalignment (solid curve). (+) indicates measured attenuation as a function of the displacement of the V - groove.

PhotoRefractive InterModal Exchangers (PRIME) in Optical Fiber: Theory and Applications.

François Ouellette, Université Laval, Département de génie électrique,
Québec, Qué., Canada G1K 7P4

Intermodal couplers in few-mode optical fiber are components of interest for applications in interferometric sensing, wavelength multi-demultiplexing, and all-optical switching. Recent experiments have demonstrated the possibility to optically write intermodal couplers in photosensitive Ge-doped optical fiber. When this fiber is irradiated with intense visible light launched simultaneously in two different modes, the beating of the modes induces a permanent refractive index grating via the photosensitivity of the fiber [1, 2]. This grating subsequently allows power exchange at the irradiation wavelength between the two writing modes, over a wavelength band that depends on the grating length and the beat length dispersion. We have called this new device a PhotoRefractive InterModal Exchanger, or PRIME.

In a general way, a given refractive index grating will allow power exchange between any two modes of the fiber, at any wavelength, providing that the grating period is equal to the intermodal beat length at this wavelength. For example, the dispersion of the intermodal beat length for the LP_{01} and LP_{11} modes allowed us to observe phase-matched mode coupling at 720nm, using a grating written with 488 nm light, where the photosensitivity of the fiber is strongest [3].

Mode coupling with a PRIME, however, is possible only because the index change is not constant across the core of the fiber. The refractive index change due to a simultaneous two-mode irradiation is proportionnal to:

$$\delta n^2 \propto A_1^2 |\vec{e}_1|^2 + A_2^2 |\vec{e}_2|^2 + 2A_1 A_2 (\vec{e}_1 \cdot \vec{e}_2) \cos[(\beta_1 - \beta_2)z] \quad (1)$$

where the A_i 's, \vec{e}_i 's and β_i 's ($i=1,2$) are the amplitudes, modal fields, and propagation constants of mode i . It can be seen that δn^2 is indeed periodic, with a period equal to the intermodal beat length. It is also seen that the periodic part is proportional to the dot product ($\vec{e}_1(r, \phi) \cdot \vec{e}_2(r, \phi)$) of the modal fields used to write the grating. Since the modal fields have specific transverse patterns, this dot product is also a function of the transverse

coordinates. It can usually be separated in two parts, that depend on the radial and azimuthal coordinates:

$$(\vec{e}_1(r, \phi) \cdot \vec{e}_2(r, \phi)) = f_{12}(r) g_{12}(\phi) \quad (2)$$

From this and from the theory of mode coupling by a periodic perturbation, it is then found that the coupling coefficient between two arbitrary modes i and j is proportionnal to:

$$\kappa_{ij} \propto \int_0^\rho f_{12}(r) f_{ij}(r) r dr \int_0^{2\pi} g_{12}(\phi) g_{ij}(\phi) d\phi \quad (3)$$

The second integral in eq.(1) is non-zero only if the product $g_{12}(\phi) g_{ij}(\phi)$ is an even function of ϕ . Thus there are restrictions (selection rules) on the azimuthal dependence of the two modes coupled by a given index grating. Coupling is automatically allowed if the two modes i and j are the modes used to write the PRIME (modes 1 and 2), since g_{12}^2 is always even.

1 meter long PRIME were written in a two-mode circular fiber by exposing it with 400 mW of 488 nm light for half an hour. The power transfer from the LP_{01} to the LP_{11} mode was measured by launching only the LP_{01} mode in the fiber, and measuring the transmission of a white light source filtered by a monochromator, when the fiber is placed between two parallel or crossed polarizers. This measurement revealed a peculiar wavelength dependence, where numerous narrow mode coupling bands appear at and around $\lambda_{irr} = 488$ nm. This result is explained by taking into account the non-degeneracy of the LP_{11} modes, which are in fact linear combinations of the exact fiber modes, i.e. TM_{01} , TE_{01} , and the degenerate even and odd HE_{21} . Since there are three different wavenumbers for these four modes, up to three different refractive index gratings are simultaneously written during the exposure. This is shown graphically on Fig.1(b), where the propagation constant difference between the four exact first order modes of the fiber, and the fundamental mode, are plotted as a function of wavelength. The intersection of the vertical line drawn at λ_{irr} with these three curves gives the three possible grating wavenumbers. Horizontal lines are then drawn from these values, and their intersections with the other two curves gives the wavelengths where phase-matched power exchange can also occur between a different first-order mode and the fundamental mode. Since the first order modes are not linearly polarized, they cannot be totally extinguished by a

crossed polarizer, and transmission peaks and corresponding dips for parallel polarizers are seen at these wavelengths.

We found that the positions of these mode coupling bands are very sensitive on the fiber parameters, i.e. the core radius ρ and the refractive index difference Δ . These parameters could not be known or measured with the accuracy required to fit the experimental spectrum with the theory. Therefore, we adjusted the value of the core radius to obtain an approximate fit. However, an exact fit would probably also require the exact refractive index profile, which may deviate from the assumed step-index profile. Inversely, this spectrum can give useful and precise information on the fiber parameters. Moreover, the positions of the mode coupling bands were also very sensitive on any perturbation of the fiber, like bending or twisting. The PRIME could therefore be a useful tool to study the effect of these perturbations on the fiber, and find applications as a sensor element.

Our experimental results show that the bandwidth of mode coupling can be very small. This bandwidth is plotted on Fig. 2 as a function of the normalized frequency V for a 1 meter long PRIME in a fiber having a core radius $\rho = 2 \mu\text{m}$, and for coupling of the LP_{01} mode with the LP_{11} , LP_{21} and LP_{02} modes. The smallest values occur close to cutoff, and are less than 0.1 nm. The bandwidth is also found to decrease like the square of the core radius, therefore even smaller values can be obtained by a proper fiber design. With such small bandwidths, the PRIME could be useful as a demultiplexer in multi-wavelength optical communication systems. Moreover, it can be shown that if the period of the refractive index grating is linearly chirped, the PRIME can also act as a dispersive filter, and regenerate a signal distorted by the chromatic dispersion of an optical fiber link.

References

- [1] H.G. Park, and B.Y. Kim, Electron. Lett. 25, p.797 (1989).
- [2] François Ouellette, OSA 1989 Annual Meeting Technical Digest, paper MLL6 (1989).
- [3] François Ouellette, Electron. Lett. 25, 1590 (1989).

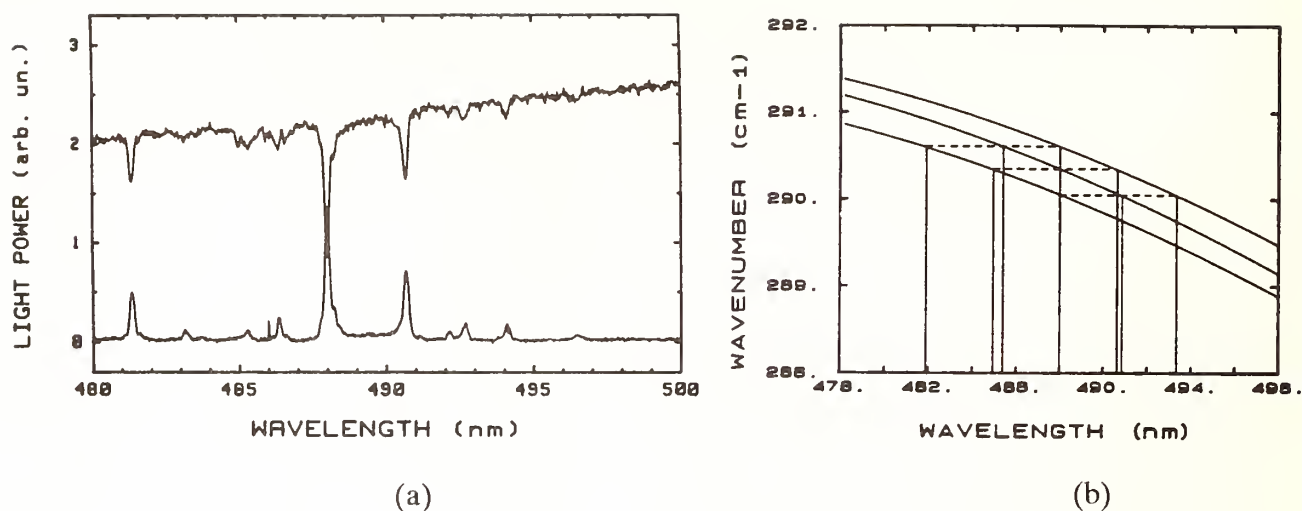


Figure 1

(a) Transmission as a function of wavelength for a PRIME inserted between parallel (upper curve) and crossed (lower curve) polarizers.

(b) Wavenumber difference between the LP_{01} and TE_{01} (upper curve), HE_{21} (middle curve), and TM_{01} (lower curve), as a function of wavelength, showing the phase matched wavelengths for the three gratings written at 488 nm.

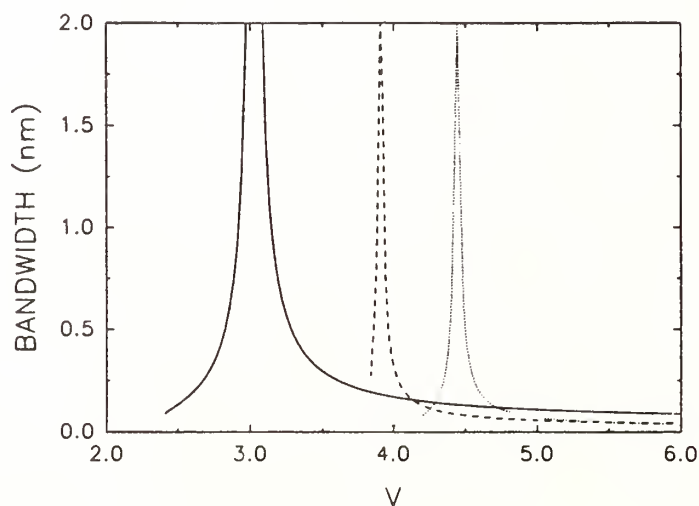


Figure 2

Bandwidth as a function of normalized frequency for a 1 meter long PRIME in a 2 micron core fiber, and coupling between LP_{01} and LP_{11} (solid line), LP_{21} (dashed), LP_{02} (dotted).

AUTHOR INDEX

Allen, J.	7	Jacobs, S. A.	49
Anderson, W. T.	1	Jungerman, R. L.	21
Artiglia, M.	7	Kapron, F. P.	1
Atkins, R. M.	155	Kerslake, R.	167
Aust, J. A.	63	Key, P. L.	15
Baines, J. G. N.	143	Kilkelly, P. D. D.	97
Beaud, P.	35	Kowaliuk, K.	167
Blake, J.	109	Kragh, L. N.	7
Blanchard, P.	31	Kranz, K. S.	43
Blondy, J-M.	183	Kurashima, T.	123
Burgmeijer, J. W.	7	Laming, R. I.	87
Caponio, N.	79	Lee, T. S. F.	179
Carr, J. J.	59	Lemaire, P. J.	43
Cavanagh, B. P.	97	Liese, W.	167
Chang, K. W.	83	Lyle, J.	97
Charczenko, W.	75	Lyons, P. B.	159
Chepyha, T.	163	MacFarlane, N.	147
Chidgey, P. J.	97	Mahoney, D. D.	191
Conrad, G.	83	Mattheus, A.	105
Cook, I. D.	55	Mickelson, A. R.	75,171,187
Curtis, L.	191	Miller, C. M.	101
DeBernardi, C.	67	Miniscalco, W. J.	93
deVries, W. J.	7	Morasca, S.	67
DiMarcello, F. V.	43	Novàk, R. P.	7,35
DiVita, P.	7	Oblas, D. W.	93
Dolfi, D. W.	21	Ohashi, M.	115
Donald, D. K.	27	Ouellette, F.	195
Emig, K. A.	135	Pagnoux, D.	183
Facq, P.	31,183	Pasturczyk, Z.	163
Feth, J.	109	Peckham, D. W.	49
Friebele, E. J.	159	Pelayo, J.	7
Gambini, P.	79	Pellaux, J. P.	119
Ghioni, M.	39	Pilon, P.	167
Giehmann, L.	105	Pitassi, S.	39
Gilgen, H. H.	35	Puleo, M.	79
Gisin, N.	7,119	Raine, K. W.	143
Hallam, A. G.	143	Ramaswamy, R. V.	71
Hickernell, R. K.	63	Reese, J. O.	93
Hjelme, D. R.	75	Ripamonti, G.	39
Hodel, W.	35	Rochereau, J.	31
Horiguchi, T.	123	Rocks, M.	105
Huff, R. G.	43		
Hussell, C. P.	71		

Saikkonen, S. L.	59	Walker, B.	11
Saravanos, C.	139,163	Walker, K. L.	43
Seignole, J-F.	183	Wei, T.	93
Shah, V.	191	Westlake, H. J.	97
Singh, M. P.	93	Williams, D. H.	59
Smith, G. E.	175	Wong, B.	139
Sorin, W. V.	27,83	Wood, H.	163
Srivastava, R.	71	Yadlowsky, M.	171
Stokes, L. F.	101	Yamabayashi, Y.	151
Sundberg, E.	7	Yang, S.	187
Svendsen, D. A.	55,147	Young, M.	129
Takara, H.	151	Young, W. C.	191
Tateda, M.	123	Yuce, H. H.	15
Taylor, E. W.	159	Zongo, P-H.	31
Tsubokawa, M.	115		
Turner, N. P.	143		
Vanoli, S.	39		
Varachi, J. P.	15		
Veasey, D. L.	63		
Von der Weid, J-P.	119		

NIST-114A (REV. 3-89)		U.S. DEPARTMENT OF COMMERCE NATIONAL INSTITUTE OF STANDARDS AND TECHNOLOGY									
BIBLIOGRAPHIC DATA SHEET		1. PUBLICATION OR REPORT NUMBER NIST/SP-792									
		2. PERFORMING ORGANIZATION REPORT NUMBER									
		3. PUBLICATION DATE September 1990									
4. TITLE AND SUBTITLE Technical Digest -- Symposium on Optical Fiber Measurements, 1990											
5. AUTHOR(S) G.W. Day and D.L. Franzen, Editors											
6. PERFORMING ORGANIZATION (IF JOINT OR OTHER THAN NIST, SEE INSTRUCTIONS) U.S. DEPARTMENT OF COMMERCE NATIONAL INSTITUTE OF STANDARDS AND TECHNOLOGY BOULDER, CO 80303-3328		7. CONTRACT/GRANT NUMBER									
8. TYPE OF REPORT AND PERIOD COVERED											
9. SPONSORING ORGANIZATION NAME AND COMPLETE ADDRESS (STREET, CITY, STATE, ZIP) Sponsored by the National Institute of Standards and Technology, in cooperation with the IEEE Optical Communications Committee and the Optical Society of America.											
10. SUPPLEMENTARY NOTES Previous symposia were held in 1980, 1982, 1984, 1986, and 1988. Technical Digests of those were published as NBS Special Publications 597, 641, 683, 720, and 748.											
<input type="checkbox"/> DOCUMENT DESCRIBES A COMPUTER PROGRAM; SF-185, FIPS SOFTWARE SUMMARY, IS ATTACHED.											
11. ABSTRACT (A 200-WORD OR LESS FACTUAL SUMMARY OF MOST SIGNIFICANT INFORMATION. IF DOCUMENT INCLUDES A SIGNIFICANT BIBLIOGRAPHY OR LITERATURE SURVEY, MENTION IT HERE.) This digest contains summaries of 45 papers presented at the Symposium on Optical Fiber Measurements, held September 11-12, 1990, at the National Institute of Standards and Technology, Boulder, Colorado.											
12. KEY WORDS (6 TO 12 ENTRIES; ALPHABETICAL ORDER; CAPITALIZE ONLY PROPER NAMES; AND SEPARATE KEY WORDS BY SEMICOLONS) fiber optics; instrumentation; measurements; optical fiber; reviews											
13. AVAILABILITY <table border="1" style="width: 100%; border-collapse: collapse;"> <tr> <td style="width: 30px; text-align: center;"><input checked="" type="checkbox"/></td> <td>UNLIMITED</td> </tr> <tr> <td style="text-align: center;"><input type="checkbox"/></td> <td>FOR OFFICIAL DISTRIBUTION. DO NOT RELEASE TO NATIONAL TECHNICAL INFORMATION SERVICE (NTIS).</td> </tr> <tr> <td style="text-align: center;"><input checked="" type="checkbox"/></td> <td>ORDER FROM SUPERINTENDENT OF DOCUMENTS, U.S. GOVERNMENT PRINTING OFFICE, WASHINGTON, DC 20402.</td> </tr> <tr> <td style="text-align: center;"><input type="checkbox"/></td> <td>ORDER FROM NATIONAL TECHNICAL INFORMATION SERVICE (NTIS), SPRINGFIELD, VA 22161.</td> </tr> </table>		<input checked="" type="checkbox"/>	UNLIMITED	<input type="checkbox"/>	FOR OFFICIAL DISTRIBUTION. DO NOT RELEASE TO NATIONAL TECHNICAL INFORMATION SERVICE (NTIS).	<input checked="" type="checkbox"/>	ORDER FROM SUPERINTENDENT OF DOCUMENTS, U.S. GOVERNMENT PRINTING OFFICE, WASHINGTON, DC 20402.	<input type="checkbox"/>	ORDER FROM NATIONAL TECHNICAL INFORMATION SERVICE (NTIS), SPRINGFIELD, VA 22161.	14. NUMBER OF PRINTED PAGES 210	
<input checked="" type="checkbox"/>	UNLIMITED										
<input type="checkbox"/>	FOR OFFICIAL DISTRIBUTION. DO NOT RELEASE TO NATIONAL TECHNICAL INFORMATION SERVICE (NTIS).										
<input checked="" type="checkbox"/>	ORDER FROM SUPERINTENDENT OF DOCUMENTS, U.S. GOVERNMENT PRINTING OFFICE, WASHINGTON, DC 20402.										
<input type="checkbox"/>	ORDER FROM NATIONAL TECHNICAL INFORMATION SERVICE (NTIS), SPRINGFIELD, VA 22161.										
		15. PRICE									

ELECTRONIC FORM

NIST *Technical Publications*

Periodical

Journal of Research of the National Institute of Standards and Technology—Reports NIST research and development in those disciplines of the physical and engineering sciences in which the Institute is active. These include physics, chemistry, engineering, mathematics, and computer sciences. Papers cover a broad range of subjects, with major emphasis on measurement methodology and the basic technology underlying standardization. Also included from time to time are survey articles on topics closely related to the Institute's technical and scientific programs. Issued six times a year.

Nonperiodicals

Monographs—Major contributions to the technical literature on various subjects related to the Institute's scientific and technical activities.

Handbooks—Recommended codes of engineering and industrial practice (including safety codes) developed in cooperation with interested industries, professional organizations, and regulatory bodies.

Special Publications—Include proceedings of conferences sponsored by NIST, NIST annual reports, and other special publications appropriate to this grouping such as wall charts, pocket cards, and bibliographies.

Applied Mathematics Series—Mathematical tables, manuals, and studies of special interest to physicists, engineers, chemists, biologists, mathematicians, computer programmers, and others engaged in scientific and technical work.

National Standard Reference Data Series—Provides quantitative data on the physical and chemical properties of materials, compiled from the world's literature and critically evaluated. Developed under a worldwide program coordinated by NIST under the authority of the National Standard Data Act (Public Law 90-396). NOTE: The Journal of Physical and Chemical Reference Data (JPCRD) is published quarterly for NIST by the American Chemical Society (ACS) and the American Institute of Physics (AIP). Subscriptions, reprints, and supplements are available from ACS, 1155 Sixteenth St., NW., Washington, DC 20056.

Building Science Series—Disseminates technical information developed at the Institute on building materials, components, systems, and whole structures. The series presents research results, test methods, and performance criteria related to the structural and environmental functions and the durability and safety characteristics of building elements and systems.

Technical Notes—Studies or reports which are complete in themselves but restrictive in their treatment of a subject. Analogous to monographs but not so comprehensive in scope or definitive in treatment of the subject area. Often serve as a vehicle for final reports of work performed at NIST under the sponsorship of other government agencies.

Voluntary Product Standards—Developed under procedures published by the Department of Commerce in Part 10, Title 15, of the Code of Federal Regulations. The standards establish nationally recognized requirements for products, and provide all concerned interests with a basis for common understanding of the characteristics of the products. NIST administers this program as a supplement to the activities of the private sector standardizing organizations.

Consumer Information Series—Practical information, based on NIST research and experience, covering areas of interest to the consumer. Easily understandable language and illustrations provide useful background knowledge for shopping in today's technological marketplace.

Order the above NIST publications from: Superintendent of Documents, Government Printing Office, Washington, DC 20402.

Order the following NIST publications—FIPS and NISTIRs—from the National Technical Information Service, Springfield, VA 22161.

Federal Information Processing Standards Publications (FIPS PUB)—Publications in this series collectively constitute the Federal Information Processing Standards Register. The Register serves as the official source of information in the Federal Government regarding standards issued by NIST pursuant to the Federal Property and Administrative Services Act of 1949 as amended, Public Law 89-306 (79 Stat. 1127), and as implemented by Executive Order 11717 (38 FR 12315, dated May 11, 1973) and Part 6 of Title 15 CFR (Code of Federal Regulations).

NIST Interagency Reports (NISTIR)—A special series of interim or final reports on work performed by NIST for outside sponsors (both government and non-government). In general, initial distribution is handled by the sponsor; public distribution is by the National Technical Information Service, Springfield, VA 22161, in paper copy or microfiche form.

U.S. DEPARTMENT OF COMMERCE
National Institute of Standards and Technology
(formerly National Bureau of Standards)
325 Broadway
Boulder, Colorado 80303-3328

OFFICIAL BUSINESS
PENALTY FOR PRIVATE USE, \$300